# BACKCALCULATION OF ASPHALT CONCRETE COMPLEX MODULUS CURVE BY LAYERED VISCOELASTIC SOLUTION

By

Ligang Lei

### A DISSERTATION

Submitted to
Michigan State University
In partial fulfillment of the requirements
For the degree of

DOCTOR OF PHILOSOPHY

**Civil Engineering** 

2011

### **ABSTRACT**

# BACKCALCULATION OF ASPHALT CONCRETE COMPLEX MODULUS CURVE BY LAYERED VISCOELASTIC SOLUTION

By

### Ligang Lei

In-situ evaluation of material properties is very important for estimating the structural adequacy of a pavement section under traffic loading. The fundamental material property for the AC layer in a flexible pavement is the complex modulus |E\*| or the equivalent relaxation modulus E(t). In-situ |E\*| can be used as a quality control tool as well as in estimation of remaining service life of existing pavements, and it is a critical input to the new Mechanism-Empirical Pavement Design Guide (M-E PDG). In this research, a method is presented to backcalculate |E\*| or E(t) for the AC layer, in addition to base and subgrade layer moduli, using Falling Weight Deflectometer (FWD) surface deflection time histories. First, the deflection time histories from FWD test data were separated as the dynamic response part, and the viscoelastic response part: The time delay of each sensor is related to wave propagation through the pavement system while the shifted deflection time history without time delay can be considered as the viscoelastic response of the pavement. Second, the time delay of each sensor was used to estimate the elastic modulus of the subgrade layer, based on the wave propagation theory. Third, a forward layered viscoelastic solution was developed based on Schapery's 'quasi-elastic' approximation. Finally, backcalculation was numerically done by Newton's method, and followed by the MATLAB internal function 'fminsearch', to match the predicted deflection time histories from estimated modulus of each layer against the shifted measurement from the FWD test. The backcalculation results show very good agreement with the actual modulus values for both numerical examples and field FWD test data. The error in the base and subgrade moduli is generally less than 3%. The AC layer relaxation and complex modulus curves match the actual functions within the ranges of 0.0001 to 0.1 sec, and 10 to 10,000 Hz, respectively. The sensitivity analysis shows that errors in the deflection time-histories are the most significant factor affecting the backcalculated AC relaxation and complex modulus curves. Also, the layer thicknesses should be as accurate as possible.

TO MY PARENTS, FAMILY AND FRIENDS

### **ACKNOWLEDGEMENT**

The author would like to express his great appreciation to his major advisor Dr. Karim Chatti, Professor of Civil Engineering at Michigan State University, for his continuous academic and financial support throughout the author's study at Michigan State University and while preparing this dissertation. The author would like to thank his co-advisor, Dr. Emin Kutay, Assistant Professor of Civil Engineering, for his valuable suggestions and kind help. This dissertation could not have been completed without their help. The author also appreciated help from other committee members, Dr. Gilbert Baladi, Professor of Civil Engineering, and Dr. Tom Pence, Professor of Mechanical Engineering, for their continuous advice and support.

Thanks are also due to the Federal Highway Administration (FHWA) for financially sponsoring this research, and to the author's graduate student colleagues at the Department of Civil and Environmental Engineering at MSU.

Last but not least, the author would like to thank his wife, Huajing Yang, for her continuous and unselfish support and company throughout his stay at Michigan State University.

# TABLE OF CONTENTS

LIST OF TABLES	ix
LIST OF FIGURES	xii
Chapter 1. Introduction	1
Chapter 2. Literature Review and Background	5
2.1 Backcalculation Approach	
2.1.1 Static Backcalculation Methods     2.1.2 Dynamic Backcalculation Methods	
2.2 Primary Response Behavior of Asphalt Concrete	8
2.3 Interconversion between E(t) and  E*  for AC Mixture	13
2.4 Interconversion between E(t) and D(t) for AC Mixture	15
2.5 Motivation for the Study	
Chapter 3. Estimating the Subgrade Elastic Modulus using Wave Propagation Med	
3.1 Introduction	22
3.2 Proposed Method to Estimate k-value	23
3.2.1 Theoretical Formulation for Spectral Element Method	
3.2.2 Dominant Frequency of the FWD Test	
3.2.3 Numerical Example to Calculate k-value	
3.2.4 Sensitivity Analysis for k-value	33
3.3 Proposed Procedure to Estimate Subgrade Elastic Modulus	38
3.4 Verification of the Proposed Method	42
3.4.1 SAPSI	42
3.4.2 LAMDA	
3.4.3 Case of Subgrade without Ground Water Table	
3.4.4 Case of Subgrade with GWT	46
3.5 Validating the Proposed Method Using Case Studies from LTPP	
3.5.1 Example of FWD Test at LTPP 04-1036 Station in 1998	
	49
3.5.2 Example of FWD Test at LTPP 32-0101 Station in 1996	
3.5.2 Example of FWD Test at LTPP 32-0101 Station in 1996	

3.5.4.2 Effect of Sampling Intervals	63
3.6 Numerical Example of Bedrock under Subgrade layer	64
3.7 Summary	67
Chapter 4. Layered Viscoelastic Forward Solution	
4.1 Introduction	68
4.2 Layered Viscoelastic Forward Solution Algorithm	68
4.3 Verification of the Layered Viscoelastic Forward Solution	76 78 83
4.4 Time Efficiency for Layered VE Forward Solution	91
4.5 Summary	
Chapter 5. Backcalculation Algorithm	
5.1 Introduction	94
5.2 Variable Identification	94
5.3 Variable Boundaries	95
5.4 Inverse Solution Theory	
5.4.1 Basic Theory Background	99
5.4.2 SVD Method	
5.4.3 Truncating Singular Values	
5.5 VE backcalculation of E(t)	
5.6 VE backcalculation of $ E^* $	
5.6.2 Calculation of E(t) and φ from  E*  by Iteration	
5.6.3 Calculation of E(t) from $ E^*(\omega) $ by Iteration $\varphi(\omega)$	112
<b>5.7 One Numerical Example of Backcalculation Result.</b> 5.7.1 Result of VE backcalculation of E(t)	116
5.8 Summary	
Chapter 6. Verification and Sensitivity Analysis	

6.1 Introduction	121
6.2 Verification of the VE Backcalculation Algorithm	121
6.2.1 VE Backcalculation using Time Histories from VE Solution	
6.2.1.1 Numerical Example 1	
6.2.1.2 Numerical Example 2	129
6.2.1.3 Numerical Example 3	
6.2.1.4 Numerical Example 4	
6.2.1.5 Discussion	
6.2.2 VE Backcalculation using Time Histories from Dynamic Solutions	
6.2.2.1 Example 5: Michigan Site	
6.2.2.2 Example 6: Texas Site	
6.2.2.3 Example 7: Florence Site	
6.2.2.4 Example 8: Kansas Site	
6.2.2.5 Discussion	158
6.2.3 VE Backcalculation using Field FWD Test Data.	158
6.2.3.1 FWD Test Conducted at L9S4	
6.2.3.2 FWD Test Conducted at L10S4	
6.2.3.3 FWD Test Conducted at L11S4	
6.2.3.4 Discussion	
6.3 Sensitivity Analysis for the AC Layer	
6.3.1 Sensitivity Analysis for Deflection Measurement of the First Sensor	
6.3.2 Sensitivity Analysis for Time Shift Error of the First Sensor	
6.3.3 Sensitivity Analysis for Post-Peak Time Offset of the First Sensor	
6.3.4 Sensitivity Analysis for Layer Thickness	
6.3.5 Discussion of Sensitivity Analyses	186
6.4 Summary	186
Chapter 7. Conclusions and Recommendations	188
7.1 Summary	188
7.2 Conclusions	189
7.3 Recommendations	
RIRI IOCD ADHV	102

## LIST OF TABLES

Table 1. Prony series coefficients for E(t) and D(t) for a typical AC mixture
Table 2: The equivalent frequency for different load duration times
Table 3: The average k-value for different cases of Poisson's ratio
Table 4: Basic information of a three-layer pavement structure without GWT 4-
Table 5: Time delay of each sensor simulated by SAPSI
Table 6: Basic information for a three-layer pavement structure with GWT
Table 7: Time delay of each sensor by LAMDA
Table 8: Time delay and peak deflection of each sensor due to the FWD test at station 04-1036 in 1998
Table 9: Structural information and MODCOMP5 backcalculated modulus at LTPP station 04-1036 in 1998
Table 10: Time delay and maximum deflection of sensors during the FWD test at LTP station 32-0101 in 1996
Table 11: Basic information and MODCOMP5 backcalculated modulus at LTPP station 32-0101 in 1996 (Trial: I)
Table 12: Basic information and MODCOMP5 backcalculated modulus at LTPP station 32-0101 in 1996 (Trial: II)
Table 13: Elastic modulus of the subgrade layer at LTPP station 32-0101 in 1996 5:
Table 14: Time delay and maximum deflection of the sensors due to the FWD test at LTP station 06-0565 in 1999
Table 15: Structural information and MODCOMP5 backcalculated modulus at LTPP station 06-0565 in 1999 (Trial: I)
Table 16: Structural information and MODCOMP5 backcalculated modulus at LTPP station 06-0565 in 1999 (Trial: II)
Table 17: Elastic modulus of the subgrade layer at station 06-0565 in 1999
Table 18: Results of data regression of resilient modulus on stress parameters using Uza

and Cornell Models 61
Table 19: The stress status of the subgrade layer in the FWD test for different $K_0$ values 62
Table 20: The range of elastic moduli predicted by nonlinear models, measured in the lab, estimated by the proposed method, and backcalculated by MODCOMP5 for the case studies (MPa)
Table 21: Arrival time for S-wave and R-wave for each sensor due to the FWD test 64
Table 22: Material properties of a three-layer pavement structure with bedrock
Table 23: Time delay of each sensor by SPASI simulation with bedrock
Table 24: Material properties of the pavement structure used in the verification example 76
Table 25: Properties of a pavement used in comparison of dynamic and VE solutions 80
Table 26: Several examples of pavement structure in the SPS-1 project
Table 27: Layer information for each pavement structure 84
Table 28: The computation times for different numbers of discrete time steps
Table 29: The  E*  parameters for different AC mixtures
Table 30: The average and boundaries for the four parameters of  E*
Table 31: The E(t) parameters for different AC mixtures
Table 32: The mean and boundaries for the four parameters of E(t)
Table 33: Basic information of a three-layer pavement structure and backcalculated result
Table 34: Basic information of pavement structure and backcalculated result for numerical example 1
Table 35: Basic information of pavement structure and backcalculated result for numerical example 2
Table 36: Basic information of pavement structure and backcalculated result for numerical example 3
Table 37: Basic information of pavement structure and backcalculated result for numerical example 4
Table 38: Basic information of Michigan pavement structure and backcalculated results 142

Table 39: Basic information of Texas pavement structure and backcalculated results 1	.46
Table 40: Basic information of a Florence pavement structure and backcalculated result. 1	.50
Table 41: Basic information of a Kansas pavement structure and backcalculated result 1	.54
Table 42: Basic information of L9S4 pavement structure and backcalculated result 1	.59
Table 43: Basic information of L10S4 pavement structure and backcalculated result 1	61
Table 44: Basic information of L11S4 pavement structure and backcalculated result 1	.63
Table 45: Layer information of each pavement structure for sensitivity analysis	66

# LIST OF FIGURES

Figure 1: Organization of this dissertation	3
Figure 2: Sinusoidal Stress and Strain in cyclic loading	9
Figure 3: Mastercurve  E*  of one asphalt concrete mixture (PG64-28)	10
Figure 4: Phase angle $\varphi(\omega)$ of one asphalt concrete mixture (PG64-28)	.11
Figure 5: Physical meaning of each parameter on the sigmoidal function	12
Figure 6: Relaxation modulus  E(t)  of one asphalt concrete mixture (PG64-28)	13
Figure 7: The generalized Maxwell model	14
Figure 8: E(t) and D(t) from interconversion for a typical AC mixture	19
Figure 9: Wave system from surface point source in ideal medium	30
Figure 10: Phase angle of each point at the surface for a specific example (t =0 s)	32
Figure 11: Sensitivity analysis for k-value (v= 0.20)	34
Figure 12: Sensitivity analysis for k-value (v= 0.25)	34
Figure 13: Sensitivity analysis for k-value (v= 0.30)	35
Figure 14: Sensitivity analysis for k-value (v= 0.35)	35
Figure 15: Sensitivity analysis for k-value (v= 0.40)	36
Figure 16: Sensitivity analysis for k-value (v= 0.45)	36
Figure 17: Sensitivity analysis for k-value (v= 0.49)	37
Figure 18: Example of FWD load and deflection time histories at LTPP station 04-1036 1998.	in 39
Figure 19: Time delay vs. location for the example of FWD test at LTPP station 04-1036 1998.	
Figure 20: Flow chart to estimate subgrade elastic modulus using k-value	41
Figure 21: Time delay vs. location for a numerical example of FWD test (without GWT).	45
Figure 22: LAMDA simulated time-history due to the FWD test (with GWT)	47

Figure 23: LAMDA simulated time-delay for the FWD test (with GWT)
Figure 24: Deflection basin from FWD test and MODCOMP5 Simulation at LTPP station 04-1036 in 1998
Figure 25: Example of FWD test results at LTPP station 32-0101 in 1996
Figure 26: Deflection basin due to the FWD test and two cases of MODCOMP5 simulation at LTPP station 32-0101 in 1996
Figure 27: Example of the FWD test history at LTPP station 06-0565 in 1999 57
Figure 28: Deflection basin during the FWD test and two cases of MODCOMP5 simulation at LTPP station 06-0565 in 1999
Figure 29: SAPSI simulated time-history of FWD test with bedrock underneath
Figure 30: Time delay vs. location for a numerical example of FWD test with bedrock 66
Figure 31: Typical geometry of a pavement structure
Figure 32: Discretization of stress history
Figure 33: Discretization of the relaxation modulus mastercurve
Figure 34: Deflections calculated for points at different distances from the centerline of the circular load at the surface
Figure 35: Illustration of the $d\sigma( au_j)$ in Eq. (32b) for each time step $ au_j$
Figure 36: Example of a pavement structure used for VE forward calculation
Figure 37: Examples of computed VE surface deflections at different radial distances from the centerline of the load
Figure 38: Implemented and actual E(t) for one AC mixture
Figure 39: Implemented and actual E(t) for one AC mixture
Figure 40: FWD test simulation by layered VE solution for a half-space AC layer
Figure 41: Sensor deflection time histories predicted by SAPSI
Figure 42: Sensor deflection time histories predicted by LAMDA
Figure 43: Comparison of deflection time histories from VE and SAPSI solutions
Figure 44: Comparison of deflection time histories from VE and LAMDA solutions 82

Figure 45: Time-shifted dynamic solution and VE solution for case 116	85
Figure 46: Time-shifted dynamic solution and VE solution for case 117	86
Figure 47: Time-shifted dynamic solution and VE solution for case 120	87
Figure 48: Time-shifted dynamic solution and VE solution for case 123	88
Figure 49: Time-shifted SAPSI and VE solution for shallow bedrock	90
Figure 50: Sensitivity analysis for relative error of maximum deflection between solution and SAPSI with bedrock depth	
Figure 51: Random Function to avoid local minimum problem.	105
Figure 52: Algorithm of backcalculation procedure of E(t)	106
Figure 53: Algorithm for Calculation of $E(t)$ and $\phi$ from $ E^* $ by iteration	.111
Figure 54: Algorithm for Calculation of $E(t)$ from $ E^* $ by iteration $\phi$	.113
Figure 55:  E*  input and calculated after converting to E(t) for one AC mixture	.114
Figure 56: Algorithm of backcalculation procedure of  E*	.115
Figure 57: Input and backcalculated time-histories of E(t) in the numerical FWD test	.117
Figure 58: Input and backcalculated E(t) for the numerical FWD test	.117
Figure 59: Input and backcalculated time-histories of $ E^* $ in the numerical FWD test	.119
Figure 60: Input and backcalculated  E*  for the numerical FWD test	.119
Figure 61: Available range in E(t) function from field FWD test backcalculation	. 122
Figure 62: Useful range in  E*  function from field FWD test backcalculation	123
Figure 63: Input and simulated time-histories by backcalculation of E(t) in example 1	125
Figure 64: Input and backcalculated E(t) in example 1	125
Figure 65: Input and simulated time-histories by backcalculation of  E*  in example 1	126
Figure 66: Input and backcalculated  E*  in example 1	. 127
Figure 67: Input and backcalculated φ in example 1	128
Figure 68: Input and simulated time-histories by backcalculation of E(t) in example 2	130

Figure 69: Input and backcalculated of E(t) in example 2	31
Figure 70: Input and simulated time-histories by backcalculation of $ E^* $ in example 2 13	32
Figure 71: Input and backcalculated of  E*  in example 2	32
Figure 72: Input and simulated time-histories by backcalculation of E(t) in example 3 13	34
Figure 73: Input and backcalculated E(t) in example 3	35
Figure 74: Input and simulated time-histories by backcalculation of  E*  in example 3 13	35
Figure 75: Input and backcalculated  E*  in example 3	36
Figure 76: Input and simulated time-histories by backcalculation of E(t) in example 4 13	38
Figure 77: Input and backcalculated E(t) in example 4	38
Figure 78: Input and simulated time-histories by backcalculation of $ E^* $ in example 4 13	39
Figure 79: Input and backcalculated  E*  in example 4	40
Figure 80: Input and simulated time-histories by backcalculation of E(t) in Michigan site14	43
Figure 81: Input and backcalculated E(t) in Michigan site	43
Figure 82: Input and simulated time-histories by backcalculation of  E*  in Michigan site14	14
Figure 83: Input and backcalculated  E*  in Michigan site	45
Figure 84: Input and simulated time-histories by backcalculation of E(t) in Texas site 14	47
Figure 85: Input and backcalculated E(t) in Texas site	47
Figure 86: Input and simulated time-histories by backcalculation of  E*  in Texas site 14	48
Figure 87: Input and backcalculated  E*  in Texas site	49
Figure 88: Input and backcalculation simulated time-histories using E(t) in Florence site 15	51
Figure 89: Input and backcalculated E(t) in Florence site	51
Figure 90: Input and backcalculation simulated time-histories using  E*  in Florence site 15	52
Figure 91: Input and backcalculated  E*  in Florence site	53
Figure 92: Input and simulated time-histories by backcalculation of E(t) in Kansas site 15	55
Figure 93: Input and backcalculated E(t) in Kansas site	55

Figure 94: Input and simulated time-histories by backcalculation of $ E^* $ in Kansas site 15	56
Figure 95: Input and backcalculated  E*  in Kansas site	57
Figure 96: Input and simulated time-histories by backcalculation of E(t) in L9S4 site 16	<b>5</b> 0
Figure 97: Input and backcalculated E(t) in L9S4 site	<b>5</b> 0
Figure 98: Input and simulated time-histories by backcalculation of E(t) in L10S4 site 16	52
Figure 99: Input and backcalculated E(t) in L10S4 site	52
Figure 100: Input and simulated time-histories by backcalculation of $E(t)$ in L11S4 site . 16	54
Figure 101: Input and backcalculated E(t) in L11S4 site	54
Figure 102: Error caused by time shift of entire pulse for one sensor	57
Figure 103: Error caused by expansion/contraction of deflection pulse in the post-peak zon for one sensor	
Figure 104: Sensitivity analysis of  E*  for deflection measurement error (Case A) 16	58
Figure 105: Sensitivity analysis of E(t) for deflection measurement error (Case A) 16	59
Figure 106: Sensitivity analysis of  E*  for deflection measurement error (Case B) 16	59
Figure 107: Sensitivity analysis of E(t) for deflection measurement error (Case B) 17	70
Figure 108: Sensitivity analysis of $ E^* $ for deflection measurement error (Case C) 17	70
Figure 109: Sensitivity analysis of E(t) for deflection measurement error (Case C) 17	71
Figure 110: Sensitivity analysis of $ E^* $ for deflection measurement error (Case D) 17	71
Figure 111: Sensitivity analysis of E(t) for deflection measurement error (Case D) 17	72
Figure 112: Sensitivity analysis of  E*  for time shift error of sensor 1 (Case A)	73
Figure 113: Sensitivity analysis of E(t) for time shift error of sensor 1 (Case A)	73
Figure 114: Sensitivity analysis of  E*  for time shift error of sensor 1 (Case B)	74
Figure 115: Sensitivity analysis of E(t) for time shift error of sensor 1 (Case B)	74
Figure 116: Sensitivity analysis of  E*  for time shift error of sensor 1 (Case C)	75
Figure 117: Sensitivity analysis of E(t) for time shift error of sensor 1 (Case C)	75
Figure 118: Sensitivity analysis of  E*  for time shift error of sensor 1 (Case D)	76

Figure 119: Sensitivity analysis of E(t) for time shift error of sensor 1 (Case D)
Figure 120: Sensitivity analysis of  E*  for post-peak time offset of sensor 1 (Case A) 17
Figure 121: Sensitivity analysis of E(t) for post-peak time offset of sensor 1 (Case A) 17
Figure 122: Sensitivity analysis of  E*  for post-peak time offset of sensor 1 (Case B) 17
Figure 123: Sensitivity analysis of E(t) for post-peak time offset of sensor 1 (Case B) 175
Figure 124: Sensitivity analysis of  E*  for post-peak time offset of sensor 1 (Case C) 175
Figure 125: Sensitivity analysis of (t) for post-peak time offset of sensor 1 (Case C) 186
Figure 126: Sensitivity analysis of $ E^* $ for post-peak time offset of sensor 1 (Case D) 180
Figure 127: Sensitivity analysis of E(t) for post-peak time offset of sensor 1 (Case D) 18
Figure 128: Sensitivity analysis of  E*  for layer thickness (Case A)
Figure 129: Sensitivity analysis of E(t) for layer thickness (Case A)
Figure 130: Sensitivity analysis of  E*  for layer thickness (Case B)
Figure 131: Sensitivity analysis of E(t) for layer thickness (Case B)
Figure 132: Sensitivity analysis of  E*  for layer thickness (Case C)
Figure 133: Sensitivity analysis of E(t) for layer thickness (Case C)
Figure 134: Sensitivity analysis of  E*  for layer thickness (Case D)
Figure 135: Sensitivity analysis of E(t) for layer thickness (Case D)

# **Chapter 1. Introduction**

Asphalt concrete (AC) mixtures consist of asphalt binder and aggregates from crushed stone or from natural resources. They were first used for pavement in 1870 in Newark, New Jersey. According to the Federal Highway Administration (FHWA, 2001), 2.5 million miles of road are paved in the USA, and 94% are paved with AC, i.e., about 2.3 million miles of road are surface-covered by AC, or approximately 9 times the distance to the moon. About 300 million tons of AC mixtures are used in highway construction every year (Papagiannakis and Masad, 2008).

Before the 1920s, only the thickness of pavement was considered in pavement design and analysis. It was believed the thicker the pavement, the longer the pavement would last. After many years of experience, three key factors are found to significantly affect pavement life: traffic or loading, environment and material properties. Traffic information is estimated by regional planning departments, while national weather stations can provide environmental conditions for a specific location. The remaining challenge for pavement engineering is the material properties of the pavement, especially the onsite materials used many years ago.

In recent years, the falling weight deflectometer (FWD) test has been the typical method for evaluating the material properties of in-service pavement. In order to accurately evaluate pavement structure, several FWD tests with different load levels are usually performed at the same location. The structural condition, or layer modulus, is the key factor for determining pavement rehabilitation strategies.

The material property is usually obtained through static or dynamic backcalculation methods,

in which layer moduli are determined by matching the deflection basin measured under a known load in the FWD test, with the deflection basin generated through a theoretical model of the pavement (Ji, 2005).

Static backcalculation is mainly based on the layered linear elastic solution, while dynamic backcalculation modifies the linear elastic property into the damped elastic property for each physical layer. However, both models of the pavement structure are theoretically incorrect, because the primary response, i.e., small load-level response, of AC mixture is viscoelastic, rather than elastic. The mechanical behaviors of viscoelastic materials are quite different from those of the elastic or damped elastic material, for example, granular materials, aggregate base, or subgrade.

The objective of this research is to develop a robust methodology to backcalculate the  $|E^*|$  and E(t) mastercurve of the AC layer, and the elastic moduli of unbound layers.

The dynamic effect due to the FWD test should be investigated first, and the pavement response is expected to be simplified as a viscoelastic response. Additionally, the elastic modulus of the subgrade layer can be estimated or identified from the dynamic response. After that, a pavement structure is simulated as viscoelastic system, and backcalculation is done in viscoelastic solution. A brief flowchart and the explanation of this dissertation are shown as following:

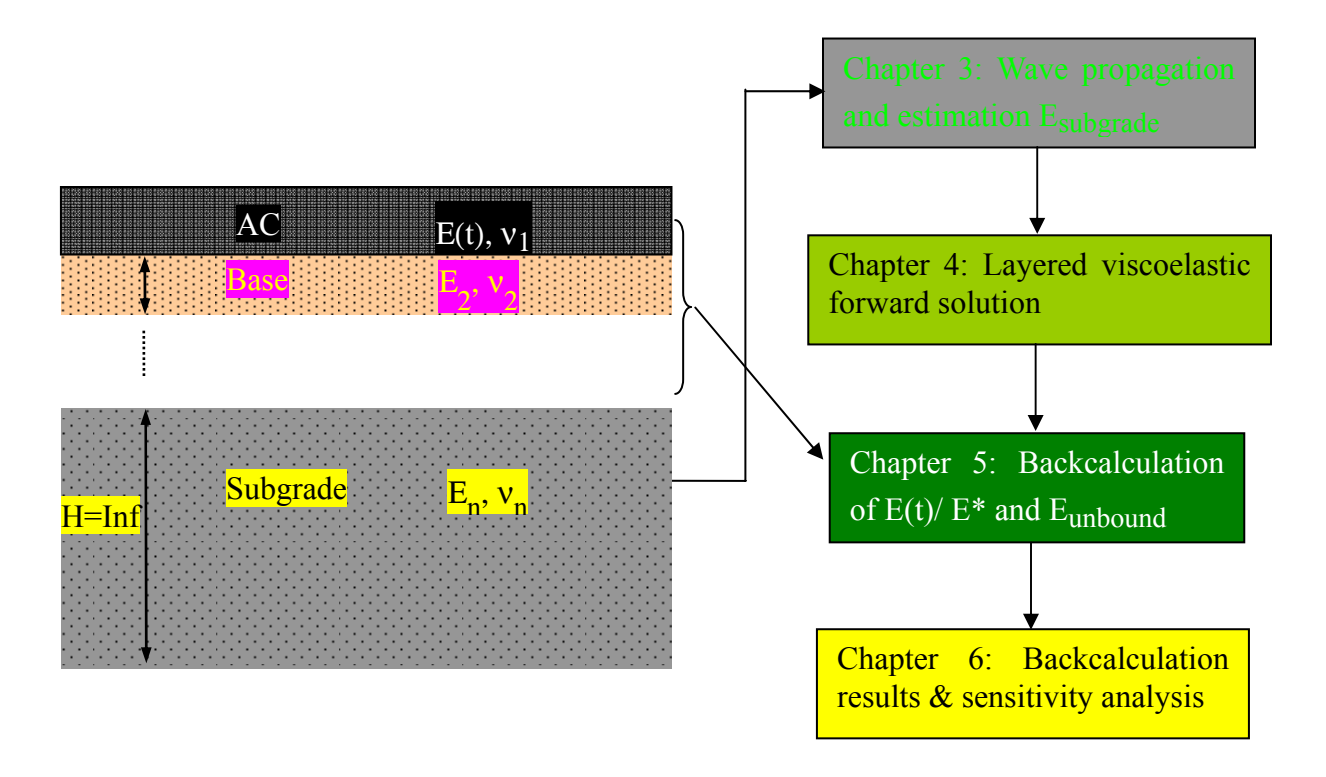


Figure 1: Organization of this dissertation

# (For interpretation of the references to color in this and all other figures, the reader is referred to the electronic version of this dissertation.)

- Chapter 2 provides a review of relevant literature on the backcalculation approaches from field FWD tests, background on the material properties of the AC mixture as viscoelastic materials, and the interconversions between |E\*|, E(t) and D(t) within the frame work of viscoelasticity. The purpose of the study is briefly given at the end of this chapter.
- Chapter 3 presents a method for calculation of E<sub>subgrade</sub> based on wave propagation theory.
   The concept of equivalent frequency is introduced, and the application of Rayleigh wave in analysis of FWD test data is explained. As a validation, four cases of field tests from Long Term Pavement Performance (LTPP) database are demonstrated. The merits and limitations are given.

- Chapter 4 introduces a layered viscoelastic forward solution. The response of viscoelastic multi-layered pavement system under FWD test is presented. The pavement is modeled as a system of the horizontal layers, and AC mixture is simulated as viscoelastic material, and the rest layers are isotropic and linear elastic. The forward solution is verified against the semi-analytical viscoelastic solution of a step surface load, and then checked against well-known dynamic solution SAPSI and LAMDA.
- Chapter 5 contains the details of the backcalculation algorithm, and some brief information on the backcalculation algorithm developed in MATLAB. A hypothetical FWD test deflection time histories, simulated by dynamic solution SAPSI, was used as the input parameters, and the modulus of each physical layer was backcalculated to verify the accuracy of the algorithm.
- Chapter 6 presents the validation of the viscoelastic backcalculation algorithm using numerical and field FWD test deflection time histories. Sensitivity analyses of various parameters on the backcalculation were conducted. The effects of inaccuracies in deflections and duration of deflection records were studied.
- Chapter 7 contains a summary of the findings, the impact of the research, and recommendations for future research.

# Chapter 2. Literature Review and Background

### 2.1 Backcalculation Approach

The elastic moduli of pavement layers are obtained from backcalculation via field FWD tests. To find the elastic modulus of each layer, backcalculation from FWD test data is usually carried out by matching the measured deflections under a known load with theoretical deflections generated by an analytical model of the pavement, usually by Newton's method (Harichandran et al, 1994). Such procedures usually use error minimization techniques to minimize either the absolute or the square error, with or without weighting factors for sensors in the FWD test.

At present, pavement moduli can be backcalculated from the FWD deflection basin, using the peak values of the deflection time-histories (static backcalculation) or using the FWD full time-history (dynamic backcalculation). However, deflection basins under static loads differ from those under dynamic or impulse loads because of geometric damping of pavement structure, and dynamic effects, such as inertia, material damping, and resonance. Dynamic analysis, or the time-history record, would therefore provide a more accurate estimation of the pavement moduli, at the cost of time.

Additionally, the interpretation of data still remains problematic (Ji, 2005). This is due to the limitation associated with the mechanical models incorporated into the backcalculation procedures and the uniqueness of the inverse solutions. Nevertheless, during the past few decades, there has been a significant improvement in the area of pavement modeling and non-destructive test (NDT) techniques. In the following sub-sections, the static and dynamic

methods and backcalculation schemes are discussed.

### 2.1.1 Static Backcalculation Methods

The simplest way to model the behavior of flexible pavements is based on Boussinesq's (1885) solution that models a flexible pavement as a homogeneous, isotropic, and elastic half-space. Later, Burmister (1943) modified this method into a two-layer system. Acum and Fox (1951) advanced this model into a three-layer system. Newer methods, including CHEVRON (Warren and Dieckmann, 1963) and KENLAYER (Huang, 2004) were implemented to analyze the interface conditions between layers. Finite element methods, such as MICH-PAVE (Yeh, 1989) were also developed. The FWD test load is simulated as a static load with the maximum magnitude of the impulse. The most recent layered elastic model is CHEVLAY2 (Stubstad et al, 2007).

Backcalculation programs typically perform on various forward computations to match the deflection basins from FWD test to the computed deflections. There are three major groups of static backcalculation methods, and each utilizes different techniques to reach the solution.

The first group is based on iteration techniques, where the layer moduli are repeatedly adjusted until a suitable match between the calculated and measured deflection basins is obtained. The typical programs for this method are MODCOMP (Irwin, 1994), BISDEF (Bush, 1985), BOUSDEF (Roesset et al, 1995), and CHEVDEF (Bush and Alexander, 1985).

The second group is based on searching a database of deflection basins. A forward calculation scheme is used to generate a database, which is then searched to find a best match for the observed deflection basin. One typical example is MODULUS (Uzan, 1994).

The third group is based on the use of regression equations fitted to a database of deflection basins generated by a forward calculation scheme. The LOADRATE program (Chua and Lytton,

1985) belongs to this category and uses regression equations generated from a database obtained by using the ILLIPAVE (Raad and Figueroa, 1980) nonlinear finite element program.

A more detailed review on static backcalculation methods can be found elsewhere (Mahmood, 1993).

### 2.1.2 Dynamic Backcalculation Methods

Most dynamic backcalculation methods use dynamic damped-elastic finite layer or finite element models for their forward solutions. The finite layer solutions are based on Kausel's formulation (Kausel and Peek, 1982) which subdivides the medium into discrete layers that have a linear displacement function in the vertical direction and satisfy the wave equation in the horizontal direction. The solution is based on the premise that if the sub-layer thickness is small relative to the wavelength of interest (around one tenth), it is possible to linearize the transcendental functions and reduce them to algebraic expressions. The typical example of this method is SAPSI (Chen, 1987). Al-Khoury et al (2001) developed an efficient forward solution, LAMDA, for the dynamic analysis of flexible pavements using the spectral element technique for the simulation of wave propagation in layered systems. The method is able to model each layer as one element without the need for subdivision into several sub-layers. However, the horizontal range (R) is required to simulate the vanishing of the wave toward the infinity. Endiran (1999) developed a non-linear dynamic model in DYNARK, a computer program accounting for non-linear properties in granular material as well as subgrade soil.

The backcalculation methods for dynamics are based on either frequency or time domain solutions. In the frequency domain, the applied load and measured deflection time-histories are transformed into the frequency domain by using the Fast Fourier Transform (FFT). Backcalculation of layer parameters is done by matching the calculated steady-state (complex)

deflection basins with the frequency component of the measured sensor deflections at one or more frequencies. In time domain backcalculation, the measured deflection time histories are directly compared with the predicted results predicted by the forward program.

The advantages of backcalculation in the frequency domain are the computational efficiency and theoretical validity. The disadvantage is that the results are very sensitive to truncation, sampling time interval, and rest period after the loading impulse. Truncation of deflection history of the sensors in the FWD tests is very common. The advantage of backcalculation in the time domain is that the matching of deflection history can be achieved for any desired time interval. The disadvantage is too many outputs in the forward calculation, so it is hard to converge for forward and backcalculated results, perhaps even impossible. A more detailed review of dynamic backcalculation can be found elsewhere (Ji, 2005).

### 2.2 Primary Response Behavior of Asphalt Concrete

It is well known that asphalt concrete (AC) behaves as a linear elastic material under small strain conditions (Kim, 2008). A typical stress/strain behavior of AC in cyclic tests is shown in Figure 2.

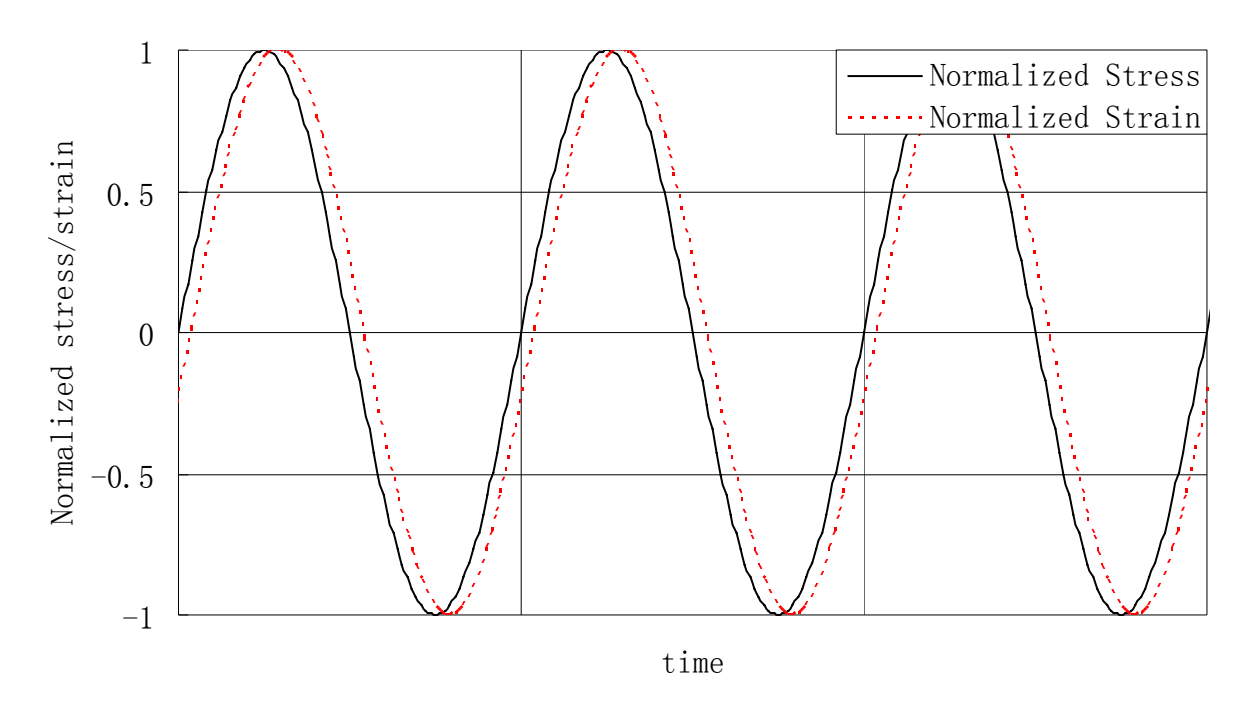


Figure 2: Sinusoidal Stress and Strain in cyclic loading

The time lag between stress and strain history illustrates that AC mixtures are viscoelastic materials. Typically, the magnitude of dynamic complex modulus  $|E^*|$  and the phase angle  $\phi$  are measured at different frequencies and at different loading temperatures. After eliminating the effect of temperature by the time-temperature superposition principle, the mastercurve  $|E^*|$  is obtained, which is the magnitudes of dynamic modulus  $E^*$  as a function of reduced frequency at reference temperature. Experimental data show both  $|E^*|$  and  $\phi$  are only function of reduced frequency  $\omega$  for a specific mixture. One example of  $|E^*|$  mastercurve is shown in Figure 3, and the phase angle function is shown in Figure 4:

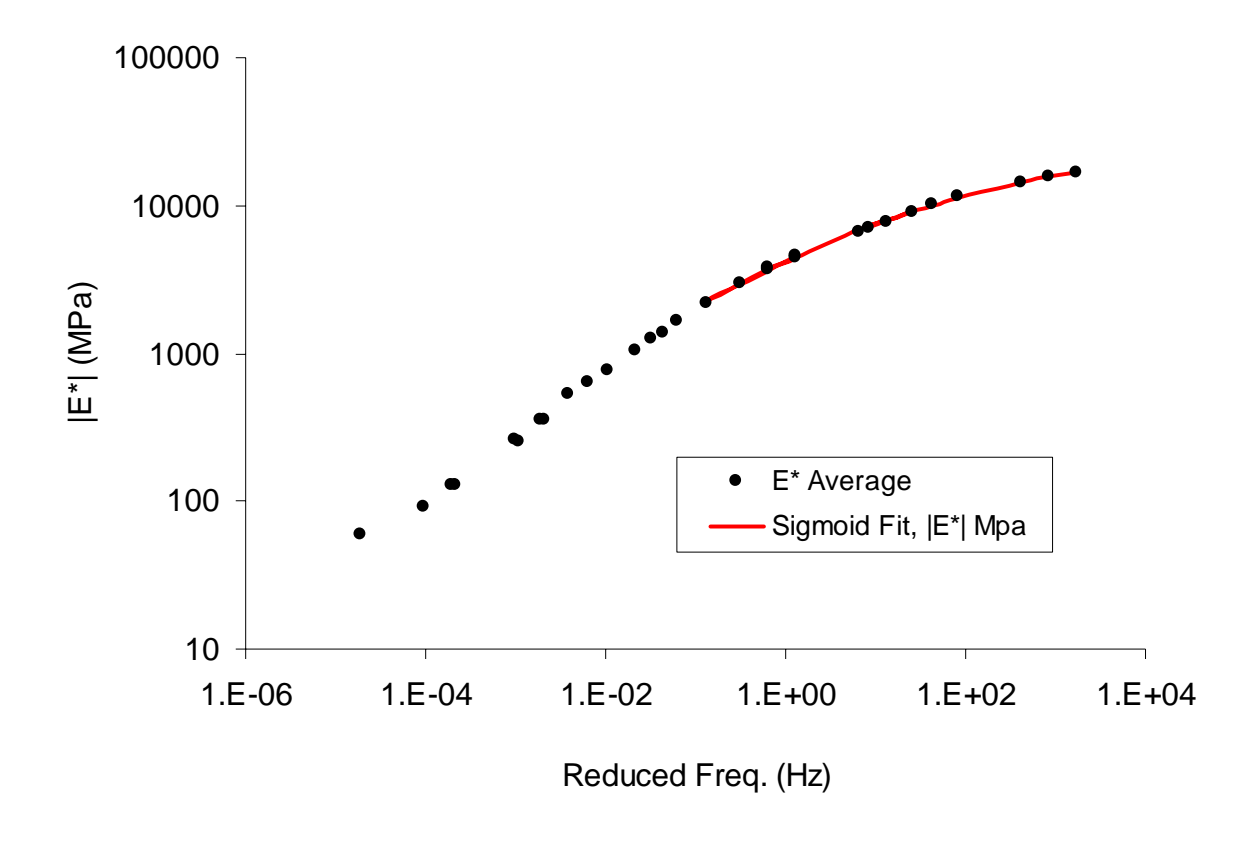


Figure 3: Mastercurve  $|E^*|$  of one asphalt concrete mixture (PG64-28) (Kutay, 2008)

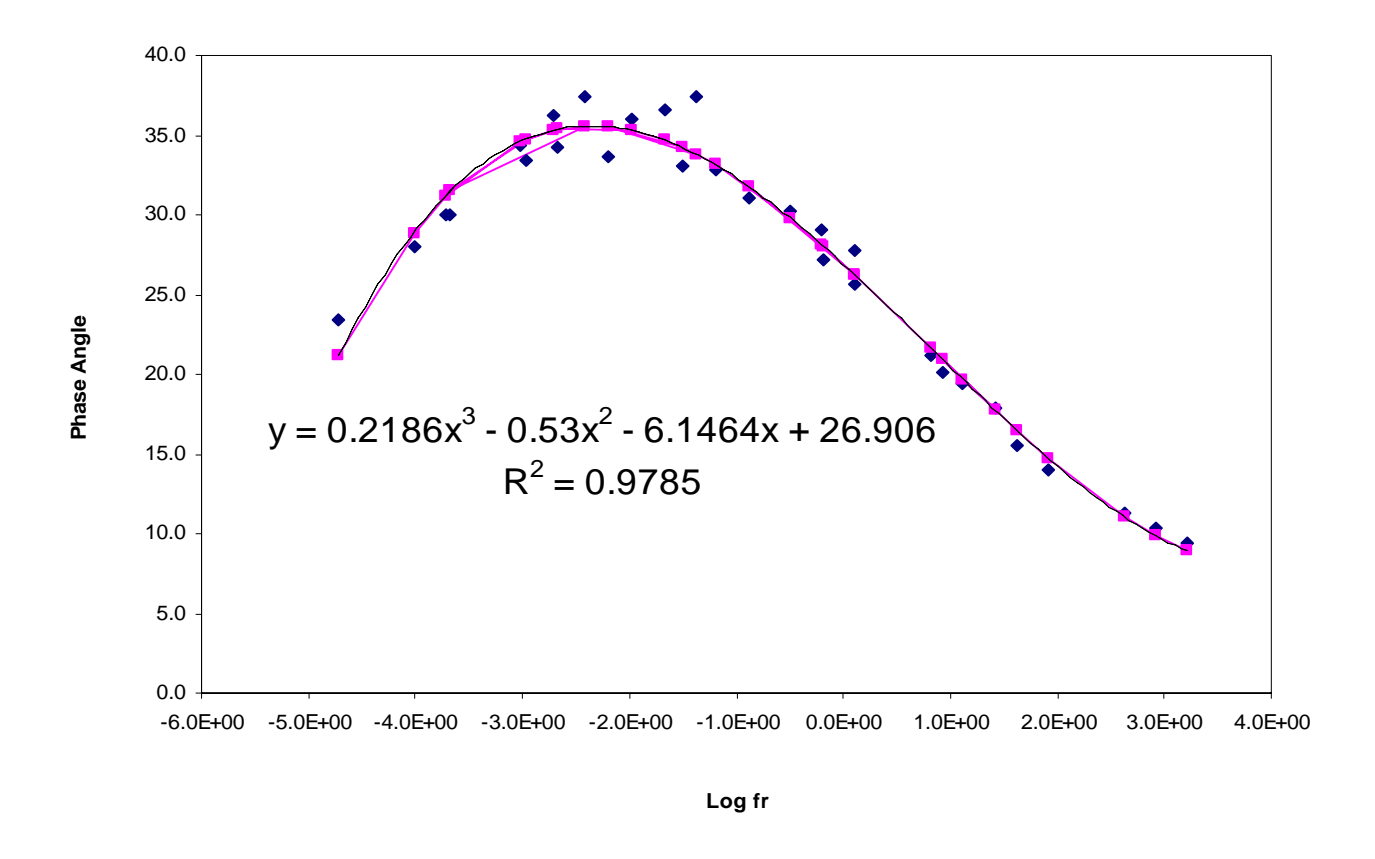


Figure 4: Phase angle  $\varphi(\omega)$  of one asphalt concrete mixture (PG64-28) (Kutay, 2008)

By regression, the mastercurve can be mathematically expressed as a sigmoidal function with four parameters (a, b, c, d) obtained by data fitting.

$$\log(|E^*|) = a + \frac{b}{1 + e^{-c - d^* \log(w_R)}}$$
 (1)

where:  $\omega_R$  is the reduced frequency at the reference temperature.

Each parameter in the sigmoidal function has a special physical meaning: 'a' represents minimum modulus values at low reference frequency; 'a + b' indicates maximum modulus values at high reference frequency; 'c' shows the horizontal position of the turning point; and 'd' influences the steepness of the function (rate of change between minimum and maximum

modulus values) (Kim, 2008). They are illustrated in Figure 5. The physical meaning of each parameter can guide the backcalculation program during convergence.

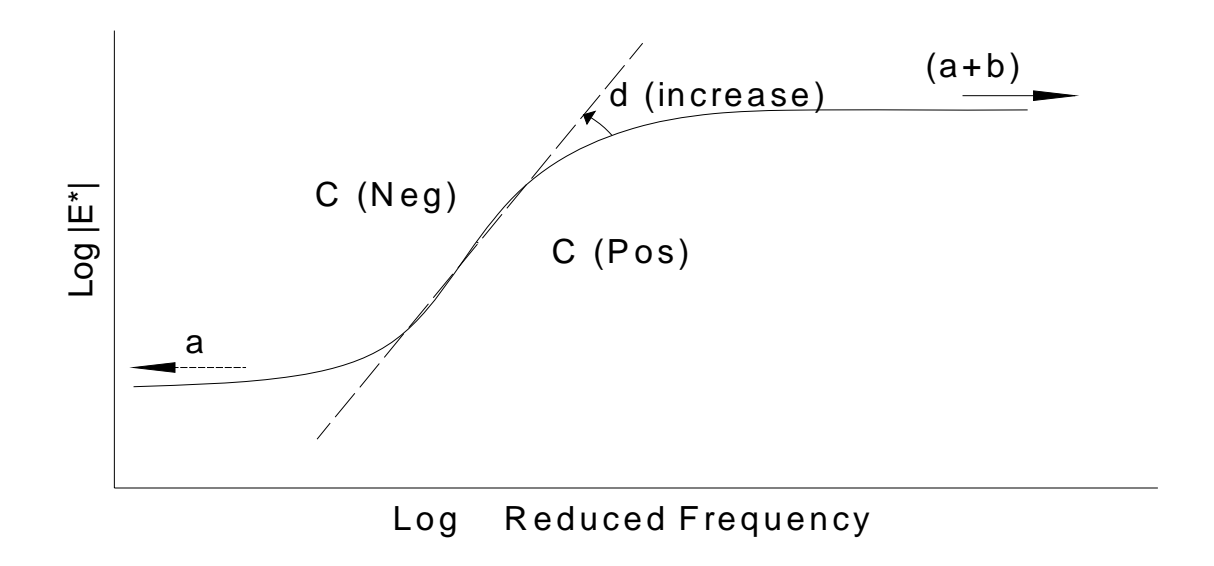


Figure 5: Physical meaning of each parameter on the sigmoidal function (Kim, 2008)

Relaxation modulus E(t) is another fundamental material property that describes the viscoelastic behavior of AC. E(t) can be computed directly from |E\*| mastercurve using an interconversion technique as described in the next subsection. It can also be characterized using a sigmoidal function with 4 parameters, as shown in Eq. (2). The relaxation modulus for the same mixture above (PG 64-28) at the same reference temperature is shown in Figure 6. It shows that the parameter group (a, b, c, d) determines the material properties of the AC mixture.

$$\log(E_t) = a + \frac{b}{1 + \frac{1}{e^{c + d*\log(t_R)}}}$$
(2)

where:  $t_R$  is the reduced time at the reference temperature.

### Relaxiation Modulus E(t)

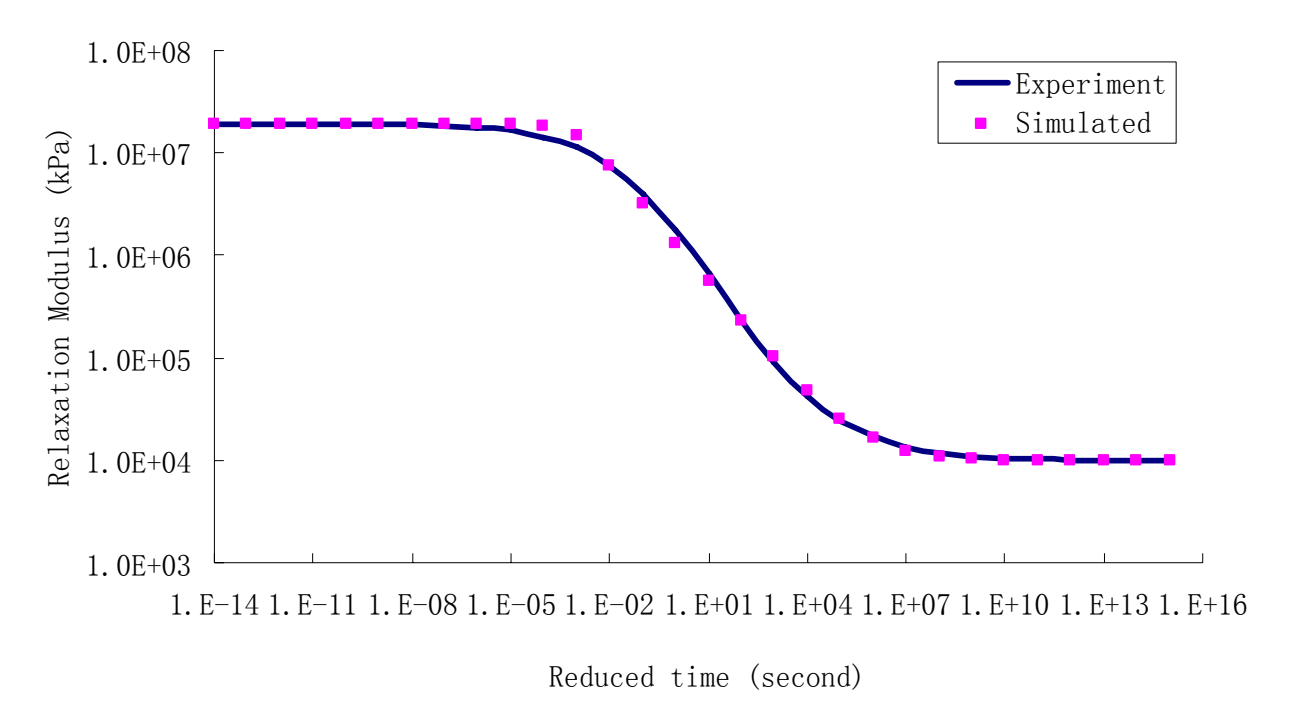


Figure 6: Relaxation modulus |E(t)| of one asphalt concrete mixture (PG64-28) (Kutay, 2008)

### 2.3 Interconversion between E(t) and |E\*| for AC Mixture

Mastercurve ( $|E^*|$ ), relaxation modulus E(t), and creep compliance D(t) are equivalent for viscoelastic materials, i.e., there is a unique relationship between  $|E^*|$ , E(t) and D(t). The interconversion between  $|E^*|$  and E(t) is discussed in this section, and the interconversion between E(t) and D(t) will be discussed in the following section.

In viscoelasticity theory, E(t) and D(t) are calculated from experimental results of mastercurve |E\*|, and are often expressed as the Prony series. It is important to note that a single polynomial model cannot be used for fitting the entire mastercurve, because the polynomial swing at low and high temperatures causes irrational modulus value predictions when

extrapolating outside the range of data (Kim, 2008). Typically, E(t) curve is represented using the generalized Maxwell model, shown in Figure 7.

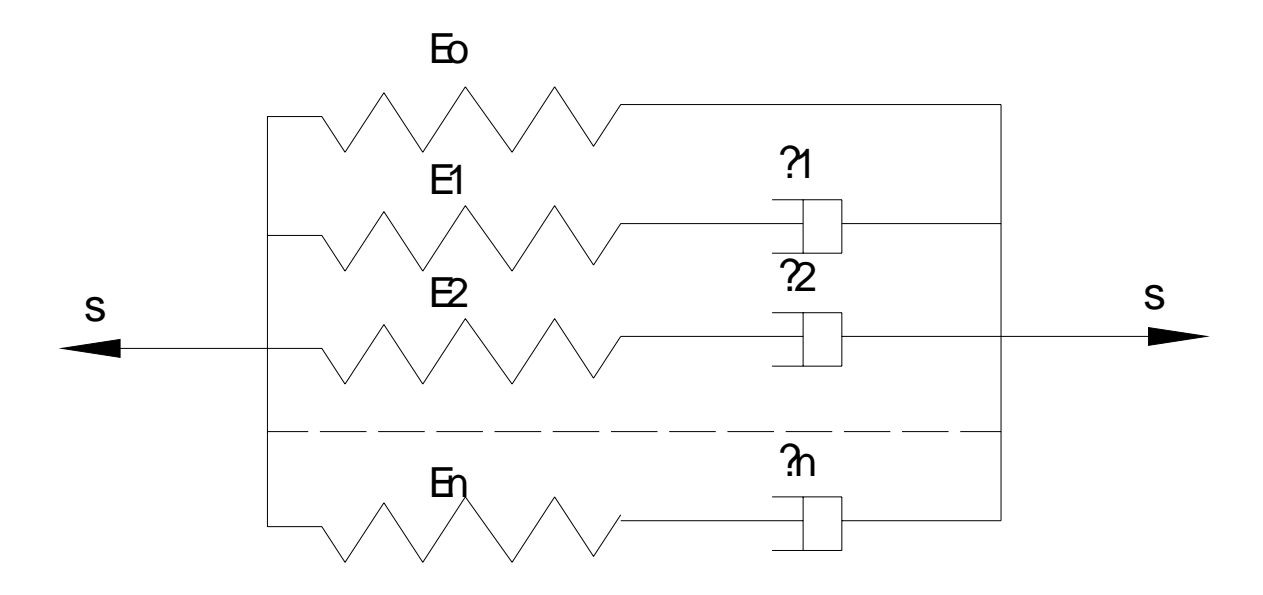


Figure 7: The generalized Maxwell model

 $E^*(\omega)$  is mathematically expressed as the storage modulus (E' ( $\omega$ )) and loss modulus (E'' ( $\omega$ )). The relationship between them is given in Eq. (3):

$$\begin{cases} E'(\omega) = \left| E^*(\omega) \right|^* \cos(\phi) = E_0 + \sum_{i=1}^N E_i \frac{(\omega T_i)^2}{1 + (\omega T_i)^2} \\ E''(\omega) = \left| E^*(\omega) \right|^* \sin(\phi) = \sum_{i=1}^N E_i \frac{\omega T_i}{1 + (\omega T_i)^2} \end{cases}$$
(3)

where:  $T_i = \frac{\eta_i}{E_i}$ , also called relaxation time.

If all the coefficients of  $E_i$  and  $T_i$  are known,  $E^*(\omega)$  can be directly calculated by Eq. (3). On the other hand, if  $E^*(\omega)$  and  $\varphi(\omega)$  are given, then  $T_i$  will be assumed for each component of

the general Maxwell model, typically ranging from  $10^{-15}$  to  $10^{15}$  seconds, and a group of linear equations is set up to solve for  $E_i$ . Usually there are more equations than unknowns, and the technology of least square root of error (LSRE) may be used to calculate  $E_i$ . If the coefficients of  $E_i$  are found, the relaxation modulus is mathematically expressed as:

$$E(t) = E_0 + \sum_{i=1}^{N} E_i e^{-\frac{t}{T_i}}$$
(4)

### 2.4 Interconversion between E(t) and D(t) for AC Mixture

The mathematical relationship between E(t) and D(t) in the time domain is given by the following integral (Kim, 2008):

$$\int_{0}^{t} E(t-\tau) \frac{dD(\tau)}{d\tau} d\tau \equiv 1$$
 (5)

Solving the integral for interconversion can be done using a numerical approach. This requires that the integral be divided into a large number of time segments, which is consistent with the relaxation modulus from the generalized Maxwell model. This can be done by using the Prony series form of the E(t) and D(t) functions. Given  $\left\{ \rho_i, E_i \left( i=1,2,...,m \right) and \, E_0 \right\} \right\}$  or  $\left\{ \tau_j, D_j \left( j=1,2,...,m \right) and \, D_0 \right\}$  and the target time constants, the unknown set of constants can be determined through a system of linear algebraic equations. For example, creep compliance in its Prony series form, D<sub>i</sub> (j=1,2,...,n), can be determined from the relaxation

modulus E(t) as follows (Kim, 2008):

$$[A]\{D\} = \{B\} \tag{6}$$

Or:  $A_{kj}D_j = B_{k \ (j=1,2,...,n;\ k=1,2,...,p)}$  where:

$$A_{kj} = \begin{cases} E_{0} \left( 1 - e^{-\frac{t_{k}}{\tau_{j}}} \right) + \\ \sum_{i=1}^{m} \frac{\rho_{i} E_{i}}{\rho_{i} - \tau_{j}} \left( e^{\frac{t_{k}}{\rho_{i}}} - e^{\frac{t_{k}}{\tau_{j}}} \right) \left( \rho_{i} \neq \tau_{j} \right) \\ E_{0} \left( 1 - e^{\frac{t_{k}}{\tau_{j}}} \right) + \\ \sum_{i=1}^{m} \frac{t_{k} E_{i}}{\tau_{j}} \left( e^{\frac{t_{k}}{\rho_{i}}} \right) \left( \rho_{i} = \tau_{j} \right) \end{cases}$$
(7)

$$B_{k} = 1 - \frac{E_{0} + \sum_{i=1}^{m} E_{i} e^{-\frac{t_{k}}{\rho_{i}}}}{E_{0} + \sum_{i=1}^{m} E_{i}}$$

The symbol  $t_k$  (k=1,2,...,p) represents a discrete time corresponding to the upper limit of integration in Eq. (5). Once the model constants  $D_j$ , and  $\tau_j$  are found, the function D(t) can be obtained in its Prony series form. Similarly, E(t) can be calculated from D(t) by solving for the unknown constants of the Prony series representation of E(t).

An example of such calculation is given here for an AC mixture. The source and target Prony series coefficients of a specific AC mixture are shown in Table 1, and the corresponding fitted data are plotted in Figure 8.

Table 1. Prony series coefficients for E(t) and D(t) for a typical AC mixture

Relaxation Modulus		Creep Compliance	
(MPa)		(1/MPa)	
$E_{\infty}$	9.8	$D_0$	5.20E-08
Prony Coefficients			
$\rho_i(s)$	E <sub>i</sub> (MPa)	$\tau_i(S)$	D <sub>i</sub> (1/MPa)
1.E-10	1.14E+02	1.E-10	3.87E-11
1.E-09	6.81E+01	1.E-09	3.03E-10
1.E-08	1.81E+02	1.E-08	5.85E-10
1.E-07	3.67E+02	1.E-07	7.52E-10
1.E-06	6.27E+02	1.E-06	1.97E-09
1.E-05	1.02E+03	1.E-05	3.42E-09
1.E-04	1.92E+03	1.E-04	6.75E-09
1.E-03	2.92E+03	1.E-03	1.35E-08
1.E-02	3.82E+03	1.E-02	2.82E-08
1.E-01	3.76E+03	1.E-01	6.47E-08
1.E+00	2.38E+03	1.E+00	1.48E-07
1.E+01	1.28E+03	1.E+01	3.48E-07
1.E+02	4.93E+02	1.E+02	1.03E-06
1.E+03	1.66E+02	1.E+03	3.02E-06
1.E+04	5.59E+01	1.E+04	8.43E-06
1.E+05	2.08E+01	1.E+05	1.63E-05
1.E+06	8.64E+00	1.E+06	2.05E-05
1.E+07	4.11E+00	1.E+07	1.76E-05
1.E+08	2.13E+00	1.E+08	1.27E-05
1.E+09	9.98E-01	1.E+09	8.80E-06
1.E+10	8.00E-01	1.E+10	4.90E-06
1.E+11	9.92E-02	1.E+11	3.64E-06
1.E+12	3.25E-01	1.E+12	1.27E-06
1.E+13	6.99E-02	1.E+13	2.11E-06

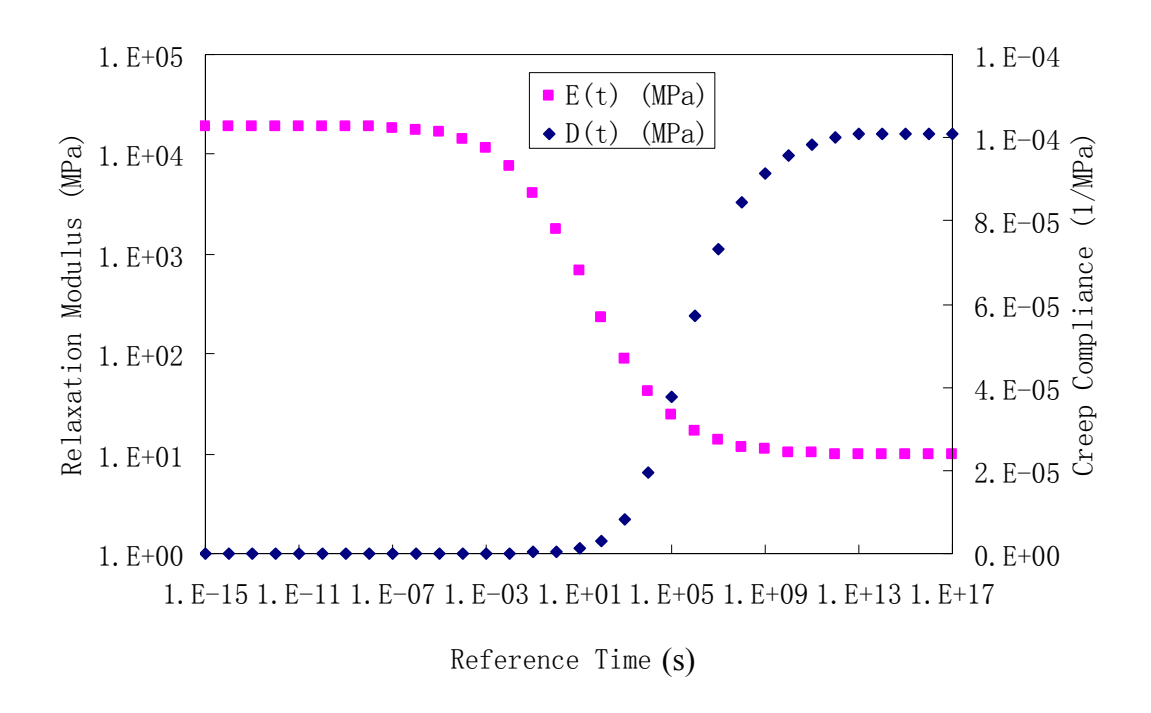


Figure 8: E(t) and D(t) from interconversion for a typical AC mixture

## 2.5 Motivation for the Study

Current backcalculation methods, both static and dynamic methods, ignore the viscoelastic behavior of AC layer. Assuming AC as a linear elastic material is no longer a valid and appropriate assumption. The new Mechanistic Empirical Pavement Design Guide (ME-PDG) utilizes the |E\*| mastercurve of AC layer. Therefore, there is a growing need for estimating entire |E\*| mastercurve of AC.

There are three major challenges for the VE backcalculation. First, the dynamic response of the pavement under field FWD test should be estimated correctly. Second, the elastic modulus of the base and subgrade layer should be as accurate as possible. Third, the AC material relaxation

modulus E(t), or the dynamic modulus mastercurve  $|E^*|$  should be expressed as a function instead of one constant value.

The pavement response under the FWD test is the response of a dynamic system after load impulse, and the phenomenon of wave propagation, as evidenced from the time delay of each sensor. Additionally, backcalculation algorithms are typically more sensitive to the elastic modulus of the base and subgrade layer than the AC layer. This indicates that the accuracy of the modulus of base and subgrade layer significantly affect the accuracy of the AC layer. Based on the wave propagation theory, the elastic modulus of the semi-infinite subgrade layer (E<sub>subgrade</sub>) can be calculated from the time delay of each sensor, if the interface of different physical layer is insignificant for wave propagation. This forward calculated modulus can be used as the seed value of E<sub>subgrade</sub> in the VE backcalculation program, and it accelerates the convergence of backcalculation. A detailed discussion will be given in Chapter 3.

In AC mixture modeling, the generalized Maxwell model is often employed to illustrate the viscous property of the material. It is the constitutive equation in the time domain. In order to capture the material constitutive behavior, usually there are more than 30 groups of Maxwell model as a whole in the physical model. If the backcalculation is done directly to calibrate the generalized Maxwell model, there would be more than 30 variables in the model, and it is almost impossible for backcalculation. If the sigmoidal function is chosen, the backcalculation is used to calculate the parameters of the sigmoidal function (a, b, c, d) in either E(t) or  $|E^*|$ , although the VE forward calculation is done in time domain. The detailed explanation of the VE forward solution is presented in Chapter 4, and the backcalculation algorithm is given in Chapter 5.

The objective of this study is to propose a methodology that is robust in the backcalculation

of both AC viscoelastic modulus and the elastic modulus of base and subgrade layer, based on viscoelasticity theory. More specifically, the thickness, the Poisson's Ratio and mass density of each layer are accurately given as input in backcalculation, only the four parameters (a, b, c, d) of the sigmodial function of E(t) or  $|E^*|$ , and the elastic modulus of the base  $(E_{base})$  and subgrade  $(E_{subgrade})$  layers need to be identified.

# Chapter 3. Estimating the Subgrade Elastic

# **Modulus using Wave Propagation Method**

## 3.1 Introduction

The Spectral Analysis of Surface Waves (SASW) method is a dynamic non-destructive test method for determining the shear wave velocity and shear modulus of soils in-situ. The test procedure was developed in the 1980s at the University of Texas, Austin, and included three steps: data acquisition, dispersion analysis, and inversion. The test is done at different frequencies, and the shear modulus is calculated by the frequency and the phase angle difference between sensors at different locations, through the dispersion curve, which is a plot of phase velocity vs. frequency. A detailed procedure of this test can be found in Ganji et al. (1998).

A similar method to estimate the elastic modulus of the subgrade layer is proposed in this chapter. It is based on the spectral element method and the wave propagation theory. The steps of the proposed procedure are as follows:

- Assume reasonable material properties for the subgrade layer, including mass density and Poisson's ratio;
- Obtain the wave propagation velocity, or Rayleigh wave velocity (V<sub>R</sub>), based on the location and the occurrence time of the peak deflection for each sensor in the FWD test;
- Obtain the k-value, or the ratio of Rayleigh wave velocity  $(V_R)$  and shear wave velocity  $(V_S)$ ;

- Calculate the shear modulus of the subgrade layer, using V<sub>s</sub> and estimated mass density;
- Calculate the elastic modulus, based on shear modulus and Poisson's ratio.

The mass density is often estimated by the level of compaction during pavement construction, based on the engineer's experience; while the Poisson's ratio is often estimated by the type of the soil material, i.e., clay, sand, or bedrock. The  $V_R$  is calculated by the distance between sensors divided by the difference of the occurrence time of the peak deflection for each sensor, from the time-history in the FWD test. The only challenge is to find the ratio between  $V_R$  and  $V_S$ , or the k-value.

For a plane wave expressed in Cartesian coordinates, the ratio (K) of the velocity of Rayleigh Wave  $(V_R)$  to the velocity of Shear Wave  $(V_S)$  is only a function of Poisson's ratio. K is the root of the following equation (Richart et al., 1970):

$$K^{6} - 8K^{4} + (24 - 16\alpha^{2})K^{2} + 16(\alpha^{2} - 1) = 0$$
, (8)

where: 
$$\alpha^2 = \frac{1 - 2\nu}{2 - 2\nu}$$

The FWD test generates axial-symmetric waves instead of plane wave, above result may not be valid, and a proposed method to estimate k-value is briefly discussed in the following section.

# 3.2 Proposed Method to Estimate k-value

First, the theoretical formulation for the spectral element method is briefly discussed. Second, the dominant frequency in the FWD test is briefly introduced. Third, numerical examples are presented to calculate the k-value for specific subgrade site at specific frequencies.

Fourth, sensitivity analysis is presented for k-value for a range of elastic moduli, with different Poisson's ratios of the subgrade layer, under cyclic loading of different frequencies.

### 3.2.1 Theoretical Formulation for Spectral Element Method

There are two types of waves in an infinite, homogeneous, isotropic elastic medium: waves of dilatation and waves of distortion. In a half-space medium, a third wave, the Rayleigh wave, is found as a solution for the equations of motion. It corresponds to a wave whose motion is confined to a zone near the boundary of the half-space (Richart et al., 1970).

In a cylindrical coordinate system, assuming a wave traveling in the radial direction, particle displacement will be independent of the angular direction. The equations of motion of an isotropic linear elastic material can be expressed in terms of the displacements by use of Navier's equations (Al-Khoury, 2001), as:

$$(\lambda + \mu) \nabla \nabla \cdot \mathbf{u} + \mu \nabla^2 \mathbf{u} = \rho \mathbf{u}^{(9)},$$

The vector  ${\bf u}$  represents the displacement components of the material, and  $\rho$  is the mass density of the material.  $\nabla$  indicates a vector differential operator,  $\nabla$ .  ${\bf u}$  is the divergence of  ${\bf u}$ , and  $\nabla^2$ .  ${\bf u}$  is the Laplace operator of  ${\bf u}$ . For axial symmetry,  $\nabla^2$  is expressed as:

$$\nabla^2 = \frac{\partial^2}{\partial r^2} + \frac{1}{r} \frac{\partial}{\partial r} + \frac{\partial^2}{\partial z^2}$$
 (10)

where  $\lambda$  and  $\mu$  are the Lame Constants expressed as:

$$\lambda = \frac{vE}{(1+v)(1-2v)},\tag{11}$$

$$\mu = G = \frac{E}{2(1+\nu)},$$
(12)

where E is Young's modulus and v is Poisson's ratio.

In the Helmholtz decomposition, the displacement vector  $\mathbf{u}$  is expressed as the sum of the gradients of a scalar potential  $\boldsymbol{\phi}$  and the curl of a vector potential  $\boldsymbol{\psi}$  as:

$$\mathbf{u} = \nabla_{\mathbf{\phi}^{+}} \nabla \times_{\mathbf{\Psi}} \tag{13}$$

In view of the axial symmetry, the vector  $\psi$  only has a component in the  $\theta$ -direction, which is  $\psi = \psi e_{\theta}$ . Denoting the displacement components in the  $\mathbf{r}$  and  $\mathbf{z}$  directions by  $\mathbf{u}$  and  $\mathbf{w}$ , respectively, the relations between the displacement components and the potentials are shown below (Yeh, 1989):

$$\begin{cases} u = \frac{\partial \phi}{\partial r} - \frac{\partial \psi}{\partial z} \\ w = \frac{\partial \phi}{\partial z} + \frac{1}{r} \frac{\partial (r\psi)}{\partial r} \end{cases}$$
(14)

Because of Eq. (9) and (13), the above potentials satisfy the following axial symmetric wave equations:

$$\begin{cases}
\frac{\partial^{2} \varphi}{\partial r^{2}} + \frac{1}{r} \frac{\partial \varphi}{\partial r} + \frac{\partial^{2} \varphi}{\partial z^{2}} = \frac{1}{c_{p}^{2}} \frac{\partial^{2} \varphi}{\partial t^{2}} \\
\frac{\partial^{2} \psi}{\partial r^{2}} + \frac{1}{r} \frac{\partial \psi}{\partial r} + \frac{\partial^{2} \psi}{\partial z^{2}} - \frac{\psi}{r^{2}} = \frac{1}{c_{s}^{2}} \frac{\partial^{2} \psi}{\partial t^{2}},
\end{cases}$$
(15)

where the constants  $\boldsymbol{c}_p$  and  $\boldsymbol{c}_S$  are defined as:

$$\begin{cases} c_{p} = \sqrt{\frac{\lambda + 2\mu}{\rho}} \\ c_{s} = \sqrt{\frac{\mu}{\rho}} \end{cases}$$
(16)

Based on Eq. (15), there are two types of waves: compression wave (P) and Shear wave (S) respectively. Because of isotropy, these waves are uncoupled from each other.

Considering the harmonic loading case with frequency  $\omega$ , the potentials can be solved by the method of separation of variables with some arbitrary constant k, assuming the format of the potentials are (Maurice et al., 1957):

$$\begin{cases}
\varphi = S(kr)T(z) \\
\psi = S_1(kr)T_1(z)
\end{cases}$$
(17)

provided that the function S and T satisfy the equations:

$$\begin{cases} \frac{d^{2}S}{dr^{2}} + \frac{1}{r}\frac{dS}{dr} + \left(\frac{\omega^{2}}{c_{p}^{2}} - \upsilon^{2}\right)S = 0\\ \frac{d^{2}T}{dz^{2}} + \upsilon^{2}T^{2} = 0 \end{cases}, \tag{18}$$

where 
$$v^2 = \frac{\omega^2}{c_p^2} - k^2 = k_\alpha^2 - k^2$$

Similar equations hold for S<sub>1</sub>, T<sub>1</sub>, with  $v'^2 = \frac{\omega^2}{c_s^2} - k^2 = k_\beta^2 - k^2$ . The second

equation of Eq. (18) has a particular solution:  $T=e^{-ivz}$ , which remains finite as  $z \to +\infty$ . The first equation of Eq. (18) is a form of Bessel's equation, which has the Bessel function solution  $J_0(kr)$ , which remains a non-zero value at r=0. Thus, two particular solutions are obtained:

$$\begin{cases}
\varphi = Ae^{-ivz}J_0(kr) \\
\psi = Be^{-iv'z}J_1(kr)
\end{cases}$$
(19)

A and B are constants determined by the boundary conditions. The solutions vanish as z—>  $\infty$  and also vanish as r—>  $\infty$ , because of the property of the Bessel function  $J_0(kr)$ . The displacements can be expressed as:

$$\begin{cases}
 u = \left(-Ake^{-ivz} + iv'Be^{-iv'z}\right)J_1(kr) \\
 w = \left(-iAve^{-ivz} + Bke^{-iv'z}\right)J_0(kr)
\end{cases}$$
(20)

The stress equations in cylindrical coordinates are:

$$\begin{cases}
\tau_{zr} = \mu \left( \frac{\partial u}{\partial z} + \frac{\partial w}{\partial r} \right) \\
\sigma_{zz} = (\lambda + 2\mu) \frac{\partial w}{\partial z} + \frac{\lambda}{r} \frac{\partial (ru)}{\partial r}
\end{cases}$$
(21)

By replacing u and w, the following equation is obtained at the surface z = 0:

$$\begin{cases} \tau_{rz} = \left[ 2ik\upsilon Au + \left( k_{\beta}^{2} - 2k^{2} \right) uB \right] J_{1} \left( kr \right) \\ \sigma_{zz} = \left[ -\left( k_{\beta}^{2} - 2k^{2} \right) uA - 2ik\upsilon 'uB \right] J_{0} \left( kr \right) \end{cases}$$

To make the problem discrete, some boundary conditions in the radial direction are introduced. At the radial boundary r = R (far away from the source), the amplification of the oscillation is considered to vanish. Only the vertical displacement w is important in the FWD test, so the horizontal component will be ignored in the future. These considerations can be implemented by the infinitely many positive roots  $\alpha_m$  of the  $J_0$  function, as  $k_m = \alpha_m/R$  (Al-Koury et al., 2001). For FWD test loading, if the maximum pressure is P, the appropriate boundary conditions are (Maurice et al., 1957):

$$\begin{cases} \tau_{rz|z=0} = 0 \\ \sigma_{zz|z=0} = PJ_0 (kr) \end{cases}$$
(23)

By combining Eq. (22) and Eq. (23), the coefficients A and B can be solved.

$$\begin{cases} A = \frac{\left(k_{\beta}^{2} - 2k^{2}\right)}{F(k)} \frac{P}{\mu} \\ B = -\frac{2ik\upsilon'}{F(k)} \frac{P}{\mu} \end{cases}, \tag{24}$$

where:  $F(k) = (2k^2 - k_\beta^2)^2 - 4k^2 \nu \nu'$ , which is called Rayleigh's function (Maurice et al, 1957). The expression of the wave propagation includes Rayleigh's function, so this wave is called Rayleigh wave (Xiang, 2009).

Fig. 9 shows different kinds of wave propagation on the surface of an ideal medium after a load impulse. It illustrates the vibration magnitude by different wave modes, and there is a tiny vibration for compression wave (P) just after the load impulse. However, the vibration of shear wave (S) and Rayleigh wave (R) happen almost simultaneously, especially if the location is near to the loading point. The time difference of S wave and R wave is insignificant as the velocities of S wave and R wave are almost identical. Thus, the distance between two adjust peaks in vertical displacement is considered the wave length. However, wave length varies by location or propagation time, and the velocity is hard to identify, because the interaction of shear wave and Rayleigh wave affects the peak displacement.

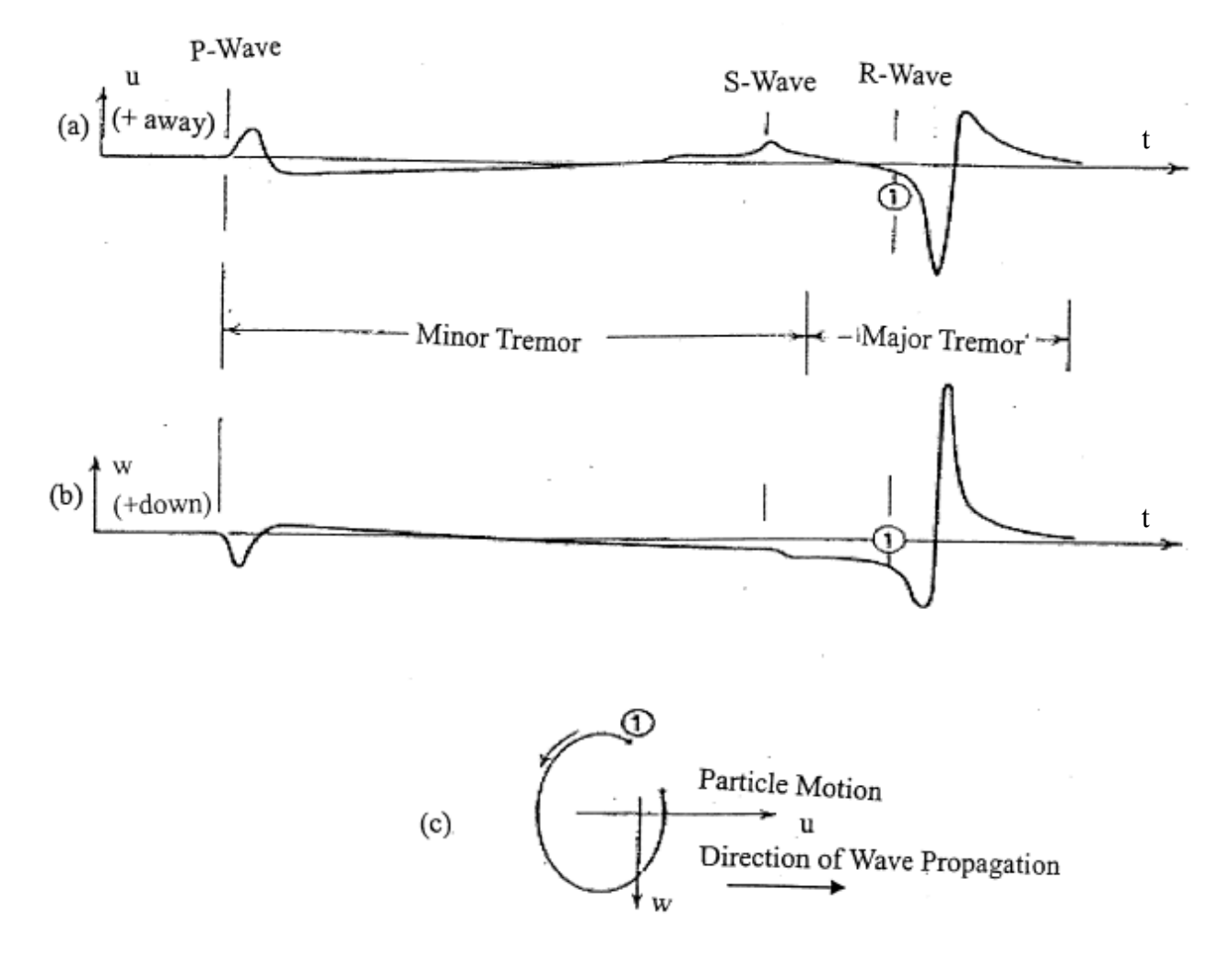


Figure 9: Wave system from surface point source in ideal medium

- (a) Effect of different wave modes on horizontal displacement
  - (b) Effect of different wave modes on vertical displacement
    - (c) The combined vibration for particle at Point ① (Richart et al., 1970)

Typically, the S wave or R wave velocity is around 150 m/s (500 ft/s) for subgrade layers, and the effective frequency in FWD test is less than 50 Hz, i.e., the S wave length is more than 3 m (10 ft), which is beyond the range of the sensor distribution in the FWD test. Thus, the occurrence time of peak deflection for each sensor is considered, noted as the time delay, rather than the deflection basin, and by the difference of the occurrence time, the velocity of R wave is identified.

### 3.2.2 Dominant Frequency of the FWD Test

Eq. (24) indicates the Rayleigh wave propagation velocity is a function of frequency, while the shear wave velocity is independent to frequency. K-value should be dependent on the loading frequency. Thus, the equivalent frequency of the FWD test, or the dominate frequency range in the FWD test should be identified.

The equivalent frequency of a loading history can be identified by: (a) the centroid of the area formed by Fourier Series; (b) the centroid of the area formed by the power spectral density (PSD) in the frequency domain; (c) the central frequency method from earthquake engineering, as defined below. In method (a), the coefficient of Fourier series is found first, and then the centroid of the coefficient corresponding to the frequency is obtained as the equivalent frequency. Method (b) is well-known as Parseval's theorem or the principle of energy conservation in time and frequency domains. The power spectral density function ( $G(\omega)$ ) is calculated by coefficients of Fourier series first, and the centroid of the PSD is called the equivalent frequency. In method

(c), the equivalent frequency is calculated as: 
$$\overline{\omega} = \sqrt{\frac{\lambda_2}{\lambda_0}}$$
 where  $\lambda_i = \int_0^{\omega_N} w^i G(\omega) d\omega$ .

For a typical FWD loading history, the loading duration is 35 ms with a haversine function. It is assumed that the rest time is 1 s with a sampling interval of 1ms, which only affects accuracy by a numerical error of 2 - 3 %. The equivalent frequency is calculated by these methods as: (a) f = 17.23 Hz. (b) f = 13.25Hz. (c) f = 16.38 Hz. Considering the actual loading is not a haversine function, and the loading time may differ from 35 ms, the equivalent frequencies for the three methods are listed in Table. 2. It shows the typical range of the dominant frequency in the FWD test is 5 - 25 Hz.

Table 2: The equivalent frequency for different load duration times

Duration time (ms)	25	30	35	40	45	50
Method (a)	24.09 Hz	20.10 Hz	17.23 Hz	15.09 Hz	13.42 Hz	12.08 Hz
Method (b)	18.56 Hz	15.47 Hz	13.25 Hz	11.60 Hz	10.31 Hz	9.28 Hz
Method (c)	22.93 Hz	19.11 Hz	16.38 Hz	14.33 Hz	12.74 Hz	11.46 Hz

## 3.2.3 Numerical Example to Calculate k-value

Eq. (24) indicates the  $V_R$  under cyclic loading depends on the loading frequency, elastic modulus and Poisson's ratio. One example of wave propagation is illustrated for the hypothetical profile which only includes the half-space subgrade layer. The cyclic loading frequency is 5 HZ, and the material properties are: elastic modulus = 68.95 MPa, and Poisson's ratio = 0.45. The phase angle of each point at the surface is shown in Fig. 10 for t = 0 second.

Phase angle at the surface of the subgrade layer at t=0 (E = 68.95 Mpa, v = 0.45, f = 5 Hz)

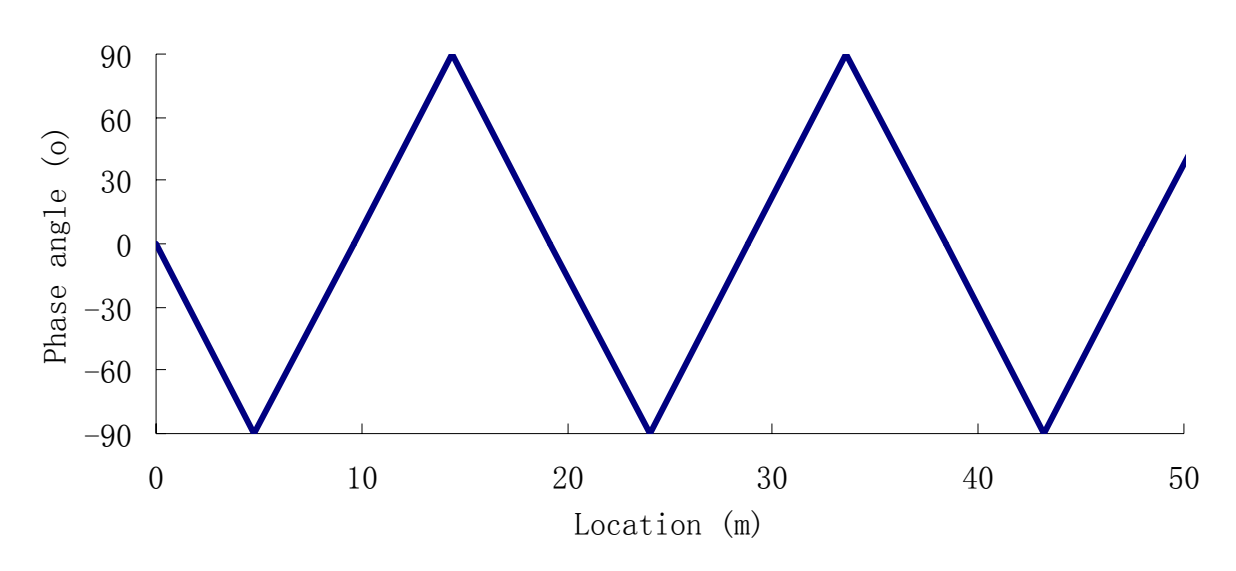


Figure 10: Phase angle of each point at the surface for a specific example (t = 0 s)

The wavelength is defined as the spatial period of the phase angle, or the distance over

which the phase angle's shape repeats. The wavelength in the above example is around 18.5 m, and the wave velocity  $(V_R)$  is around 92.5 m/s, as the loading frequency is 5 Hz.

The mass density ( $\rho$ ) of the subgrade layer is assumed as 2000 kg/m<sup>3</sup>, and the shear modulus (G) is 23.78 MPa, calculated from elastic modulus and Poisson's ratio (Eq. 12). The shear wave velocity is 109 m/s, from Eq. (25).

$$V_{s} = \sqrt{\frac{G}{\rho}}$$
 (25)

The k-value is 0.8486, which is  $V_R$  divided by  $V_s$  (Eq. 26).

$$k = \frac{V_R}{V_S} \tag{26}$$

The k-value only depends on the Poisson's ratio in plane wave, independent of loading frequency and elastic modulus of the subgrade layer. Similar conclusion is expected for the axial symmetric FWD test.

Cyclic loading is applied in the SASW method; however, only load impulse is applied in the FWD test. The phase angle for each point at the surface of the subgrade layer can be replaced by the occurrence time of the peak deflection.

### 3.2.4 Sensitivity Analysis for k-value

The typical range of the elastic modulus of subgrade is 35 - 280 MPa (5 to 40 ksi) (NCHRP, 2004). The dominant frequency in the FWD test is 5 to 25 Hz. Since the typical Poisson's ratio ranges from 0.20 to 0.49, a sensitivity analysis for k-value with different combinations of elastic

modulus and frequency was conducted for possible values of Poisson's ratio (Fig. 11 - 17).

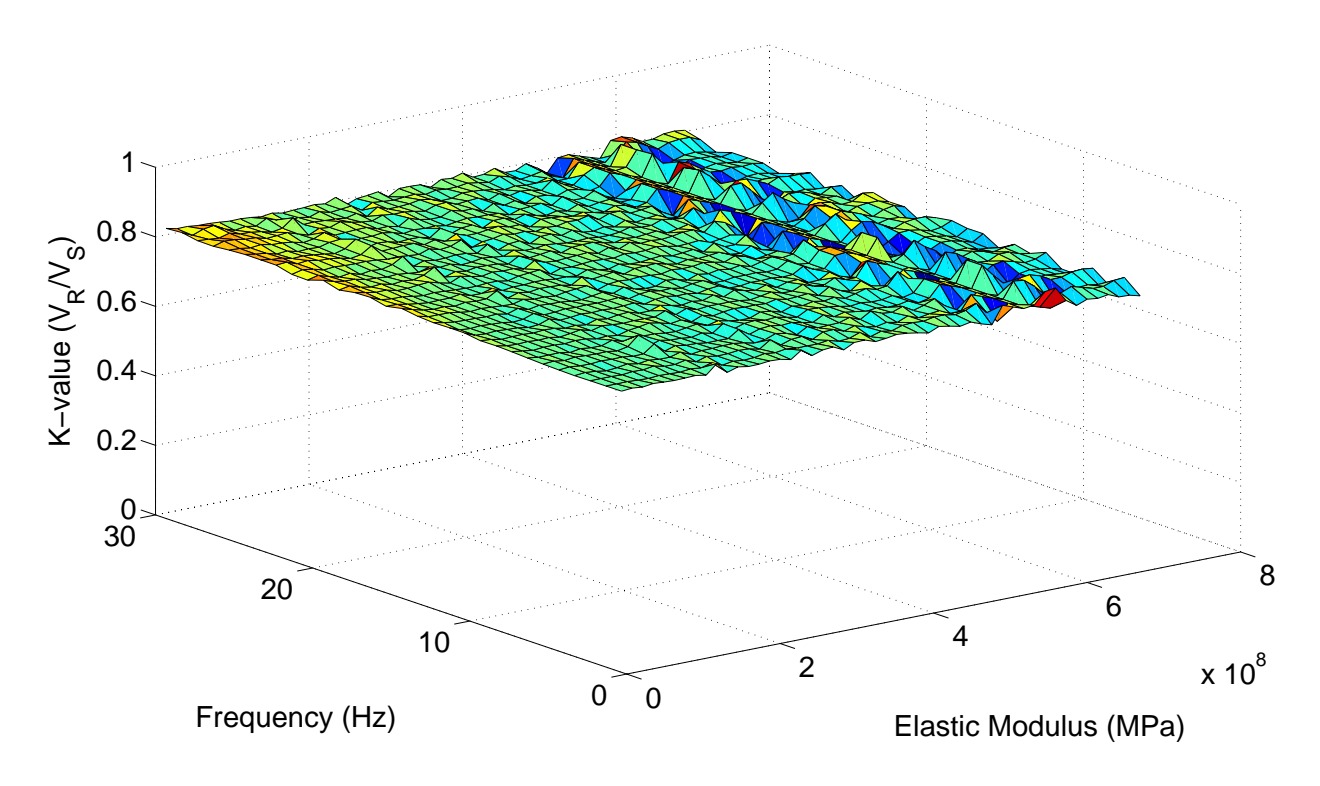


Figure 11: Sensitivity analysis for k-value (v= 0.20)

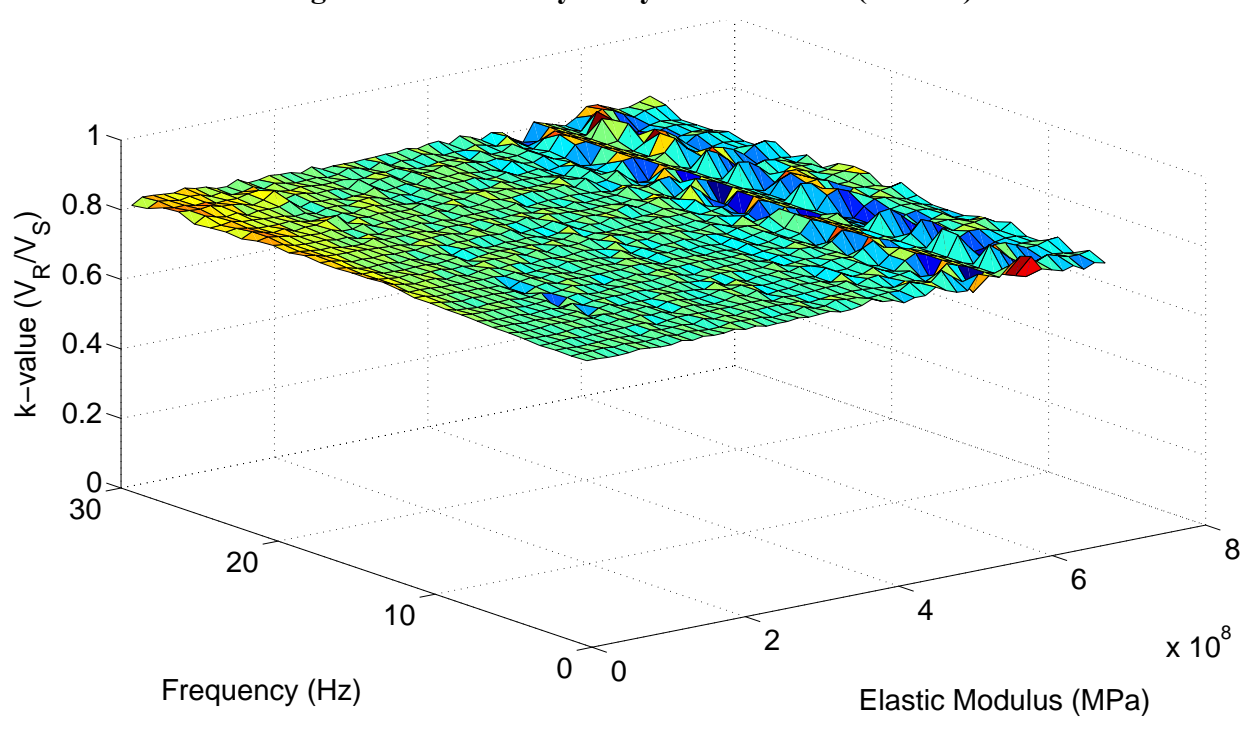


Figure 12: Sensitivity analysis for k-value (v= 0.25)

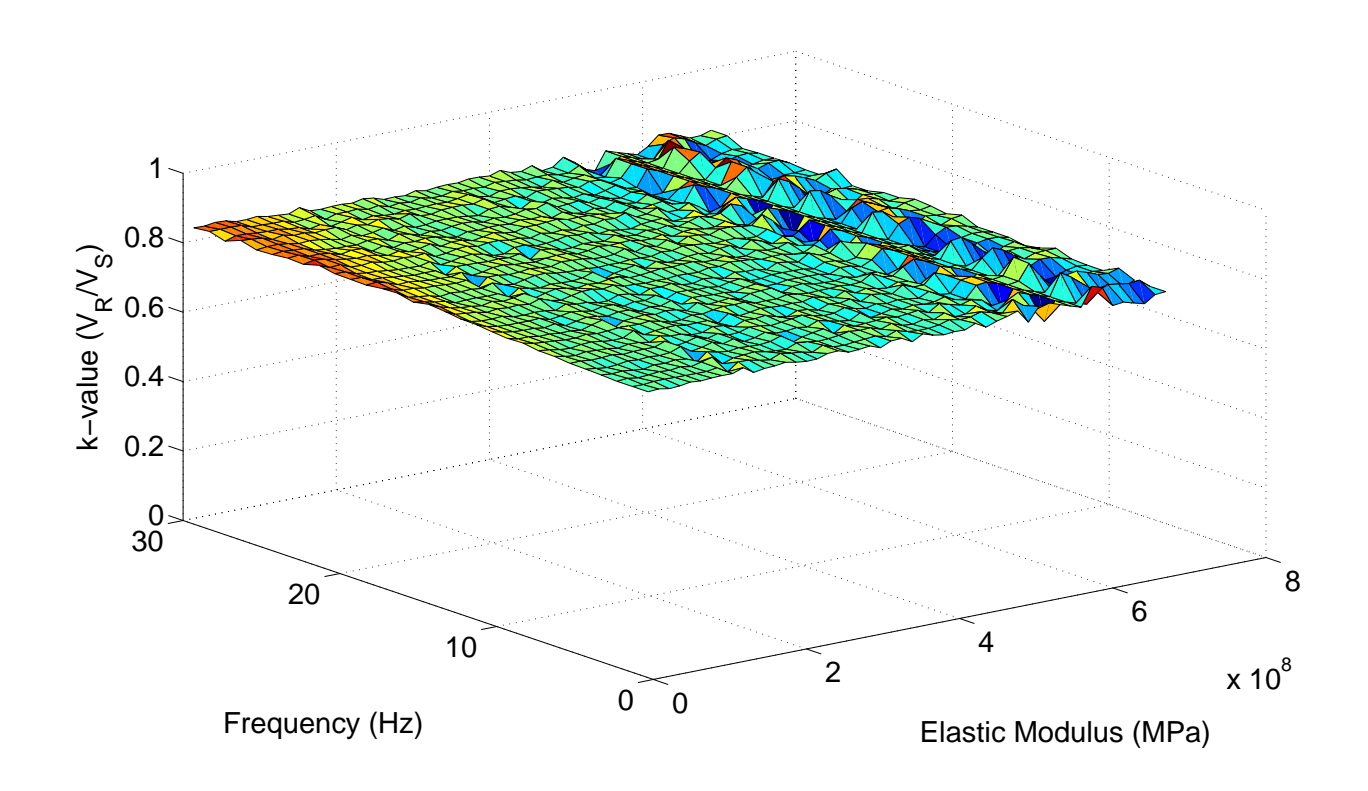


Figure 13: Sensitivity analysis for k-value (v= 0.30)

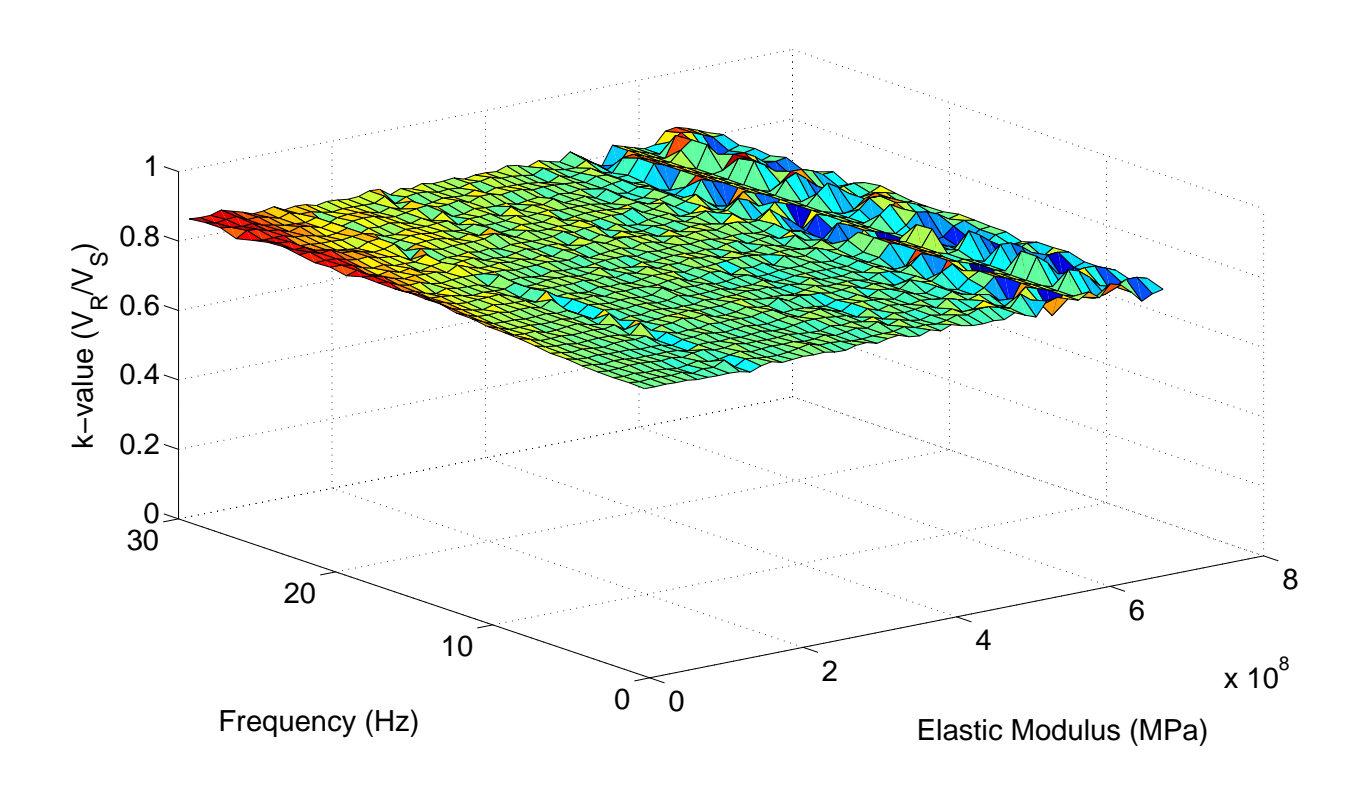


Figure 14: Sensitivity analysis for k-value (v= 0.35)

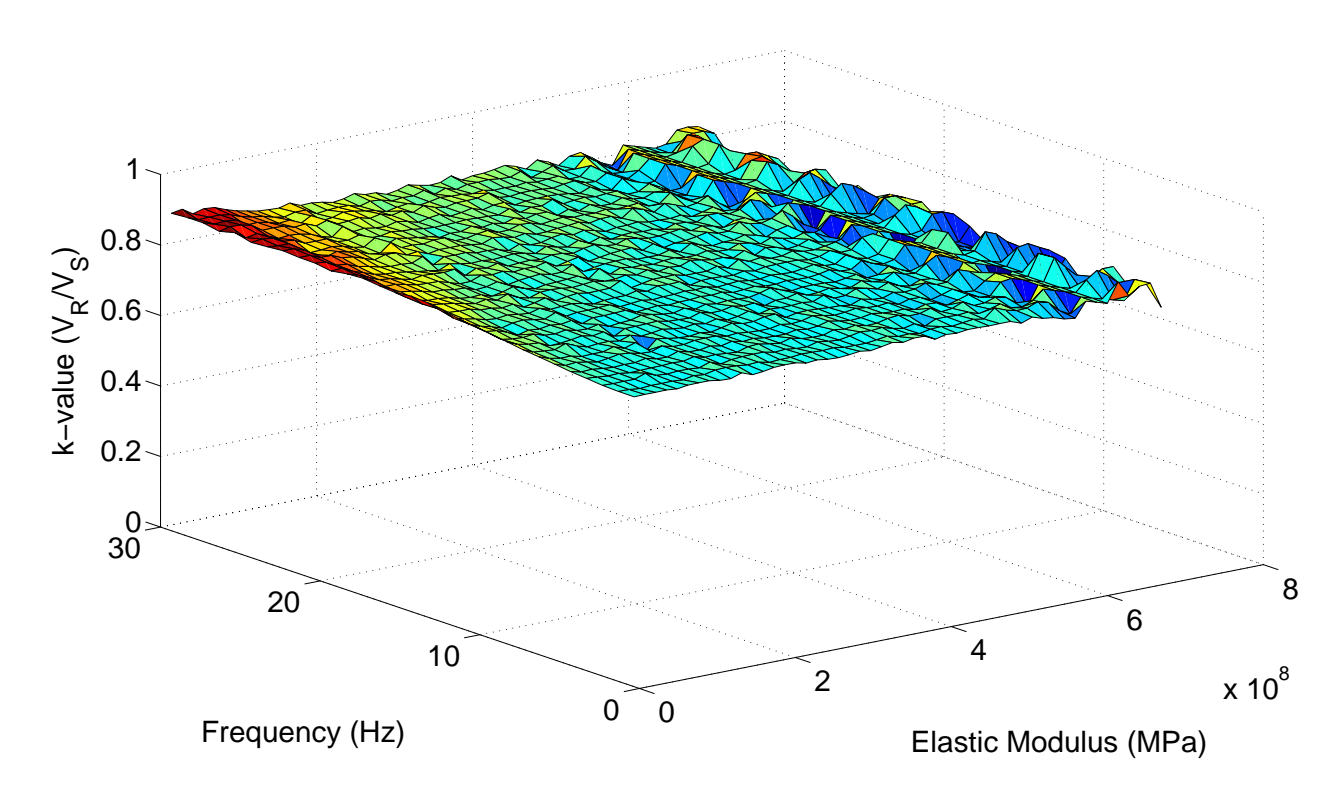


Figure 15: Sensitivity analysis for k-value (v= 0.40)

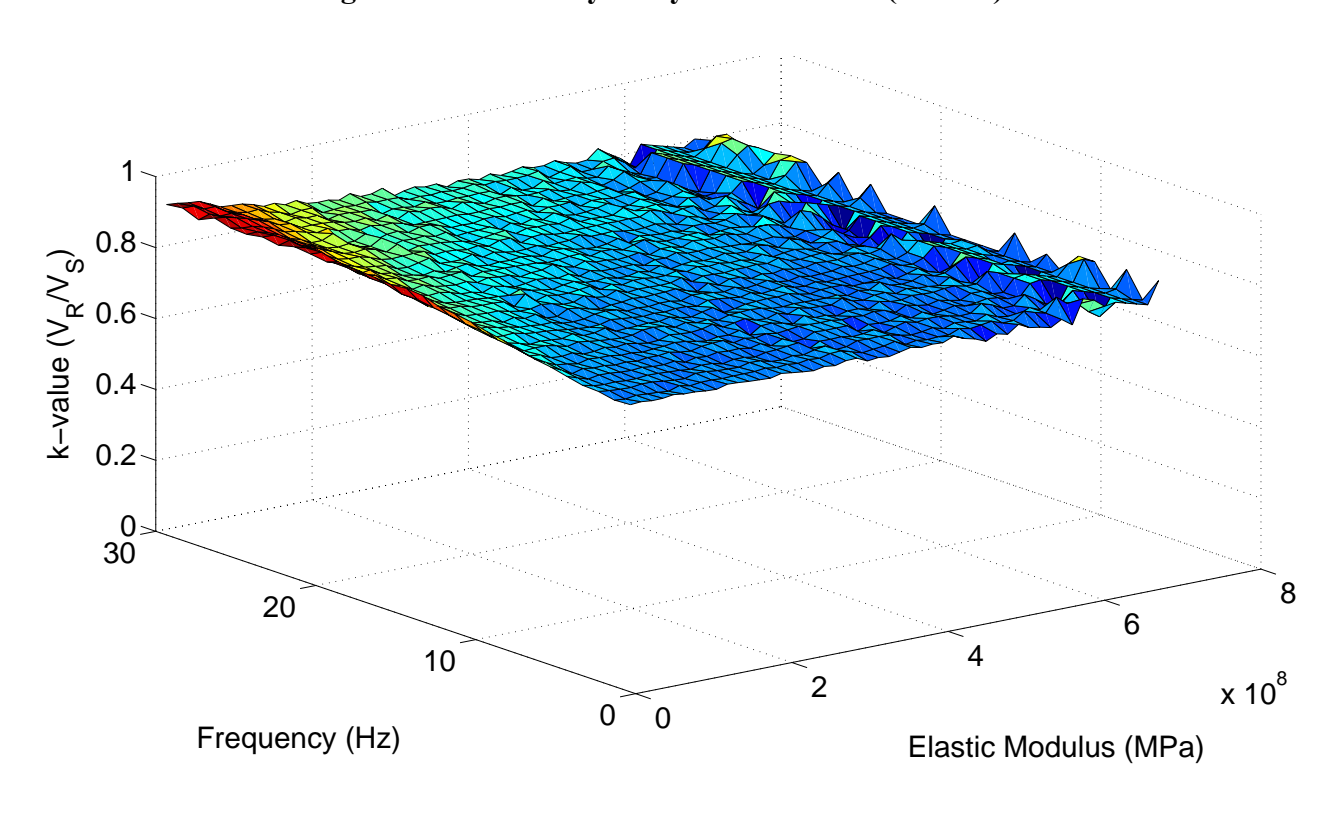


Figure 16: Sensitivity analysis for k-value (v= 0.45)

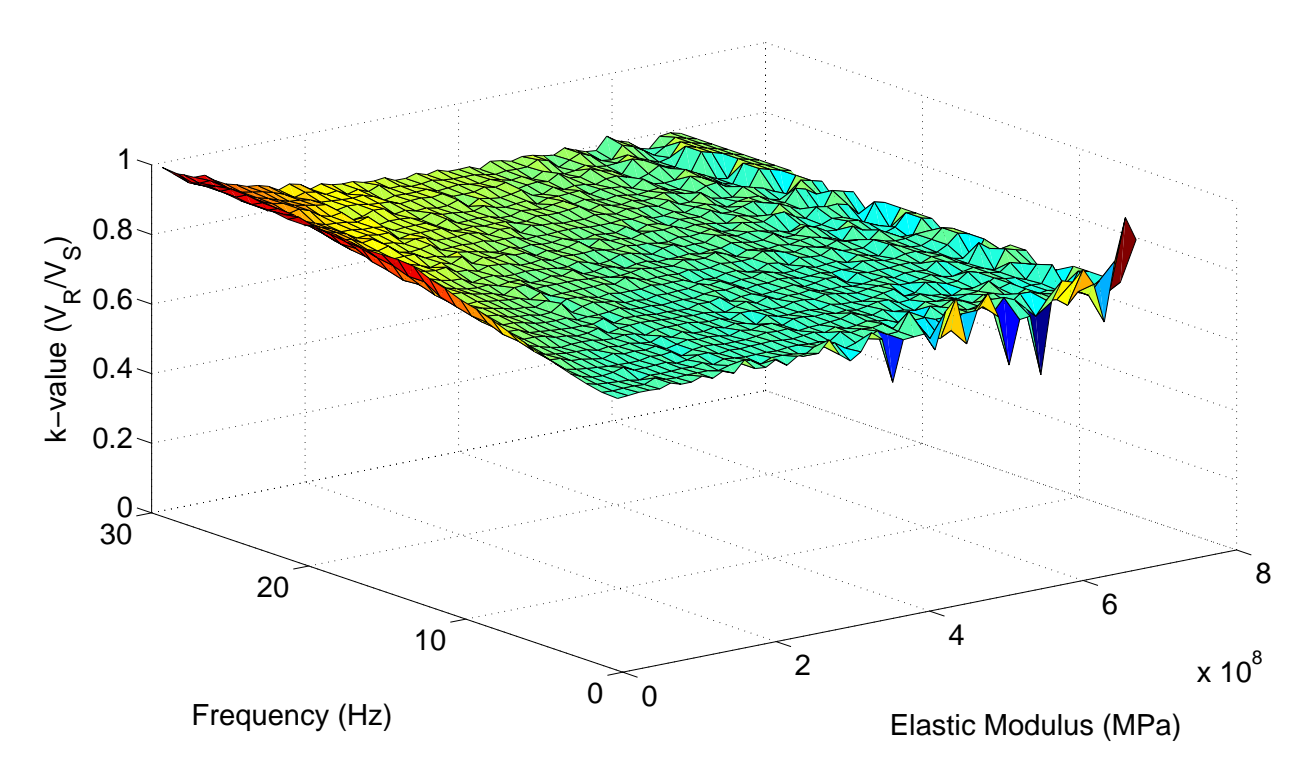


Figure 17: Sensitivity analysis for k-value (v=0.49)

Sensitivity analysis indicates the k-value is almost constant if the elastic modulus of the subgrade is less than 500 MPa (70 ksi); it is not sensitive to the frequency of the loading for the dominant range in the FWD test, but it is slightly affected by Poisson's ratio. Thus, one average k-value could be used for each Poisson's ratio. Table 3 shows the average k-value of all the entire sensitivity range as well as for the more practical range of moduli (5 to 40 ksi) and frequencies (5 to 25 Hz).

Table 3: The average k-value for different cases of Poisson's ratio

Poi	sson's ratio	0.20	0.25	0.30	0.35	0.40	0.45	0.49
Average	Entire range	0.7957	0.8051	0.8132	0.8176	0.8173	0.8102	0.7970
k-value	Practical range	0.7955	0.8056	0.8140	0.8189	0.8197	0.8154	0.8073
COV	Entire range	1.63	1.58	1.65	1.89	2.34	3.32	5.48
(%)	Practical range	0.83	0.76	0.94	1.22	1.78	2.77	4.66

Table 3 shows the average k-value does not significantly affected by Poisson's ratio. It would be much better to use a single average k-value to simplify the problem; k=0.8109 is suggested. However, it should be mentioned that the k-value may be quite different if there is a stiff layer underneath, as the cases are not verified for subgrade with elastic modulus higher than 700 MPa (100 ksi).

# 3.3 Proposed Procedure to Estimate Subgrade Elastic Modulus

Based on the result in Section 3.2, the following steps are applied to estimate the elastic modulus of the subgrade layer using k-value.

- 1. Estimate the Poisson's ratio (ν) and mass density (ρ) of the subgrade layer. The Poisson's ratio depends on the soil type, and it is well documented in the literature. The soil type, compaction level during construction, and water table level will affect the mass density, ranging from 1500 to 2000 kg/m<sup>3</sup>. However, the estimated elastic modulus is not significantly affected by the mass density, and the engineers' experience will be helpful for the estimation.
- 2. Find the slope in the plot of time delay vs. location. Six sensors are located at different positions in the FWD test, and the occurrence time of peak deflection for each sensor is different. Time delay of each sensor is defined as the difference between the time of peak loading and the time of peak deflection. Time delay and locations can be plotted in one figure, and the slope (m) for the farther sensors is found by linear regression.

One example of the load impulse and time-history for the FWD test are shown in Fig. 18. The test was conducted at LTPP (Long Term Pavement Performance) station 04-1036 in 1998. The plot of time delay vs. location is shown in Fig. 19. The slope in Fig.19 is

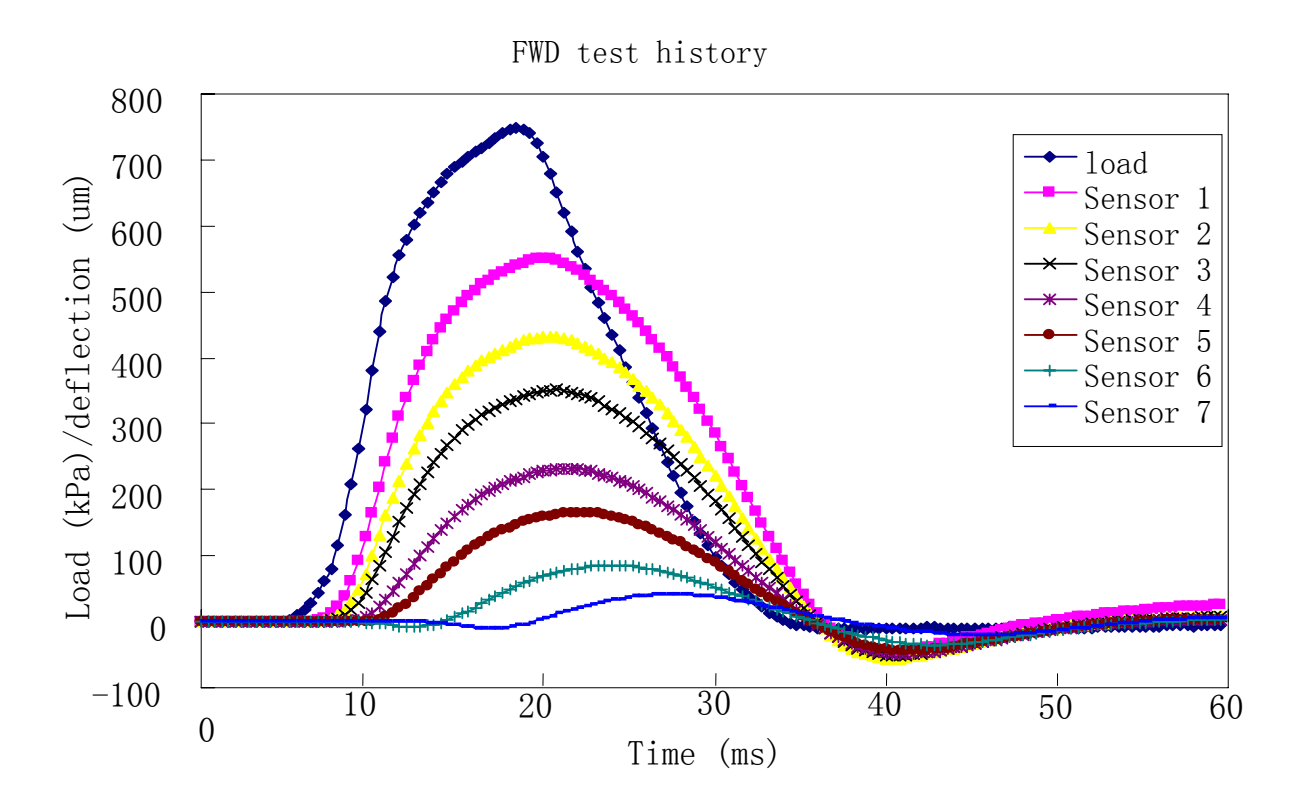


Figure 18: Example of FWD load and deflection time histories at LTPP station 04-1036 in 1998

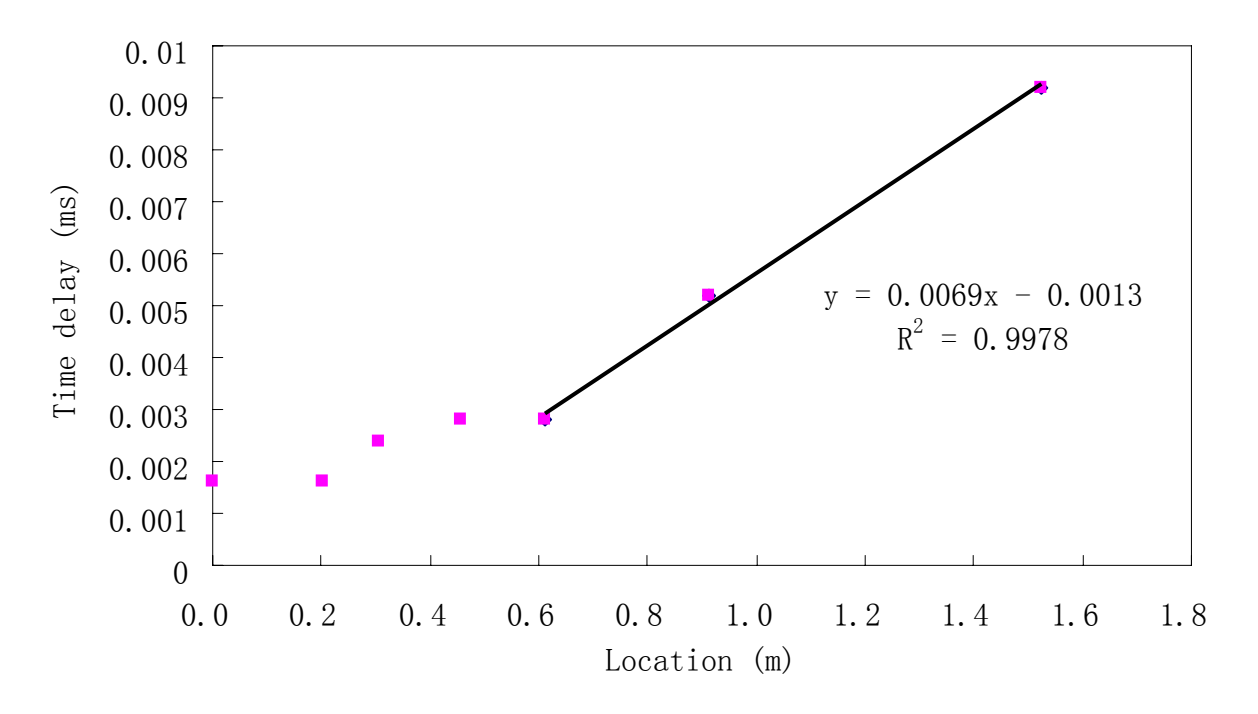


Figure 19: Time delay vs. location for the example of FWD test at LTPP station 04-1036 in 1998

- 3. Calculate the Rayleigh wave velocity  $(V_R)$ . The wave propagation velocity is the inverse of the slope (m) in the plot of time delay vs. location. In the current example,  $V_R$  = 1/0.0069 = 144.9 m/s.
- 4. Calculate the Shear wave velocity ( $V_s$ ). The  $V_s$  is  $V_R$  divided by k-value. In this example,  $V_s = 144.9/0.8109 = 178.1$  m/s.
- 5. Calculate the shear modulus (G) of the subgrade layer. The mass density is estimated in step 1, as  $\rho$ =1800 kg/m<sup>3</sup>. The relationship between G and V<sub>s</sub> is shown in Eq. (27), which is similar to Eq. (25) in Section 3.2.

$$G = V_s^2 * \rho \tag{27}$$

The shear modulus is calculated as: G= 57.1 MPa in the current example.

6. Calculate the elastic modulus (E) of the subgrade layer by Eq. (28), with assumed Poisson's ratio (v) in Step 1.

$$E = 2(1+\nu)G \tag{28}$$

The elastic modulus in this example is E = 165.6 MPa, assuming v = 0.45.

For simplification, a flow chart for this procedure is presented in Fig. 20.

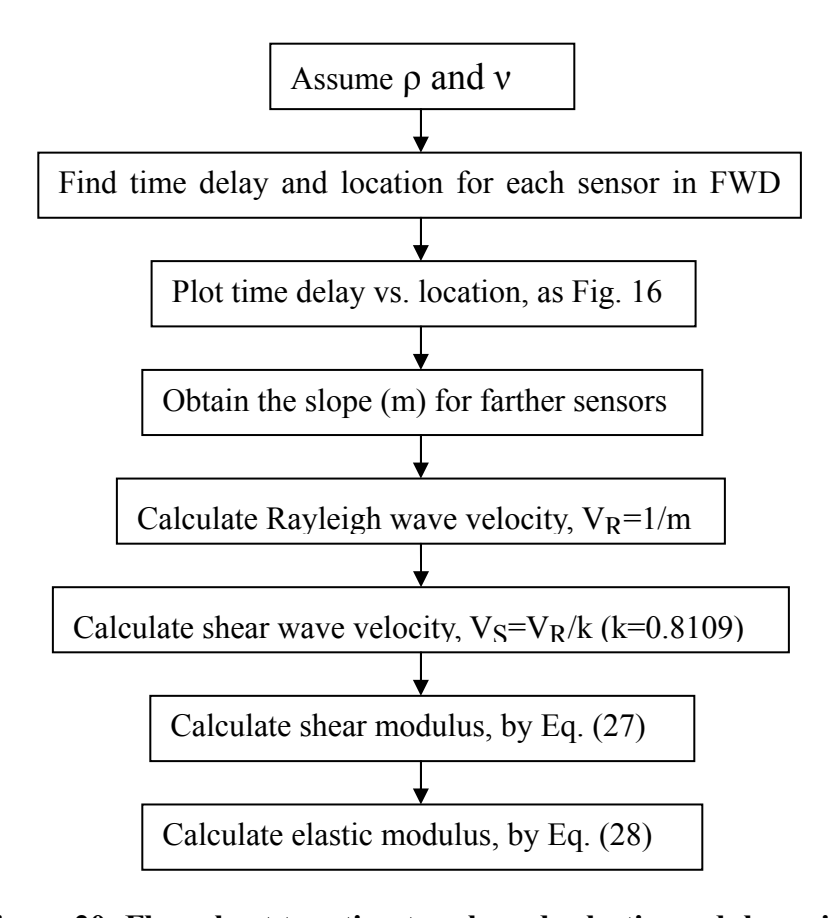


Figure 20: Flow chart to estimate subgrade elastic modulus using k-value

It is difficult to identify how many sensors should be used in step 2. Often there are 6 - 7

sensors in the FWD test, so the farther sensors would be sensors 4 - 6 or 5 - 7. There are interactions between interfaces of different layers, so the time delay for close sensors is influenced by the combined effect of different layers. Farther sensors are less affected by interactions, and it is preferable to obtain the m-value from multiple sensors. The slope between the farthest sensors is the dominant factor for m-value, and the time delay for other sensors should be ignored if including them reduces the regression R<sup>2</sup> to below 0.98.

The proposed procedure uses the time delay of each sensor in the FWD test, while the SASW method uses the phase angle of each sensor. Although load impulse can be converted to summation of different magnitudes of cyclic loading at different frequencies by Fourier Transform, the phase angle for each frequency is very sensitive in converting. Furthermore, FWD time histories are typically truncated before they fully decay, leaving errors when using field measurements. The pavement response in the frequency domain is not as accurate as in the time domain. Therefore, the time delay instead of phase angle is used in the proposed method.

# 3.4 Verification of the Proposed Method

No field data are available with all the information on the pavement profile, so only numerical examples are used to validate the proposed method. The time-history of the field FWD test is simulated by two well-known dynamic solutions: SAPSI and LAMDA. Both are briefly introduced first, and numerical examples of subgrade layer with and without ground water table are presented later, to illustrate the theoretical error of the proposed method.

#### **3.4.1 SAPSI**

The forward program SAPSI (Chen, 1987) models the pavement structure as a system of

finite layers that are infinite in the horizontal direction and underlain by an elastic half-space with viscous boundaries. The finite layer solution is based on Kausel's formulation (Kausel, 1981; Doyle, 1997) which subdivides the medium into discrete layers that have a linear displacement function in the vertical direction (finite element method with lumped mass formulation) and satisfy the wave equation in the horizontal direction (exact formulation). The solution is based on the premise that if the sublayer thickness is small relative to the wavelength of interest, it is possible to linearize the transcendental functions and reduce them to algebraic expressions. The materials are assumed to be isotropic and linearly elastic with hysteretic damping. Full interface bonding is assumed at the layer interfaces. The mass densities and elastic moduli change with depth, from layer to layer, but are assumed to be constant within each layer. The top layer represents the asphalt concrete surface, which can be modeled as a viscoelastic material by allowing its (complex) modulus to be a function of frequency.

#### **3.4.2 LAMDA**

Al-Khoury et al. (2001) developed an efficient axial-symmetric forward solution, called LAMDA, for the dynamic analysis of flexible pavements using the spectral element method for the simulation of wave propagation in layered systems. The spectral element method developed by Doyle (1997) combines elegantly the exact solution of wave motions with the finite element organization of the system matrices. The system is solved by double summation over the involved frequencies and the wave numbers (Rizzi and Doyle, 1992). The double summation approach using Fourier series is computationally advantageous over Kausel's formulation, which relies on the numerical evaluation of integrals between zero and infinity. This type of integration involves singularities if the system has no damping or very sharp peaks for small damping, and it requires considerable computational time and capacity. The mass distribution is modeled exactly

and hence only one element is sufficient to describe a whole layer without the need for subdivisions. This makes the resulting system of dynamic equations very small and hence computationally efficient.

## 3.4.3 Case of Subgrade without Ground Water Table

One specific numerical example of a pavement without ground water table (GWT) subjected to the FWD test is analyzed in SAPSI, and simulated by the Finite Element Software ABAQUS. Table 4 presents a summary of the pavement parameters.

Table 4: Basic information of a three-layer pavement structure without GWT

Physical Layer	Elastic Modulus (MPa (ksi))	Poisson's ratio	Mass density (kg/m <sup>3</sup> )	Thickness (m (in))
AC	Experimental data	0.35	2300	0.1 (4)
Base	150 (21.8)	0.35	2000	0.3 (12)
Subgrade	100 (14.5)	0.45	1500	Infinity

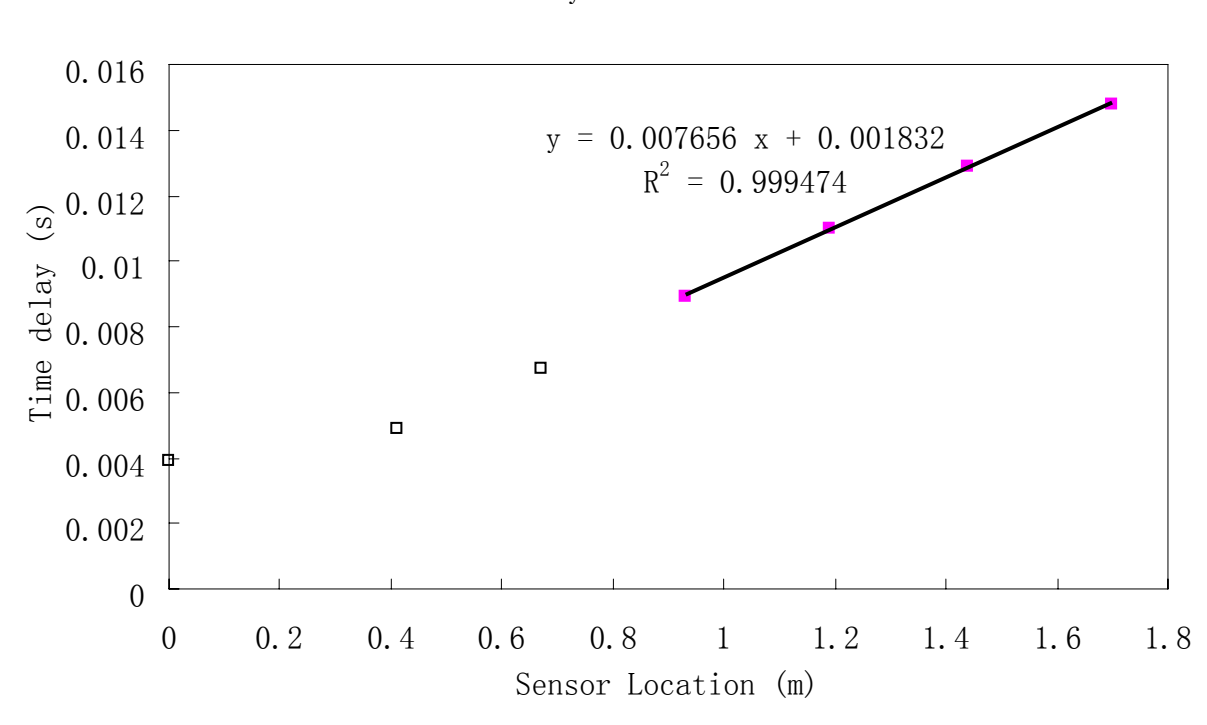
The FWD load is assumed as a haversine function with duration time of 50 ms, and the maximum pressure is 707 kPa with a loading plate radius of 0.15 m. In SAPSI, 3% damping ratio is applied for the subgrade layer, as it is a typical value for clay and can eliminate the free vibration of the system after dynamic loading. The time delay of each sensor is given in Table 5.

Table 5: Time delay of each sensor simulated by SAPSI

Sensor	1	2	3	4	5	6	7
Physical distance (m)	0.00	0.41	0.67	0.93	1.19	1.44	1.70
Time delay (s)	0.0039	0.0049	0.0067	0.0089	0.011	0.0129	0.0148

Since the sampling interval is 0.1 ms in the numerical simulation, the error from calculation may be relatively high. For the elastic modulus of the subgrade layer, the time delay and the location of sensors 4 - 7 are used given the thickness of the pavement structure is 0.4 m (16 in).

The linear regression for the time delay of these sensors is shown in Fig. 21.



Time delay VS. Location

Figure 21: Time delay vs. location for a numerical example of FWD test (without GWT)

From the statistical analysis of these sensors, the slope is obtained directly by SAPSI, as m = 0.007656 s/m. The Rayleigh wave velocity is the inverse of the slope m, i.e., the Rayleigh wave velocity  $V_R = 1/m = 130.6$  m/s.

The Poisson's ratio of the subgrade layer is assumed as v = 0.45, which is a typical value for clay. The average k-value equals 0.8109. Thus,  $V_s = V_R/k = 160.5$  m/s. The mass density of

the subgrade layer is assumed as  $\rho=1500~kg/m^3$ , so the shear modulus of the subgrade layer is calculated in Eq. (18) as G= 38.6 MPa. From elasticity theory, the elastic modulus E is calculated in Eq. (14) as E= 112.1 MPa. Given the input parameters of the

pavement structure (Table 3), this value of E is relatively accurate with an error of 12.1%. This level of error is acceptable in pavement engineering.

## 3.4.4 Case of Subgrade with GWT

One specific numerical example of a pavement with GWT during the FWD test is analyzed in SAPSI, with GWT 2 ft below the surface of the subgrade layer. The material properties of the saturated subgrade layer are calculated by the assumption that the shear wave velocity is the same as that in the dry subgrade layer, while the compression wave velocity equals the sound propagation velocity in water (1450 m/s). Table 6 gives a summary of the parameters of the pavement profile with GWT.

Table 6: Basic information for a three-layer pavement structure with GWT

Physical Layer	Elastic Modulus (MPa (ksi))	Poisson's ratio	Mass density (kg/m <sup>3</sup> )	Thickness (m (in))
AC	Experimental data	0.35	2300	0.15 (6)
Base	108 (15.0)	0.30	2000	0.3 (12)
Dry subgrade	34.5 (5.0)	0.45	1500	0.6 (24)
Saturated subgrade	42.9 (6.2)	0.4979	1682	Infinity

The FWD load is assumed as a haversine function with duration time of 35 ms, and the maximum pressure is 707 kPa with a loading plate radius of 0.15 m. In LAMDA, 3% damping ratio is applied for the subgrade layer, as it is a typical value for clay and can eliminate the free vibration of the system after dynamic loading. The simulated time-history of the field FWD test is shown in Fig. 22.

#### Deflection history with GWT (2ft)

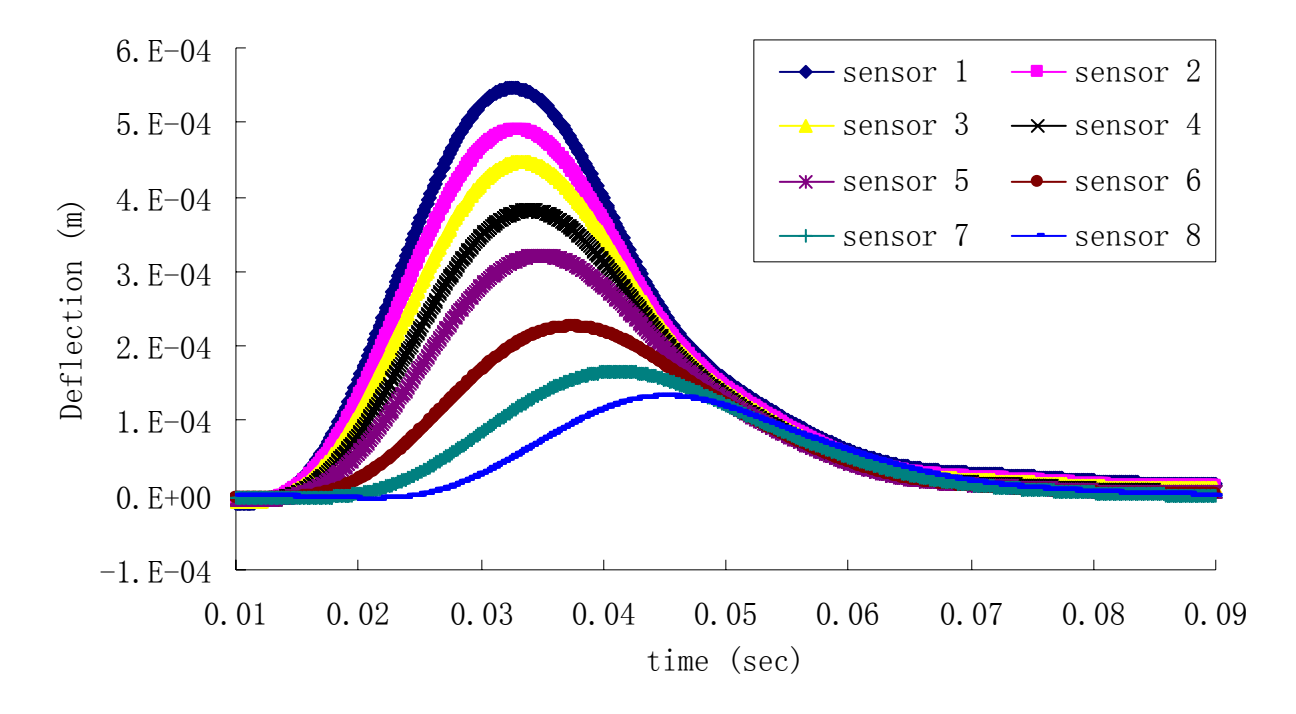


Figure 22: LAMDA simulated time-history due to the FWD test (with GWT)

The time delay of each sensor is given in Table 7.

Table 7: Time delay of each sensor by LAMDA

Sensor	1	2	3	4	5	6	7	8
Distance (m)	0.00	0.20	0.30	0.46	0.61	0.91	1.22	1.52
Delay (s)	0.0051	0.0055	0.0058	0.0065	0.0074	0.01	0.0137	0.0175

Since the sampling interval is 0.1 ms in numerical simulation, the error from calculation may be relatively high. For the elastic modulus of the subgrade layer, the time delay and the location of sensors 6 - 8 are considered, given the thickness of the pavement structure 0.45 m (18 in). The linear regression for the time delay for these sensors is plotted in Fig. 23.

Time delay vs. location (GWT=2ft)

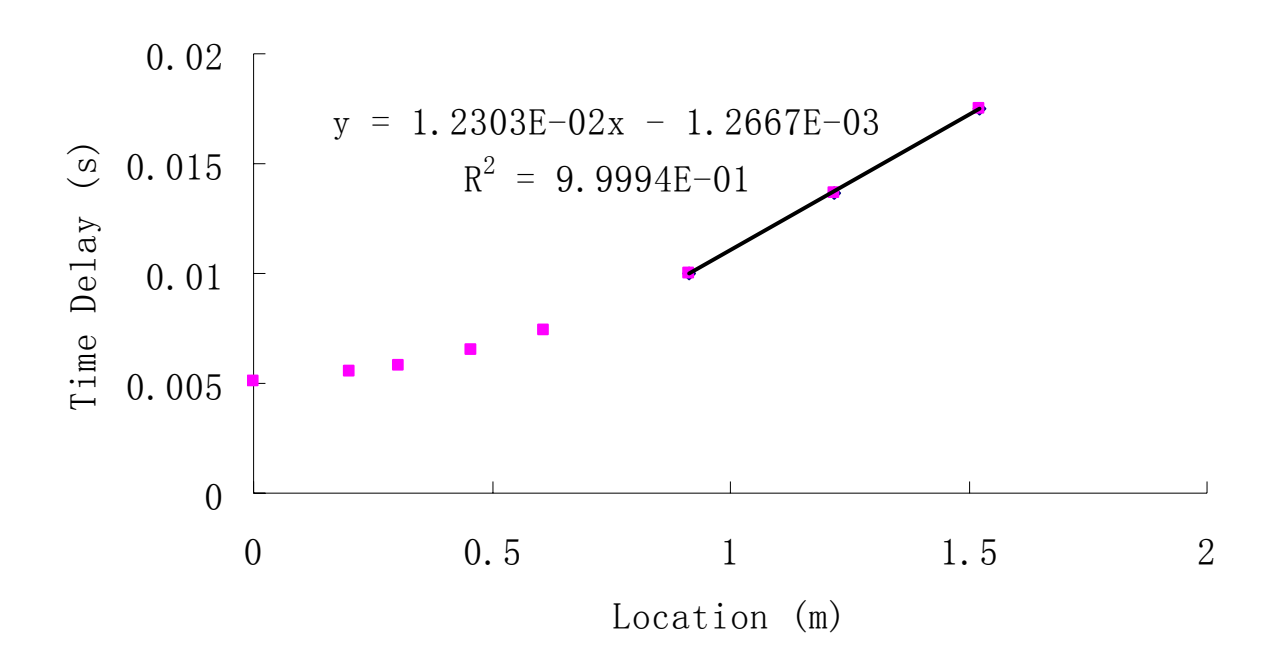


Figure 23: LAMDA simulated time-delay for the FWD test (with GWT)

From the statistical analysis of these sensors, the slope is obtained directly by LAMDA, as m = 0.00123 s/m. The Rayleigh wave velocity is the inverse of the slope m, i.e., the Rayleigh wave velocity  $V_R = 1/m = 81.3$  m/s.

The Poisson's ratio of the subgrade layer is assumed as v = 0.45, which is a typical value for clay. Using the average k-value of 0.8109, we obtain  $V_s = V_R/k = 99.9$  m/s. The mass density of the subgrade layer is assumed as  $\rho = 1500 \ kg/m^3$ , so the shear modulus of the subgrade layer is calculated in Eq. (25) as G = 15.0 MPa. From elasticity theory, the elastic modulus E is calculated in Eq. (11) as E = 43.4 MPa. Given the input parameters of the pavement structure (Table 6), this value of E is almost exactly the elastic modulus of the saturated subgrade layer, with an error of 1.0%. Although the estimated modulus is higher than the modulus of the dry

subgrade layer, with an error of about 27.6%, this estimated value is commonly accepted as reasonable in pavement engineering.

These two numerical examples show that the proposed method to estimate elastic modulus of the subgrade layer is valid in both cases (without and with GWT), and the validation is checked by field FWD time-histories from the Long-Term Pavement Performance (LTPP) database, although the actual elastic modulus of the subgrade layer is unknown.

# 3.5 Validating the Proposed Method Using Case Studies from LTPP

Three cases are chosen from the LTPP database in this section, and their pavement profiles and time-histories are shown in each sub-section. Two different methods are used to estimate the modulus of the subgrade layer. One is calculated by the most common backcalculation software, MODCOMP5, which is based on minimizing the root mean squared error (RMSE) of the deflection basin. The other is the proposed method using Rayleigh wave velocity, which is based on the time delay of each sensor. Since the proposed method works very well in numerical examples, it is expected that the estimation of the elastic modulus from Rayleigh wave is better than that from the backcalculation software MODCOMP5.

# 3.5.1 Example of FWD Test at LTPP 04-1036 Station in 1998

One example of a FWD test at 04-1036 station (Arizona) in 1998 was selected for analysis, and the FWD test load and deflection histories are shown in Fig. 18 in section 3.3. It illustrates that the deflection histories yields information on viscoelasticity. There are several overlays above the original pavement; however, they are combined into one layer as they are all thin AC mixtures. The maximum pressure during the FWD test is 749 kPa (108.63 psi).

The time delay and maximum deflection of each sensor for this example are summarized in Table 8. Note that the measured time delay values are not as accurate because of the sampling time interval being too coarse (0.4 ms).

Table 8: Time delay and peak deflection of each sensor due to the FWD test at station 04-1036 in 1998

Sensor	1	2	3	4	5	6	7
Distance (in)	0.00	8.0	12.0	18.0	24.0	36.0	60.0
Time delay (ms)	1.6	1.6	2.4	2.8	2.8	5.2	9.2
Peak deflection (mils)	21.69	17.05	13.86	9.13	6.50	3.35	1.65

Using the wave velocity method proposed in this chapter, the Rayleigh wave velocity is 144.2 m/s, and the elastic modulus is 156.9 MPa (22.7 ksi), assuming the mass density of the subgrade layer is 1800 kg/m<sup>3</sup>.

By MODCOMP5, the elastic modulus of each layer can be calculated, given the pavement structural profile. The pavement structure information and the back-calculated results from MODCOMP 5 are shown in Table 9.

Table 9: Structural information and MODCOMP5 backcalculated modulus at LTPP station 04-1036 in 1998

Physical Layer	Thickness (m (in))	Poisson's ratio	Mass density (kg/m <sup>3</sup> )	Elastic Modulus (MPa (ksi))
AC	0.122 (4.8)	0.35	2300	4771 (692)
Base (GB)	0.472 (18.6)	0.30	2000	86.9 (12.6)
Subgrade (SS)	Infinity	0.45	1800	222.7 (32.3)

The deflection basins from the FWD test and the backcalculation result by MODCOMP5 are shown in Fig. 24. It is clear that the deflection basin is simulated reasonably well, and the deflections of close sensors match almost exactly. Hence, the backcalculation program converges, although the result may be unrealistic.

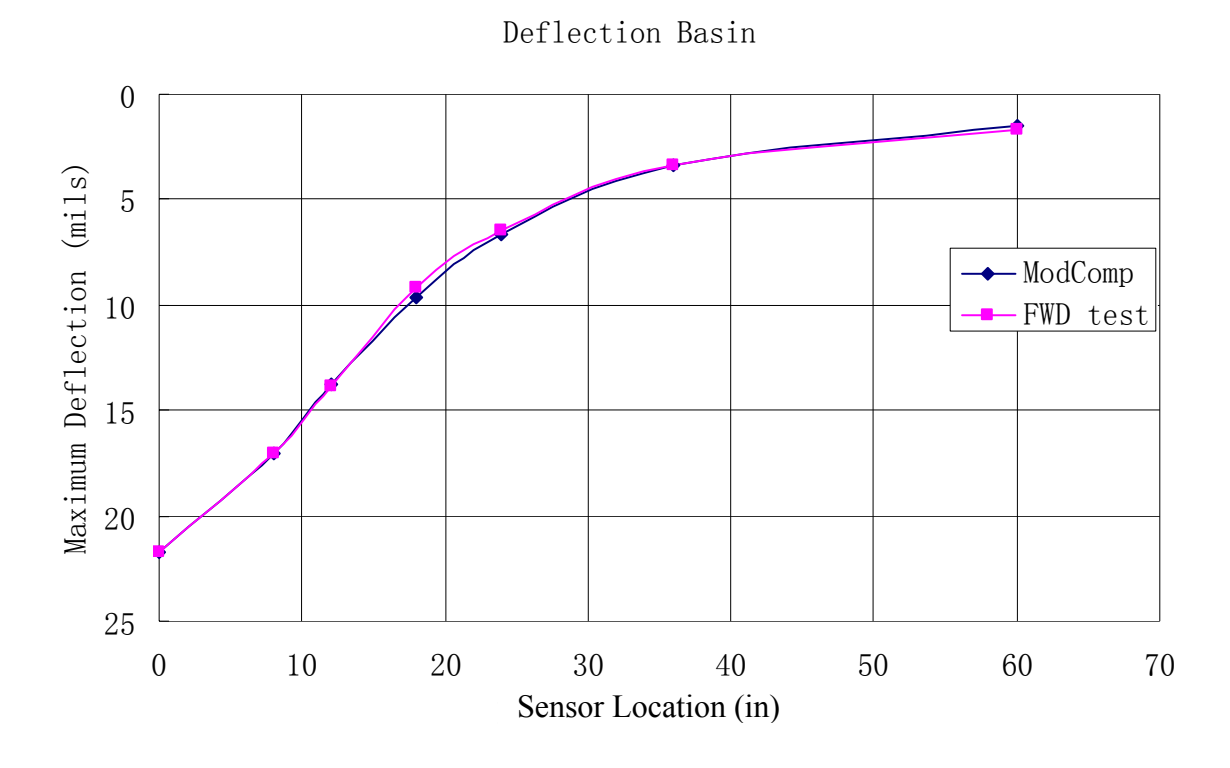


Figure 24: Deflection basin from FWD test and MODCOMP5 Simulation at LTPP station 04-1036 in 1998

From the LTPP database, the resilient modulus of the subgrade layer is tested at different confining pressures and different axial loads, and the summary of the test results is given in Table TST\_UG07\_SS07\_WKSHT\_SUM in the Test Module of the LTPP database. Typically, the confinement of the subgrade layer is 41.3 kPa (6 psi) in design (Federal Highway Administration, 1996), and the corresponding resilient modulus can be calculated as 102 MPa (14.8 ksi) by interpolation.

The elastic modulus from the backcalculation by MODCOMP5 is 222.7 MPa (32.3 ksi), and the modulus from the wave velocity method proposed here is 156.9 MPa (22.7 ksi). Thus, the difference between the experimental data and the backcalculation result is roughly 118.3%, while the difference between the experimental data and the result from the proposed wave velocity

method is 53.4%. These values are summarized in Table 10.

Table 10: Elastic modulus of the subgrade layer at LTPP station 04-1036 in 1998

Lab_ measured	Predicted by	MODCOMP5	Difference	Difference
M <sub>R</sub> @ 6psi	k-value	backcalculation	between M <sub>R</sub> and	between M <sub>R</sub>
confinement	$(E_{k-value})$	$(E_{MODCOMP})$	E <sub>k-value</sub>	and E <sub>MODCOMP</sub>
102 MPa	156.9 MPa	222.7 MPa	53.4 %	118.3 %
(14.8 ksi)	(22.7 ksi)	(32.3 ksi)	33.4 %	118.3 70

# 3.5.2 Example of FWD Test at LTPP 32-0101 Station in 1996

Another example is chosen from LTPP station 32-0101 in 1996. The FWD test load and deflection histories are shown in Fig. 25. There are 5 relatively thick physical layers. For the backcalculation analysis, they are separated into each physical layer first, and then they are combined together if the results from backcalculation are unrealistic. The test was done in Nevada in early winter. The maximum test pressure was 454 kPa (65.85 psi).

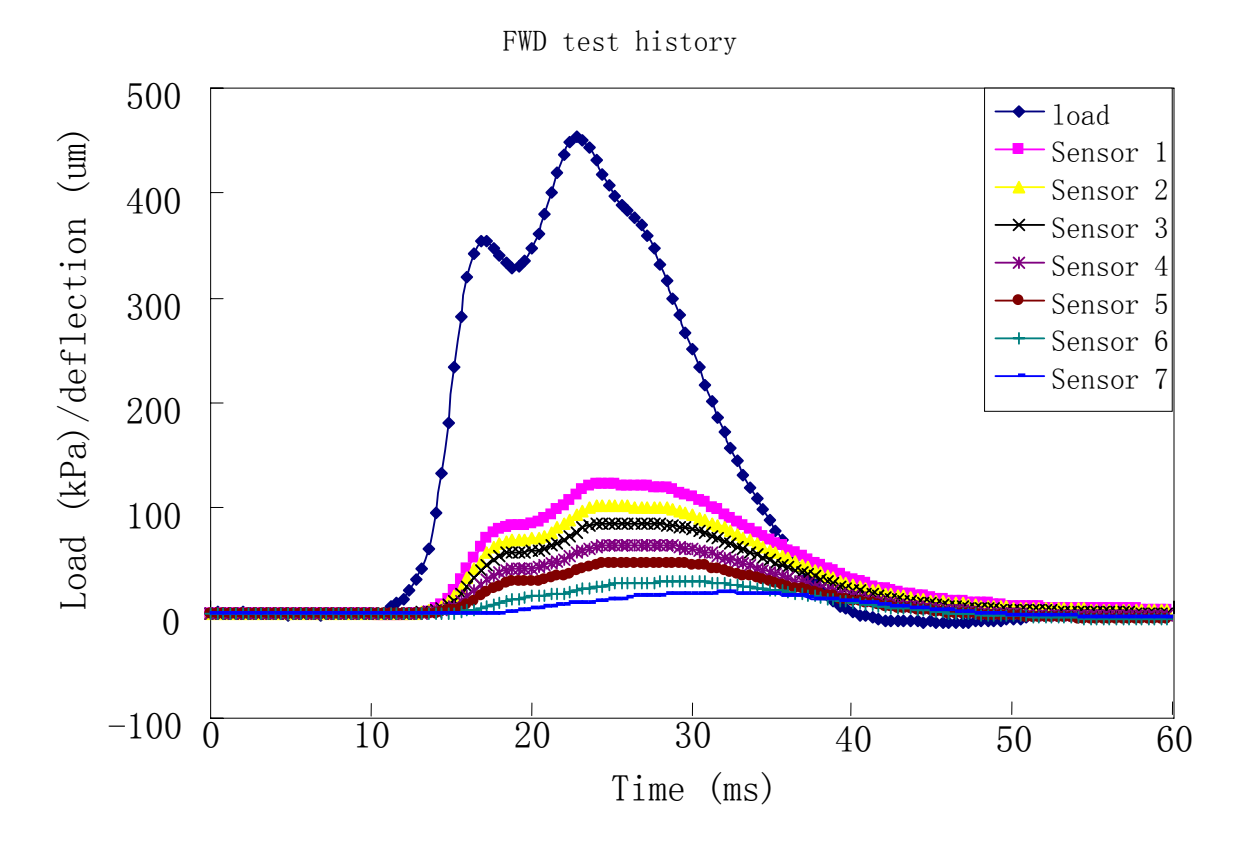


Figure 25: Example of FWD test results at LTPP station 32-0101 in 1996

The time delay and maximum deflection of each sensor at station 32-0101 in 1996 are summarized in Table 10. Again, it is worth noting that the measured time delays are not as accurate, because of the large sampling time intervals (0.4 ms).

Table 10: Time delay and maximum deflection of sensors during the FWD test at LTPP station 32-0101 in 1996

Sensor	1	2	3	4	5	6	7
Distance (in)	0.00	8.0	12.0	18.0	24.0	36.0	60.0
Time delay (ms)	1.2	1.6	1.6	2.0	2.0	5.2	8.8
Peak Deflection (mils)	4.84	4.06	3.39	2.56	1.89	1.18	0.79

Using the proposed method, the Rayleigh wave velocity is 138.5 m/s, and the elastic modulus is 120.6 MPa (17.5 ksi), assuming the mass density of the subgrade layer is 1500 kg/m<sup>3</sup>.

The pavement structural information and the back-calculated results from MODCOMP 5 are shown in Table 11.

Table 11: Basic information and MODCOMP5 backcalculated modulus at LTPP station 32-0101 in 1996 (Trial: I)

Physical Layer	Thickness (m (in))	Poisson's ratio	Mass density (kg/m <sup>3</sup> )	Elastic Modulus (MPa (ksi))
AC	0.183 (7.2)	0.35	2300	7997 (1160)
Base (GB)	0.216 (8.5)	0.30	2000	60.7 (8.8)
Subbase (GS)	0.579 (22.8)	0.45	1800	5405 (784)
Subbase (TS)	0.305 (12)	0.45	1800	250969 (36400)
Subgrade (SS)	Infinity	0.45	1500	165 (24.0)

The result of backcalculation for the subbase (TS) seems to be unreasonable. Another trial was conducted, in which all the base and subbase layers were combined into one single base layer with a total thickness of 1.10 m (44.3 in). The results are shown in Table 12.

Table 12: Basic information and MODCOMP5 backcalculated modulus at LTPP station 32-0101 in 1996 (Trial: II)

Physical Layer	Thickness (m (in))	Poisson's ratio	Mass density (kg/m <sup>3</sup> )	Elastic Modulus (MPa (ksi))
AC	0.183 (7.2)	0.35	2300	6640 (963)
Base (combined)	1.10 (43.3)	0.40	2000	298 (43.2)
Subgrade (SS)	Infinity	0.45	1500	281 (40.8)

The modulus is more reasonable in this trial, although the deflection basin may generate a higher RMSE. The deflection basins from the FWD test and the backcalculation results obtained by MODCOMP5 are shown in Fig. 26. It illustrates that the deflection basin is simulated reasonably well.

#### Deflection Basin

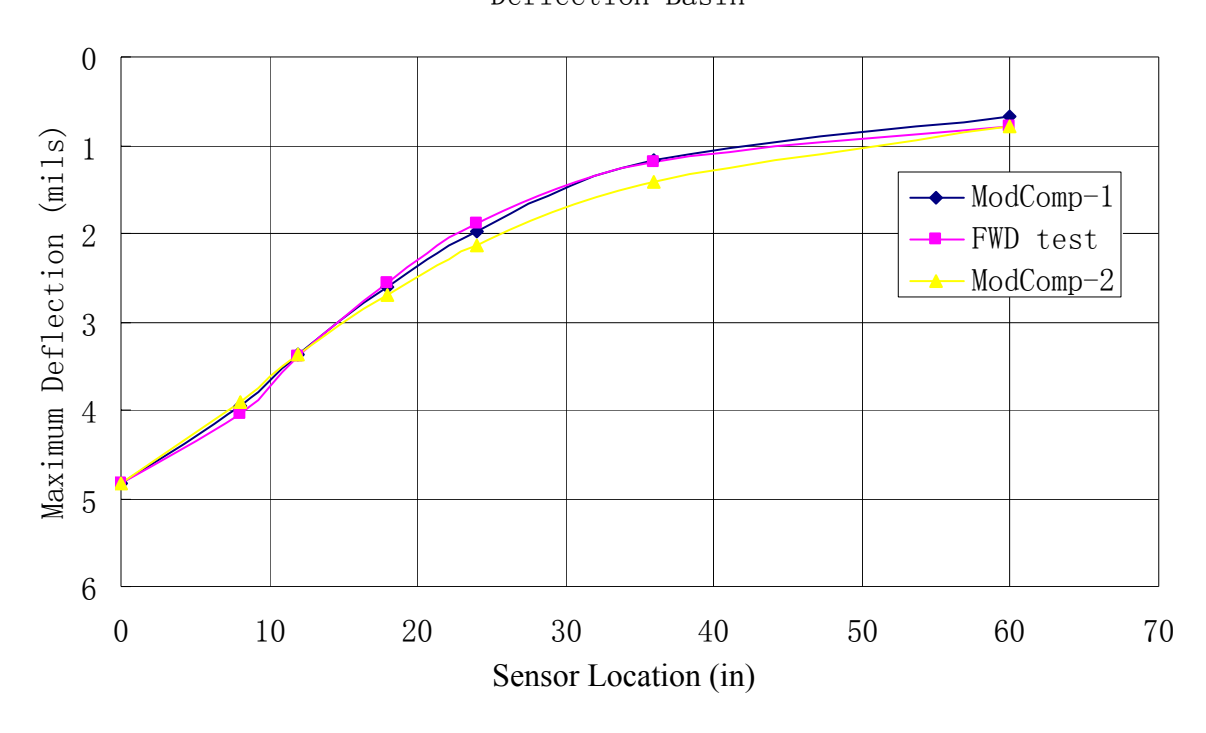


Figure 26: Deflection basin due to the FWD test and two cases of MODCOMP5 simulation at LTPP station 32-0101 in 1996

Similar to the previous example, the subgrade resilient modulus is estimated from the triaxial laboratory test results to be 64.0 MPa (9.3 ksi) at 6 psi confinement. The elastic modulus obtained from backcalculation by MODCOMP5 is 281 MPa (40.8 ksi), and the elastic modulus by the wave velocity method is 120.6 MPa (17.5 ksi). Thus, the difference between the laboratory experimental data and the backcalculation is 339.1%, as compared to 88.2% when using the wave velocity approach. These values are summarized in Table 13.

Table 13: Elastic modulus of the subgrade layer at LTPP station 32-0101 in 1996

Lab_ measured	Predicted by	MODCOMP5	Difference	Difference
M <sub>R</sub> @ 6psi	k-value	backcalculation	between M <sub>R</sub> and	between M <sub>R</sub> and
confinement	$(E_{k-value})$	$(E_{MODCOMP})$	E <sub>k-value</sub>	E <sub>MODCOMP</sub>
64.0 MPa	120.6 MPa	281 MPa	88.2%	339.1%
(9.3 ksi)	(17.5 ksi)	(40.8 ksi)	00.2/0	339.170

The difference between the experimental data and the result from proposed wave velocity method is still high, because the total thickness of the pavement structure is 50.5 inches, and the distance for the farthest sensor in the FWD test is only 60 inches, so the time delay for sensor 7 does not directly indicate the elastic modulus of the subgrade layer, rather it is the combination of the subgrade and the subgrade layers.

The freezing Index for this station is 246.63 degree-day, and the frost penetration depth is about 25 inches by interpolation from the chart (Yoder and Witczak, 1975). The thickness of the total pavement structure is more than 50 inches, so the frost problem should not affect the subbase (TS) and subgrade layer.

Since only one FWD test is input in MODCOMP5, the nonlinear property of the subgrade layer cannot be obtained, and the subgrade layer is assumed as linear elastic material, or the modulus is independent of the stress condition. This simplification would significantly increase the error from MODCOMP5.

# 3.5.3 Example of the FWD Test at LTPP Station 06-0565 in 1999

Another example is chosen from LTPP station 06-0565 in California in 1999. The FWD test load and deflection histories are shown in Fig. 27. There are 5 relatively thin AC layers, so they are combined into one AC layer for analysis, although they were constructed at different times. The maximum applied pressure is 532 kPa (77.16 psi).

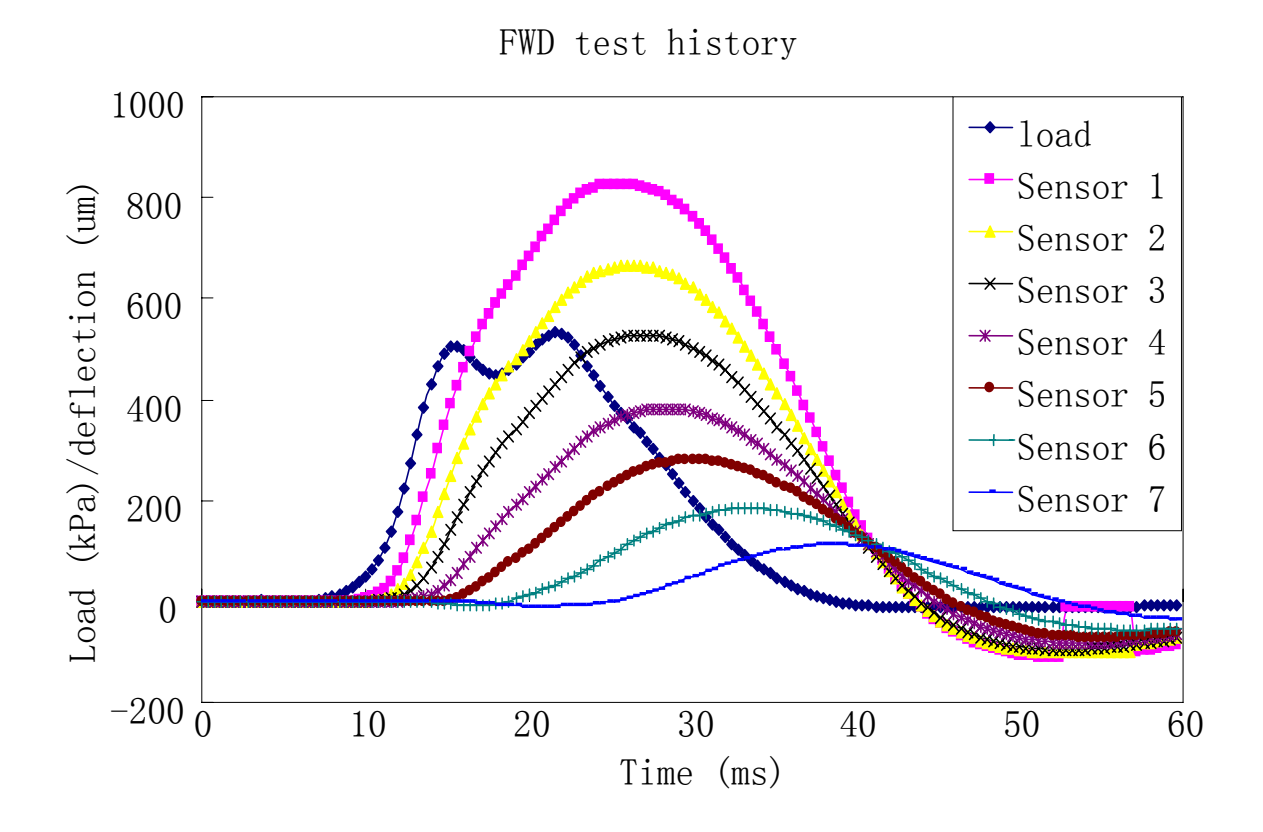


Figure 27: Example of the FWD test history at LTPP station 06-0565 in 1999

The time delay and maximum deflection of each sensor are summarized in Table 14.

Table 14: Time delay and maximum deflection of the sensors due to the FWD test at LTPP station 06-0565 in 1999

Sensor	1	2	3	4	5	6	7
Distance (in)	0.00	8.0	12.0	18.0	24.0	36.0	60.0
Time delay (ms)	3.6	4.4	5.2	6.4	8.0	11.2	16.0
Peak deflection (mils)	32.56	26.18	20.75	15.04	11.02	7.24	4.41

Following the proposed method, the Rayleigh wave velocity is 116.0 m/s, and the elastic modulus is 101.5 MPa (14.7 ksi), assuming the mass density of the subgrade layer is 1800 kg/m<sup>3</sup>.

The pavement structure information and the back-calculated results from MODCOMP 5 (trial I) are shown in Table 15.

Table 15: Structural information and MODCOMP5 backcalculated modulus at LTPP station 06-0565 in 1999 (Trial: I)

Physical Layer	Thickness (m (in))	Poisson's ratio	Mass density (kg/m <sup>3</sup> )	Elastic Modulus (MPa (ksi))
AC	0.208 (8.2)	0.35	2300	834.3 (121.0)
Base (TB)	0.119 (4.7)	0.30	2000	6.9 (1.0)
Subbase (GS)	0.544 (21.4)	0.45	1800	344738 (50000)
Subgrade (SS)	Infinity	0.45	1800	9.7 (1.4)

The result of backcalculation for the subbase (GS) is unreasonable, partially due to the soft subgrade, and partially due to the soft base (TB) layer. Another trial is conduced by combining all the base and subbase layers into one single base layer. The results for trial II are shown in Table 16.

Table 16: Structural information and MODCOMP5 backcalculated modulus at LTPP station 06-0565 in 1999 (Trial: II)

Physical Layer	Thickness (m (in))	Poisson's ratio	Mass density (kg/m <sup>3</sup> )	Elastic Modulus (MPa (ksi))
AC	0.208 (8.2)	0.35	2300	703.3 (102)
Base (combined)	0.663 (26.1)	0.40	2000	55.8 (8.1)
Subgrade (SS)	Infinity	0.45	1800	57.2 (8.3)

The modulus is more reasonable in trial II, although the deflection basin may generate a higher RMSE. The deflection basins from the FWD test and the backcalculation results by MODCOMP5 are shown in Fig. 28. It shows that the deflection basin is simulated reasonably well.

#### Deflection Basin

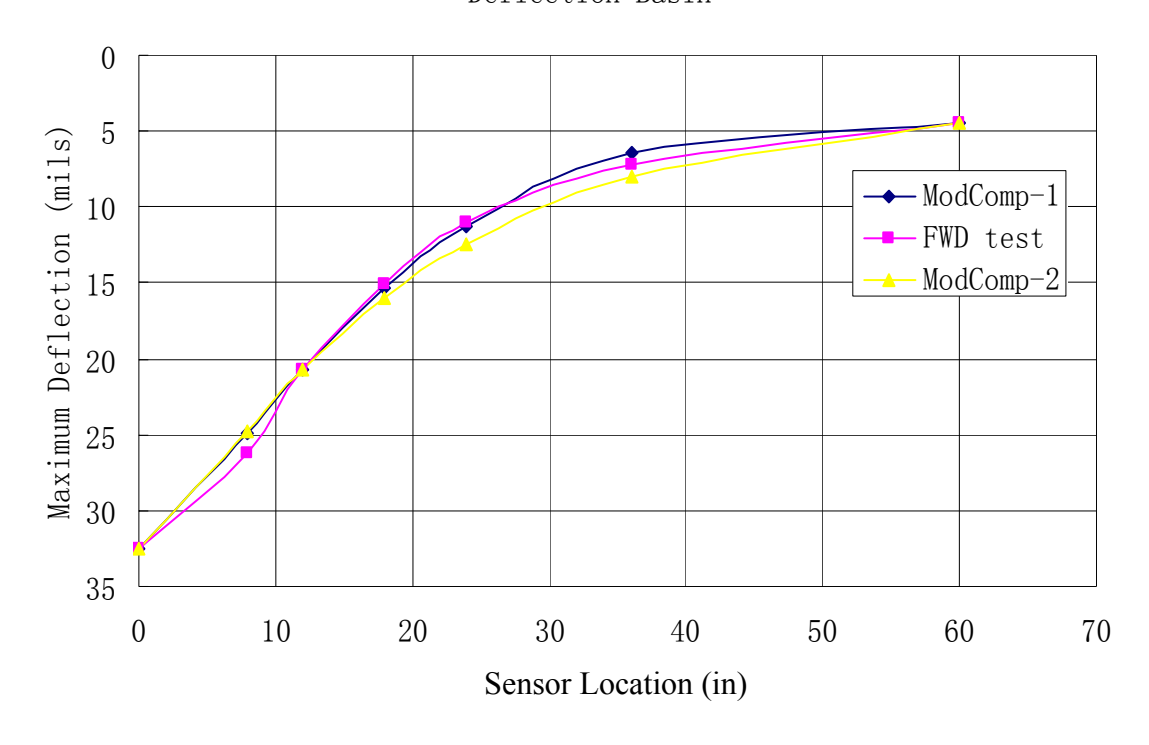


Figure 28: Deflection basin during the FWD test and two cases of MODCOMP5 simulation at LTPP station 06-0565 in 1999

Using laboratory measured values of 6 psi confinement, the subgrade resilient modulus is 83.2 MPa (12.1 ksi). The elastic modulus obtained by the backcalculation by MODCOMP5 is 57.2 MPa (8.3 ksi), and the modulus by the wave velocity method is 101.5 MPa (14.7 ksi). Thus, the difference between the experimental data and the backcalculation is 31.3%, compared to 21.5% when using the proposed wave velocity method. These values are summarized in Table 17.

Table 17: Elastic modulus of the subgrade layer at station 06-0565 in 1999

Lab_ measured	Predicted by	MODCOMP5	Difference	Difference
M <sub>R</sub> @ 6psi	k-value	backcalculation	between M <sub>R</sub>	between M <sub>R</sub> and
confinement	(E <sub>k-value</sub> )	$(E_{MODCOMP})$	and $E_{k\text{-value}}$	E <sub>MODCOMP</sub>
83.2 MPa	101.5 MPa	57.2 MPa	21.5 %	31.3 %
(12.1 ksi)	(14.7 ksi)	(8.3 ksi)	21.3 70	31.3 %

#### 3.5.4 Discussion of Case Studies Obtained from LTPP

The three examples illustrate that the proposed method generates reasonable results. The results obtained by wave propagation method are closer (20% to 80%) to the experimental data than the backcalculation results obtained by MODCOMP5 (30% to 300%). However, this observation is based on the lab-measured resilient modulus at the confinement of 6 psi, which may not be right for the case studies above. Another experimental model is applied to estimate the field elastic modulus of each subgrade layer, based on the possible compaction level during construction and the load applied by FWD test.

#### 3.5.4.1 Effect of Confinement

From experimental data, the resilient modulus (kPa), or elastic modulus, of the subgrade layer is usually expressed as the Uzan model (Chen et al., 2007), in Eq. (29):

$$M_R = k_1 \theta^{k_2} \tau^{k_3} \tag{29}$$

where: 
$$\theta$$
 is the bulk stress (kPa);  $\tau = \frac{1}{3} \sqrt{(\sigma_1 - \sigma_2)^2 + (\sigma_1 - \sigma_3)^2 + (\sigma_3 - \sigma_2)^2}$ 

is the octahedral shear stress (kPa), and  $\sigma_1$ ,  $\sigma_2$ , and  $\sigma_3$  are the principal normal stresses; and  $k_1$ ,  $k_2$ ,  $k_3$  are the regression coefficients.

If the axial stress is almost identical to the confinement pressure, the octahedral shear stress is around zero, and the regression is not easy, so the modified model, Cornell model (Irwin, 1994), is also implemented to better capture the above relationship, as in Eq. (30).

$$M_R = k_1 \theta^{k_2} (\tau + 1)^{k_3} \tag{30}$$

The experimental results of the above three examples are summarized for different cases of axial load and confinement based on the LTPP database, and the RMSE technique is applied to find the regression coefficients. There are no laboratory data for station 06-0565; however, the experimental data for 06-0564 are available with two locations (BA9, BA10). One can assume the subgrade should be the same since the two stations are separated for only 100 ft. The results of data regression are shown in Table 18.

Table 18: Results of data regression of resilient modulus on stress parameters using Uzan and Cornell Models

G. J. ID		Uzan	model		Cornell model			
Station ID	$k_{I}$	$k_2$	$k_3$	$R^2$	$k_{I}$	$k_2$	$k_3$	$R^2$
04-1036	29295	0.1963	-0.0278	0.631	29696	0.2068	-0.0521	0.712
32-0101	4991	0.5341	-0.0708	0.597	5224	0.5427	-0.1027	0.614
06-0564-BA9	45994	0.1444	-0.0322	0.364	44761	0.1690	-0.0665	0.424
06-0564-BA10	24216	0.2177	-0.0493	0.277	26140	0.2240	-0.0910	0.331

With the exception of data from station 06-0564 at location BA10, all other data are reasonable with regression R<sup>2</sup>>0.40 (Baladi, 2010). For simplification and better estimation, the experimental data from 06-0564-BA9 were used for station 06-0565 for further analysis.

The actual confinement of the subgrade layer is unknown, although it was assumed to be 41.3 kPa (6 psi) in the design procedure. The coefficient of lateral earth pressure at rest ( $K_0$ ) for subgrade may vary from 0.4 to 2.0, depending on the compaction level during construction. The overburden stress in the Z-direction can be approximately calculated based on the mass density of each layer, as the thickness of each layer is known. The stress status inside the subgrade layer

can be calculated based on the coefficient of lateral earth pressure at rest  $(K_0)$ .

For the FWD test, the stress inside the pavement can be directly obtained by the layered elastic program JULEA, and the total stress is the summation of the stress at rest added to the stress from the FWD load. Since the subgrade layer is semi-infinite, only the stress at 1 ft below the subgrade surface (the compaction depth in construction) is considered, and the horizontal distances are chosen for the location of sensors 5, 6 and 7.

The calculation variables and outcomes at station 04-1036 are shown in Table 19, given the maximum FWD test pressure is 749 kPa (108.63 psi).

Table 19: The stress status of the subgrade layer in the FWD test for different K<sub>0</sub> values

Sensor	Horiz.	Depth	At rest	FWD	FWD	FWD	Total E	Bulk Stres	ss (psi)	Octa.
No.	dist. (in)	(in)	$\sigma_{z}$ (psi)	$\sigma_{x}$ (psi)	$\sigma_{y}(psi)$	$\sigma_{z}$ (psi)	$k_0 = 0.4$	$k_0 = 1.0$	$k_0 = 2.0$	τ (psi)
5	24.0	35.4	2.52	-0.14	0.22	1.54	6.2	9.2	14.2	0.98
6	36.0	35.4	2.52	-0.10	0.35	0.82	5.6	8.6	13.7	0.67
7	60.0	35.4	2.52	-0.04	0.27	0.20	5.0	8.0	13.0	0.28

Based on the bulk stress and octahedral shear stress ranges, the range of the resilient modulus ( $M_R$ ) can be determined, given the regression coefficients in Table 18. A similar procedure was done for stations 32-0101 and 06-0565. The range of  $M_R$  calculated using the non-linear model, the elastic modulus from forward calculation by Rayleigh wave method, and backcalculation by MODCOMP5 for the three cases in the LTPP database are shown in Table 20.

Table 20: The range of elastic moduli predicted by nonlinear models, measured in the lab, estimated by the proposed method, and backcalculated by MODCOMP5 for the case studies (MPa)

C4-4:	Nonline	ar model p	rediction	Lab-Measured	E-4:4141	MODCOMBS
Station ID	Minimum	Average	Maximum	M <sub>R</sub> @ 6 psi confinement	Estimated by the proposed method	
04-1036	58.4	64.6	72.7	102.0	156.9	222.7
32-0101	43.9	59.8	79.0	64.0	120.6	281.0
06-0565	79.0	86.2	93.8	83.2	101.5	57.2

The difference in subgrade moduli predicted by the three methods was smallest at station 06-0565, and largest at station 04-1036. As the bulk stress affects the  $M_R$  more than the octahedral shear stress, the bulk stress, or the confinement is more important in determining the  $M_R$  of the subgrade layer. The maximum bulk stress at station 04-1036 is 13 psi or less, as shown in Table 16, meaning the confinement is much less than 6 psi. At station 06-0565, the bulk stress is much higher than that at 04-1036 (values are not shown here), as the pavement structure is thicker in the base layer, and the confinement pressure may be around 6 psi.

The confinement of the subgrade layer is unknown, and the error may be less if the actual confinement is known. The Poisson's ratio and mass density are assumed in the proposed method, and that have a linear effect on the final result. In the above examples, the mass density is estimated from Stubstad (2002). If the mass density were more accurate, the error would be smaller.

# 3.5.4.2 Effect of Sampling Intervals

Theoretically, it is possible to accurately predict the modulus of subgrade layers, if the sampling interval is small enough and more sensors are available. Practically, the sampling time is around 0.4 ms, and there are typically 7 sensors within 72 inches from the FWD load, so the error may be significant. Assuming the S-wave velocity is 150 m/s, and R-wave velocity is 142.4

m/s, the time required for each wave to arrive at each sensor in the FWD test is listed in Table 21.

Table 21: Arrival time for S-wave and R-wave for each sensor due to the FWD test

Sensor	1	2	3	4	5	6	7
Location (m)	0	0.3	0.6	0.9	1.2	1.5	1.8
S-wave (ms)	0	2.0	4.0	6.0	8.0	10.0	12.0
R-wave (ms)	0	2.1	4.2	6.3	8.4	10.5	12.6

If the sampling interval is 0.4 ms in the FWD test, the time difference between S-wave and R-wave propagation cannot be clearly identified for close sensors, which causes a significant error for subsequent sensors. The vibrations of R-wave and S-wave are in opposite directions (Fig. 9 in section 3.2.1). Because the two waves interact, the occurrence time of the peak deflection is not accurate, and thus the error can be as high as 30%. The error difference between numerical examples and case studies from the LTPP can be explained by differences in sample time intervals. In order to reduce the error in estimation of subgrade elastic modulus from wave propagation, the frequency of sampling should be increased.

# 3.6 Numerical Example of Bedrock under Subgrade layer

As shown in section 3.2.4, k-values vary if the elastic modulus of the subgrade layer is higher than 500 MPa (70 ksi). However, in some cases, a shallow bedrock may underlie the subgrade. In this section, the effect of existing shallow bedrock is investigated by numerical simulation.

Bedrock is assumed to be located 5 ft below the surface of the subgrade layer, and the time-history is simulated by SAPSI. Table 22 is a summary of the material properties of the

pavement profile.

Table 22: Material properties of a three-layer pavement structure with bedrock

Physical Layer	Elastic Modulus (MPa (ksi))	Poisson's ratio	Mass density (kg/m <sup>3</sup> )	Thickness (m (in))
AC	Experimental data	0.35	2300	0.15 (6)
Base	108 (21.8)	0.30	2000	0.3 (12)
Subgrade	34.5 (5.0)	0.45	1500	1.5 (60)
Bedrock	7000 (1000)	0.25	2800	Infinity

The FWD load is assumed as a haversine function with a duration time of 35 ms, and the maximum pressure is 707 kPa with a loading plate radius of 0.15 m. The simulated FWD time-history is plotted in Fig. 29, and the time delay of each sensor is given in Table 23.

Deflection history with Bedrock (5 ft)

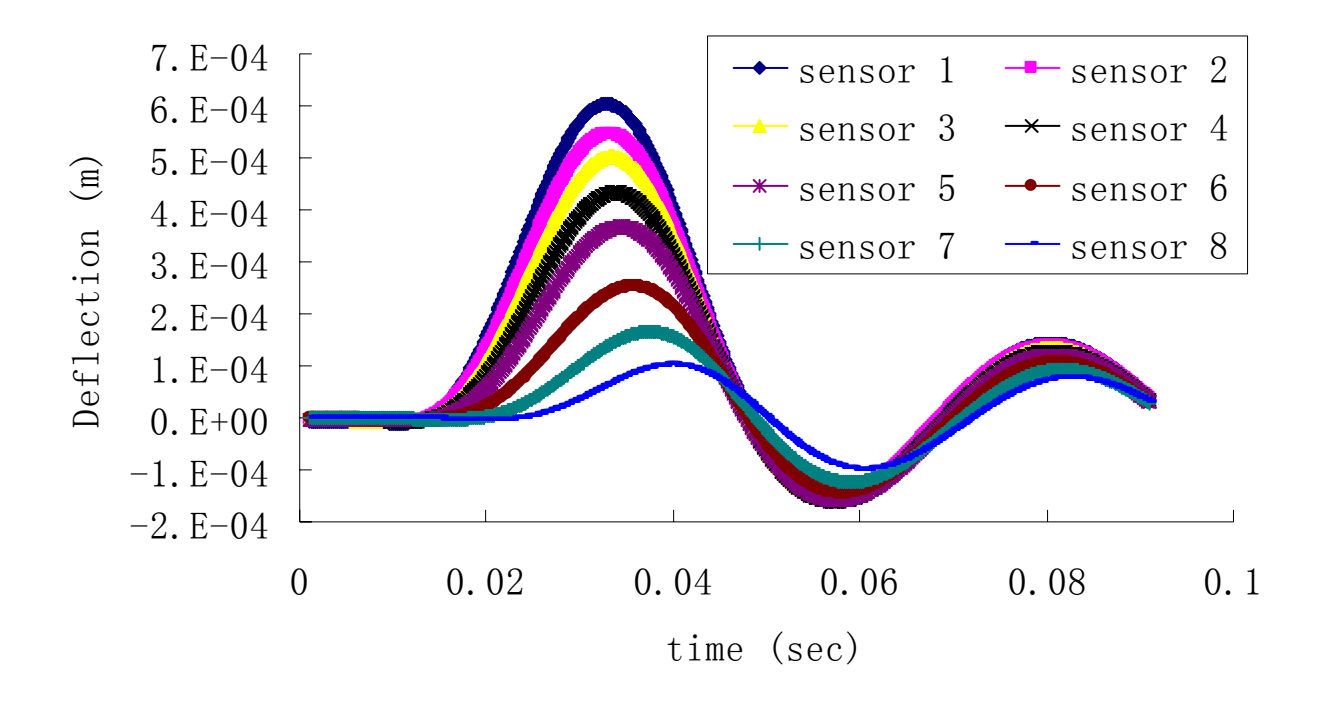


Figure 29: SAPSI simulated time-history of FWD test with bedrock underneath

Table 23: Time delay of each sensor by SPASI simulation with bedrock

Sensor	1	2	3	4	5	6	7	8
Distance (m)	0.00	0.20	0.30	0.46	0.61	0.91	1.22	1.52
Time delay (s)	0.0053	0.0056	0.0059	0.0064	0.0069	0.0083	0.01	0.0122

Fig.28 shows there is free vibration after the FWD test, due to the stiff layer underneath. The time delay vs. location is plotted in Fig. 30.

Time delay vs. location (Bedrock 5 ft)

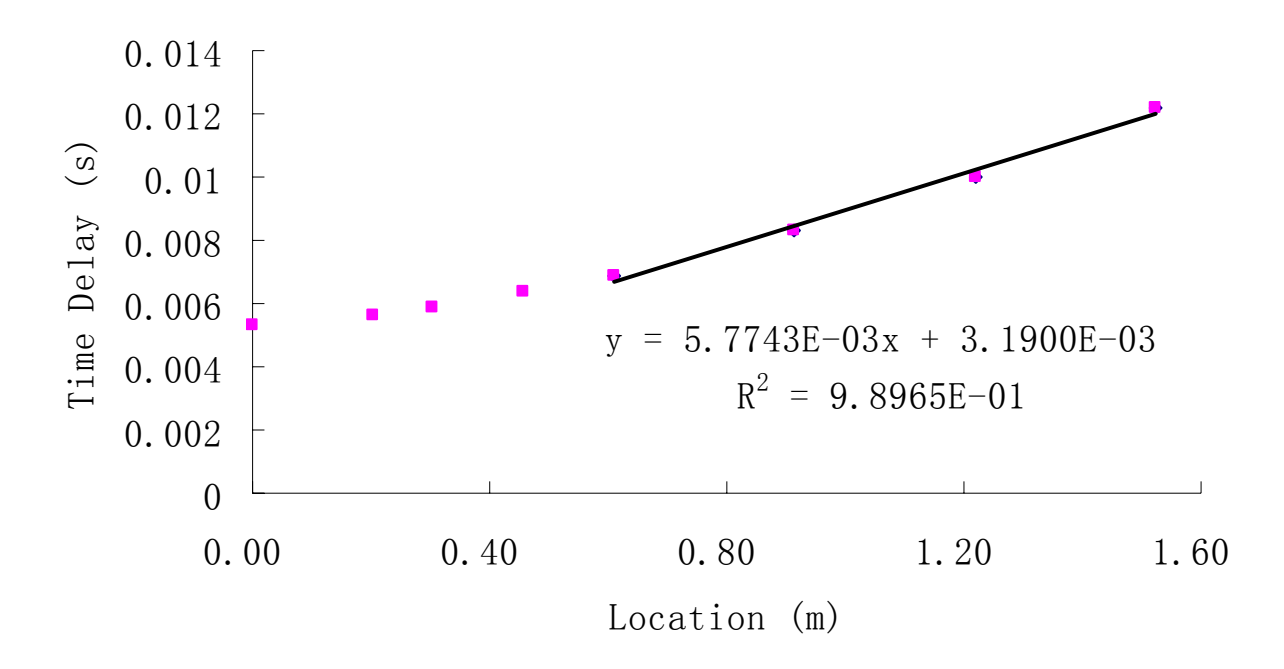


Figure 30: Time delay vs. location for a numerical example of FWD test with bedrock

The slope can be obtained by linear regression, as m = 0.005774 s/m. Following the proposed procedure in section 3.3, the elastic modulus of the subgrade layer can be calculated as: E = 368.0 MPa, which is quite different from the modulus of the subgrade layer or the bedrock layer. It is the combination of the two layers, as the more distant sensors are significantly

affected by the interaction at the interface of the subgrade layer and bedrock.

Therefore, the proposed method is not appropriate in the case of shallow bedrock. In wave propagation theory, the path of wave propagation changes if there is a stiff layer underneath and the wave is called Love wave instead of Rayleigh wave. A detailed explanation can be found in reference (Richart et al., 1970). However, the existence of shallow bedrock can be easily identified by the free vibration response of the pavement under FWD testing.

# 3.7 Summary

- Both numerical examples and case studies obtained from the LTPP database showed that the subgrade elastic modulus calculated by the proposed method based on wave propagation theory was acceptable for pavement engineering application, compared to the static backcalculation, no matter whether there is GWT underneath or not.
- The estimation of the subgrade elastic modulus can be improved in field FWD tests by increasing the sampling frequency of each sensor.
- When shallow bedrock presents, the subgrade elastic modulus cannot be estimated accurately, as the Rayleigh wave is theoretically based on one layer of semi-infinite medium, and it is only valid for layered elastic systems with higher modulus of the surface layers.
- The existence of shallow bedrock underneath the subgrade layer is indicated by free vibration in the pavement response due to the FWD test; in this case, the elastic modulus of subgrade layer cannot be obtained by the proposed method.

# Chapter 4. Layered Viscoelastic Forward

# **Solution**

# 4.1 Introduction

In each loop of any backcalculation algorithm, there is a forward solution that predicts the theoretical response, which is compared to the field measured response. Since a backcalculation program often converges after many loops of iteration, time-efficiency and accuracy are critical factors.

The forward viscoelastic solution is presented in this chapter. It utilizes the concept of 'quasi-elastic' approximation suggested by Schapery (1974). Both time-efficiency and accuracy are compared, and the viscoelastic solution is chosen for further analysis, mainly based on the consideration of time-efficiency. The error and limitation of the proposed solution is investigated later in this chapter.

# 4.2 Layered Viscoelastic Forward Solution Algorithm

# 4.2.1 Theoretical Background

The time-dependent response of linear viscoelastic material subjected to a random loading history can be computed using the following Boltzmann's superposition integral (Schapery, 1974):

$$R^{ve}(t) = \int_{\tau=0}^{t} R_H^{ve}(t-\tau) \, dI(\tau)$$
 (31)

where  $R^{ve}(t)$  is the linear viscoelastic response,  $R^{ve}_H(t)$  is the viscoelastic response to a unit step function of input (I(t) = H(t), where H(t) is the Heaviside step function) and  $dI(\tau)$  is the change in input at time  $\tau$ .

In the case of a layered system with a circular load as shown in Fig. 31, the time dependent input is the contact stress (i.e.,  $I(t) = \sigma(t)$ ) and the response of interest may be the deflections (i.e.,  $R^{ve}(t) = u^{ve}(t)$ ) at certain locations. Then we can rewrite Eq. (31) as follows:

$$u^{ve}(t) = \int_{\tau=0}^{t} u_H^{ve}(t-\tau) d\sigma(\tau)$$
(32a)

where  $u_H^{ve}$  is the deflection due to a unit contact stress (i.e.,  $\sigma(t)=1$ ). It is noted that  $u_H^{ve}$  can be either the vertical or radial deflection, although in this paper, only the vertical surface deflection is considered. The generalized formula for Eq. (32a) can be written, in cylindrical coordinates, as follows:

$$u_{vertical}^{ve}(t,z,r) = \int_{\tau=0}^{t} u_{H-vertical}^{ve}(t-\tau,z,r) d\sigma(\tau)$$
 (32b)

$$u_{radial}^{ve}(t,z,r) = \int_{\tau=0}^{t} u_{H-radial}^{ve}(t-\tau,z,r) d\sigma(\tau)$$
 (32c)

 $u_{vertical}^{ve}(t,z,r)$  and  $u_{radial}^{ve}(t,z,r)$ , respectively, are the displacements in vertical and radial directions, observed at time t and at location (r,z);  $u_{H-vertical}^{ve}(t-\tau,z,r)$  and  $u_{H-radial}^{ve}(t-\tau,z,r)$ , respectively, are the viscoelastic deflections due to a unit contact stress (i.e.,  $\sigma(t)=1$ ).

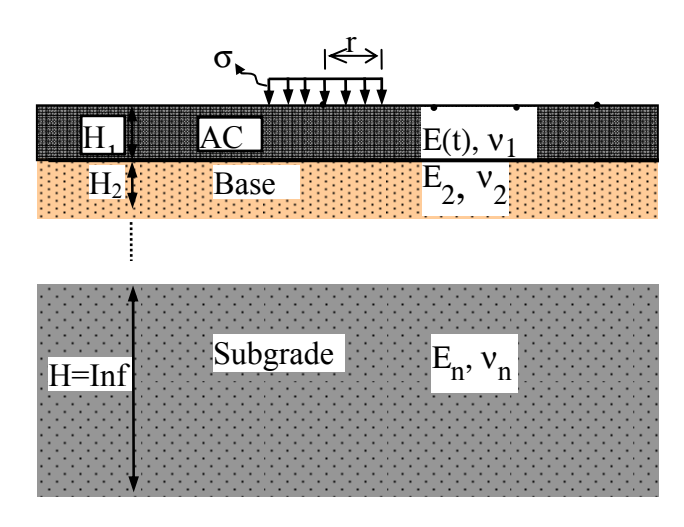


Figure 31: Typical geometry of a pavement structure

The viscoelastic deflection due to a unit contact stress ( $u_H^{ve}$ ) can efficiently and accurately be computed by using Schapery's 'quasi-elastic' approximation (Schapery 1965; 1974). Quasi-elastic theory states that unit viscoelastic response (e.g.,  $u_H^{ve}(t)$  = surface deflection) at any time t can be approximated by the unit elastic response (e.g.,  $u_H^{e}(E^{ve}(t))$  = elastic surface deflection), which is calculated using the modulus (E) equal to viscoelastic modulus  $E^{ve}(t)$  evaluated at time t, i.e.:

$$u_{\mathrm{H}}^{\mathrm{ve}}(t) \cong u_{\mathrm{H}}^{\mathrm{e}}(\mathrm{E}^{\mathrm{ve}}(t)) \quad , \tag{33}$$

where  $u_H^e$  is the elastic deflection due to a unit step load computed using a layered elastic solution where  $E = E^{ve}(t)$  is utilized for the AC layer.

The detailed derivation of Eq. (33) can be found in Levenberg (2008) and will not be repeated here for brevity. In this implementation, the unit response  $u_H^{ve}(t) \cong u_H^e(t)$  values at the points of interest were computed using the CHEVLAY2 layered elastic analysis program. Then the convolution integral in Eq. (32b) is used to calculate the viscoelastic deflection  $u^{ve}(t)$ . The algorithm is described in the following section.

# 4.2.2 Algorithm Steps

Based on the theoretical formulation, the following steps are applied to implement the Viscoelastic (VE) solution from the linear elastic layered solution of CHEVLAY2.

- 1. Define the geometry (layer thicknesses, contact pressure...etc) of a layered system similar to the one in Fig. 31.
- 2. Select a stress versus time history,  $\sigma(t)$ , and divide the data into  $N_s$  discrete intervals as shown in Fig. 32.

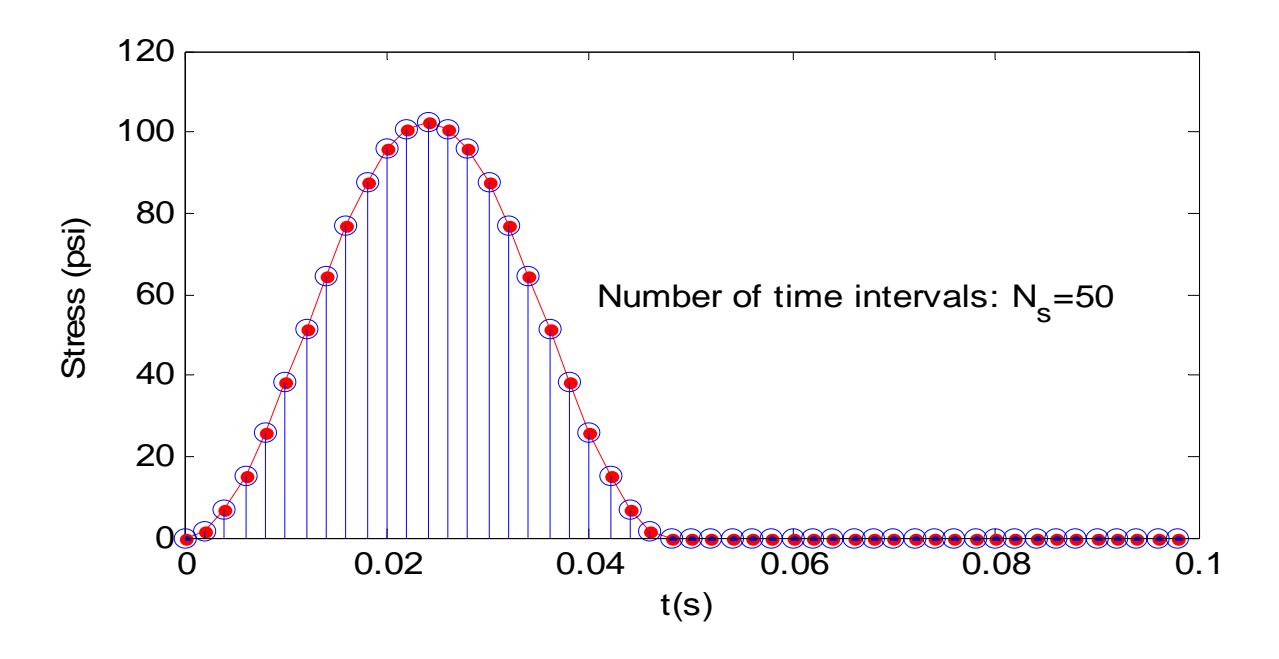


Figure 32: Discretization of stress history

3. Divide the relaxation modulus E(t) mastercurve into N<sub>E</sub> number of time steps (Fig. 33).

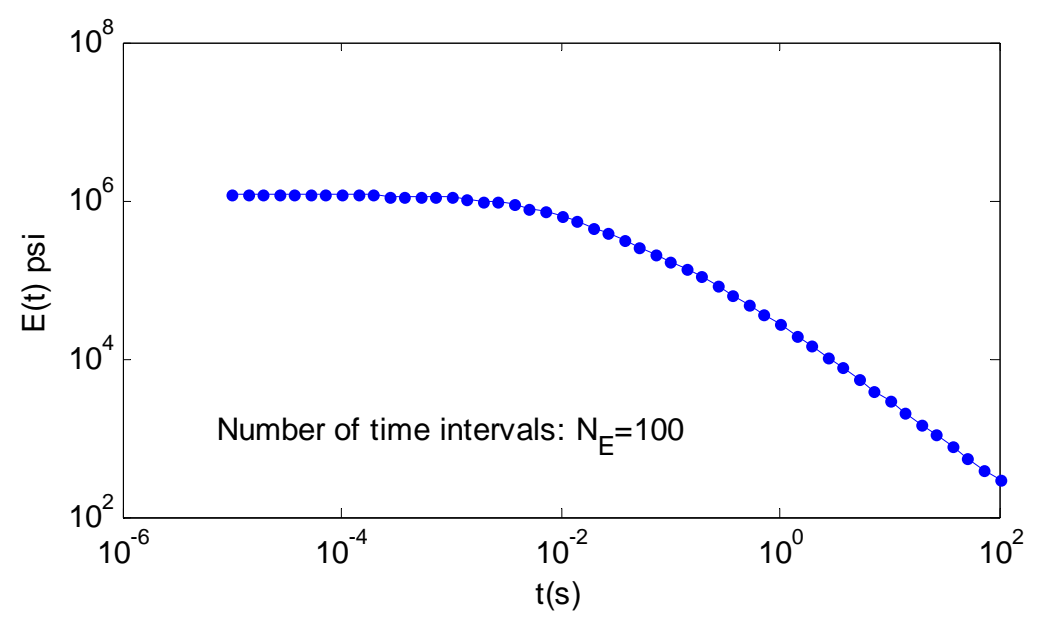


Figure 33: Discretization of the relaxation modulus mastercurve

4. Calculate the elastic response of the structure to a unit stress (step function of the load input) using the  $E(t_i)$  evaluated at different times (i.e.,  $t_1$ ,  $t_2$ ,  $t_3$  .... $t_{NE}$ ). In this present implementation, the surface deflections at several radial distances to a circular plate load shown in Fig. 31 were of interest. Therefore, these surface deflections were computed using the CHEVLAY2 program using the modulus value corresponding to different times in Fig. 34; i.e.,  $E(t_1)$ ,  $E(t_2)$ ,  $E(t_3)$ ,  $E(t_4)$ ...  $E(t_{NE})$ :

$$u_H^{ve}(t_i) \cong u_H^e$$
 calculated using  $E(t_i)$  where  $i=1,2,3...N_E$  (34)

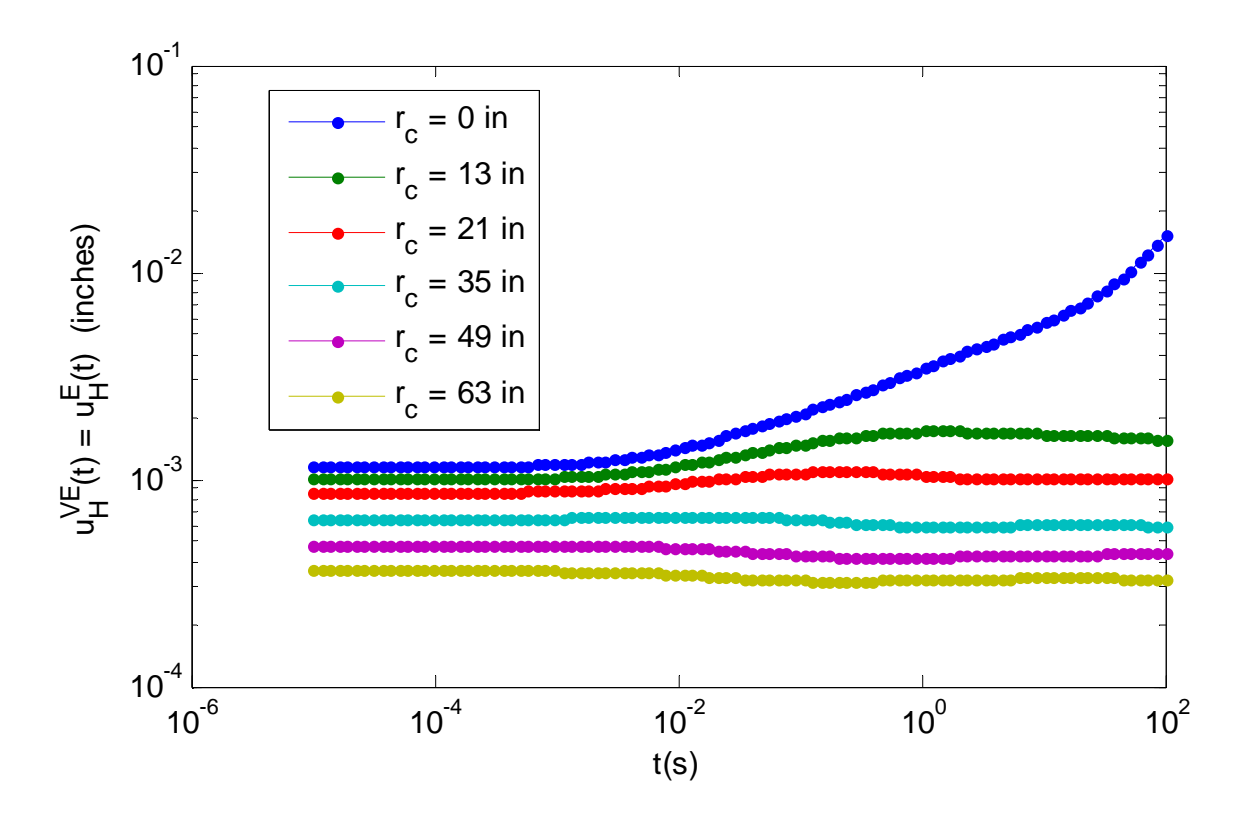


Figure 34: Deflections calculated for points at different distances from the centerline of the circular load at the surface

Fig. 34 shows the  $u_H^e$  values calculated for points at different distances from the centerline of the circular load at the surface. These curves are herein called "unit response mastercurves".

5. Calculate the viscoelastic response using the discrete form of Eq. (33) given in Eq. (35) below. Eq. (35) is evaluated at each discrete time  $t_i$  using the stress history shown in Fig. 32. Fig. 35 below illustrates the  $d\sigma(\tau_j)$  in Eq. (35) for each time step  $\tau_j$ .

$$u^{ve}(t_i) = \sum_{j=0}^{i} u_H^{ve}(t_i - \tau_j) d\sigma(\tau_j),$$
where  $i = 1, 2, ...N_s$  (35)

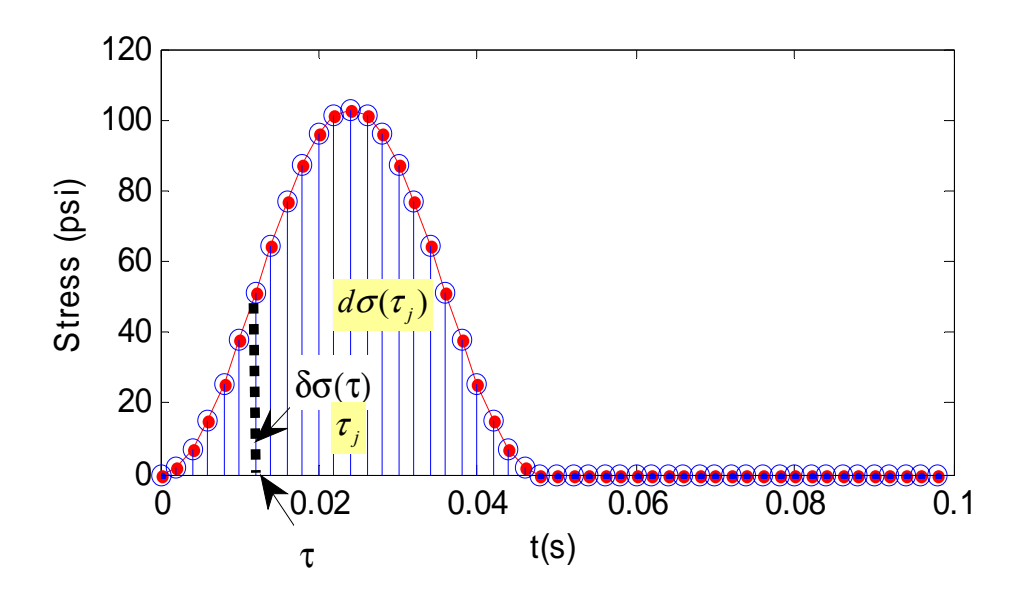


Figure 35: Illustration of the  $d\sigma( au_j)$  in Eq. (32b) for each time step  $au_j$ 

In order to illustrate an example, the viscoelastic surface deflections of the three-layered pavement structure shown in Fig. 36 are computed. Fig. 37 shows the vertical surface deflections at points located at different radial distances from the centerline of the load, and clearly shows the relaxation behavior of deflection at each point.

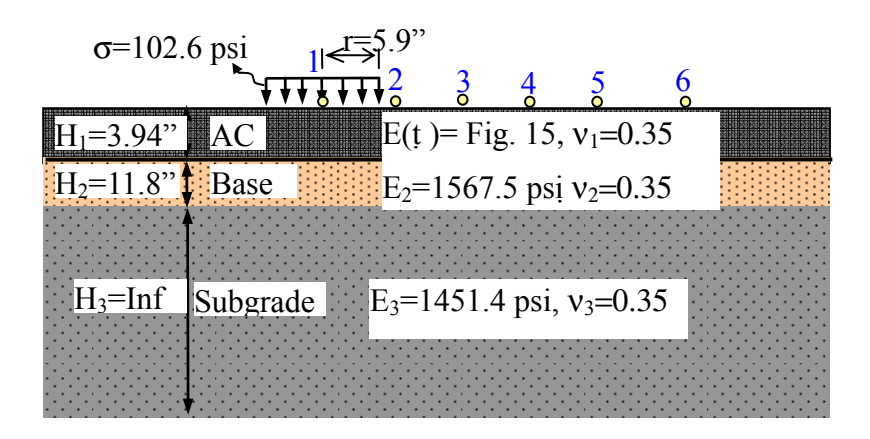


Figure 36: Example of a pavement structure used for VE forward calculation

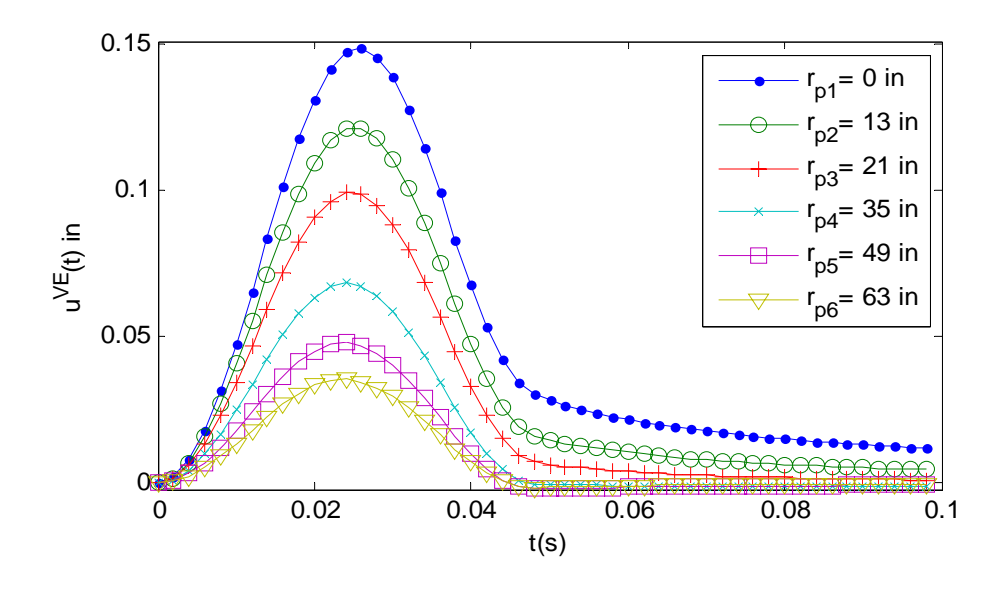


Figure 37: Examples of computed VE surface deflections at different radial distances from the centerline of the load

# 4.3 Verification of the Layered Viscoelastic Forward Solution

First, verification of 'quasi-elastic' approximation was performed. Chen (2009) introduced a theoretical solution for response of viscoelastic (VE) pavement layers. The unit responses computed using Chen's method (Chen and Pan, 2007) was compared against the 'quasi-elastic' approximation shown in Eq. (33). Second, the proposed VE solution is compared against the well-known dynamic solutions by SAPSI and LAMDA. The effect of wave propagation was eliminated from these dynamic solutions. Later, the time-efficiencies of both solutions are compared in the next section.

# 4.3.1 Verification of Quasi-Elastic Approximation

A semi-analytical solution for a multilayered viscoelastic pavement under surface loading was derived by Chen (2009; Chen et al, 2009). This solution was used to verify the accuracy of the quasi-elastic approximation. The structural properties of the pavement used in this verification are listed in Table 24.

Table 24: Material properties of the pavement structure used in the verification example

Physical Layer	Elastic Modulus (MPa (ksi))	Poisson's Ratio	Thickness (m (in))
AC	Experimental data	0.35	0.15 (6.0)
Base	108 (15.6)	0.30	0.30 (12.0)
Subgrade	34.5 (5.0)	0.45	Infinity

Only 11 terms of the Prony series of E(t) can be implemented by the solution developed by Chen (2009). The input E(t) curve was therefore approximated with a 11-term Prony series, as shown in Fig. 38. It is noted that 11-term Prony series did not accurately approximate the actual E(t) curve.

#### Implemented VS. actual E(t) of one AC layer

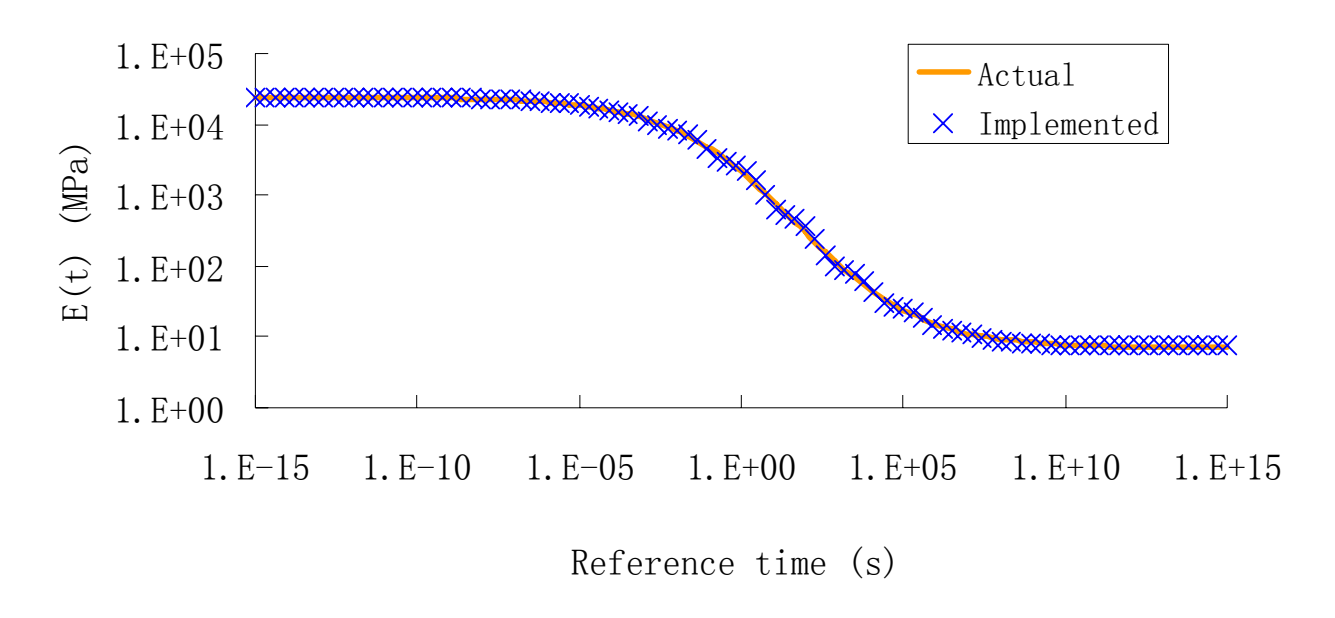


Figure 38: Implemented and actual E(t) for one AC mixture

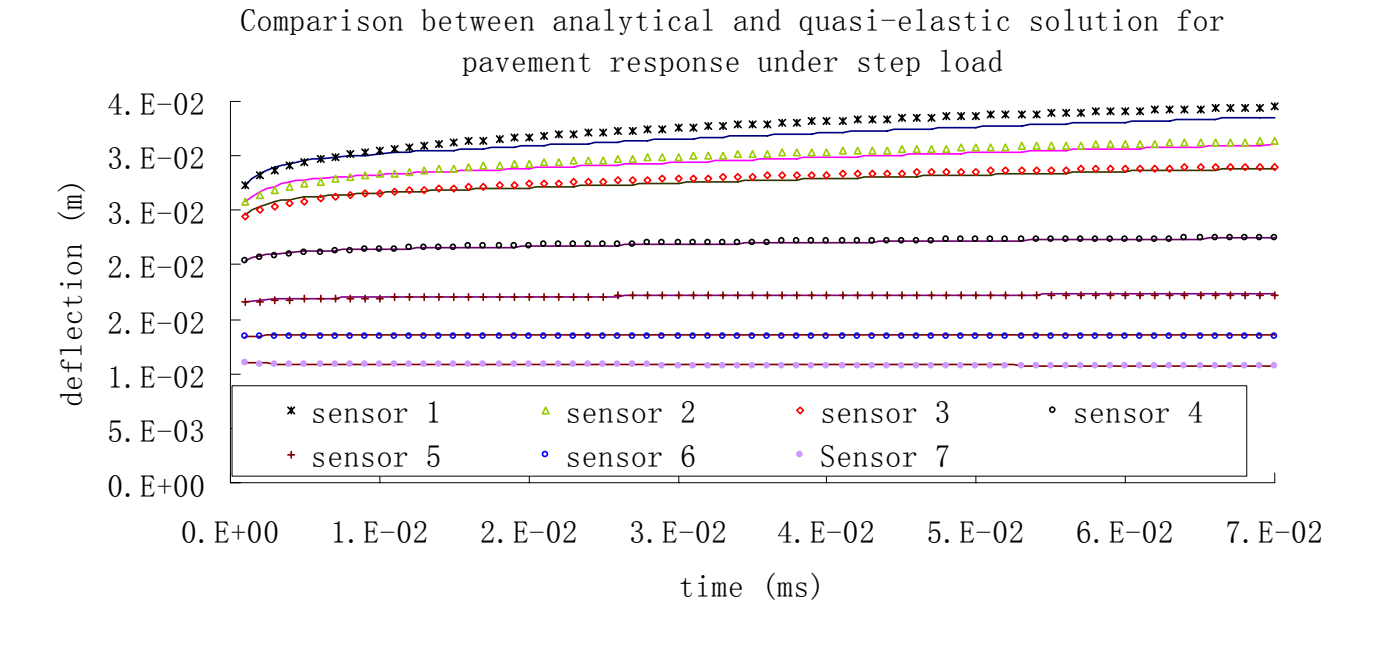


Figure 39: Implemented and actual E(t) for one AC mixture
(Solid lines represent the analytical solution, symbols represent the quasi-elastic approximation)

Fig. 39 illustrates that the quasi-elastic approximation did a very good job in predicting unit response. The maximum error was around 3% for sensor 1, and error decreased as sensor number increased. This difference might be due to the 11-term Prony series approximation of E(t) used in Chen's method.

### 4.3.2 Comparison between the Layered VE Solution and Dynamic Solutions

The layered VE forward solution is also verified against the well-known dynamic solutions, SAPSI and LAMDA. As discussed previously, wave propagation is ignored in the layered VE solution. Therefore, the deflection time histories given by SAPSI and LAMDA were shifted, so that the peaks of all sensors coincide.

In order to illustrate the absence of wave propagation, a FWD load pulse of duration 35 ms was hypothetically apply to an infinitely deep AC layer, and the response was simulated using the layered VE solution. The time-histories of the pavement response due to the FWD test simulation are shown in Fig. 40.

# FWD deflection history

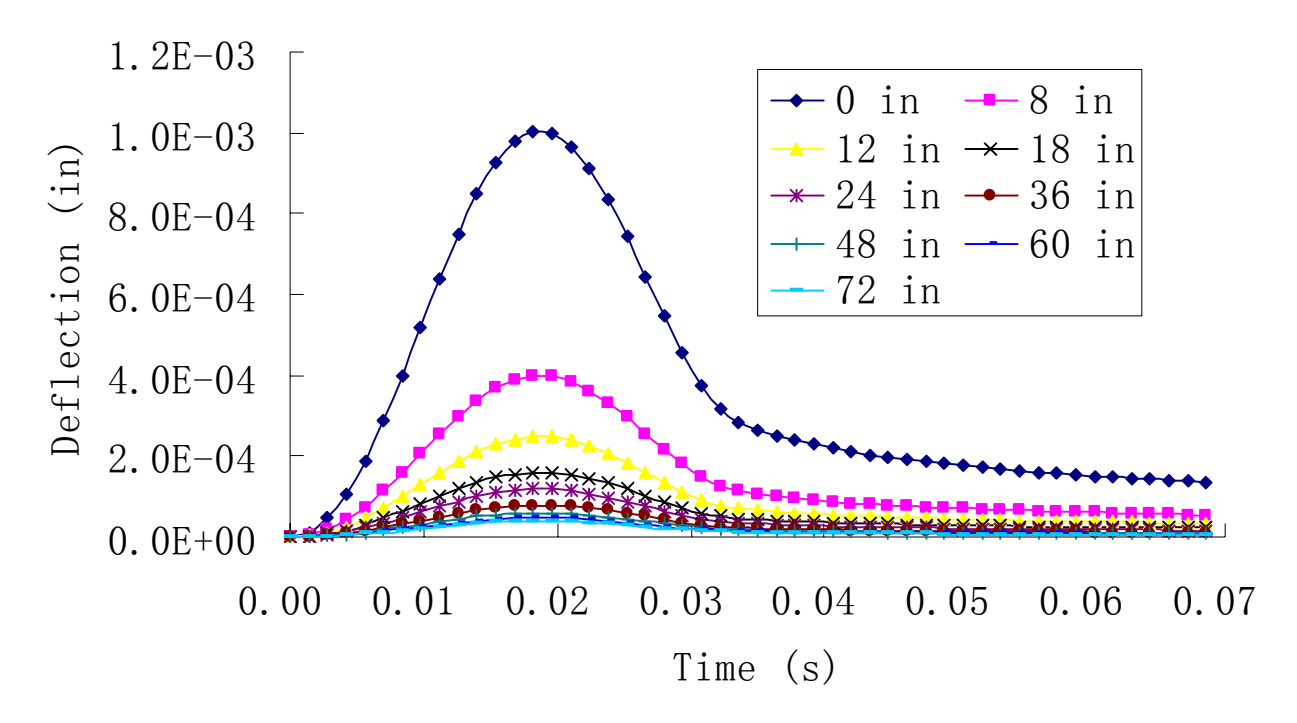


Figure 40: FWD test simulation by layered VE solution for a half-space AC layer

Delayed recovery of the displacements/deflection, which is a clear indication of viscoelastic response, is visible in Fig. 40. However, there is no time delay of the peaks between the sensors, i.e., the wave propagation cannot be simulated by layered VE solution. Since the focus of this study is on the viscoelasticity property, not the dynamic response of the system, the wave propagation response is eliminated by shifting the time histories of all sensors such that their peaks occur at the same time.

The layered VE solution is superimposed on the time-shifted dynamic solutions, in order to better compare the shape of the deflection time histories, and to show the accuracy of the layered VE solution.

Table 25 shows that the properties of a pavement structure used in comparing dynamic and

layered VE solutions. Fig. 41 and Fig. 42 show the response of the pavement under a FWD test calculated by SAPSI and LAMDA, respectively.

Table 25: Properties of a pavement used in comparison of dynamic and VE solutions

Physical Layer	Elastic Modulus (MPa (ksi))	Poisson's Ratio	Thickness (m (in))	Density (kg/m <sup>3</sup> )
AC	Experimental data	0.35	0.10 (4.0)	2300
Base	108 (15.6)	0.40	0.3 (12.0)	2000
Subgrade	34.5 (5.0)	0.45	Infinity	1500

FWD deflection history

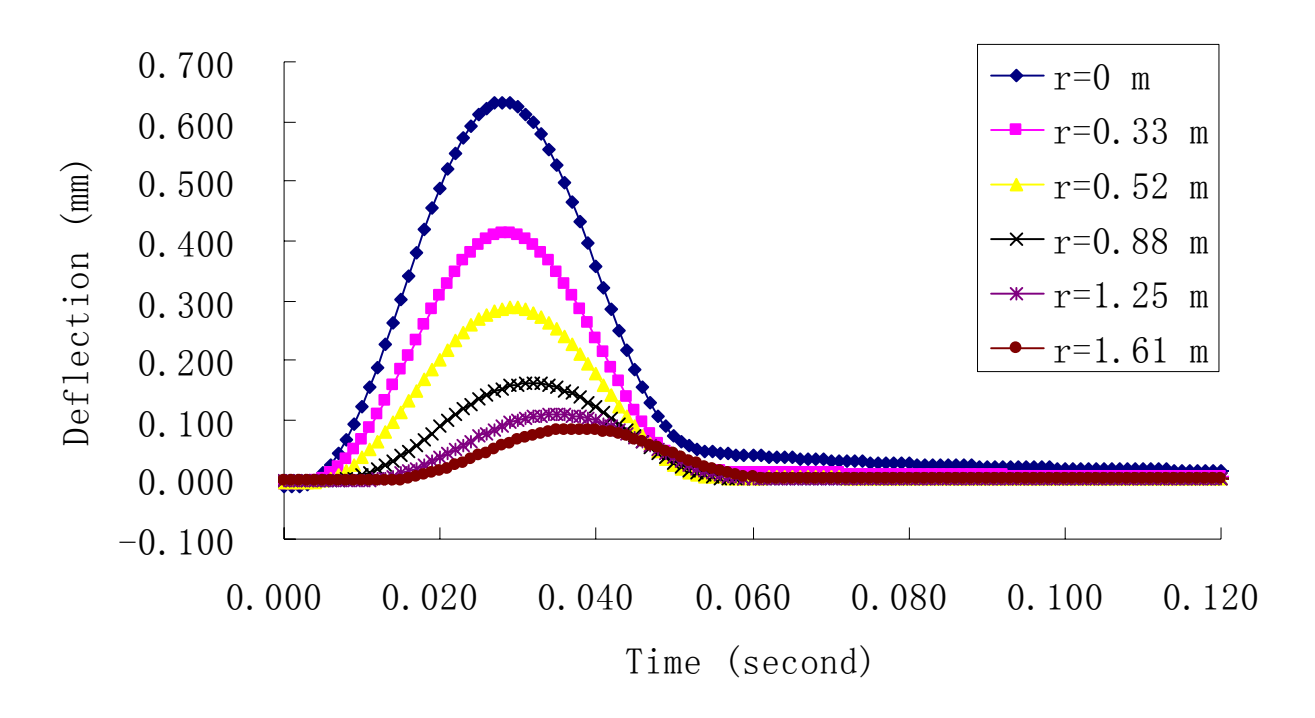


Figure 41: Sensor deflection time histories predicted by SAPSI

# FWD deflection history

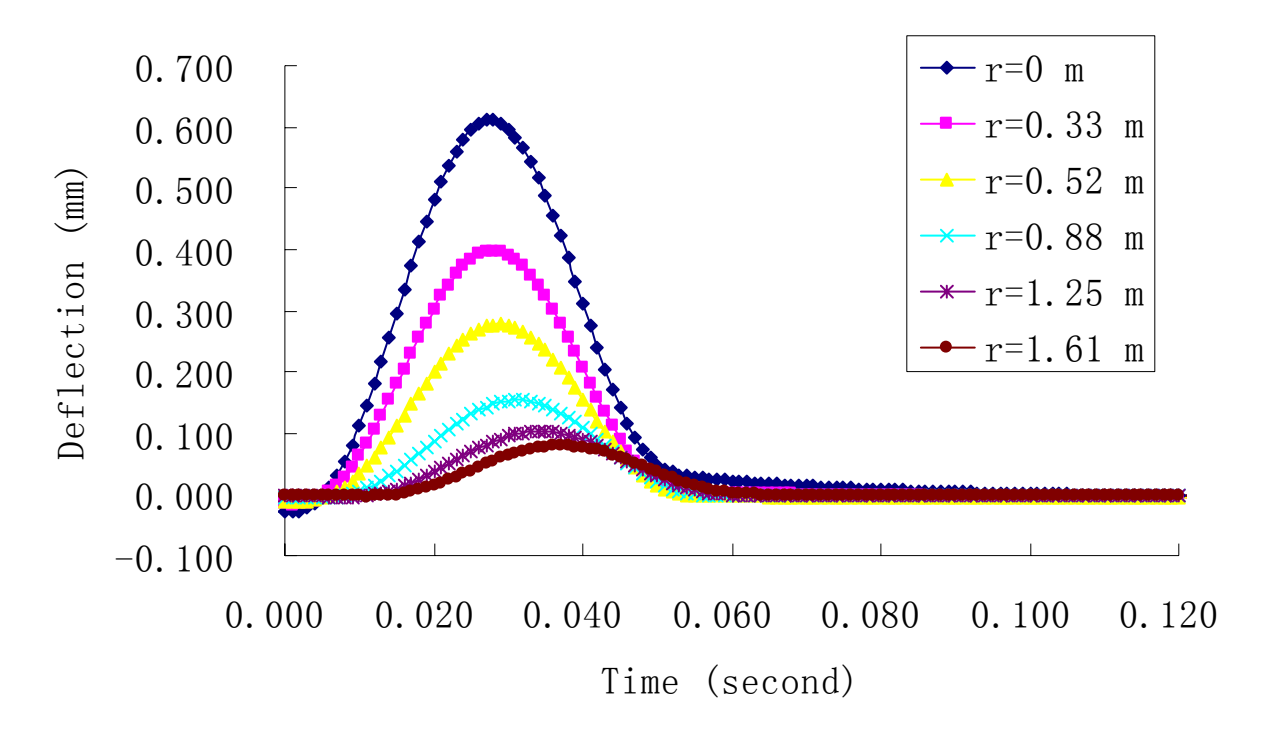


Figure 42: Sensor deflection time histories predicted by LAMDA

The layered VE solution and the time-shifted dynamic solutions for the same example are shown in Fig. 43 and Fig. 44. As shown in these figures, layered VE solution and dynamic solutions by SAPSI and LAMDA match very well. It is noted that the computational efficiency of VE solution is much better than SAPSI and LAMDA, where it takes around 20 minutes to obtain a solution from SAPSI and LAMDA, while it only takes 1 minute, or even a few seconds, to reach a solution using layered VE solution.

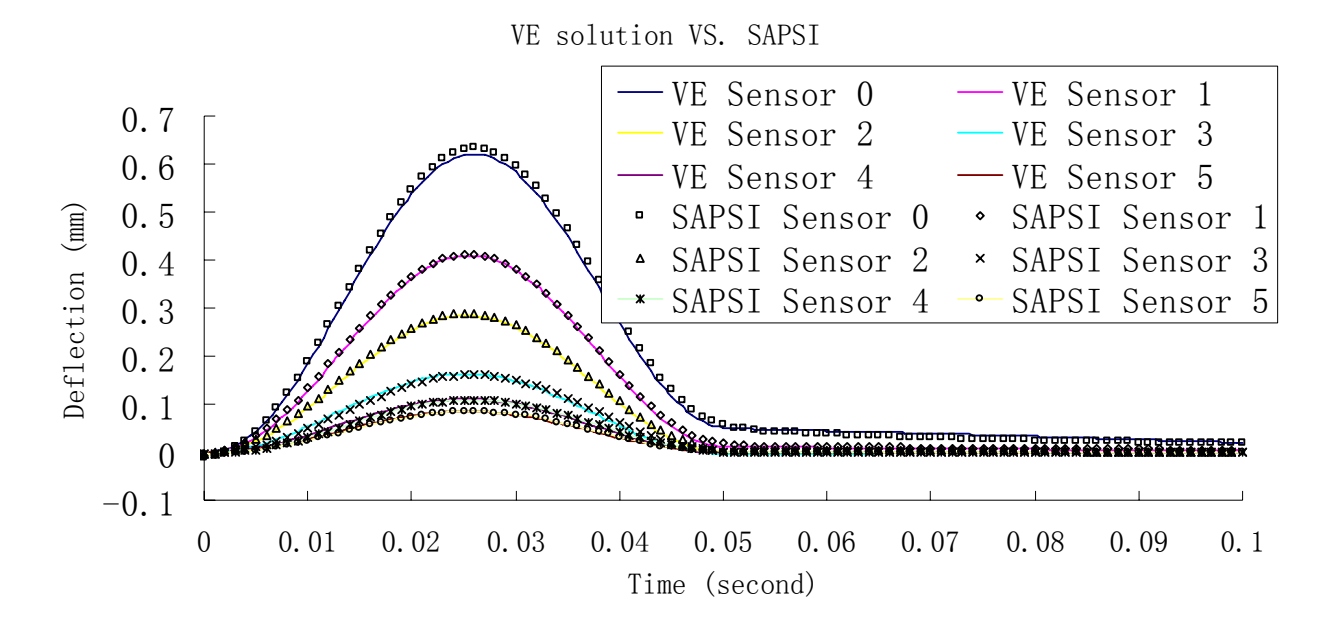


Figure 43: Comparison of deflection time histories from VE and SAPSI solutions (Solid lines represent the VE solution, symbols represent the SAPSI result)

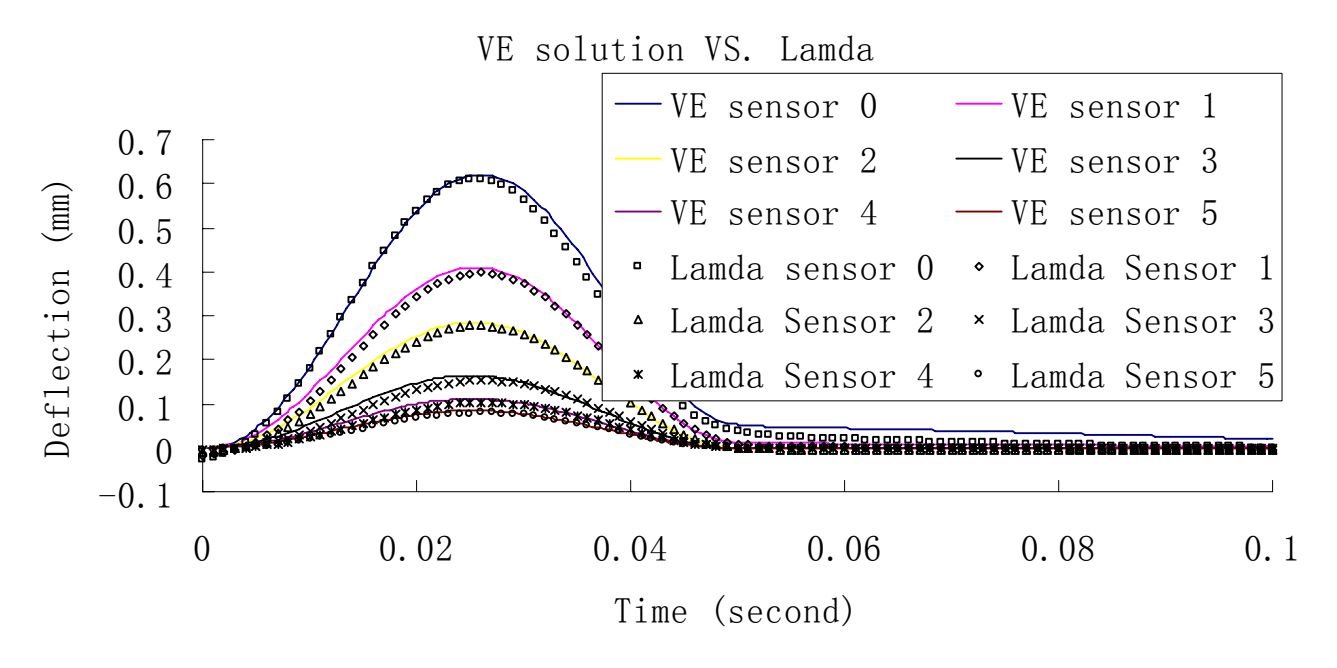


Figure 44: Comparison of deflection time histories from VE and LAMDA solutions (Solid lines represent the VE solution, symbols represent the LAMDA result)

# 4.3.3 Verification Examples using Pavement Structures from the LTPP Database

Table 26: Several examples of pavement structure in the SPS-1 project

Case No.	Layer No.	Layer Description				
116	4	Original Surface Layer (Layer Type: AC)1.8 Inch				
	3	AC Layer Below Surface (Binder Course) (Layer Type:AC)2.1 Inch				
	2	Base Layer (Layer Type:TB)12 Inch				
	1	Subgrade (Layer Type:SS)				
	Layer No.	Layer Description				
117	6	Original Surface Layer (Layer Type:AC)1.7 Inch				
	5	AC Layer Below Surface (Binder Course) (Layer Type:AC)1.5 Inch				
	4	AC Layer Below Surface (Binder Course) (Layer Type:AC)3.2 Inch				
	3	Base Layer (Layer Type:TB)5.2 Inch				
	2	Base Layer (Layer Type:GB)4 Inch				
	1	Subgrade (Layer Type:SS)				
	Layer No.	Layer Description				
120	5	Original Surface Layer (Layer Type:AC)1.8 Inch				
	4	AC Layer Below Surface (Binder Course) (Layer Type:AC)1.8 Inch				
	3	Base Layer (Layer Type:PATB)4 Inch				
	2	Base Layer (Layer Type:GB)8 Inch				
	1	Subgrade (Layer Type:SS)				
	Layer No.	Layer Description				
123	6	Original Surface Layer (Layer Type:AC)1.8 Inch				
	5	AC Layer Below Surface (Binder Course) (Layer Type:AC)2 Inch				
	4	AC Layer Below Surface (Binder Course) (Layer Type:AC)2.4 Inch				
	3	Base Layer (Layer Type:TB)8 Inch				
	2	Base Layer (Layer Type:PATB)4 Inch				
	1	Subgrade (Layer Type:SS)				

In order to further verify the layered VE solution, four pavement structures are selected from the LTPP database. Table 26 shows the selected pavement structures from the SPS-1 experiment of the LTPP database.

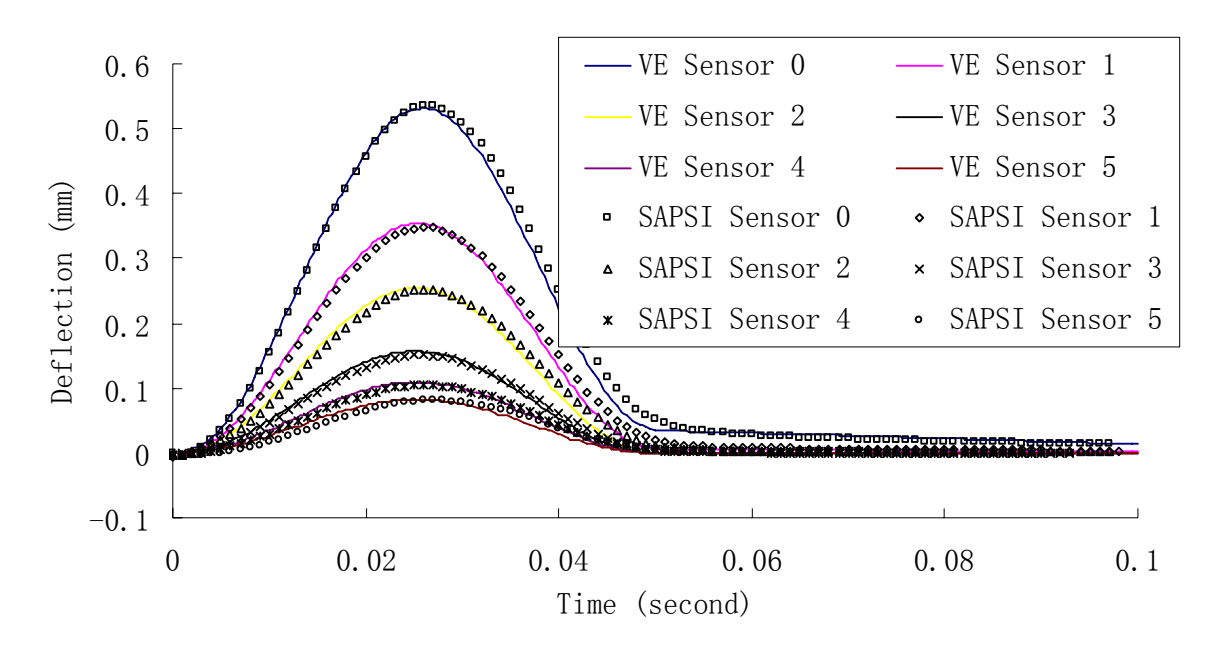
As shown in Table 26, there are several sublayers of AC. For computational efficiency, similar layers were combined into one layer, as shown in Table 27.

Table 27: Layer information for each pavement structure

Case	Physical	Elastic Modulus	Thickness	Poisson's	Mass density			
No.	Layer	(MPa (ksi))	(m (in))	Ratio	$(kg/m^3)$			
116	AC	Experimental Data	0.099 (3.9)	0.35	2300			
	Base	200 (29.0)	0.305 (12.0)	0.40	2000			
	Subgrade	100 (14.5)	Infinity	0.45	1800			
117	AC	Experimental Data	0.163 (6.4)	0.35	2300			
	Base	200 (29.0)	0.132 (5.2)	0.40	2000			
	Granular Base	150 (21.8)	0.102 (4.0)	0.40	2000			
	Subgrade	100 (14.5)	Infinity	0.45	1800			
120	AC	Experimental Data	0.091m (3.6)	0.35	2300			
	PATB*	180 (26.1)	0.102 (4.0)	0.40	2000			
	Granular Base	150 (21.8)	0.204 (8.0)	0.40	2000			
	Subgrade	100 (14.5)	Infinity	0.45	1800			
123	AC	Experimental Data	0.157 (6.2)	0.35	2300			
	Base	200 (29.0)	0.204 (8.0)	0.40	2000			
	PATB*	180 (26.1)	0.102 (4.0)	0.40	2000			
	Subgrade	100 (14.5)	Infinity	0.45	1800			
Note: PATB = Permeable Asphalt Treated Base								

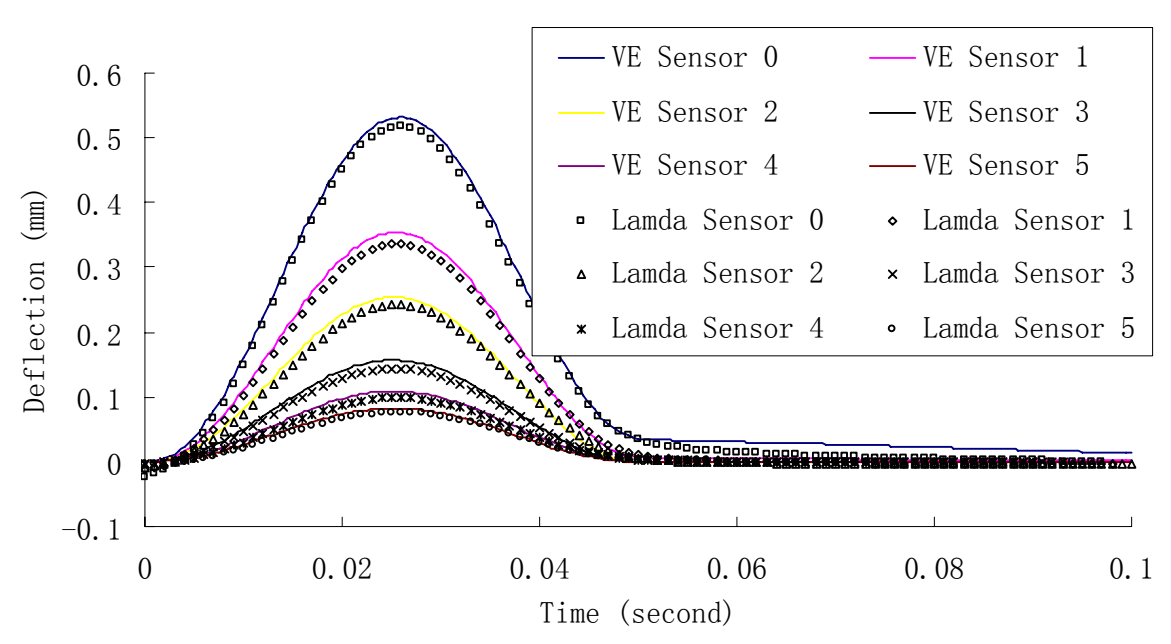
The deflection time histories predicted by SAPSI, LAMDA (after eliminating the time delay, or time-shifted dynamic solution) and by the VE solution are shown in Figures 45 to 48.

#### VE solution VS. SAPSI for Case 116



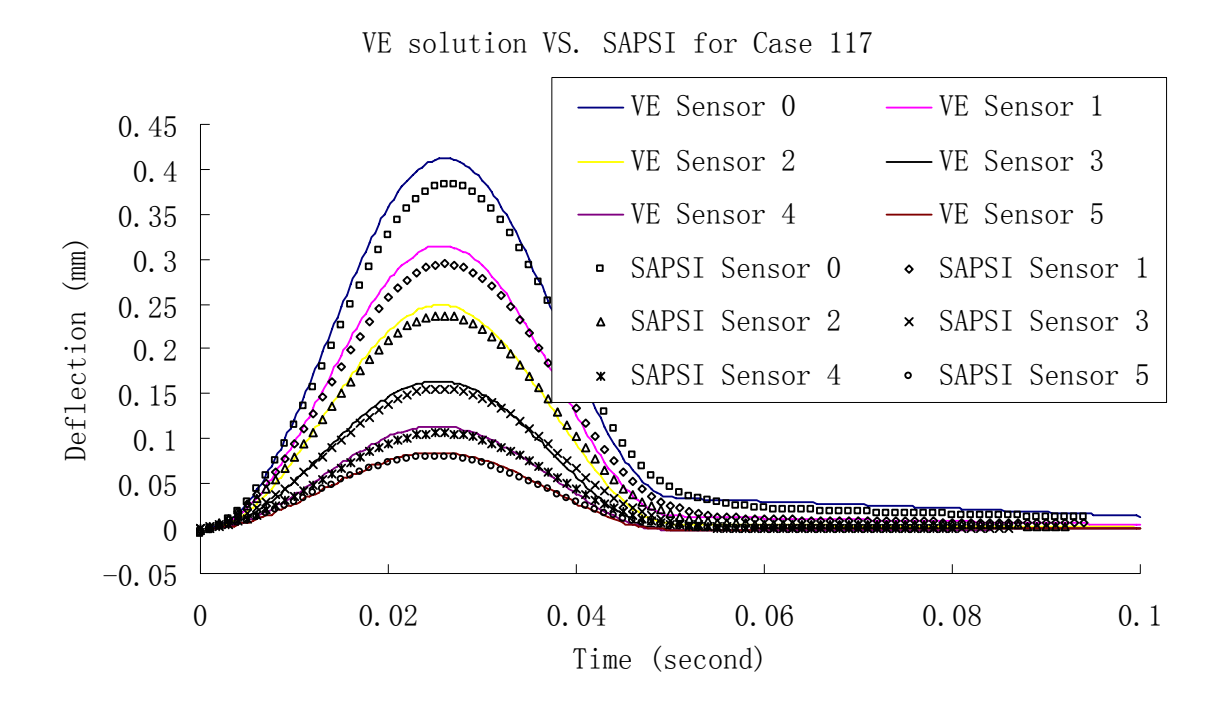
#### (a) VE solution and SAPSI

VE solution VS. Lamda for Case 116



#### (b) VE solution and LAMDA

Figure 45: Time-shifted dynamic solution and VE solution for case 116 (Solid lines represent the VE solution, symbols represent the SAPSI / LAMDA result)



#### (a) VE solution and SAPSI

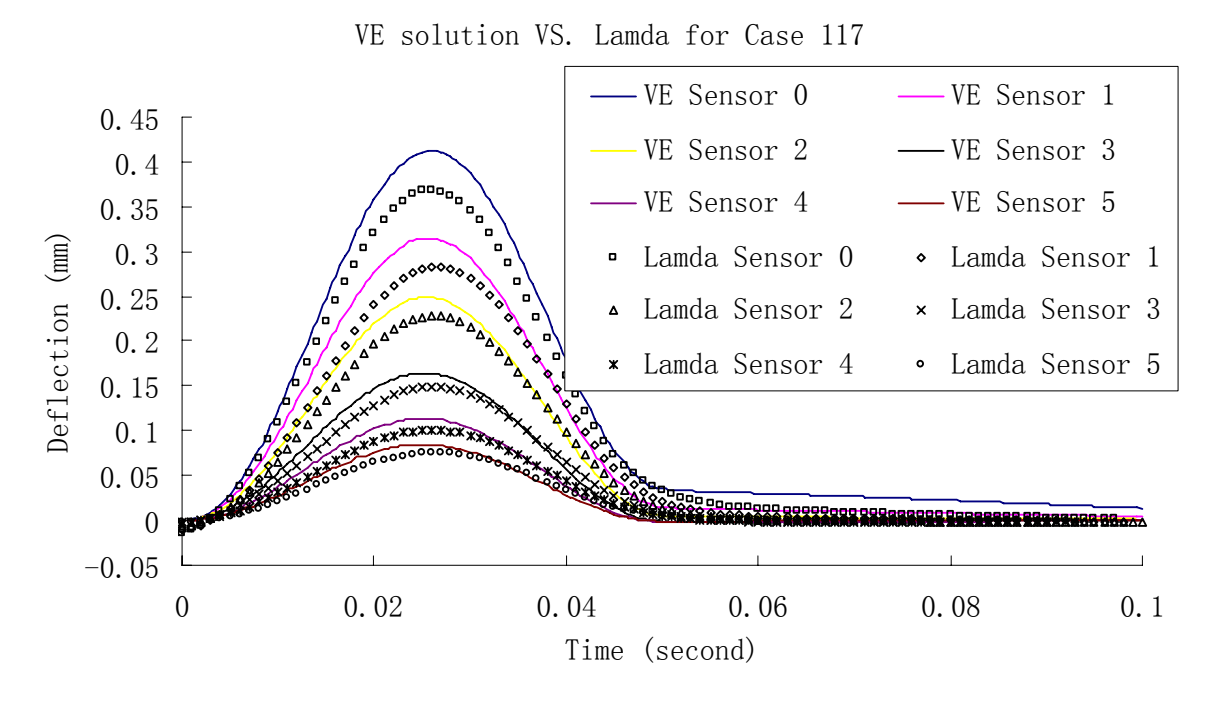
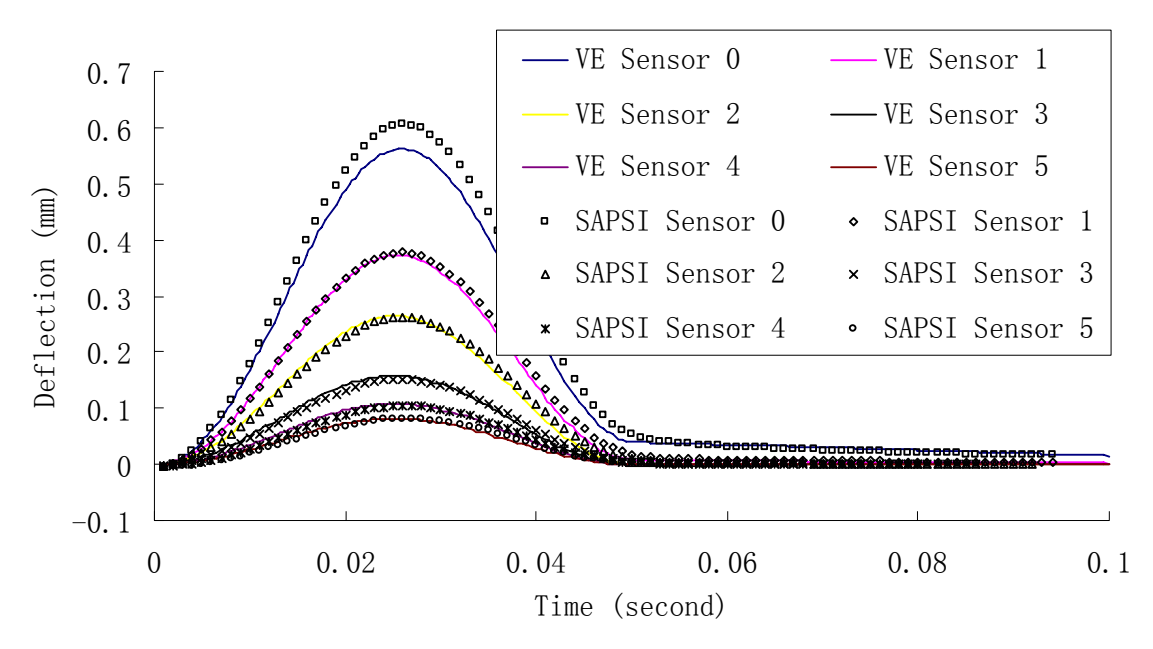


Figure 46: Time-shifted dynamic solution and VE solution for case 117 (Solid lines represent the VE solution, symbols represent the SAPSI / LAMDA result)

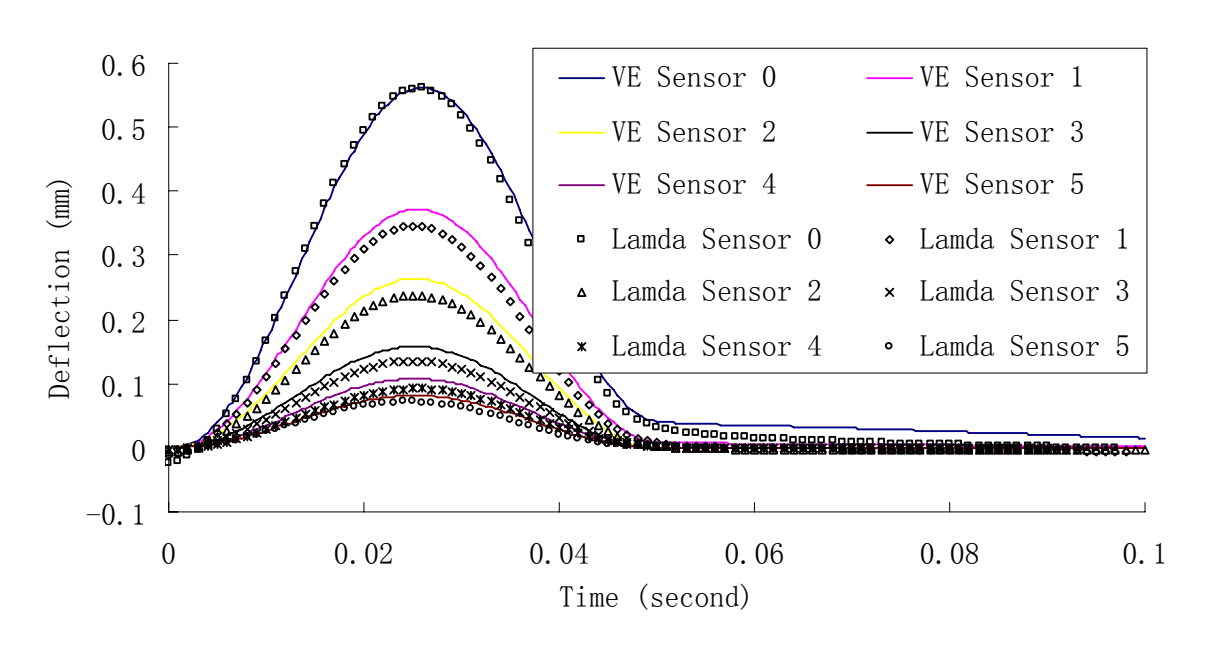
(b) VE solution and LAMDA

#### VE solution VS. SAPSI for Case 120



#### (a) VE solution and SAPSI

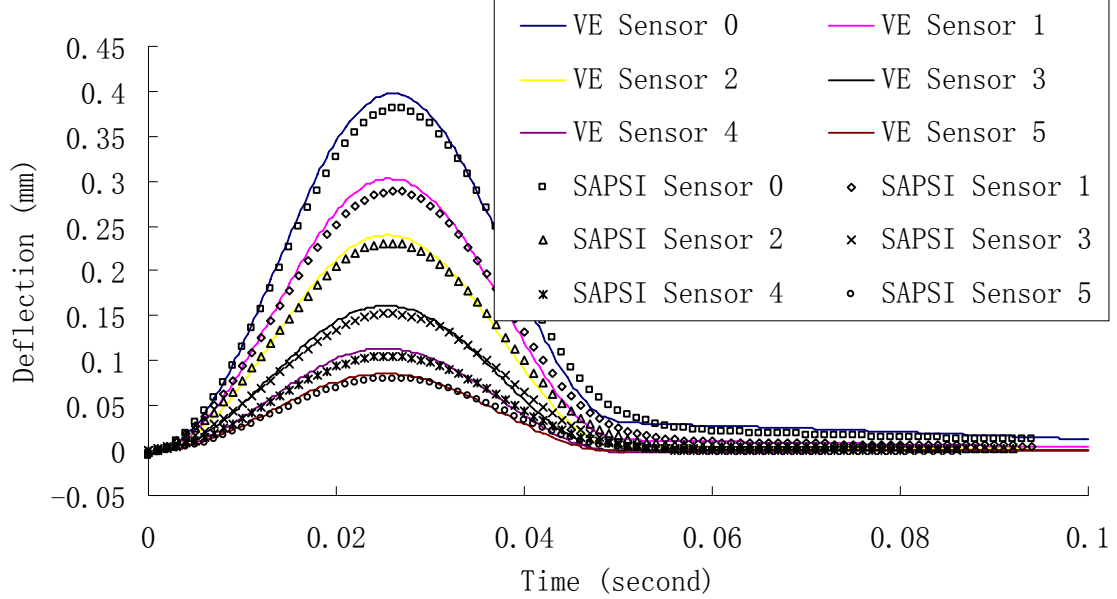
VE solution VS. Lamda for Case 120



### (b) VE solution and LAMDA

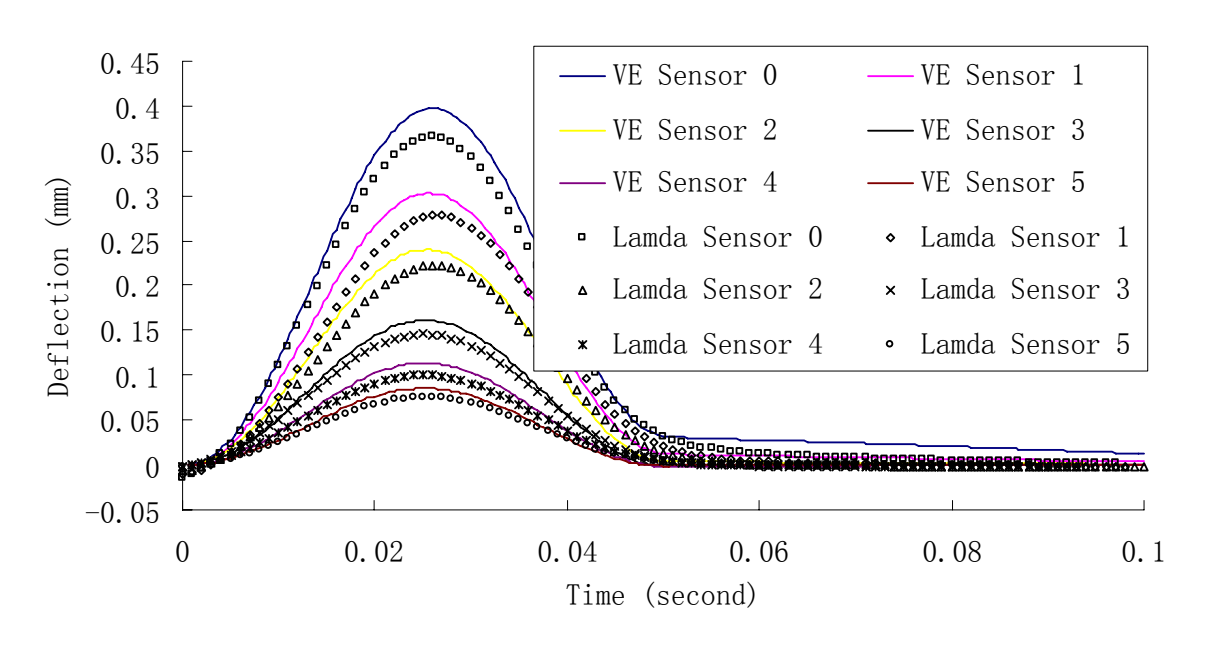
Figure 47: Time-shifted dynamic solution and VE solution for case 120 (Solid lines represent the VE solution, symbols represent the SAPSI / LAMDA result)





#### (a) VE solution and SAPSI

VE solution VS. Lamda for Case 123



(b) VE solution and LAMDA

Figure 48: Time-shifted dynamic solution and VE solution for case 123 (Solid lines represent the VE solution, symbols represent the SAPSI / LAMDA result)

Figures 45 - 48 show that the typical difference between the results by the VE solution and those by time-shifted dynamic analysis is about 6%, with the maximum difference as high as 10%. The difference appears to be slightly higher when the AC layer is thicker, or when there are more physical layers in the pavement structure. Most importantly, the shapes of the response pulses from dynamic and VE solutions are consistent with each other. Therefore, the four numerical examples show that the difference between the responses from the dynamic solutions (SAPSI or LAMDA) and from the VE solution is minimal.

### 4.3.4 A Numerical Example with the Bedrock

The existence of bedrock may cause problems in numerical simulation. The previous chapter shows that the proposed method to estimate the elastic modulus of the subgrade layer by Rayleigh wave is invalid if there is shallow bedrock underneath. In addition, the reflection of the waves and resulting response can overshadow the effects of viscoelasticity. Fig. 49 shows the responses calculated by SAPSI and layered VE solution. As expected, dynamic response by SAPSI is significant, while layered VE solution does not show the effect of wave propagation.

# Comparison of deflection history with Bedrock (5 ft)

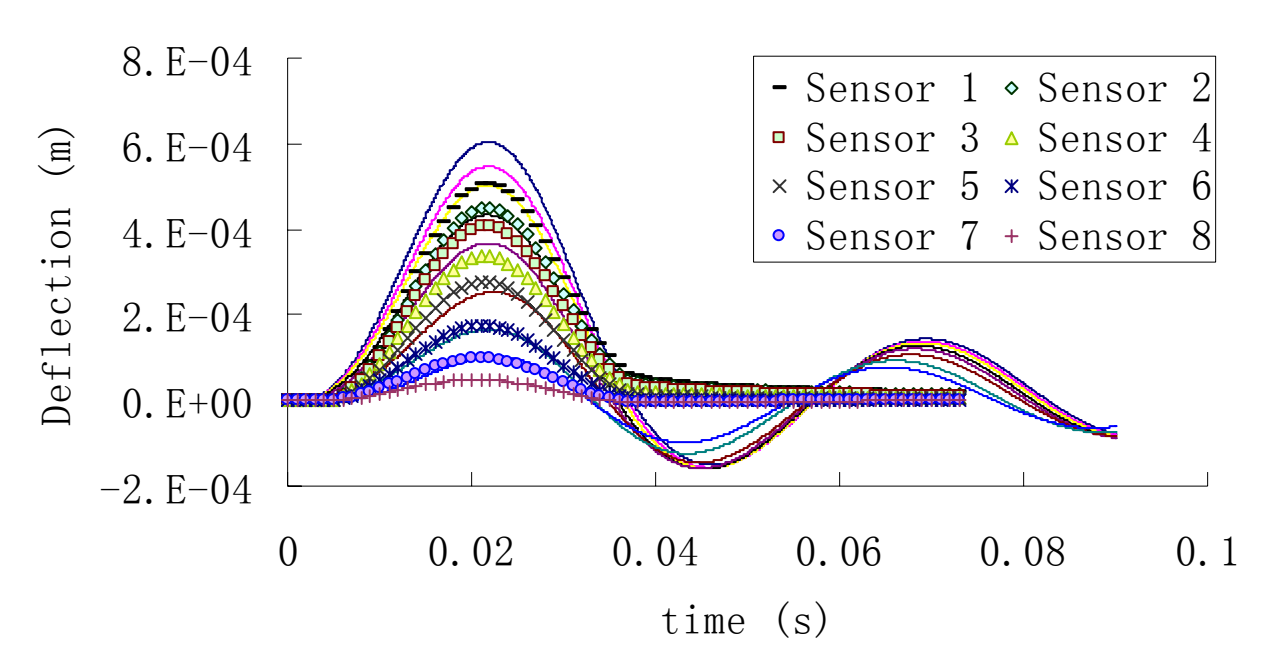


Figure 49: Time-shifted SAPSI and VE solution for shallow bedrock (Solid lines represent the SAPSI result, symbols represent the VE solution)

Fig. 49 illustrates that the layered VE solution cannot accurately simulate the pavement response if there is shallow bedrock underneath. Therefore, the layered VE solution should not be used for simulating the pavement response if there is a shallow, stiff layer underneath. The magnitude of error of the simulation depends on the relative level of stiffness between physical layers, and the relative depth of the bedrock

A sensitivity analysis for the depth of the bedrock is done for the numerical example, and the only input variable is the thickness of the subgrade layer, or the depth of the bedrock, and the output variable is the relative error of the maximum deflection for each sensor between dynamic solution SAPSI and VE forward solution. The result is shown in Fig. 50. Depending on the

accuracy of the simulation requirement, the effect of bedrock is insignificant if the depth is 15 ft or more.

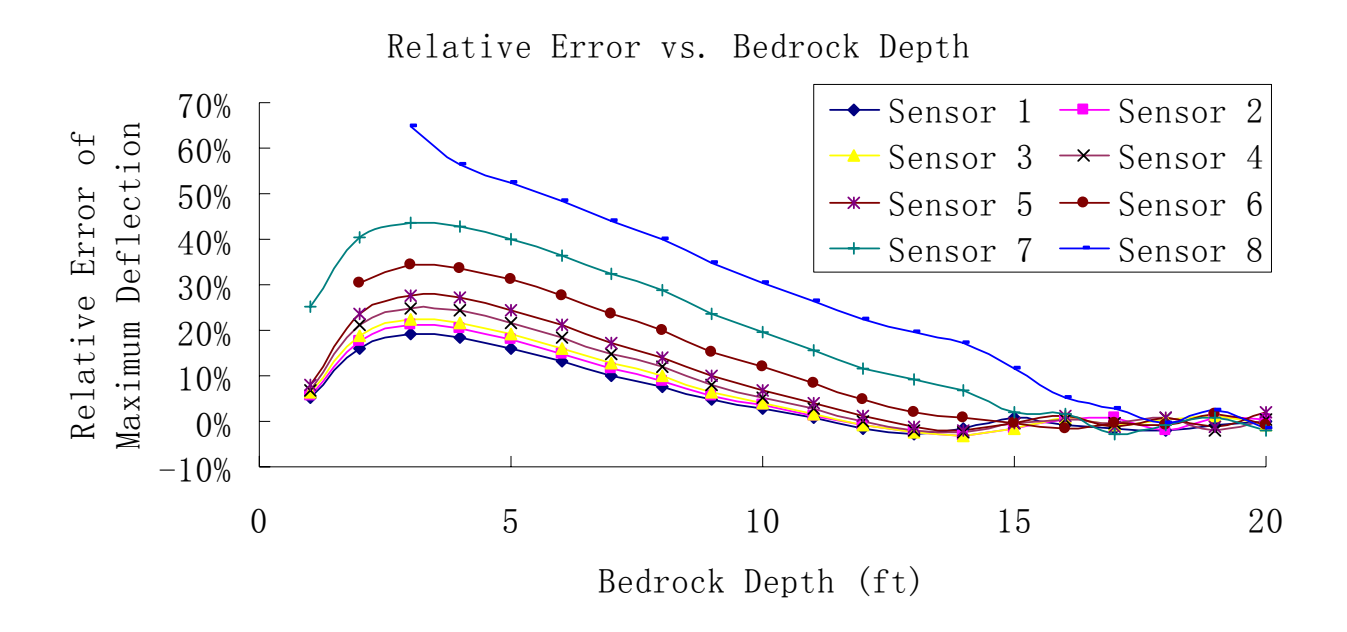


Figure 50: Sensitivity analysis for relative error of maximum deflection between VE solution and SAPSI with bedrock depth

# 4.4 Time Efficiency for Layered VE Forward Solution

One of the primary reasons for implementing Schapery's "quasi-elastic" approximation is its extreme computational efficiency. It takes more than 25 minutes to calculate the pavement response under step load by semi-analytical solution, and it takes around 20 minutes to simulate the pavement response under FWD test by dynamic solution SAPSI or LAMDA, while it takes less than one minute to calculate the response by VE solution. Many repetitions are required for the forward simulation, so time efficiency is a very important factor.

Using a Pentium (4) 3.20 GHz computer with 1.99 GB ram, the computation time of the results shown in Fig. 37 is 44.72 seconds, where the solution was for the 3-layered system shown

in Fig. 31 and  $N_S = 50$ ,  $N_E = 50$ . Table 28 shows the computation times for different numbers of discrete time steps for the 3-layered system shown in Fig. 35. The difference in Table 28 is defined as square root of the relative difference of the peak deflection compared to the most difficult (reference) case with  $N_S = 200$  and  $N_E = 200$ . Mathematically the difference is expressed as:

Difference = 
$$\sqrt{\frac{1}{N} \sum_{i=1}^{N} \left( \frac{\omega_i \left( peak \text{ in case} \right) - \omega_i \left( peak \text{ reference} \right)}{\omega_i \left( peak \text{ reference} \right)} \right)^2}$$
, (36)

where: N = No. of Sensors.

Table 28: The computation times for different numbers of discrete time steps

$N_{s}$	NE	Elapsed time for computation (seconds)	Difference (%)
50	50	22.60	0.069
24	100	45.41	0.360
50	100	44.72	0.077
100	100	45.35	0.011
100	200	89.38	0.018
200	200	89.73	0.000

Table 28 shows that  $N_S$  = 100 and  $N_E$  = 100 is enough to generate a reasonable result, i.e., the sampling time for the FWD test is around 0.5 ms, and the time cost of each forward simulation is around 45 seconds.

Therefore, the VE forward solution is accurate and time efficient, and is chosen as the numerical simulation of the pavement under FWD test in future analysis.

## 4.5 Summary

- A computation procedure for layered VE solution has been provided in this chapter. It
  was simple in understanding, efficiency in calculation, and easy for implementation in
  MATLAB.
- The accuracy of the proposed forward solution was checked against a semi-analytical solution for a step load, and was checked against dynamic solutions SAPSI and LAMDA for FWD test simulation. The time delay of each sensor cannot be simulated, and the deflection time-histories can be calculated within error around 5% for maximum deflection.
- The proposed layered VE forward solution was chosen for future backcalculation because of its accuracy and time-efficiency.
- If there is shallow bedrock underneath the pavement, the effect of mass inertia cannot be ignored, and the proposed VE solution is not appropriate.

# Chapter 5. Backcalculation Algorithm

#### 5.1 Introduction

In this chapter, the outputs of the backcalculation program are identified, and the boundaries of each output variable are measured from the lab as guidance for the convergence of the program. Then the basic theory of inverse problem is briefly introduced. A detailed flowchart of the backcalculation program is presented, and one numerical example of the backcalculation result is shown in the end.

#### **5.2 Variable Identification**

The input variables are thickness of each layer, Poisson's ratio of each layer, applied load history and deflection time history of each sensor during a FWD test. The output variables are the elastic modulus of base and subgrade layers, and a function of relaxation modulus E(t) or dynamic modulus mastercurve  $|E^*|$  of the AC layer. The elastic modulus of base and subgrade layers is noted separately as  $E_{base}$  and  $E_{subgrade}$ .

Mathematically E(t) is commonly expressed as Prony series with more than 30 variables, however, it is almost impossible for any backcalculation to converge with so many variables. A pre-described function must be required to reduce the unknown parameters. The sigmoid function is preferred for  $|E^*|$  in frequency domain and E(t) in time domain, as Eq. (1) for  $|E^*|$  and Eq. (2) for E(t) respectively. The backcalculation is used to calculate the parameters of the

sigmoidal function (a, b, c, d) for  $|E^*|$  in frequency domain or E(t) in time domain respectively, although the forward calculation is done in time domain.

#### **5.3 Variable Boundaries**

A reasonable range for the value of each output variable helps to converge the backcalculation. If the intermediate output value crosses the boundary, it is forced to be within the range by the algorithm.

The elastic modulus of base and subgrade layer is suggested to be less than 700 MPa (100 ksi). If not, it is not appropriate for the proposed wave propagation method to estimate the elastic modulus of the subgrade layer (as discussed in Chapter 3) and for the proposed layered VE solution to simulate the pavement response.

The boundaries of the parameters for the AC layer in the sigmoid function are found in the experiment data of many mixtures. The seed value of the four parameters can be set as the average value, and the boundary limit is identified via the minimum or maximum value of each variable. The corresponding  $|E^*|$  or E(t) components are discussed in the following separate sections.

### 5.3.1 Boundary Limits for |E\*|

About 30 sets of  $|E^*|$  were obtained from FHWA (Kutay, 2008) and other sources (Mogawer et al, 2010). Their coefficients for the dynamic modulus mastercurve  $|E^*|$  are shown in Table 29.

Table 29: The |E\*| parameters for different AC mixtures

Mixture Name	a	b	c	d
PG64-28 Control no-PPA (AI)	1.699	2.765	0.823	0.483
ALF Control 70-22	0.797	3.593	1.372	0.503
SBS 64-40	1.338	2.843	0.164	0.561
Terpolymer	1.468	2.799	0.491	0.583
CR-AZ	-0.202	4.695	1.122	0.346
SBS LG	1.341	2.857	0.876	0.556
CR-TB	0.807	3.519	1.066	0.407
Air Blown	0.553	3.868	1.285	0.405
Fiber	0.504	3.838	1.535	0.504
Control 70-22 KIM	1.585	2.955	1.077	0.558
Advera	2.156	1.801	0.546	0.854
Control	0.458	3.772	0.948	0.389
Sasobit	-0.26	4.907	0.787	0.268
PPA	1.552	2.408	0.602	0.702
PPA + Elvaloy	1.579	2.317	0.582	0.543
SBS	1.72	2.21	0.519	0.73
SBS + PPA	1.568	2.505	0.464	0.643
SBS PG64-34	0.851	2.391	0.157	0.682
PG64-28 Control no-PPA (AI)	1.569	2.65	0.855	0.668
PG64-28 with PPA (Hudson)	1.49	2.677	0.777	0.639
PG64-34 (SEM)	1.689	2.394	0.156	0.681
PG76-22 (Citgo)	1.646	2.476	0.954	0.705
PG64-22 with 12% GTR (Gorman)	1.245	2.851	1.151	0.483
PG64-28 no-PPA(AI)with2.0%Latex	1.507	2.678	0.905	0.572
WAM Control	0.92	3.371	1.387	0.595
WAM Foam	1.13	3.168	1.244	0.641
Asphamin	1.261	2.985	1.284	0.598
Control	1.195	3.127	1.333	0.552
Sasobit-1	1.423	2.791	1.423	0.578
Sasobit-2	1.266	3.012	1.375	0.543
Evatherm-1	1.112	3.162	1.245	0.546
Evatherm-2	1.191	3.144	1.258	0.497

The average, minimum and maximum values of each variable are listed in Table 30.

Table 30: The average and boundaries for the four parameters of  $|E^*|$ 

	a	b	С	d
Average value	1.192	3.016	0.93	0.563
Minimum value	-0.26	1.801	0.156	0.268
Maximum value	2.156	4.907	1.535	0.854

## 5.3.2 Boundary Limits for E(t)

The relaxation modulus E(t) of the same 30 examples of AC mixture is expressed via the sigmoid function, and values of the four parameters of the function are listed in Table 31.

Table 31: The E(t) parameters for different AC mixtures

Mixture Name	a	b	c	d
PG64-28 Control no-PPA (AI)	1.721	2.735	0.326	-0.491
ALF Control 70-22	0.841	3.540	0.860	-0.515
SBS 64-40	1.342	2.832	-0.399	-0.563
Terpolymer	1.472	2.790	-0.095	-0.584
CR-AZ	0.045	4.400	0.731	-0.380
SBS LG	1.351	2.842	0.313	-0.559
CR-TB	0.895	3.411	0.634	-0.428
Air Blown	0.682	3.717	0.855	-0.431
Fiber	0.561	3.772	1.025	-0.519
Control 70-22 KIM	1.598	2.937	0.512	-0.562
Advera	2.155	1.800	-0.307	-0.845
Control	0.558	3.645	0.532	-0.411
Sasobit	0.150	4.378	0.436	-0.314
PPA	1.553	2.405	-0.100	-0.699
PPA + Elvaloy	1.586	2.306	0.030	-0.546
SBS	1.720	2.208	-0.211	-0.725
SBS + PPA	1.570	2.501	-0.180	-0.641
SBS PG64-34	0.851	2.388	-0.523	-0.679
PG64-28 Control no-PPA (AI)	1.571	2.646	0.185	-0.666
PG64-28 with PPA (Hudson)	1.493	2.671	0.135	-0.638
PG64-34 (SEM)	1.689	2.391	-0.523	-0.678
PG76-22 (Citgo)	1.647	2.473	0.247	-0.702
PG64-22 with 12% GTR (Gorman)	1.278	2.810	0.653	-0.494
PG64-28 no-PPA(AI)with2.0%Latex	1.515	2.666	0.326	-0.574
WAM Control	0.934	3.352	0.789	-0.599
WAM Foam	1.136	3.159	0.601	-0.642
Asphamin	1.272	2.971	0.681	-0.601
Control	1.216	3.101	0.774	-0.559
Sasobit-1	1.438	2.772	0.837	-0.583
Sasobit-2	1.289	2.984	0.823	-0.551
Evatherm-1	1.132	3.137	0.692	-0.552
Evatherm-2	1.227	3.100	0.749	-0.508

The average, minimum and maximum values of each variable are listed in Table 32.

Table 32: The mean and boundaries for the four parameters of E(t)

	a	b	c	d
Average value	1.234	2.964	0.356	-0.570
Minimum value	0.045	1.800	-0.523	-0.845
Maximum value	2.155	4.400	1.025	-0.314

#### **5.4 Inverse Solution Theory**

The objective of any backcalculation solution is to find a set of parameters. In this case, the parameters are the set (a, b, c, d) of the AC mixture, the elastic modulus of base (E<sub>base</sub>), and the elastic modulus of the subgrade layer (E<sub>subgrade</sub>). In the end, the calculated deflection history will match the measured values within a specified tolerance. To accomplish this goal, the algorithm repeatedly adjusts the parameter values until a suitable match is obtained.

#### **5.4.1 Basic Theory Background**

The VE backcalculation algorithm in this research is an extension of the solution used in the MICHBACK program (Harichandran et al., 1994). It uses the modified Newton method to obtain a least squares solution of an over determined set of equations. In the MICHBACK solution, these sets are real-valued and correspond to the peak deflection values. In this research, the author will use deflection time histories, or many deflection basins (corresponding to different times after eliminating the time delay of all sensors), since the proposed backcalculation scheme uses a layered VE solution to predict the time-dependent deflection basins.

 $E_{base}$  and  $E_{subgrade}$  are not known, and the AC layer can be expressed as a function of four parameters (a, b, c, d). The unknown vectors become

 $\{X\} = \{a \quad b \quad c \quad d \quad E_{base} \quad E_{subgrade} \}^T \text{ , assuming all other information for base,}$  sub-base and roadbed layers are known.

The vector of measured responses is therefore expressed as:

$$\{U(t)\} = \begin{cases} [w_1(t_s) & \dots & w_m(t_s)], \dots, \\ [w_1(t_k) & \dots & w_m(t_k)], \dots, \\ [w_1(t_f) & \dots & w_m(t_f)] \end{cases},$$
(37)

where m is the number of sensors in the FWD test,  $w_j(t_s)$  is the deflection of sensor j at the starting time and  $w_j(t_f)$  is the deflection of sensor j at the final time of the specified range.

Following the derivation by Harichandran et al. (1994), the increment to the unknown parameters in iteration i,  $\{\Delta x\}_i$ , is obtained by solving the linear set of equations:

$$\{\hat{U}(t)\}^{i} + [G]^{i} \{\Delta X\}_{i} = \{U(t)\},$$
(38)

where:  $\{\hat{U}(t)\}^i$  is the vector of deflections at individual time steps within the specified time range, computed using the estimates of the parameters  $\{\hat{x}\}^i$  at iteration i, and  $[G]^i$  is the gradient matrix at iteration i given by:

$$\left[G\right]^{i} = \left[\frac{\partial \left\{U(t)\right\}}{\partial \left\{X\right\}}\right]_{\left\{X\right\} = \left\{\hat{x}\right\}^{i}}$$
(39)

The partial derivatives in the gradient matrix must be evaluated numerically using:

$$\frac{\partial w_{j}(t)}{\partial x_{k}}\bigg|_{\{X\}=\{\hat{x}\}^{i}} = \frac{w_{j}([R]\{\hat{x}\}^{i}) - w_{j}(\{\hat{x}\}^{i})}{r\hat{x}_{k}^{i}}, \qquad (40)$$

$$j = 1, 2, ..., m, \quad k = 1, 2, 3, 4, 5, 6$$

where: [R] is a diagonal matrix with the k<sup>th</sup> diagonal element being (1+r) and all other diagonal elements being one. A separate call to the forward calculation program is required to compute the partial derivatives in each column of the gradient matrix.

If there are n individual time steps, Eq. (38) represents a set of m by n equations for 6 unknowns. Since there are more equations than unknown, a more robust method for solving the problem is to use the singular value decomposition (SVD). This method will be briefly introduced later.

After the increments  $\{\Delta x\}_i$  are obtained by solving Eq. (38), the revised parameters for  $\{X\}$  are obtained from Eq. (40), as below:

$$\{\hat{x}\}^{i+1} = \{\hat{x}\}^i + \{\Delta x\}_i \tag{41}$$

The iteration is terminated when the changes in the six parameters are smaller than a set of specified tolerances:

$$abs\left(\frac{\hat{x}_{k}^{i+1} - \hat{x}_{k}^{i}}{\hat{x}_{k}^{i+1}}\right) \le \varepsilon \quad k = 1, 2, 3, 4, 5, 6$$
 (42)

#### 5.4.2 SVD Method

SVD is a very powerful set of techniques for dealing with sets of equations or a matrix that are either singular or numerically very close to singular. SVD methods are based on the following theorem of linear algebra (Press et al, 1989). Any M×N matrix [A] whose number of rows M is greater than or equal to its number of columns N, can be written as the product of an M×N column-orthogonal matrix [U], an N×N diagonal matrix [W] with positive or zero elements (the singular values), and the transpose of an N×N orthogonal matrix [V].

The matrix [A] can be decomposed as three matrices as following:

$$[A] = [U] * [W] * [V]^T = [U] * \begin{bmatrix} \omega_1 & & & \\ & \omega_2 & & \\ & & \ddots & \\ & & & \omega_N \end{bmatrix} * [V]^T, \quad (43)$$

where: 
$$[U]^*[U]^T = I$$
,  $[V]^*[V]^T = I$ , and  $[W]$  is diagonal matrix.

For the following ill conditioned system of equations:

$$[A]*{X} = {b}$$

Inversing [A] by SVD method,  $\{X\}$  can then be expressed as:

$$\{X\} = [V] * \left[\frac{1}{W}\right] * [U] * \{b\} = [V] * \begin{bmatrix} \frac{1}{\omega_{1}} & & & \\ & \frac{1}{\omega_{2}} & & \\ & & \ddots & \\ & & & \frac{1}{\omega_{N}} \end{bmatrix} * [U] * \{b\}, \quad (45)$$

where: 
$$[U]^*[U]^T = I$$
,  $[V]^*[V]^T = I$ , and  $\left[\frac{1}{W}\right]$  is a diagonal matrix.

#### 5.4.3 Truncating Singular Values

Reference (Press et al., 1989) defines the condition number of a matrix as a ratio of the largest  $\omega_i$  of to the smallest  $\omega_i$ .

Condition number = 
$$\frac{\omega_{\text{max}}}{\omega_{\text{min}}}$$
 (46)

A matrix [A] is singular or ill conditioned if its condition number is too large. Reference (Press et al., 1989) suggested this number should be adjusted according to the experiment with the specific problem.

Define the threshold of truncation as:

$$\omega_j < \omega_{\text{max}} * 10^{-Threshold},$$

$$j = 1, 2, ..., N$$
(47)

After selecting the threshold of a condition number, the SVD algorithm will simply

replace 
$$\overline{\omega_j}$$
 with zeros.

To reduce the possibility of ill conditioning in the inverse problem, the technique of scaling can be applied. In this program, the magnitude of  $E_{base}$  and  $E_{subgrade}$  is within the magnitude of 100 MPa (14.5 ksi), but the magnitude of the four parameters in the sigmoid function for AC layer is around 0-5, as shown in Table 30 & 32. The condition number would be very high, thus, scaling technique is required.  $E_{base}$  and  $E_{subgrade}$  are scaled by 100 MPa in this backcalculation program. More information can be found in the references (Ji, 2005).

### 5.5 VE backcalculation of E(t)

Besides the above proposed Newton's method, MATLAB internal function "fminsearch" works very well for backcalculation problems, if the seed value is close to the actual solution. Thus, the proposed Newton's method is to scan all possible values and eliminate the local minimum values for the error in Eq. (42).

Avoiding the local minimum problem in backcalculation is essential, so a random function inside the backcalculation algorithm is used to prevent the solution converging to local minimum values. A simplified flow chart is shown in Fig. 51, for the i<sup>th</sup> loop of the backcalculation.

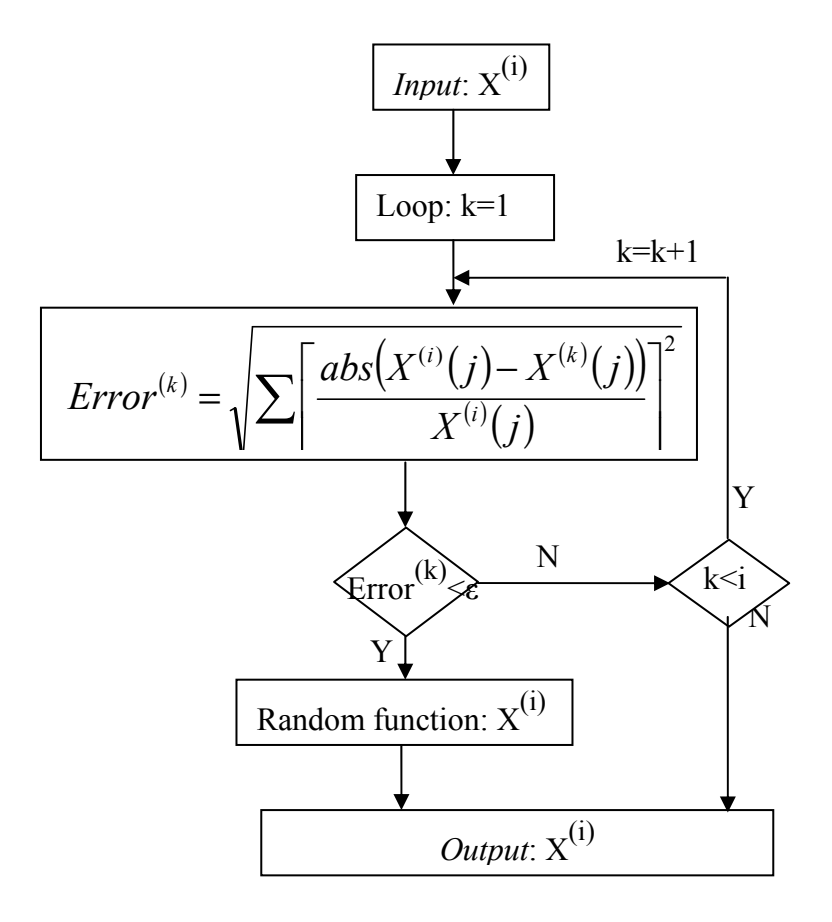


Figure 51: Random Function to avoid local minimum problem

Fig. 51 shows the program cannot always avoid local minimum problem. However, as the number of loops increases, the chance that the program will converge to the global minimum point increases, at the cost of time-efficiency. The proposed wave propagation method in Chapter 3 is used to estimate the seed value of E<sub>subgrade</sub>. A flow chart for this algorithm is shown in Fig. 52.

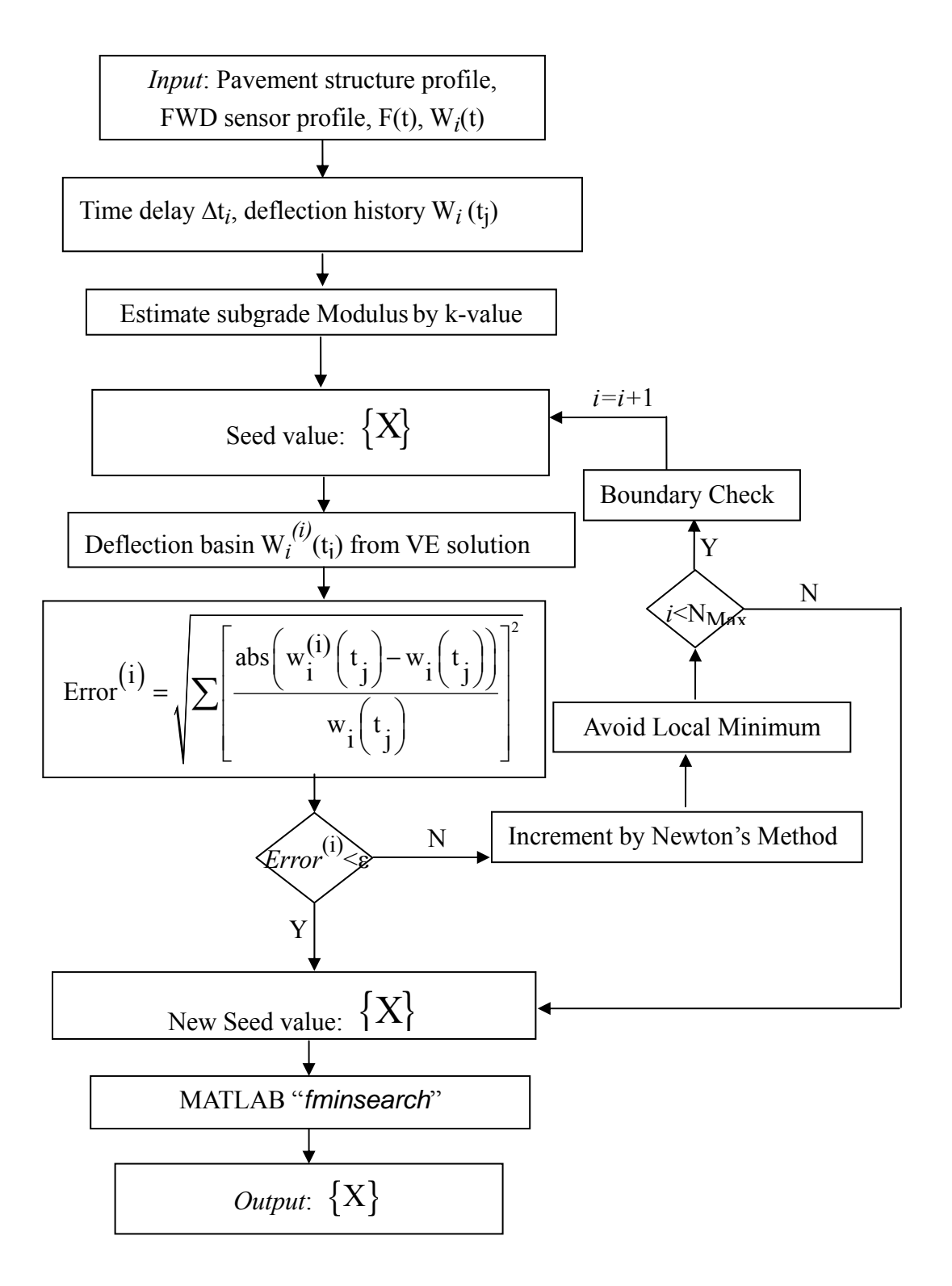


Figure 52: Algorithm of backcalculation procedure of E(t)

### 5.6 VE backcalculation of |E\*|

An independent backcalculation algorithm is developed in this section if  $|E^*|$  of the AC mixture is concerned. The output variables are the same as section 5.5, except the set of (a, b, c, d) is to express  $|E^*|$  in the sigmoid function. Since the VE solution is calculated in the time domain, the converting from  $|E^*|$  to E(t) is required, assuming the phase angel function  $\phi(\omega)$  may be unknown.

#### 5.6.1 Forward calculation of E(t) from $|E^*|$ and $\phi$

If the mastercurve  $|E^*(\omega)|$  and  $\varphi(\omega)$  are obtained from the experiment data, the coefficients  $E_i$  (spring stiffness) of the Generalized Maxwell model can be directly calculated by the inverse of the coefficient matrix A, as:

$$E = A^{-1} * b = (A'*A)^{-1} * (A'*b), \tag{48}$$

where: 
$$A = [a_{ij}]_{\text{and}} a_{ij} = \frac{(\omega_i T_j)^2}{1 + (\omega_i T_j)^2}$$

$$b = [b_j]_{\text{and}} b_j = E'(\omega_j) - E'(\infty) = |E^*(\omega_j)| * \sin(\varphi(\omega_j)) - |E^*(\infty)| * \sin(\varphi(\infty))$$

Then the relaxation modulus E(t) can be expressed by  $E_{i}$ , as Eq. (4).

However, in the back calculation problem, this procedure is invalid, because it assumes that in laboratory testing the phase angle  $\varphi(\omega)$  is known, but  $\varphi(\omega)$  is not known in the case of backcalculation.

One potential solution to this problem is to increase the total number of variables in the backcalculation procedure from 4 parameters (a, b, c, d) to 8 parameters (a, b, c, d, e, f, g, h). However, this makes the backcalculation problem more complex and less likely to be solved. Two other possible solutions are discussed in below sections.

#### 5.6.2 Calculation of E(t) and $\varphi$ from $|E^*|$ by Iteration

The dynamic modulus mastercurve  $|E^*(\omega)|$  can be mathematically expressed by coefficients of the spring stiffness  $E_i$  by Generalized Maxwell model, as shown in Eq. (49).

$$[E'(\omega)]^2 + [E''(\omega)]^2 = [E * (\omega)]^2$$
(49)

where: 
$$E'(\omega) = \sum_{i=0}^{N} E_i m_i(\omega) = E_0 + \sum_{i=1}^{N} E_i \frac{(\omega T_i)^2}{1 + (\omega T_i)^2}$$

$$E''(\omega) = \sum_{i=0}^{N} E_i n_i(\omega) = \sum_{i=1}^{N} E_i \frac{\omega T_i}{1 + (\omega T_i)^2}$$

Eq. (49) is a continuous function of frequency,  $\omega$ , and there are N unknown variables, so the minimum Root Mean Square Error (RMSE) method can be applied to solve for the N unknown variables, by discrete frequency  $\omega$  for M equations. The mathematical expression is:

$$Min[F(E)] = Min \left\{ \sum_{j=1}^{M} \left[ \left( \sum_{k=1}^{N} m_{kj} E_k \right)^2 + \left( \sum_{k=1}^{N} n_{kj} E_k \right)^2 - \left| E^* \right|_j^2 \right]^2 \right\}, \quad (50)$$

where: 
$$m_{kj} = \frac{(\omega_j T_k)^2}{1 + (\omega T_k)^2}$$
 and  $m_{k0} = 1$ 

$$n_{kj} = \frac{\omega_j T_k}{1 + (\omega T_k)^2}$$
 and  $n_{k0} = 0$ 

By finding the Stationary point of function F(E), a set of M equations can be obtained. In order to avoid the problem of indeterminate system of equations, one can assume M = N for simplification. Following the Gauss-Seidel iteration method, or the iteration method of successive replacement, one can solve for  $E_k$  by equation number k in the equation set.

$$\frac{\partial F}{\partial E_k} = 2K_j \left( 2m_{kj} \sum_{k=1}^{N} m_{kj} E_k + 2n_{kj} \sum_{k=1}^{N} n_{kj} E_k \right) \equiv 0, \tag{51}$$

where: 
$$K_{j} = \left(\sum_{k=1}^{N} m_{kj} E_{k}\right)^{2} + \left(\sum_{k=1}^{N} n_{kj} E_{k}\right)^{2} - \left|E^{*}\right|_{j}^{2}$$

The above Eq. (51) translates to a set of cubic polynomial functions of  $E_i$ , and mathematically there are three roots for each equation. It is possible to solve the above set of equations by iteration, i.e., assuming the seed value of  $E_i$ , and then calculating each coefficient  $K_j$ . Thus, the above equation can be simplified to one set of linear equations, and it can be uniquely identified for new values of  $E_i$ . By numerical iteration, a better set of  $E_i$  can be obtained by inversing the coefficient matrix with the minimum RMSE values.

In case of non-invertible matrix, one variable  $E_i$  can be solved in the *i*th equation, assuming  $K_j$  and the rest  $E_j$  are known from the seed value. The mathematical equation is expressed in Eq. (52), and the algorithm is shown below briefly in Fig. 53:

$$E_{k} = -\sum_{m=1, m \neq k}^{N} \frac{\sum_{j=1}^{N} K_{j} (m_{jk} m_{jm} + n_{jk} n_{jm})}{\sum_{j=1}^{N} K_{j} (m_{jk}^{2} + n_{jk}^{2})} E_{m}$$
 (52)

It is important to note that this procedure is a proposed idea that has not been validated. One concern is that the cubic polynomial equation is simplified into a set of linear equations, which may imply that convergence may not be achieved.

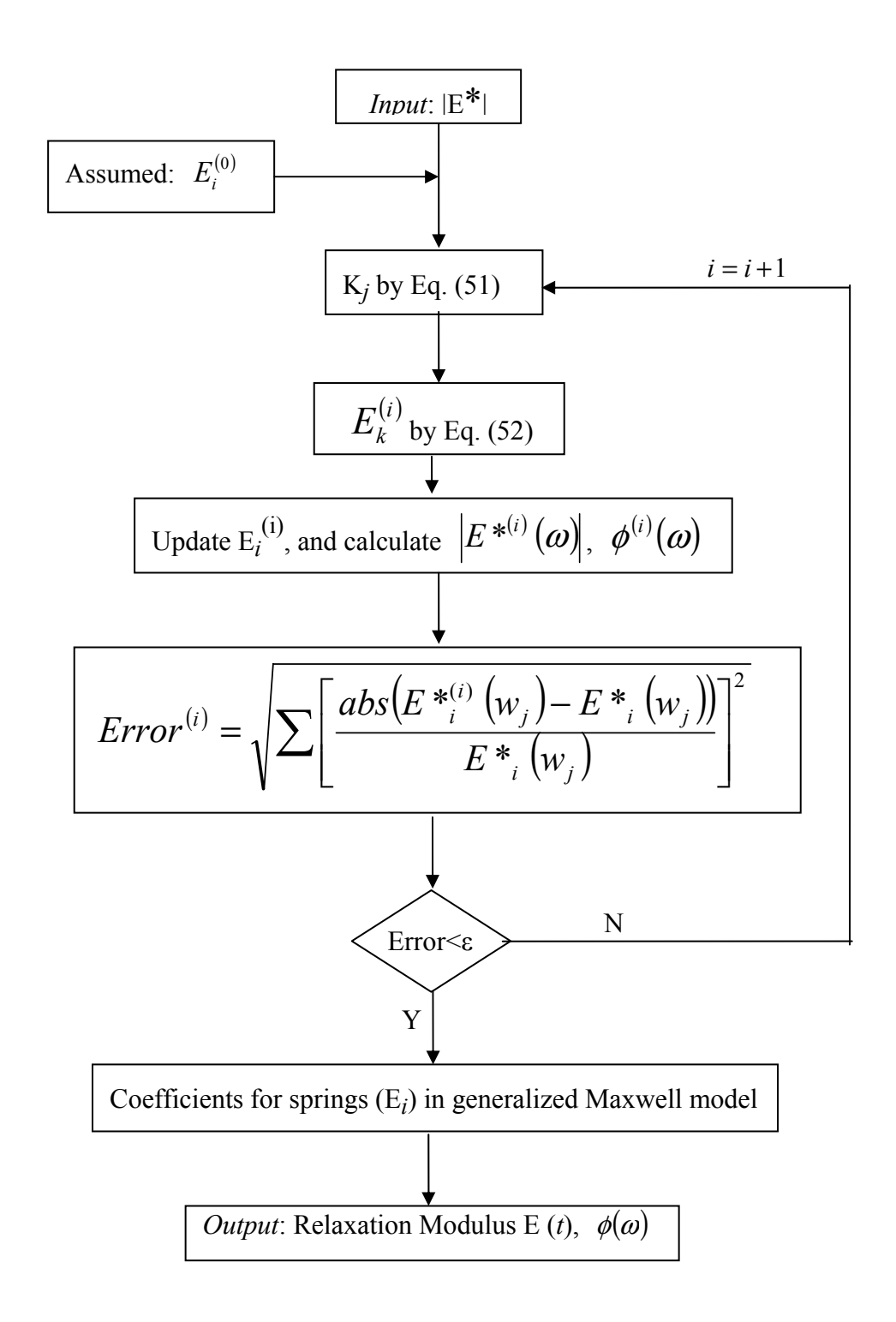


Figure 53: Algorithm for Calculation of E(t) and  $\phi$  from  $|E^*|$  by iteration

After programming in MATLAB, it was found that the convergence of this method is

questionable. As the numerical solution approaches the exact solution,  $K_j$  value in Eq. (51) approaches zero, and the difference between numerical solution and exact solution will be amplified by Eq. (52) as  $K_j$  is in the denominator. Mathematically, the error from simplification is too large to converge in calculation, as the cubic polynomial equation is simplified into a set of linear equations.

#### 5.6.3 Calculation of E(t) from $|E^*(\omega)|$ by Iteration $\varphi(\omega)$

There is no problem in convergence for the first method in Section 5.6.1, while there is iteration for the second method in Section 5.6.2 without theoretical confliction. Hence, a better way is to combine the advantage of the above two methods. Another proposed method is introduced in this section, and the algorithm is shown below briefly in Fig. 54.

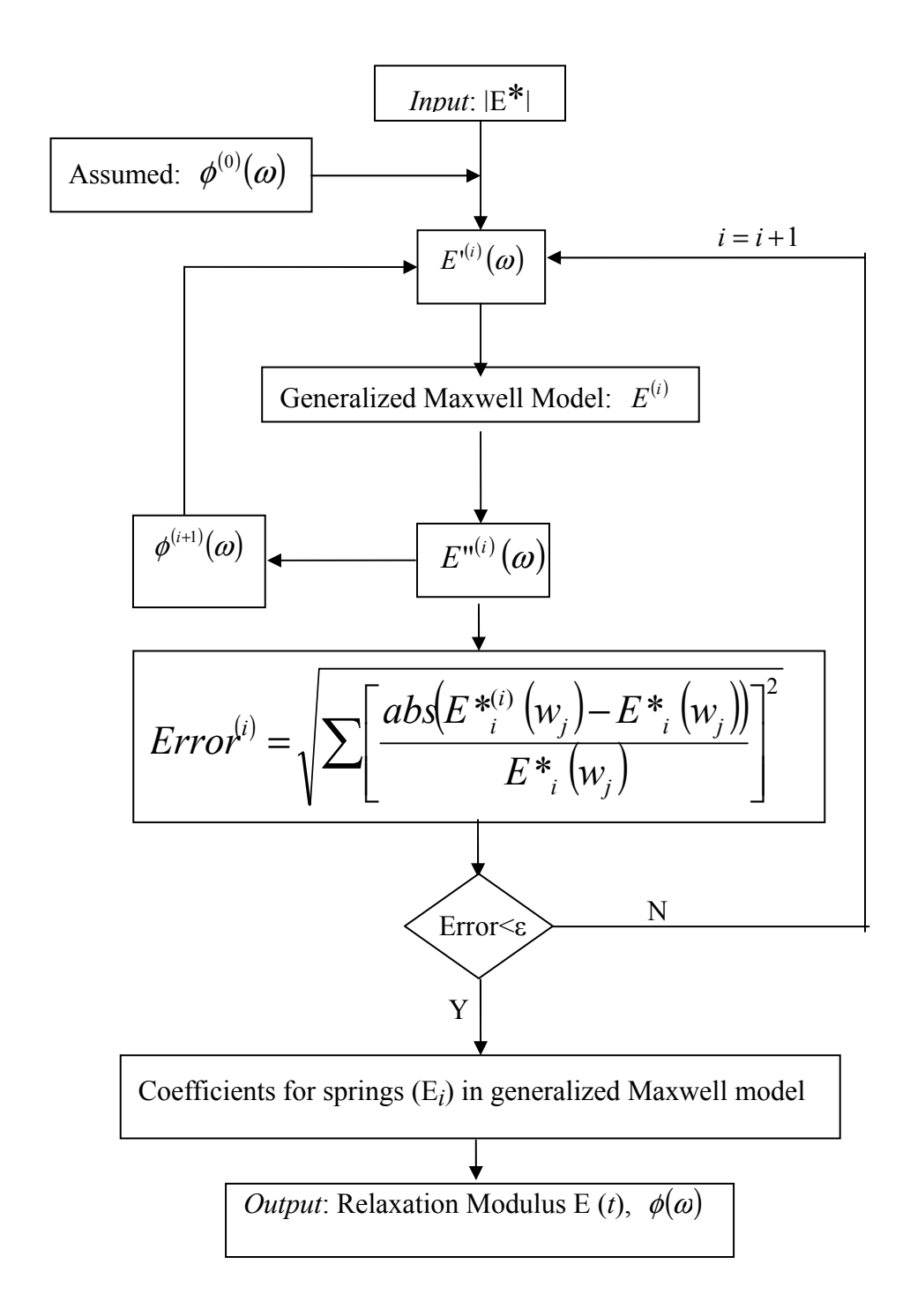


Figure 54: Algorithm for Calculation of E(t) from  $|E^*|$  by iteration  $\varphi$ 

After many cases of running, results for the identification of the phase angle  $\phi$  are questionable, however, the magnitude of E(t) works well at low reduced time. The dynamic modulus mastercurve  $|E^*|$  of one example before and after the conversion is shown in Fig. 55.

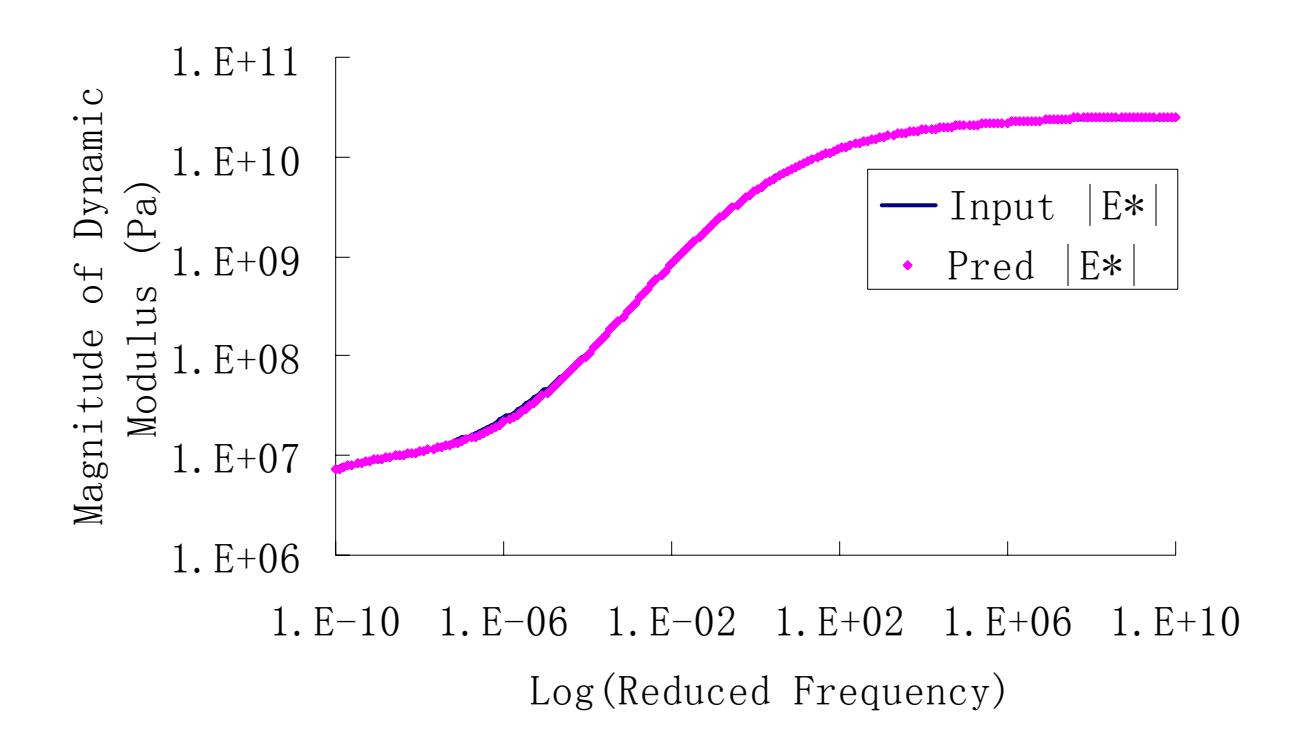


Figure 55: |E\*| input and calculated after converting to E(t) for one AC mixture

Based on above discussion, there are only 4 parameters (a, b, c, d) required in backcalculation for  $|E^*|$  for the AC layer, and the phase angle shift function  $\varphi(\omega)$  with parameters (e, f, g, h) are intermediately calculated in the program.

#### 5.6.4 Flowchart of VE backcalculation of |E\*|

Similar considerations in Section 5.5 are required in this section, but they are ignored here for brevity. The flow chart of VE backcalculation with AC material property expressed as |E\*| is shown in Fig. 56.

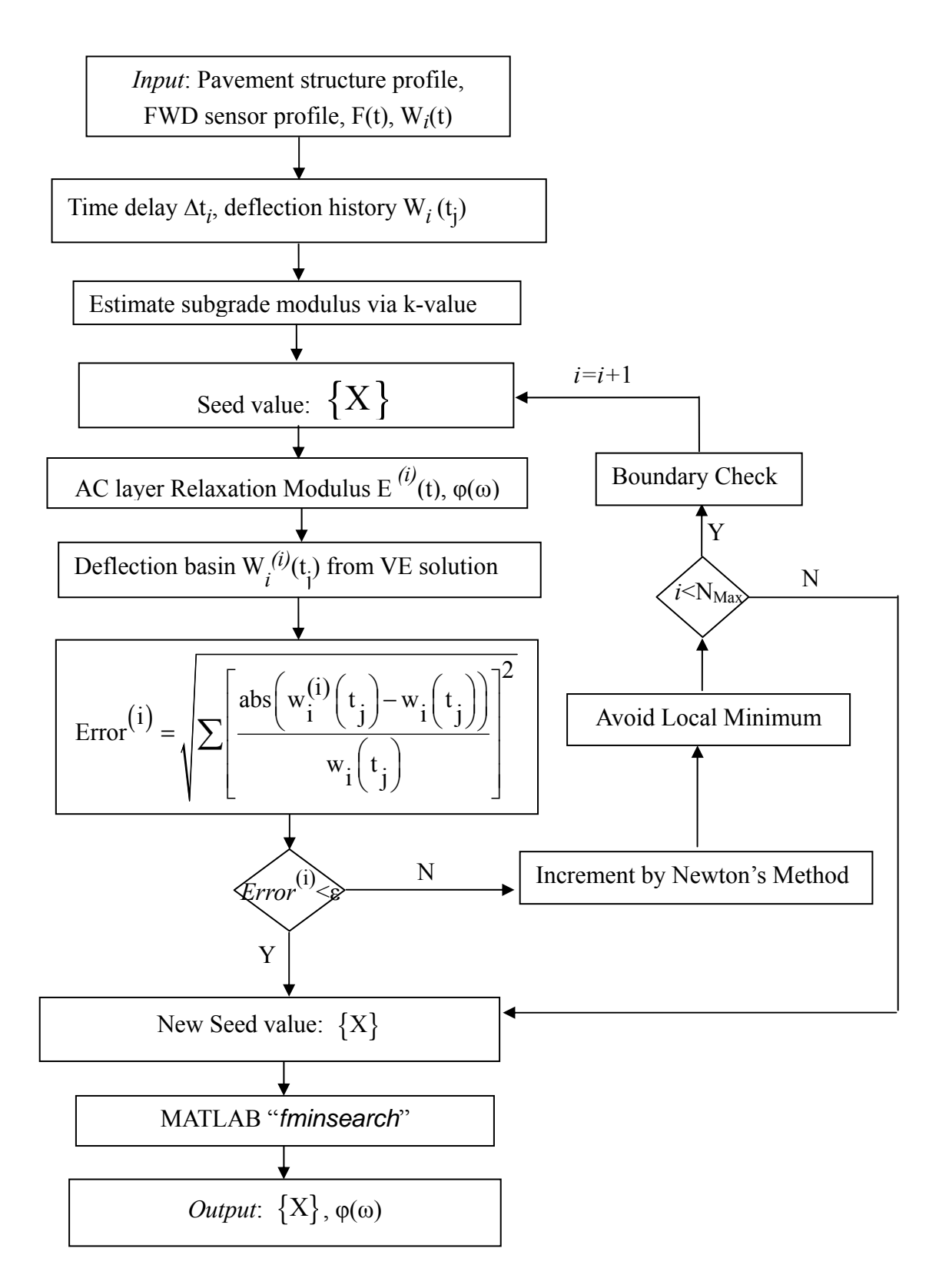


Figure 56: Algorithm of backcalculation procedure of  $|\mathbf{E}^*|$ 

### 5.7 One Numerical Example of Backcalculation Result

A hypothetical pavement profile is assumed, and the response of the pavement under FWD test is simulated by layered VE solution in Chapter 4. The estimation of elastic modulus of the subgrade layer is inappropriate, as the effect of mass inertia cannot be simulated via layered VE solution. Thus, the elastic modulus of the subgrade layer is directly backcalculated. The result of the backcalculation program is listed by  $|E^*|$  or E(t) of AC layer separately.

#### 5.7.1 Result of VE backcalculation of E(t)

The actual pavement profile and the backcalculated result of each layer are listed in Table 33. The input and backcalculated deflection histories are shown in Fig. 57, and the input and backcalculated E(t) functions of the AC layer are shown in Fig. 58.

Table 33: Basic information of a three-layer pavement structure and backcalculated result

Physical Layer	Elastic Modulus (MPa (ksi))	Poisson's Ratio	Thickness (m (in))	E(t) Backcalculation (MPa (ksi))	E*  Backcalculation (MPa (ksi))
AC	E*(f)/E(t)	0.35	0.1 (4)	Fig. 56	Fig. 58
Base	100 (14.5)	0.35	0.3 (12)	98.6 (14.3)	106.7 (15.5)
Subgrade	35.0 (5.1)	0.45	Infinity	35.0 (5.1)	34.9 (5.1)

#### Deflection history simulation (E(t))

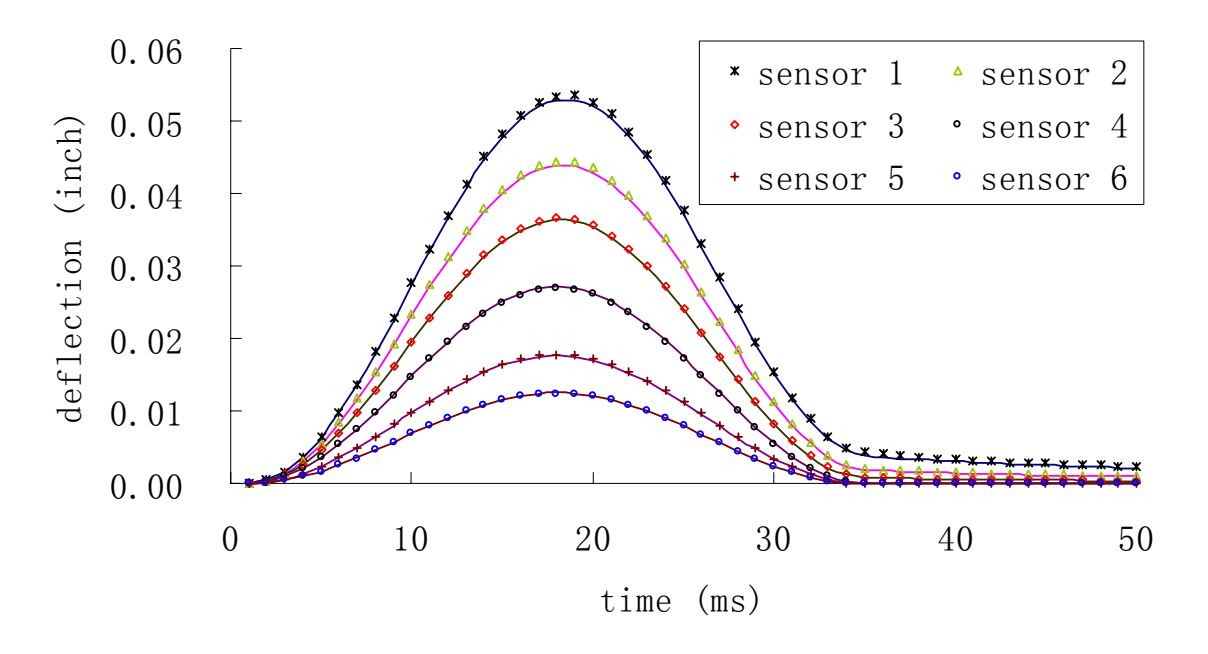


Figure 57: Input and backcalculated time-histories of E(t) in the numerical FWD test

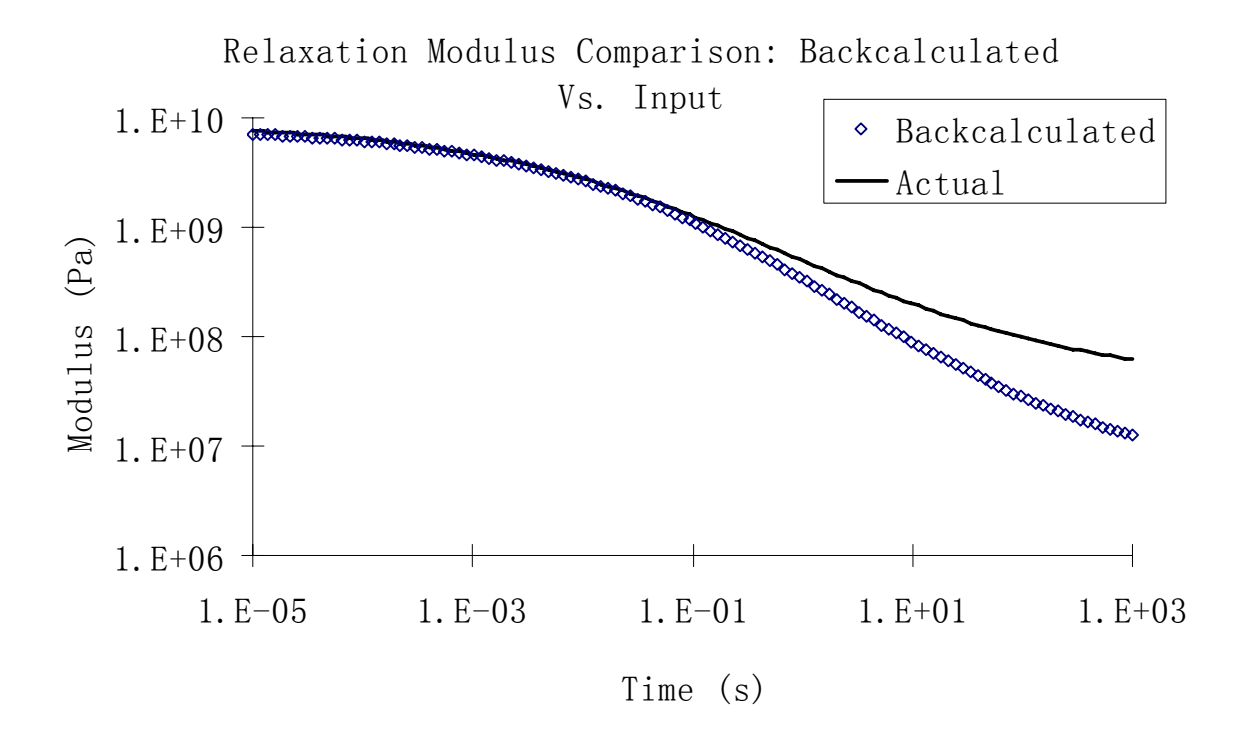


Figure 58: Input and backcalculated E(t) for the numerical FWD test

Table 33 shows that the error of the elastic modulus for base layer is around 1.5%, while the error for subgrade layer is 0.0%. Fig. 57 illustrates that the simulated deflection history matches very well with the input deflection history, thus, the program converges in calculation. Fig.58 illustrates that the backcalculated E(t) does not match very well with the actual input E(t) function. However, this result is expected because the critical range in the E(t) function is 0.0001 - 0.1 second, which is used in both the forward and backcalculation program. The result of the long-time response part of E(t) can be improved if the AC mixture design is given, based on Witczak's regression equation. Therefore, this proposed backcalculation algorithm works reasonably well in this problem.

#### 5.7.2 Result of VE backcalculation of |E\*|

The actual pavement profile and the backcalculated result of each layer are listed in Table 33 in above section. The input and backcalculated deflection history is shown in Fig. 59, and the input and backcalculated E(t) of the AC layer is shown in Fig. 60.

#### Deflection history simulation (|E\*|)

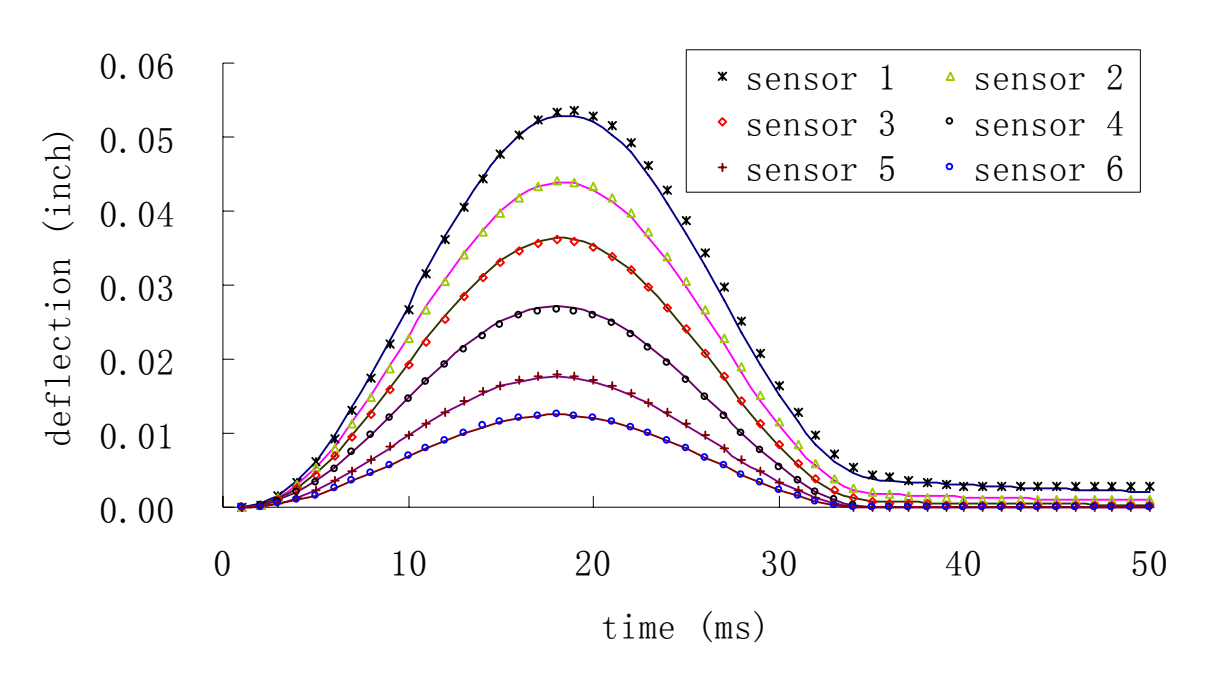


Figure 59: Input and backcalculated time-histories of |E\*| in the numerical FWD test

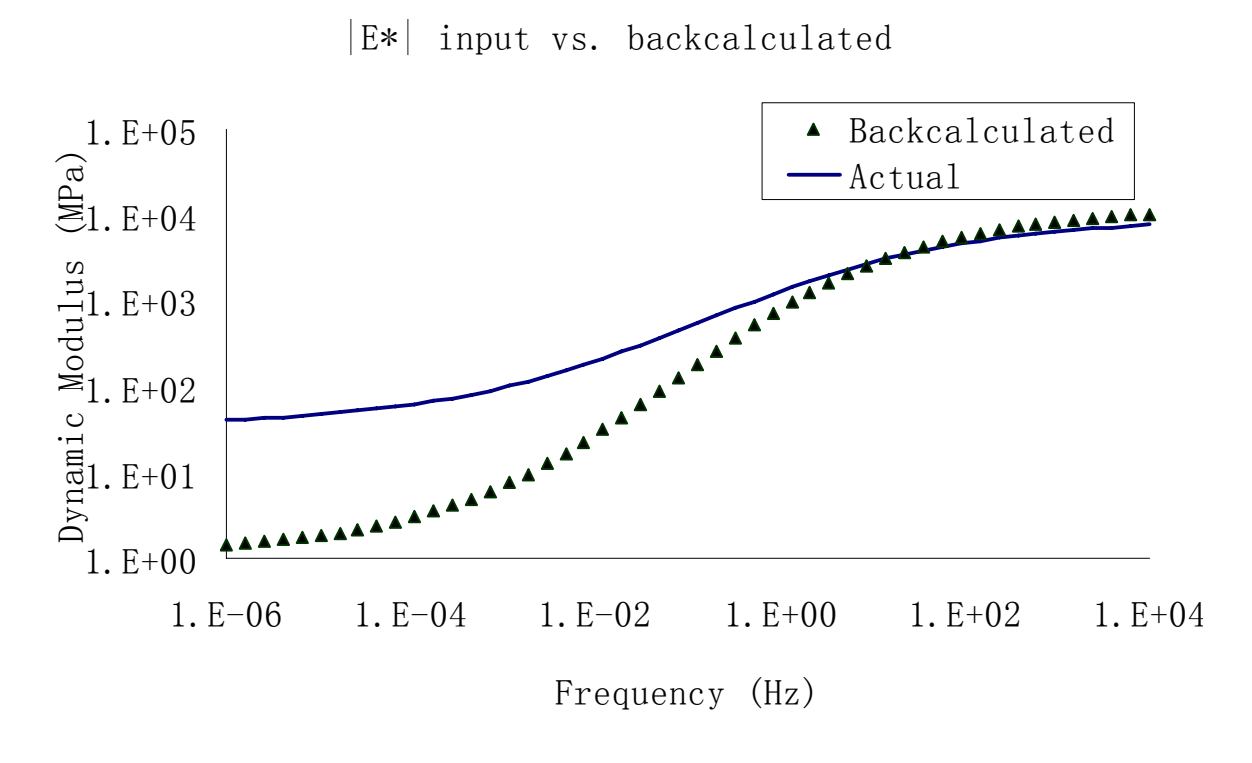


Figure 60: Input and backcalculated |E\*| for the numerical FWD test

Table 33 shows that the error of the elastic modulus via |E\*| backcalculation for base layer is around 7%, while the error for subgrade layer is around 0.3%. Fig. 59 illustrates that the simulated deflection history matches very well with the input deflection history, thus, the program converges in calculation. Fig. 60 illustrates that the backcalculated |E\*| does not match very well with the actual input |E\*| function. Similarly, this result is expected because the correspondingly critical range in the |E\*| function is 10 - 10000 Hz. The result of the low-frequency part of |E\*| can be improved by Witczak's regression equation if the AC mixture design is given.

Therefore, this proposed backcalculation algorithm works reasonably well in this problem.

#### 5.8 Summary

- The output variables of the backcalculation algorithm are identified, and the corresponding boundaries are found.
- The theoretical background is briefly investigated. Newton's method is chosen to scan all possible solutions, random function is used to avoid the problem of local minimum, and the results from MATLAB internal function "fminsearch" are chosen as the final results.
- A step-by-step procedure for backcalculation algorithm is provided in this chapter, and both cases of |E\*| and E(t) backcalculation for the AC mixture are independently investigated. The accuracy of the proposed algorithm is numerically checked.

# **Chapter 6. Verification and Sensitivity Analysis**

#### **6.1 Introduction**

So far, only hypothetical pavement responses were used in the backcalculation algorithm (Chapter 5). In this chapter, more numerical simulations from both VE forward solution and dynamic solutions, SAPSI and LAMDA, are used as the input for the backcalculation algorithm, and the accuracy of the program is checked against the actual modulus values. One example (Texas site) of a three-layer pavement is used to check the limitations of the new backcalculation algorithm. Additionally, field FWD test deflection histories are input for the backcalculation program, and the accuracy of the backcalculation results are checked against the lab measured values. Finally, a sensitivity analysis is conducted for each input variable, and only the viscoelastic parameters of the AC layer are backcalculated. The critical variables are found from sensitivity analysis.

### 6.2 Verification of the VE Backcalculation Algorithm

In this section, the results from backcalculation algorithm of  $|E^*|$  and E(t) for the AC layer are proposed together in each example. The parameters in the sigmoid function for the AC layer, and elastic modulus of base and subgrade layers are the final output results.

The verification part includes three separate methods. First, four VE forward simulation results are input in the backcalculation program to check the accuracy of the algorithm. Second, four actual pavements are investigated (Ji, 2005), and the FWD tests are simulated by the

dynamic solution in SAPSI and LAMDA. The simulated deflection histories, as well as the layer thickness and sensor locations, are entered in the backcalculation program. Third, three field FWD test deflection histories are used to check the potential usage of the algorithm in the future.

The FWD test is usually conducted at a specific temperature, and the backcalculation is done for the same temperature. There is no need for time temperature superposition, and the actual time scale is the reference time scale. In the field FWD test, the typically sampling time interval is 0.4ms, and the total recording time is 60 ms. The available range from FWD test should be between 0.4 ms to 60 ms, i.e., the valid range of the E(t) for the AC layer is only the proportion between 0.4 ms to 60 ms. Although the E(t) function is characterized by sigmoidal function, theoretically only a portion of E(t) can be obtained from backcalculation, shown in Fig. 61.

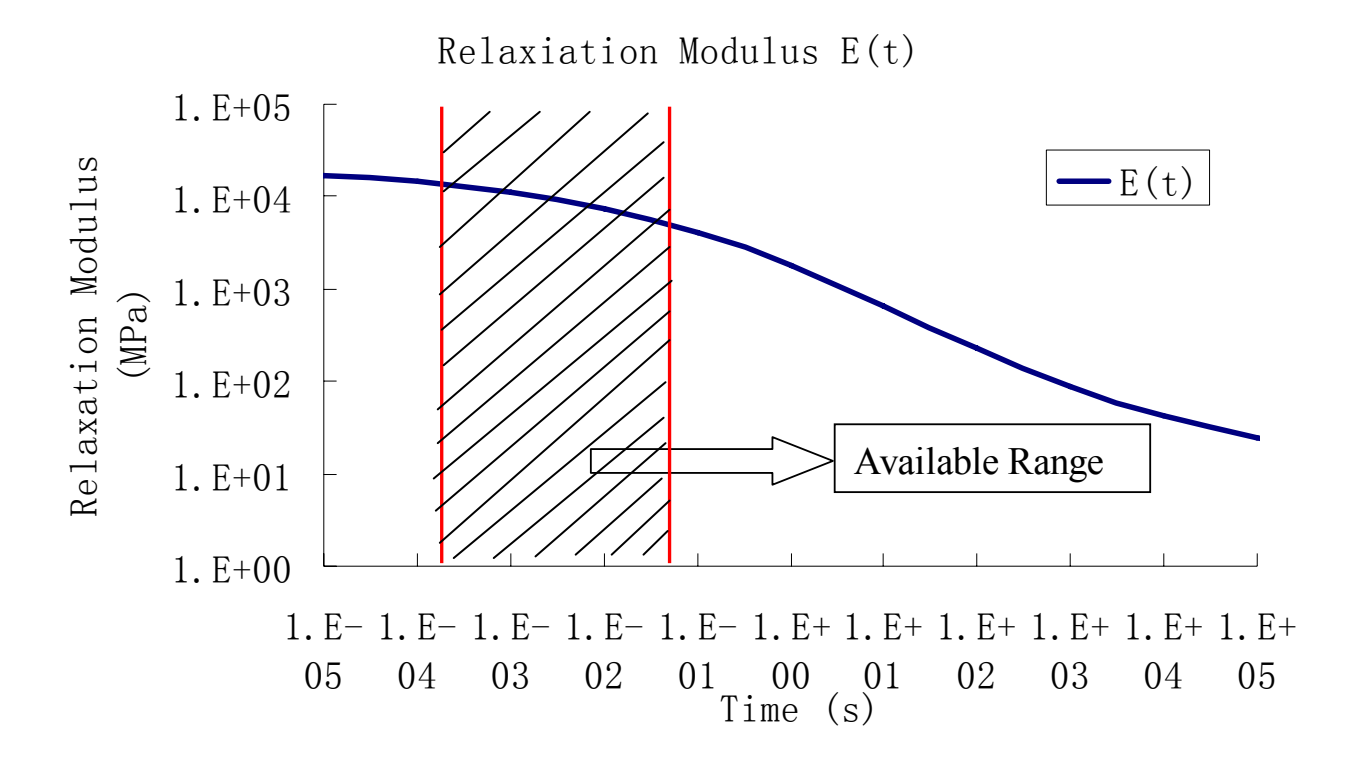


Figure 61: Available range in E(t) function from field FWD test backcalculation

Approximately, the available range of |E\*| in the frequency domain can be identified by

f=1/(2\*t), i.e., the valid range of the |E\*| for the AC layer is only the proportion between 8 Hz to 1250 Hz, if it is backcalculated from field FWD test, shown in Fig. 62.

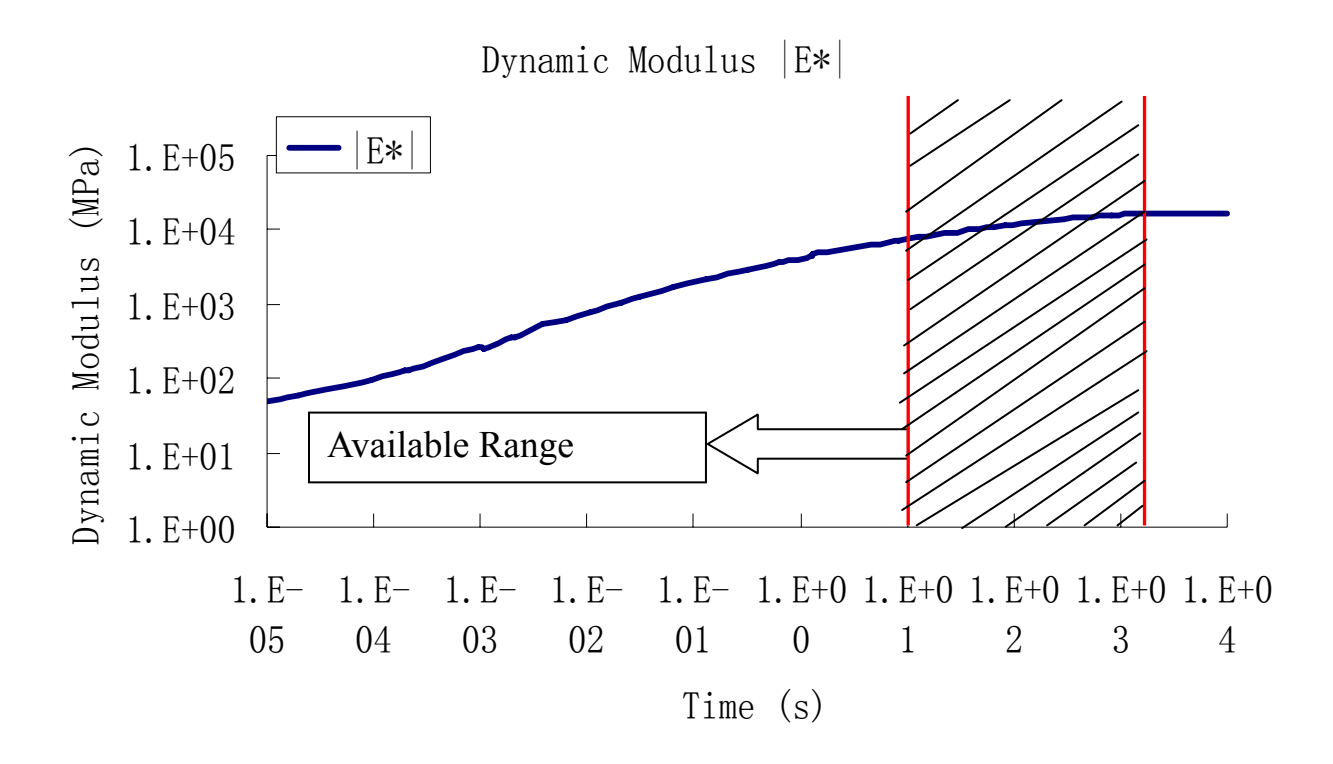


Figure 62: Useful range in |E\*| function from field FWD test backcalculation

The modification of the FWD test equipment may be required if the useful range needs to be enlarged. In this dissertation, the typical FWD test equipment is utilized in the backcalculation algorithm, and proportion of E(t) or  $|E^*|$  in the useful range is concerned.

### 6.2.1 VE Backcalculation using Time Histories from VE Solution

Four numerical examples of FWD test deflection histories are simulated by the layered VE solution, which was discussed in Chapter 4. Then, the deflection histories from sensors and pavement structural information without modulus are entered into the VE backcalculation program to check the accuracy of the backcalculation results.

#### 6.2.1.1 Numerical Example 1

The pavement response under FWD dynamic load is simulated by VE forward solution, and the deflection time-history of each sensor is used as input to the VE backcalculation program. In order to compare the accuracy of this VE program against common elastic backcalculation programs, the deflection basin is used to backcalculate the elastic modulus of each physical layer by MODCOMP5. The actual pavement profile and the backcalculated result of each layer are listed in Table 34. The input and VE backcalculated deflection histories using E(t) are shown in Fig. 63, the input and VE backcalculated deflection histories using  $|E^*|$  are shown in Fig. 65; the input and backcalculated E(t) of the AC layer are shown in Fig. 64, and the input and backcalculated  $|E^*|$  of the AC layer are shown in Fig. 66.

Table 34: Basic information of pavement structure and backcalculated result for numerical example 1

Physical Layer	Elastic Modulus (MPa (ksi))	Poisson Ratio	Thickness (m (in))	MODCOMP5 Backcalculation (MPa (ksi))		E*  Backcalculation (MPa (ksi))
AC	E*(f)/E(t)	0.35	0.152 (6.0)	8067 (1170.0)	Fig. 64	Fig. 66
Base	206.8 (30.0)	0.30	0.670 (24)	215.1 (31.2)	207.7 (30.3)	236.6 (34.3)
Subgrade	34.5 (5.0)	0.45	Infinity	34.3 (5.0)	34.5 (5.0)	33.7 (4.9)

Table 34 shows the elastic modulus of base and subgrade layer are almost the same from VE backcalculation and MODCOMP5, although the VE backcalculation program using E(t) may give slightly worse results for the base elastic modulus than that using  $|E^*|$ . However, MODCOMP5 can only backcalculate one value for the modulus of the AC layer, which can be considered as an effective value, but cannot be taken as a fundamental property of the AC material. The VE backcalculation program, on the other hand, can overcome this problem and

gives the AC material property as a function of time or frequency.

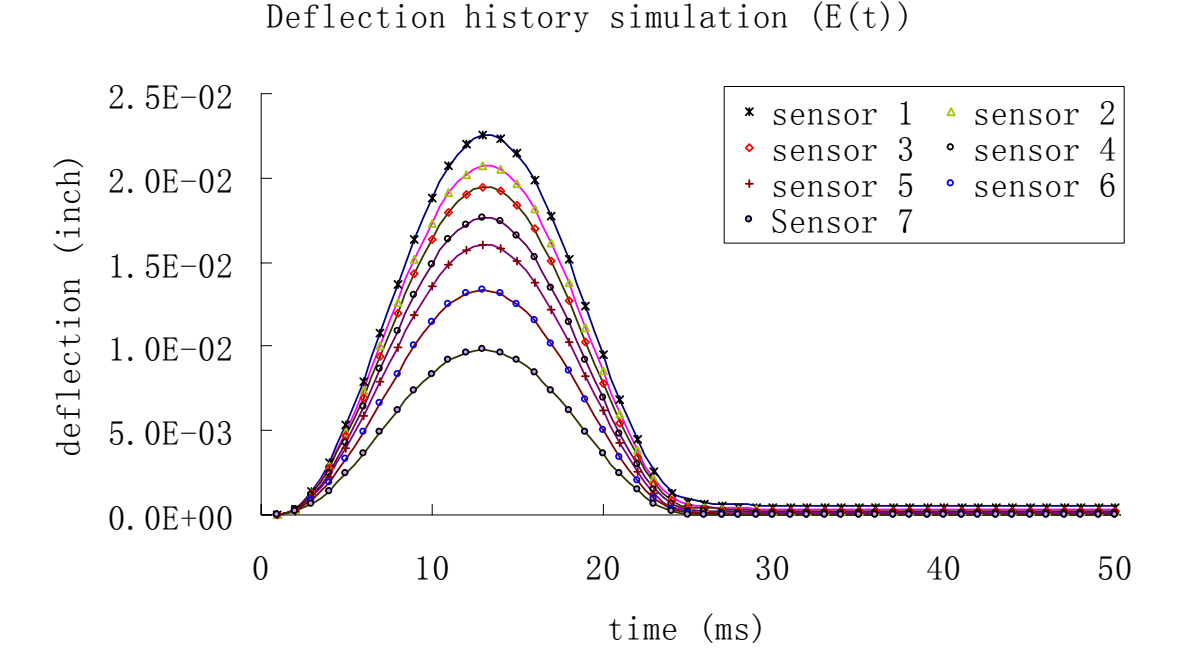
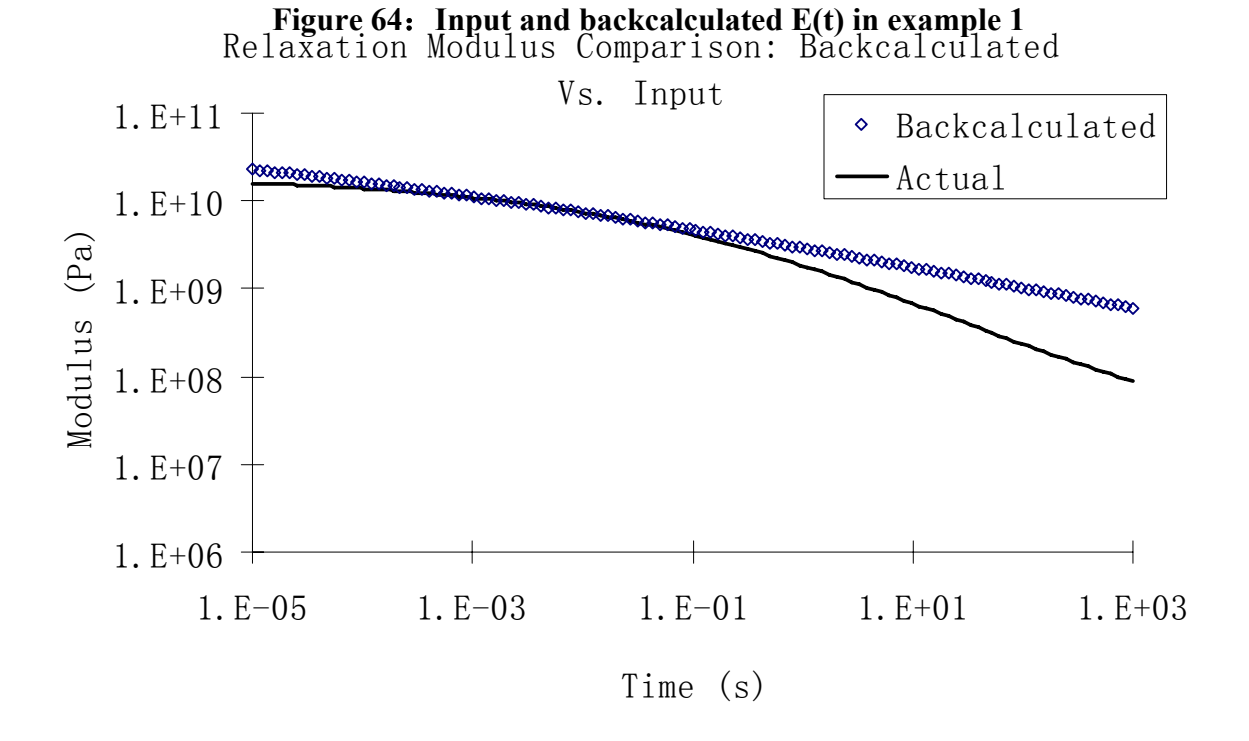


Figure 63: Input and simulated time-histories by backcalculation of E(t) in example 1 (Solid lines represent the input deflection history, symbols represent the VE simulation)



Figures 63 shows an excellent match between the actual and predicted deflection time histories using E(t) for every sensor. Figure 64 shows that the backcalculated function E(t) is very close to the input function only in the concerned time range around 0.0001 - 0.1 s.

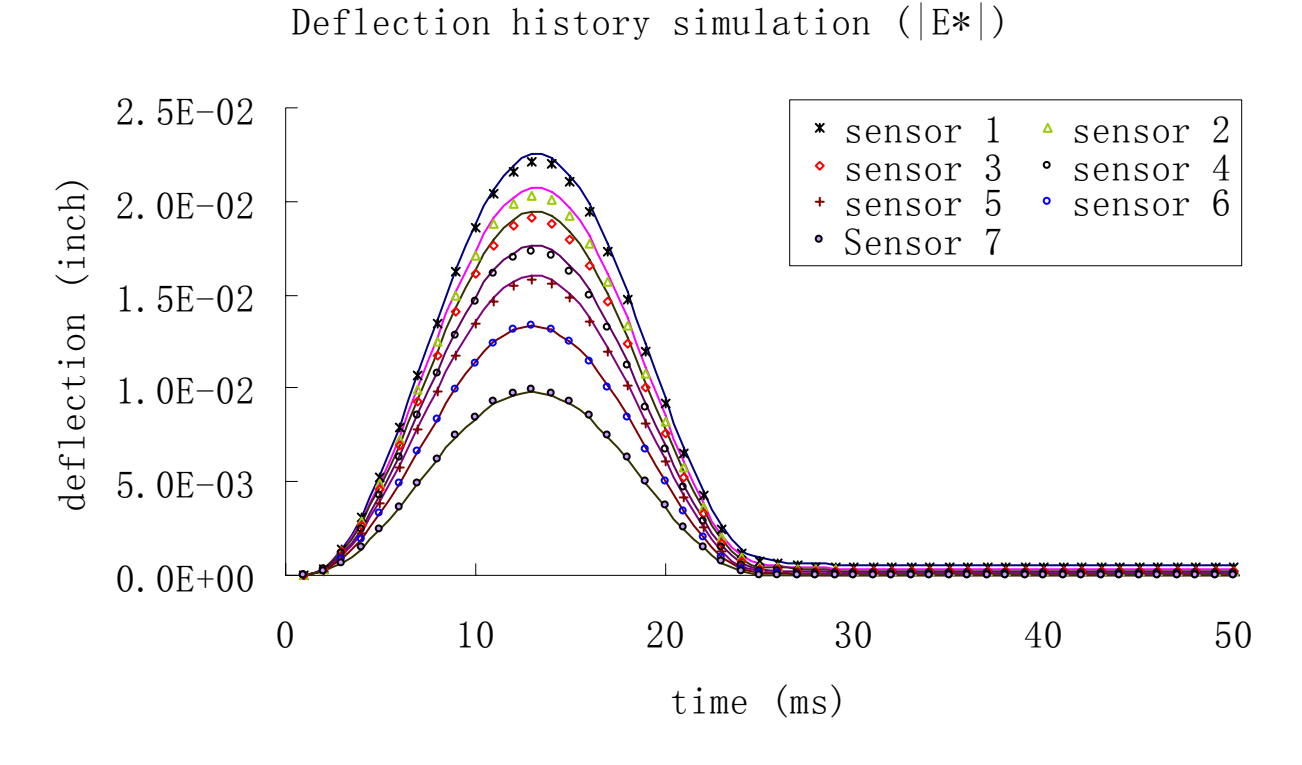
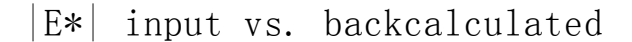


Figure 65: Input and simulated time-histories by backcalculation of  $|E^*|$  in example 1 (Solid lines represent the input deflection history, symbols represent the VE simulation)



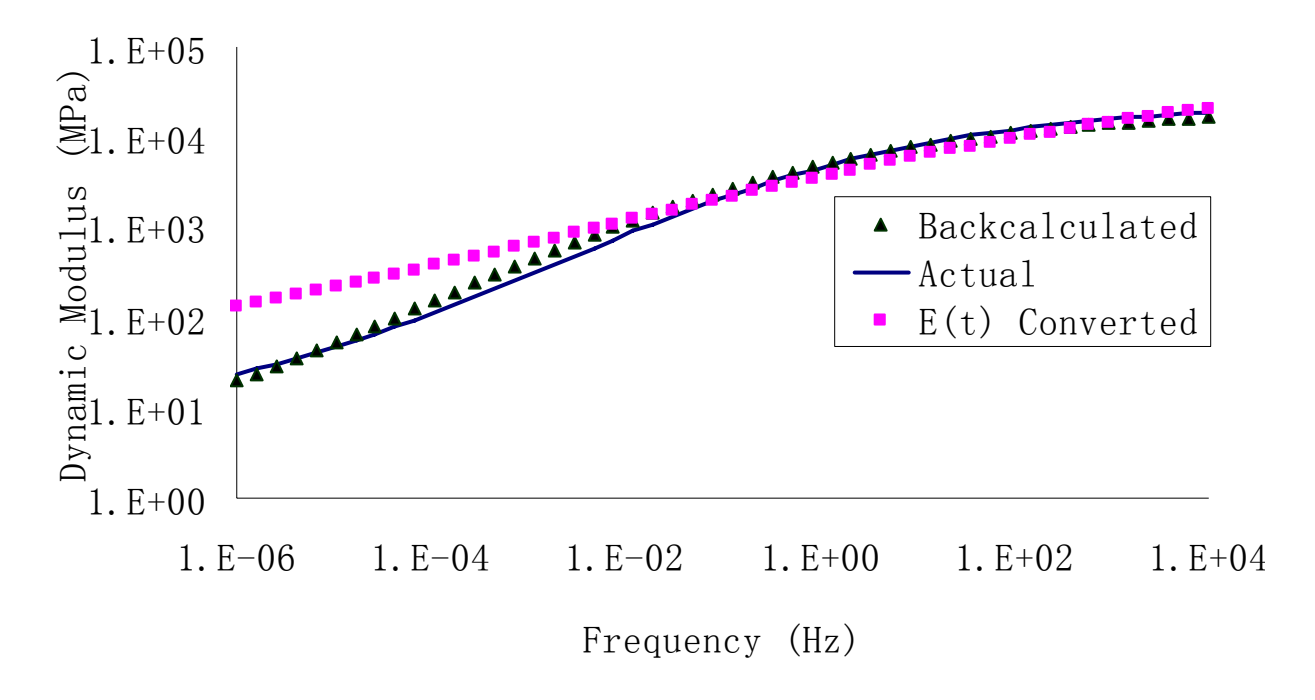


Figure 66: Input and backcalculated |E\*| in example 1

Figure 65 shows a very good match between actual and predicted deflection time histories using  $|E^*|$  for every sensor. Figure 66 shows that the backcalculated function of  $|E^*|$  for the AC layer is very close to the input function in the entire frequency range. It is not expected that the predicted function matches well with the actual  $|E^*|$  function for every frequency, since only a portion of the  $|E^*|$  function is used in both forward and backcalculation solution.

As discussed in Chapter 2, the  $|E^*|$  can be mathematically calculated from E(t) function. If the E(t) function is backcalculated as Figure 64, the corresponding  $|E^*|$  curve is plotted in Figure 66. The coverted  $|E^*|$  matches very well with the actual  $|E^*|$  function in the concerned frequency range, i.e., 10 to 10000 Hz.

Phase Angle shift function: Backcalculated Vs.
Actual

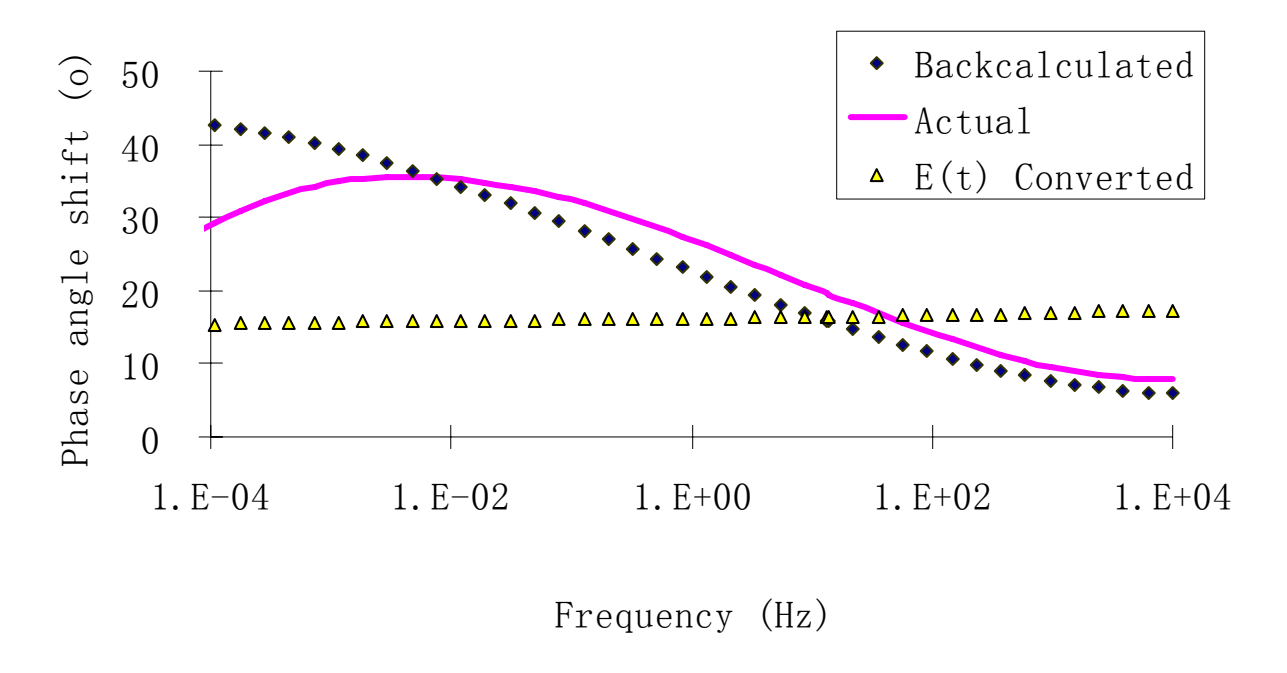


Figure 67: Input and backcalculated  $\varphi$  in example 1

Figure 67 shows that the backcalculated phase angle  $\phi$  for the AC material matches fairly to the input function in the concerned range. Another predicted  $\phi$  was obtained from the interconversion of E(t), as discussed in Chapter 2. Although the predicted E(t) matches very well to the input function in the concerned range (Figure 67), the converted  $\phi$  does not match the input function. In general, it seems  $\phi$  cannot be well predicted in either E(t) backcalculation, or  $|E^*|$  backcalculation, although it works in above example. Therefore, the backcalculation of  $\phi$  is ignored in the future examples.

In this example, the VE backcalculation program works well for both |E\*| and E(t) backcalculation, and the match between backcalculated and actual deflection time-histories is very good. The elastic modulus for the subgrade layer is very accurate, with an error of only 1%;

the function E(t) and  $|E^*|$  for AC layer match fairly well with the input functions in the VE forward calculation; the elastic modulus of the base layer may have an error of up to 10%.

## 6.2.1.2 Numerical Example 2

Similarly to the first example, the pavement response under FWD dynamic load is simulated by the VE forward solution, and the deflection time-history of each sensor is used as input to the VE backcalculation program. However, in this example, a stiff cement treated base (CTB) is included in the pavement structure. In order to compare the accuracy of the VE program against common elastic backcalculation program, the deflection basin is used to backcalculate the elastic modulus of each physical layer by MODCOMP5. The actual pavement profile and the backcalculated results of each layer are listed in Table 35. The input and VE backcalculated deflection histories of E(t) are shown in Fig. 68; the input and VE backcalculated deflection histories of |E\*| are shown in Fig. 70; the input and backcalculated E(t) of the AC layer are shown in Fig. 69; and the input and backcalculated |E\*| of the AC layer are shown in Fig. 71.

Table 35: Basic information of pavement structure and backcalculated result for numerical example 2

Physical Layer	Elastic Modulus (MPa (ksi))	Poisson Ratio	Thickness (m (in))	MODCOMP5 Backcalculation (MPa (ksi))		E*  Backcalculation (MPa (ksi))
AC	$E^*(f)/E(t)$	0.35	0.102 (4.0)	10618 (1540)	Fig. 69	Fig. 71
Base	5000 (725)	0.20	0.152 (6.0)	4165 (604)	5104 (740)	5153 (747)
Subgrade	69.0 (10.0)	0.45	Infinity	69.6 (10.1)	72.1 (10.5)	70.8 (10.3)

Table 35 shows the VE backcalculated modulus of base and subgrade layers are almost the same as the actual value, and MODCOMP5 gives slightly worse result for the CTB layer, with an error of about 20%. Also, MODCOMP5 can only backcalculate one value for the modulus of the

AC layer, which can be considered as an effective value, but cannot be taken as a fundamental property of the AC material. The VE backcalculation program, on the other hand, can overcome this problem and gives the AC material property as a function of time or frequency.

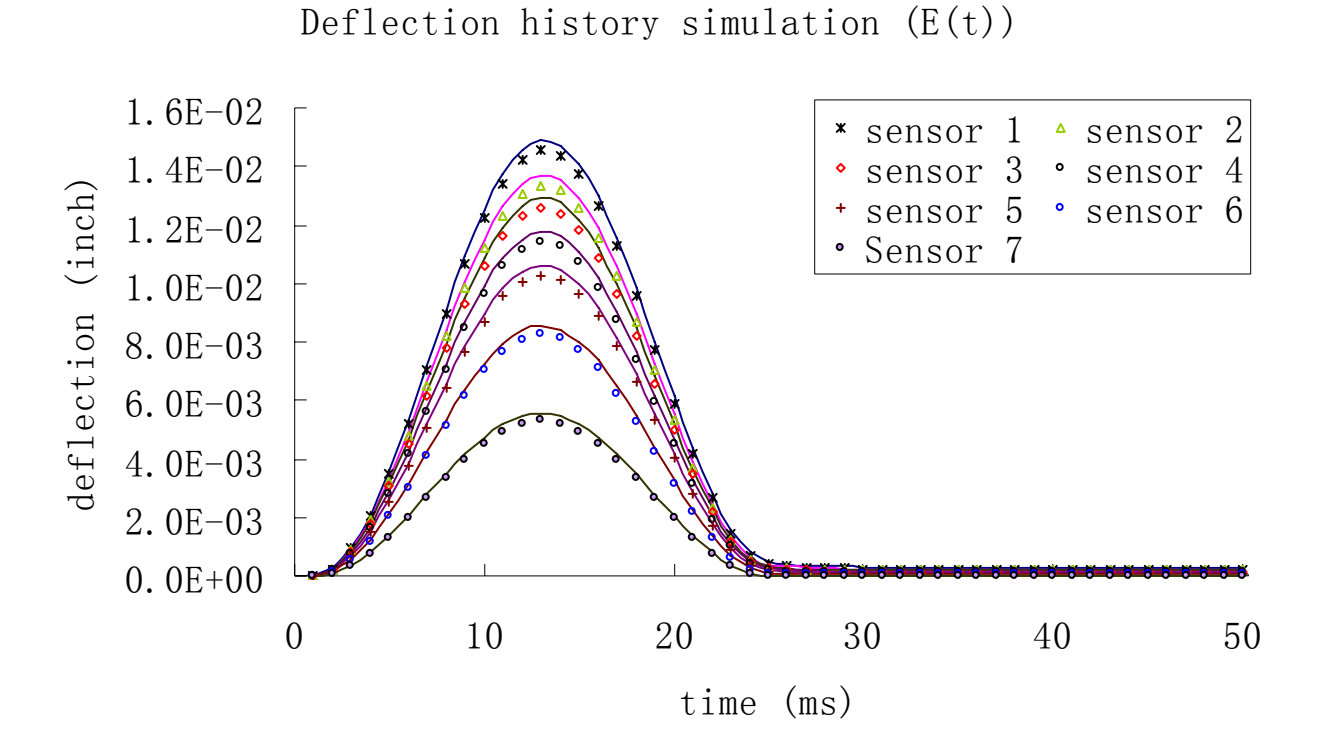


Figure 68: Input and simulated time-histories by backcalculation of E(t) in example 2 (Solid lines represent the input deflection history, symbols represent the VE simulation)

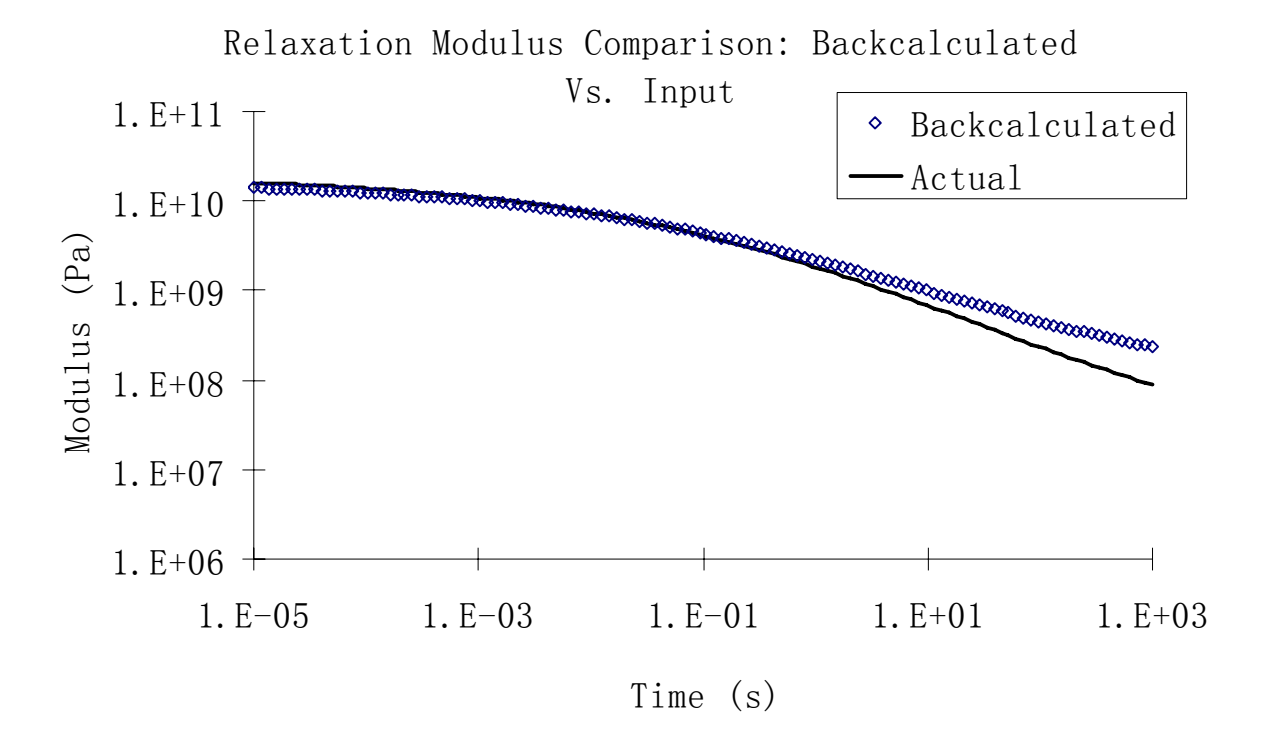


Figure 69: Input and backcalculated of E(t) in example 2

Fig. 68 shows a very good match between actual and predicted deflection time histories using E(t) for every sensor. Fig. 69 shows that the backcalculated function E(t) is very close to the input function in the concerned time range, approximately 0.0001 - 0.1 s.

## Deflection history simulation (|E\*|)

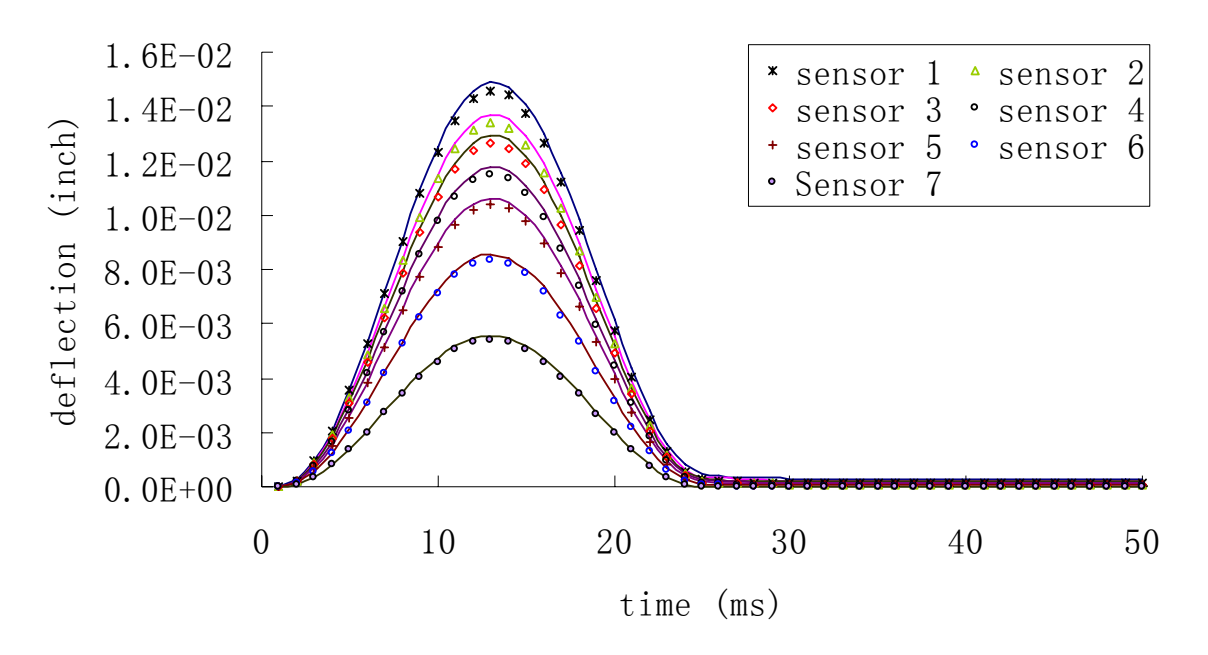


Figure 70: Input and simulated time-histories by backcalculation of  $|E^*|$  in example 2 (Solid lines represent the input deflection history, symbols represent the VE simulation)

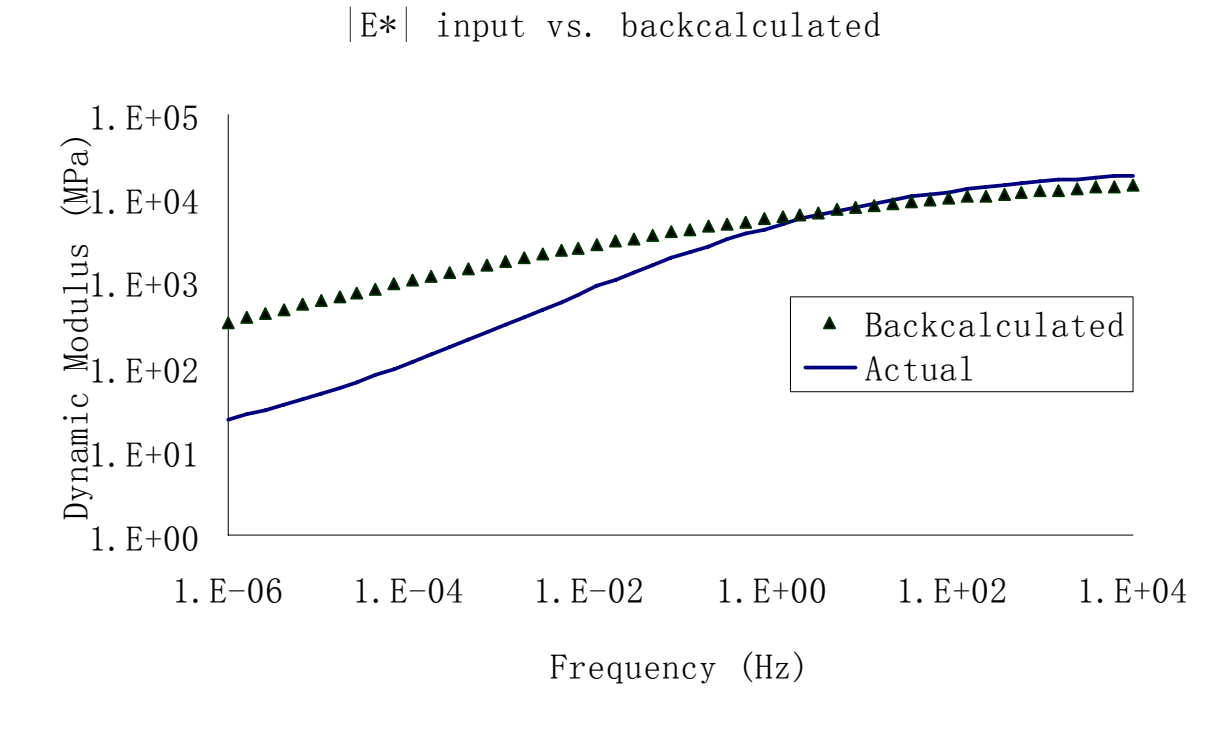


Figure 71: Input and backcalculated of |E\*| in example 2

Fig. 70 shows a very good match between actual and predicted deflection time histories using  $|E^*|$  for every sensor. Fig. 71 illustrates that the backcalculated function  $|E^*|$  for the AC layer is very close to the input function in the concerned frequency range, 10 - 10000 Hz. Here the lower frequency part of  $|E^*|$  is quite different between input and backcalculated results.

In summary, the VE backcalculation program works well for both  $|E^*|$  and E(t) backcalculation, and the match between actual and backcalculated deflection time-histories is very good. The elastic modulus for the CTB base and subgrade layer is very accurate, with an error of 3%, and the functions E(t) and  $|E^*|$  for the AC layer match fairly well with the input function within certain time and frequency ranges.

## 6.2.1.3 Numerical Example 3

In this example, a weak pavement section is used. The actual pavement profile and the backcalculated results of each layer are listed in Table 36. The input and VE backcalculated deflection histories of E(t) are shown in Fig. 72; the input and VE backcalculated deflection histories of  $|E^*|$  are shown in Fig. 74; the input and backcalculated E(t) of the AC layer are shown in Fig. 73, and the input and backcalculated  $|E^*|$  of the AC layer are shown in Fig. 75.

Table 36: Basic information of pavement structure and backcalculated result for numerical example 3

Physical Layer	Elastic Modulus (MPa (ksi))	Poisson Ratio	Thickness (m (in))	MODCOMP5 Backcalculation (MPa (ksi))	E(t) Backcalculation (MPa (ksi))	E*  Backcalculation (MPa (ksi))
AC	$E^*(f)/E(t)$	0.35	0.102 (4.0)	27028 (3920)	Fig. 73	Fig. 75
Base	10.8 (1.57)	0.35	0.204 (8.0)	124 (18.0)	10.45 (1.52)	10.9 (1.58)
Subgrade	10.0 (1.45)	0.35	Infinity	13.2 (1.92)	10.1 (1.47)	9.76 (1.42)

Table 36 shows the VE backcalculated elastic modulus of base and subgrade layer are almost the same as the actual values, but MODCOMP5 gives quite different result for the base layer. Moreover, only one modulus value is given in MODCOMP5 for the AC layer. The VE backcalculation program can overcome this problem and gives the AC modulus as a function of time or frequency.

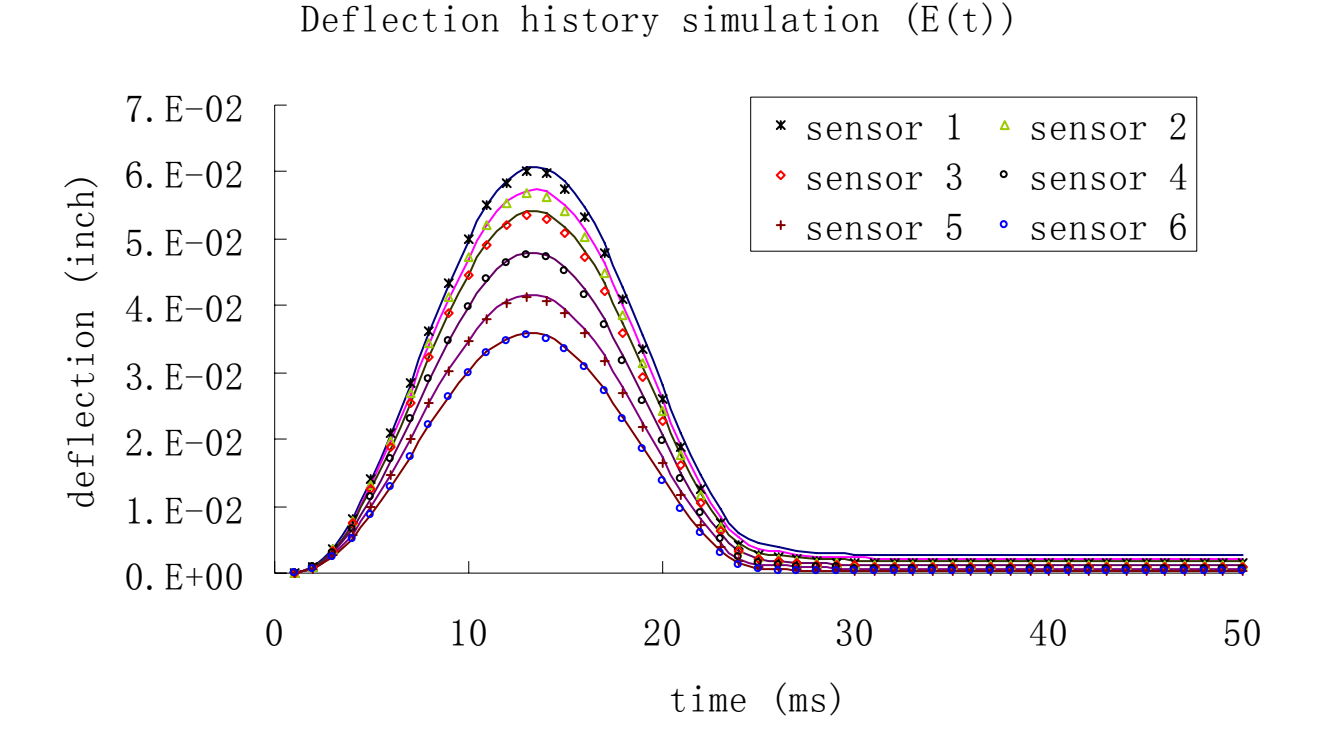


Figure 72: Input and simulated time-histories by backcalculation of E(t) in example 3 (Solid lines represent the input deflection history, symbols represent the VE simulation)

Fig. 72 shows a very good match between actual and predicted deflection time histories using E(t) for every sensor, with the exception of sensor 1 in the rest period. This is why the backcalculated function E(t) is very close to the input function only in the concerned time range 0.0001 - 0.1 s (Fig. 73).

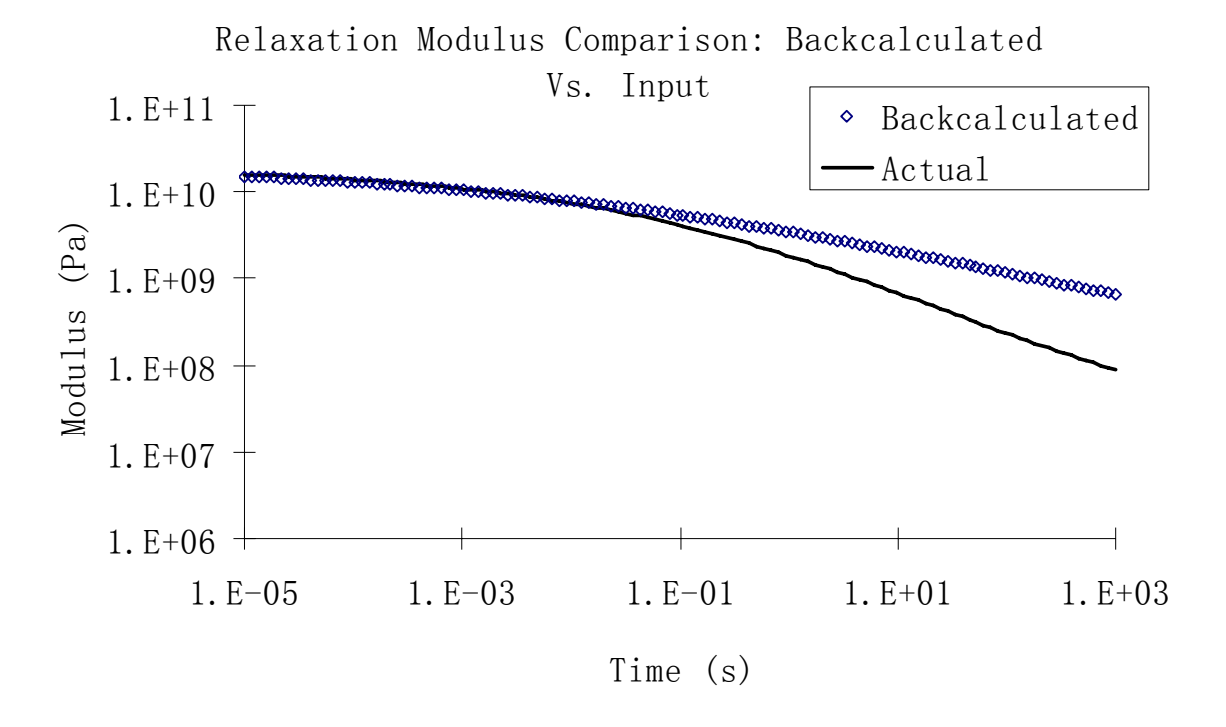


Figure 73: Input and backcalculated E(t) in example 3

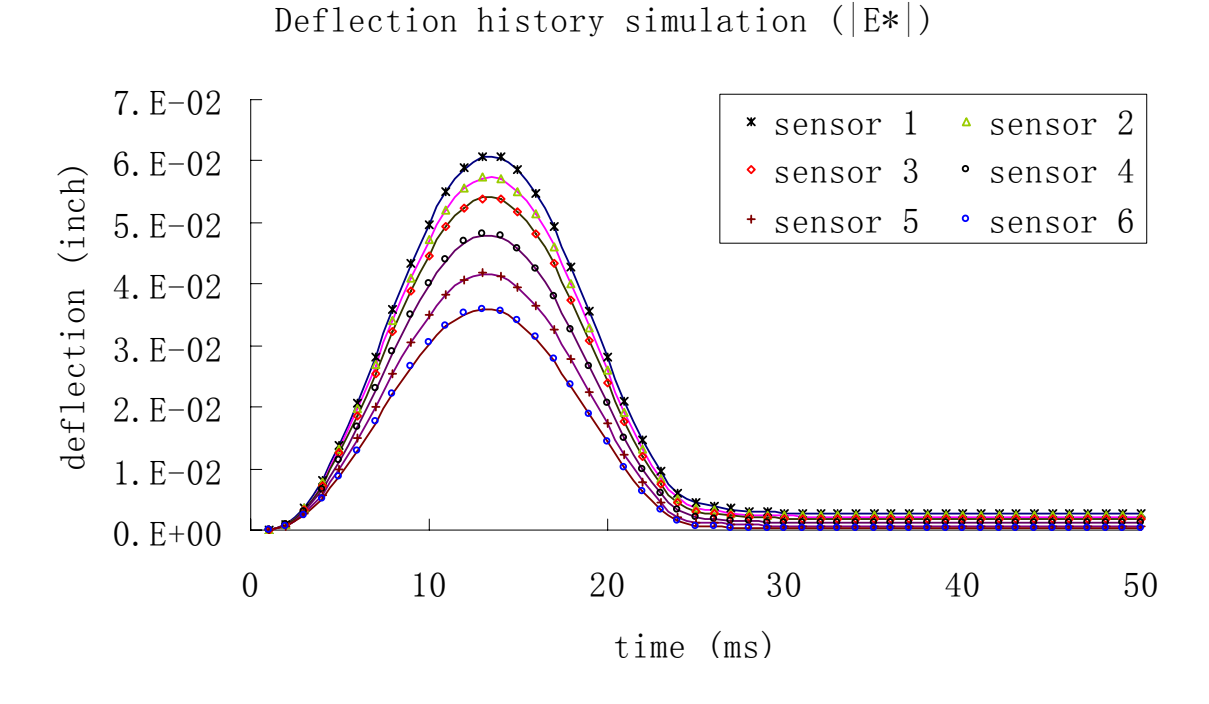
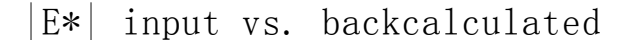


Figure 74: Input and simulated time-histories by backcalculation of  $|E^*|$  in example 3 (Solid lines represent the input deflection history, symbols represent the VE simulation)



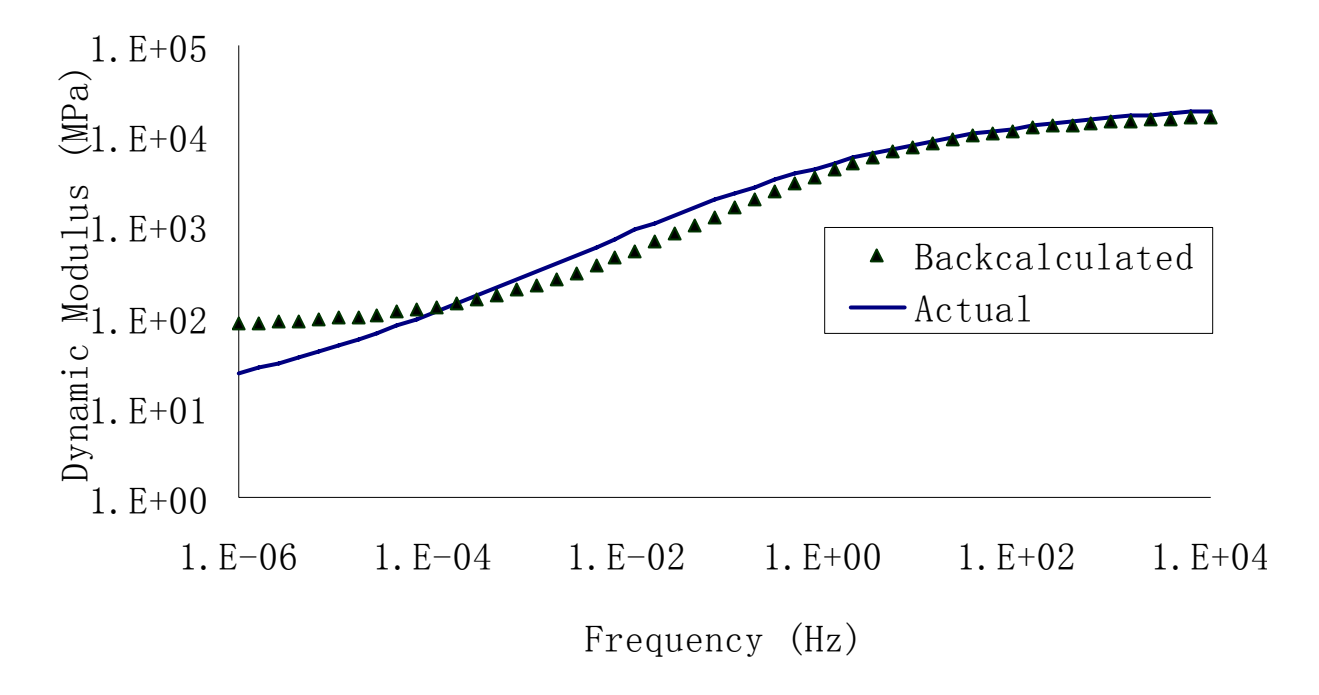


Figure 75: Input and backcalculated |E\*| in example 3

Fig. 74 and 75 show good agreement between deflection time histories and  $|E^*|$  curves. The simulated time-history for sensor 1 is almost the same as the input deflection history, so the backcalculated  $|E^*|$  function for the AC layer is very close to the input function in the concerned frequency range 10 - 10000 Hz.

In summary, the VE backcalculation program works well for both  $|E^*|$  and E(t) backcalculation, and the match between actual and backcalculated deflection time-histories is very good. The backcalculated elastic modulus for the base and subgrade layer is very accurate, with an error of 3%, and the function E(t) and  $|E^*|$  for AC layer match fairly well with the actual function for limited ranges in time and frequency. Since the moduli of the base and subgrade layer are very similar, MODCOMP5 does not work well in this case.

## 6.2.1.4 Numerical Example 4

In this fourth example, the same pavement section as the one in the previous example is used, except that a different AC mixture is used. The actual pavement profile and the backcalculated result of each layer are listed in Table 37. The input and VE backcalculated deflection histories of E(t) are shown in Fig. 76; the input and VE backcalculated deflection histories of E(t) are shown in Fig. 78; the input and backcalculated E(t) of the AC layer are shown in Fig. 77; and the input and backcalculated E(t) of the AC layer are shown in Fig. 79.

Table 37: Basic information of pavement structure and backcalculated result for numerical example 4

Physical Layer	Elastic Modulus (MPa (ksi))	Datio	Thickness (m (in))	MODCOMP5 Backcalculation (MPa (ksi))	( )	E*  Backcalculation (MPa (ksi))
AC	$E^*(f)/E(t)$	0.35	0.102 (4.0)	9515 (1380)	Fig. 77	Fig. 79
Base	10.8 (1.57)	0.35	0.204 (8.0)	103.4 (15.0)	10.5 (1.52)	10.6 (1.54)
Subgrade	10.0 (1.45)	0.35	Infinity	9.45 (1.37)	9.9 (1.44)	9.80 (1.42)

Table 37 shows the VE backcalculated elastic modulus of base and subgrade layer are almost the same from the actual value, but MODCOMP5 gives quite different result for the base layer, due to the fact that the base modulus is almost the same as the subgrade layer. Moreover, only one modulus value is given in MODCOMP5 for AC layer. The VE backcalculation program can overcome this problem and gives the AC modulus as a function of time or frequency.

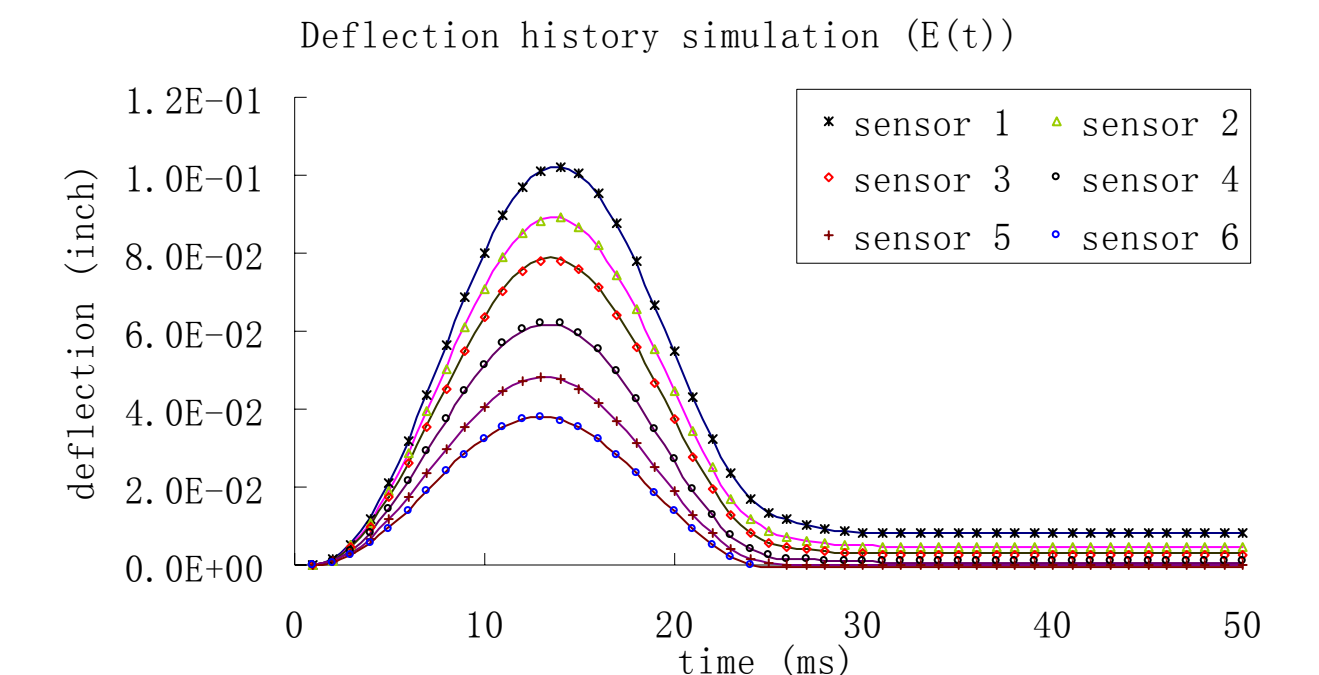


Figure 76: Input and simulated time-histories by backcalculation of E(t) in example 4 (Solid lines represent the input deflection history, symbols represent the VE simulation)

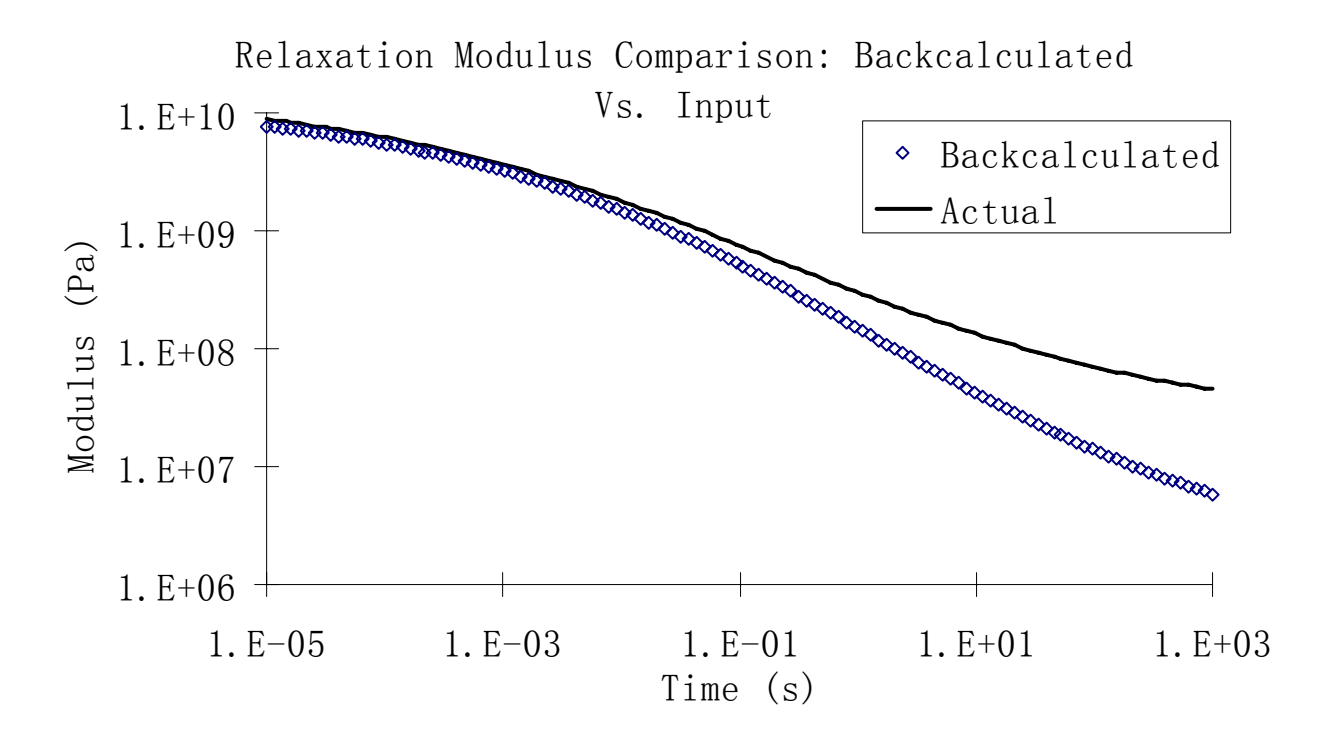


Figure 77: Input and backcalculated E(t) in example 4

Fig. 76 and 77 show comparisons of backcalculated and actual deflection time histories and E(t) curve. The backcalculated E(t) function is very close to the input function only in the concerned time range, 0.0001 - 0.01 s.

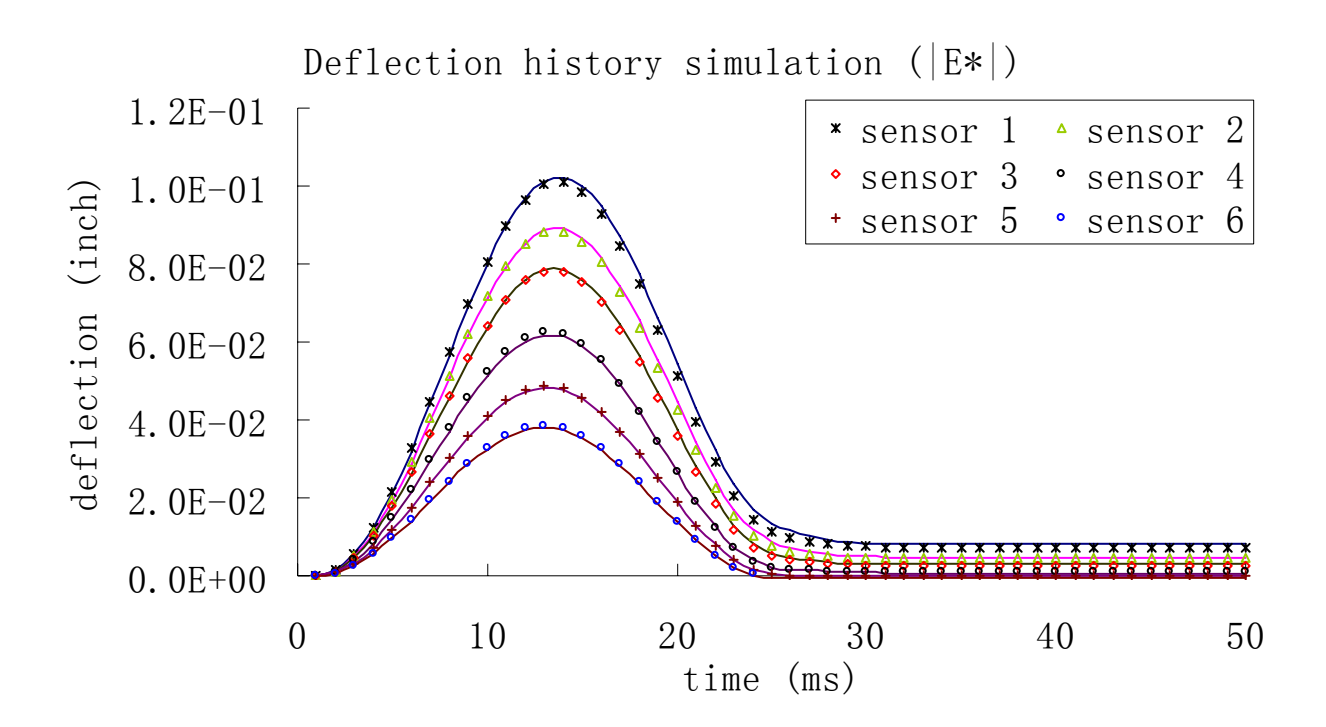


Figure 78: Input and simulated time-histories by backcalculation of  $|E^*|$  in example 4 (Solid lines represent the input deflection history, symbols represent the VE simulation)

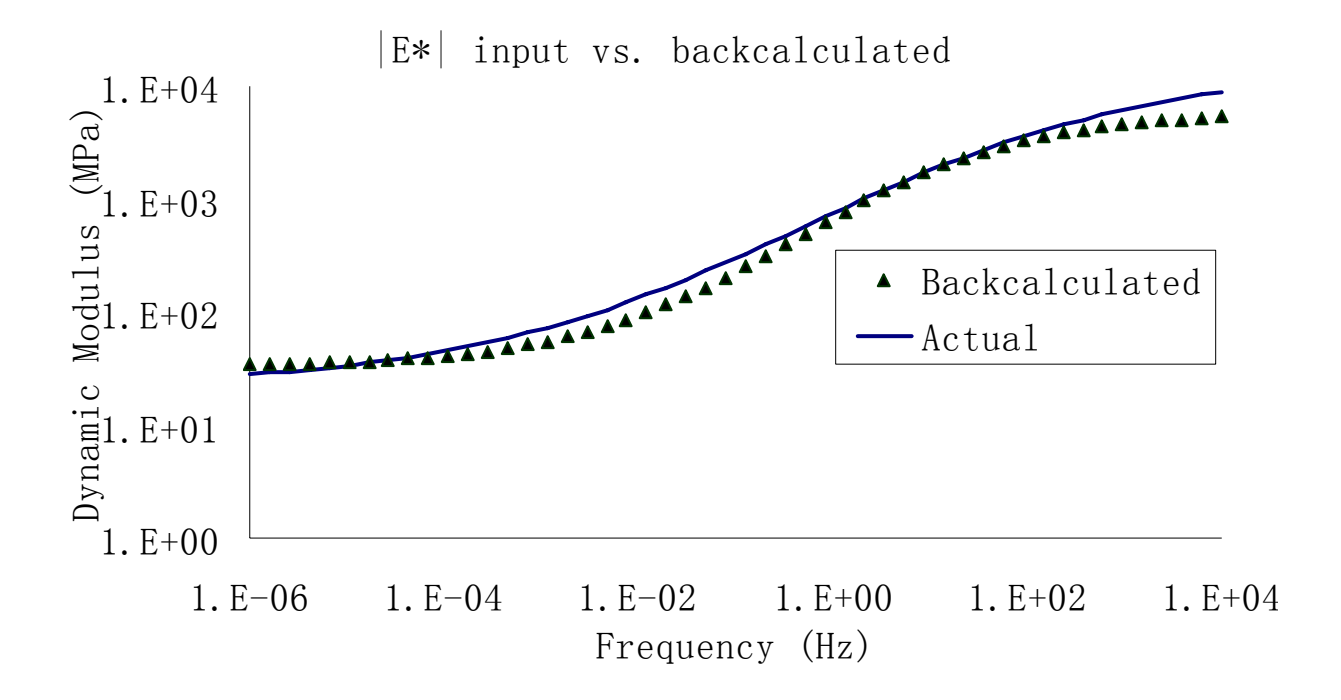


Figure 79: Input and backcalculated  $|E^*|$  in example 4

Fig. 78 and 79 illustrate good agreements between backcalculated and actual deflection time histories and  $|E^*|$  curves. The simulated time-history for sensor 1 is close to the input deflection history, so the backcalculated function for the AC layer is reasonably close to the input function in the concerned frequency range 10 - 10000 Hz, although larger errors exist in other frequency ranges.

In summary, another AC mixture is used in this numerical example, and the backcalculation results are still reasonable. The elastic moduli for the base and subgrade layer are very accurate, with an error of 3%, and the functions E(t) and  $|E^*|$  for AC layer match fairly well with the input functions in the concerned time and frequency ranges. Since the modulus of the base and subgrade layer is very similar, MODCOMP5 does not work well in this case.

#### 6.2.1.5 Discussion

The above four numerical examples indicate that the backcalculation algorithm works well, even when there is a stiff base. Since the forward simulation is from VE solution, the dynamic effect of FWD test cannot be shown, and the elastic modulus of the subgrade layer is obtained directly from backcalculation, not using the ratio of shear and Rayleigh wave velocity discussed in Chapter 3.

# 6.2.2 VE Backcalculation using Time Histories from Dynamic Solutions

In the previous section, the layered VE solution was used for both forward and backcalculation algorithm. This allowed for the verification of the inverse solution. In this section, we use completely different solution to calculate the deflection time histories under FWD test. Four numerical examples of FWD test deflection histories are simulated by dynamic solution SAPSI or LAMDA. Then, the deflection histories from sensors and pavement structural information without modulus are entered into VE backcalculation program to check the accuracy of the backcalculation results. One of the examples includes a site of shallow stiff layer underneath pavement.

# 6.2.2.1 Example 5: Michigan Site

The pavement response under FWD dynamic load is simulated by SAPSI, and the deflection time-history of each sensor is the input to the VE backcalculation program. In order to compare the accuracy of this VE program against common elastic backcalculation program, the deflection basin is used to backcalculate the elastic modulus of each physical layer by MODCOMP5. The

actual pavement profile and the backcalculated result of each layer are listed in Table 38. The input and VE backcalculated deflection histories using E(t) are shown in Fig. 80; the input and VE backcalculated deflection histories using  $|E^*|$  are shown in Fig. 82; the input and backcalculated E(t) of the AC layer are shown in Fig. 81; and the input and backcalculated  $|E^*|$  of the AC layer are shown in Fig. 83.

Table 38: Basic information of Michigan pavement structure and backcalculated results

Physical Layer	Elastic Modulus (MPa (ksi))	Poisson Ratio	Thickness (m (in))	MODCOMP5 Backcalculation (MPa (ksi))	( )	E*  Backcalculation (MPa (ksi))
AC	$E^*(f)/E(t)$	0.35	0.178 (7.0)	4240 (614.9)	Fig. 81	Fig. 83
Base	206.8 (30.0)	0.35	1.321 (52)	206.2 (29.9)	208.6 (30.3)	208.7 (30.3)
Subgrade	310.3 (45.0)	0.45	Infinity	286.1 (41.5)	313.0 (45.4)	312.4 (45.3)

Table 38 shows the elastic modulus of base and subgrade layers are almost the same from VE backcalculation and MODCOMP5, although the VE backcalculation program gives slightly better results. However, only one modulus value is given in MODCOMP5 for the AC layer. The VE backcalculation program can overcome this problem and gives the AC modulus as a function of time or frequency.

## Deflection history simulation (E(t))

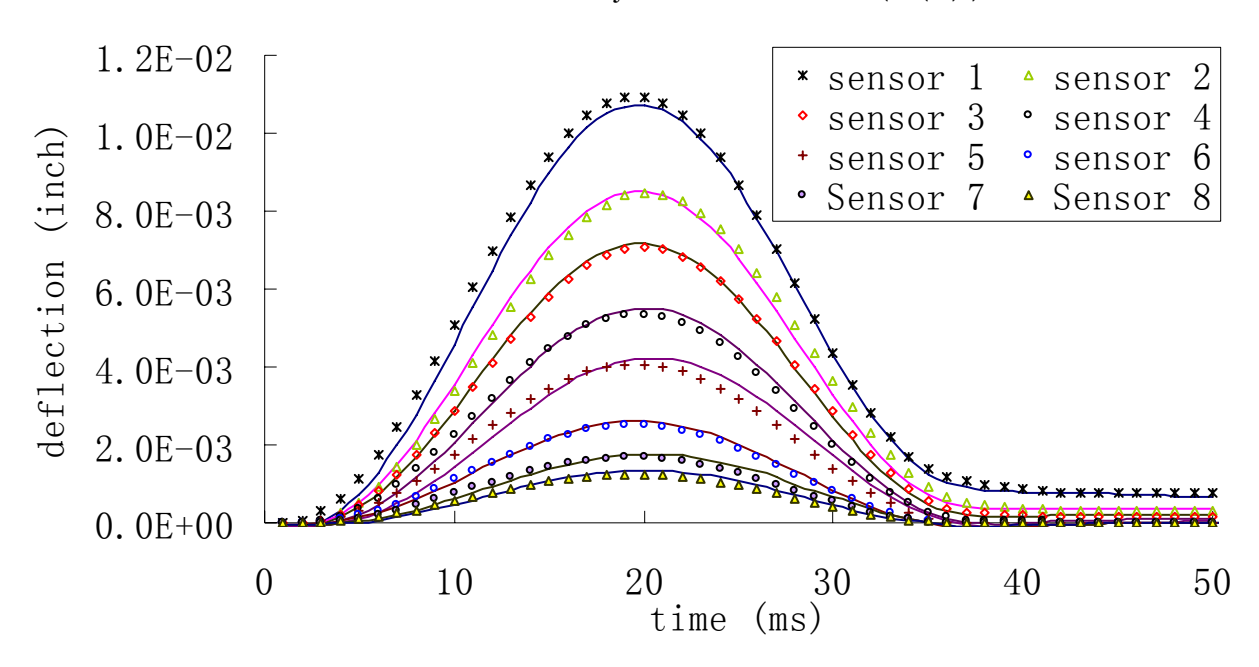


Figure 80: Input and simulated time-histories by backcalculation of E(t) in Michigan site (Solid lines represent the input deflection history, symbols represent the VE simulation)

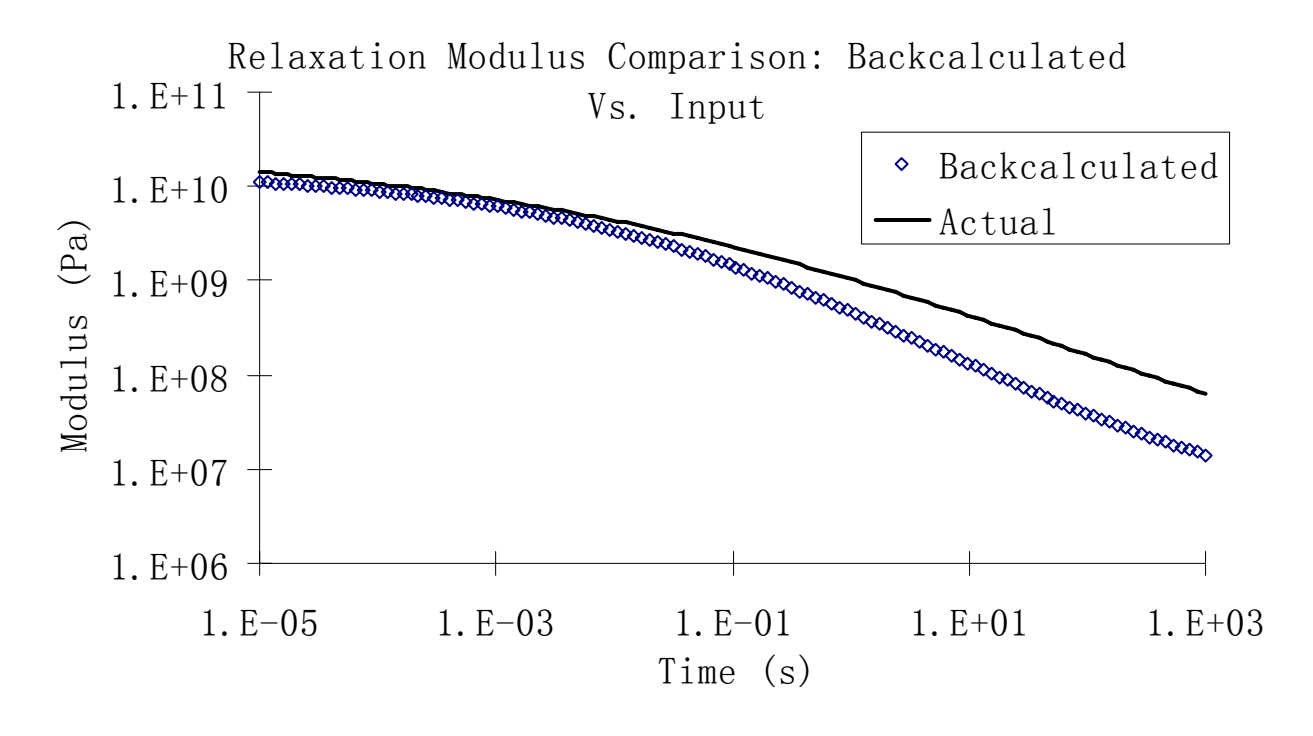


Figure 81: Input and backcalculated E(t) in Michigan site

Fig. 80 and 81 show good agreement between backcalculated and actual deflection time histories and E(t) curves. The difference between input and simulated time-history for sensor 1 is not significant, so the backcalculated and input E(t) mach well (Fig. 81), especially in the relevant time range 0.0001 - 0.1 s.

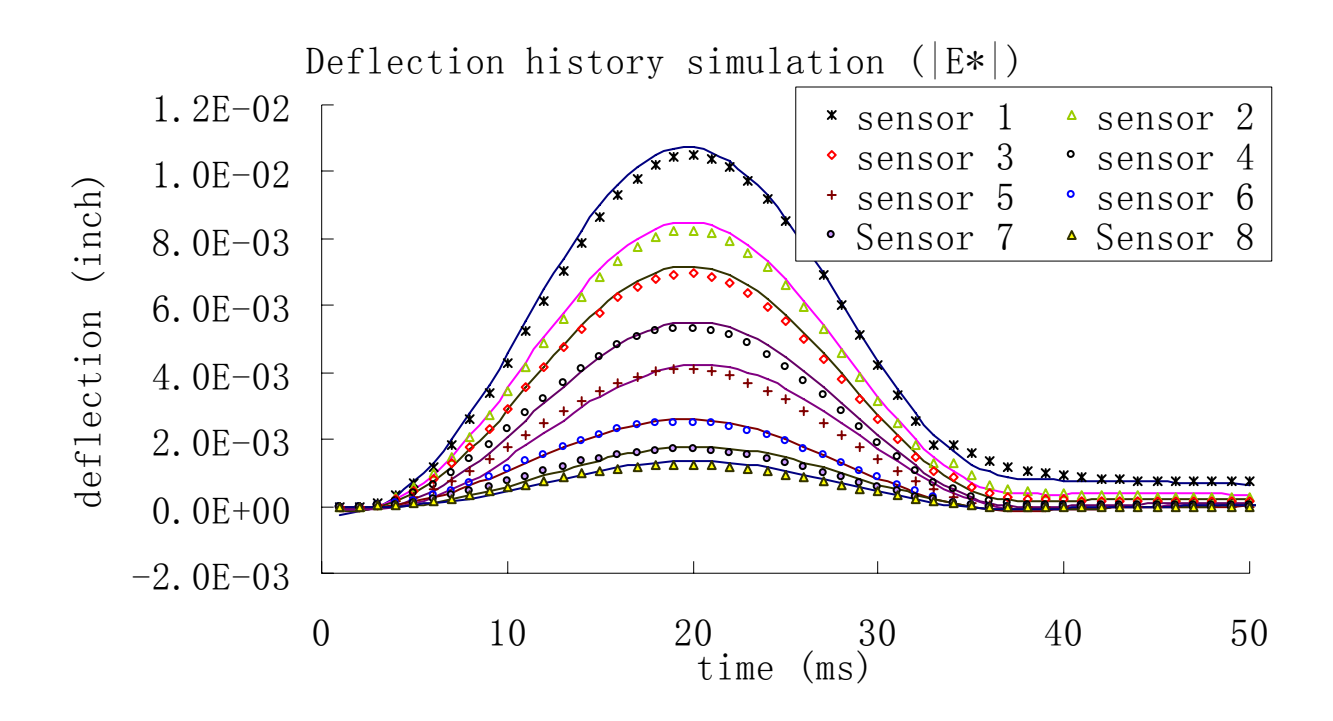


Figure 82: Input and simulated time-histories by backcalculation of  $|E^*|$  in Michigan site (Solid lines represent the input deflection history, symbols represent the VE simulation)

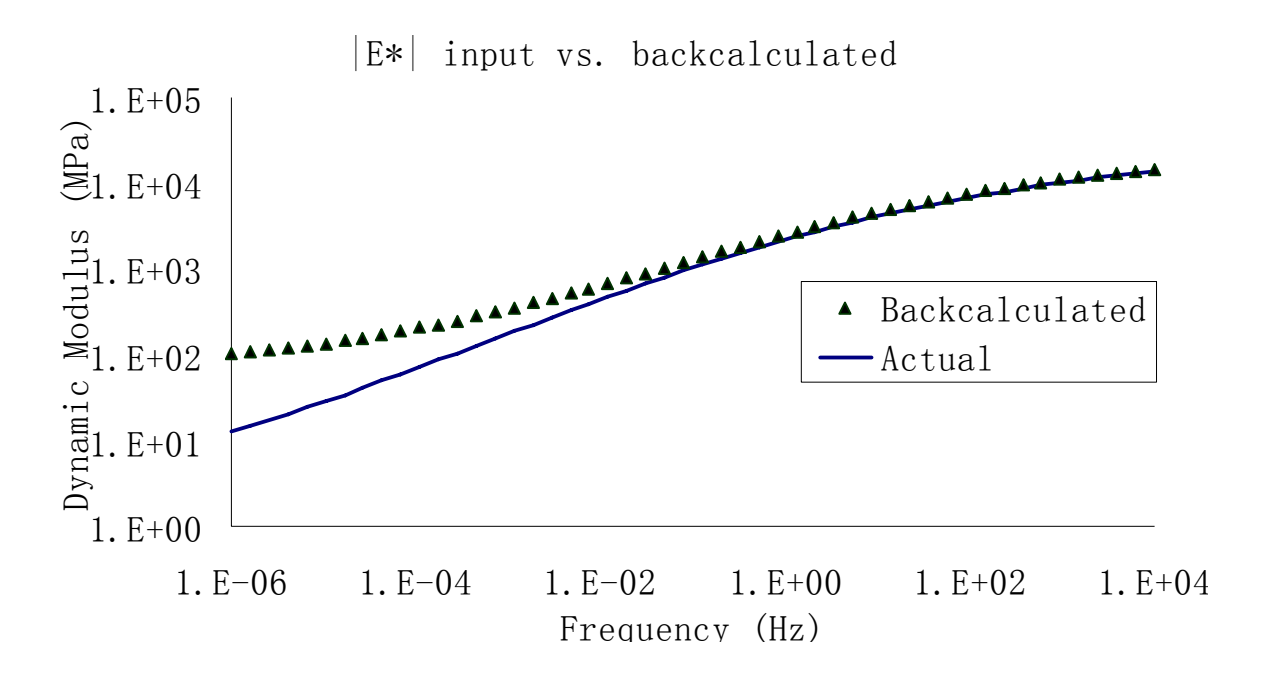


Figure 83: Input and backcalculated |E\*| in Michigan site

Fig. 82 and 83 illustrate good agreement between backcalculated and actual deflection time histories and |E\*| curves. The difference between input and simulated time-history for sensor 1 is good enough, so the backcalculated |E\*| function for the AC layer is very close to the input function in the concerned frequency range 10 to 10000 Hz.

In summary, the VE backcalculation program works well for both  $|E^*|$  and E(t) backcalculation, and the backcalculated results are to input deflection time-histories. The elastic moduli for the base and subgrade layer are very accurate, with an error of 1%, while the E(t) and  $|E^*|$  functions for AC layer match fairly well with the input function in SAPSI.

# 6.2.2.2 Example 6: Texas Site

A similar procedure is done for one pavement profile in Texas site, where there is a shallow stiff layer underneath. The actual pavement profile and the backcalculated result of each layer are

listed in Table 39. The input and VE backcalculated deflection histories using E(t) are shown in Fig. 84; the input and VE backcalculated deflection histories using  $|E^*|$  are shown in Fig. 86; the input and backcalculated E(t) of the AC layer are shown in Fig. 85; and the input and backcalculated  $|E^*|$  of the AC layer are shown in Fig. 87.

Table 39: Basic information of Texas pavement structure and backcalculated results

Physical Layer	Elastic Modulus (MPa (ksi))	Poisson Ratio	Thickness (m (in))	MODCOMP5 Backcalculation (MPa (ksi))	E(t) Backcalculation (MPa (ksi))	E*  Backcalculation (MPa (ksi))
AC	$E^*(f)/E(t)$	0.35	0.203 (8.0)	4206 (610.0)	Fig. 85	Fig. 87
Base	172.4 (25.0)	0.45	1.702 (67.0)	152.4 (22.1)	184.6 (27.0)	197.3 (28.6)
Subgrade	861.8 (125)	0.25	Infinity	500.6 (72.6)	903.9 (131.1)	887.7 (128.8)

Table 39 shows the elastic modulus of base and subgrade layers are almost the same from VE backcalculation and MODCOMP5, although the VE backcalculation program gives slightly better results. However, only one modulus value is given in MODCOMP5 for the AC layer. The VE backcalculation program can overcome this problem and gives the AC modulus as a function of time or frequency.

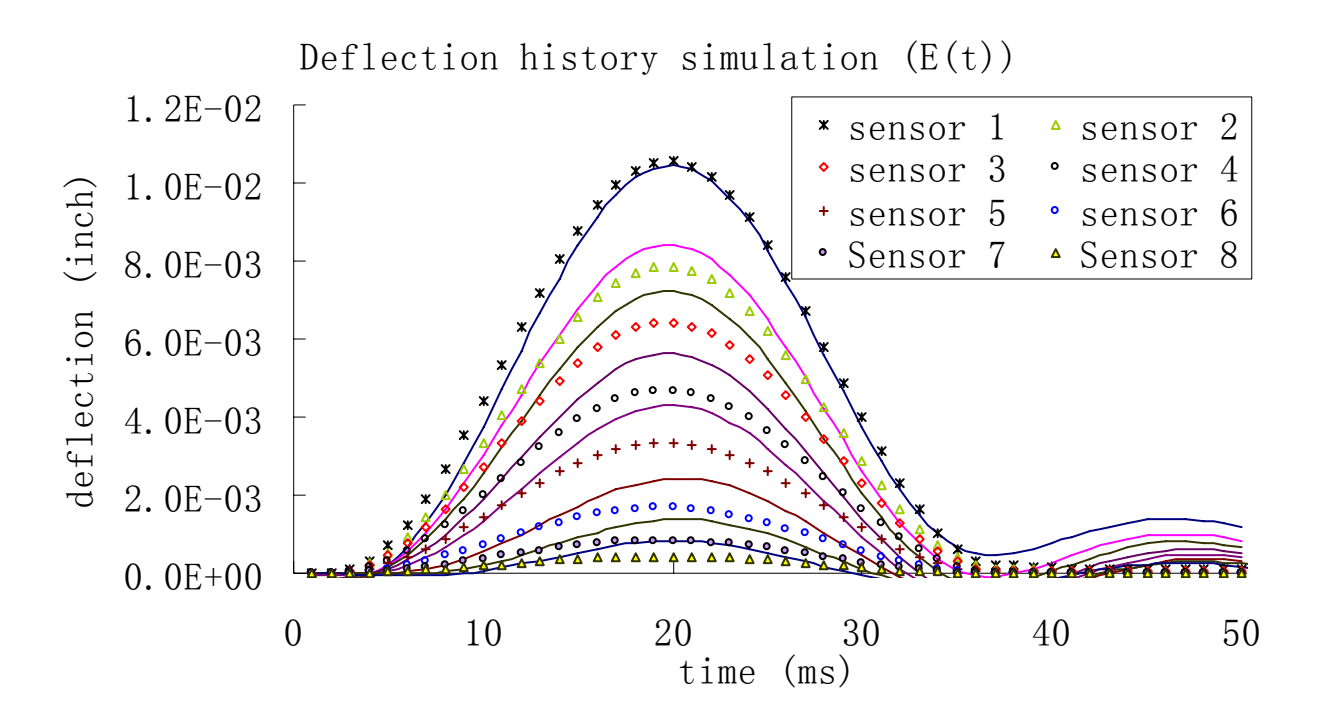


Figure 84: Input and simulated time-histories by backcalculation of E(t) in Texas site (Solid lines represent the input deflection history, symbols represent the VE simulation)

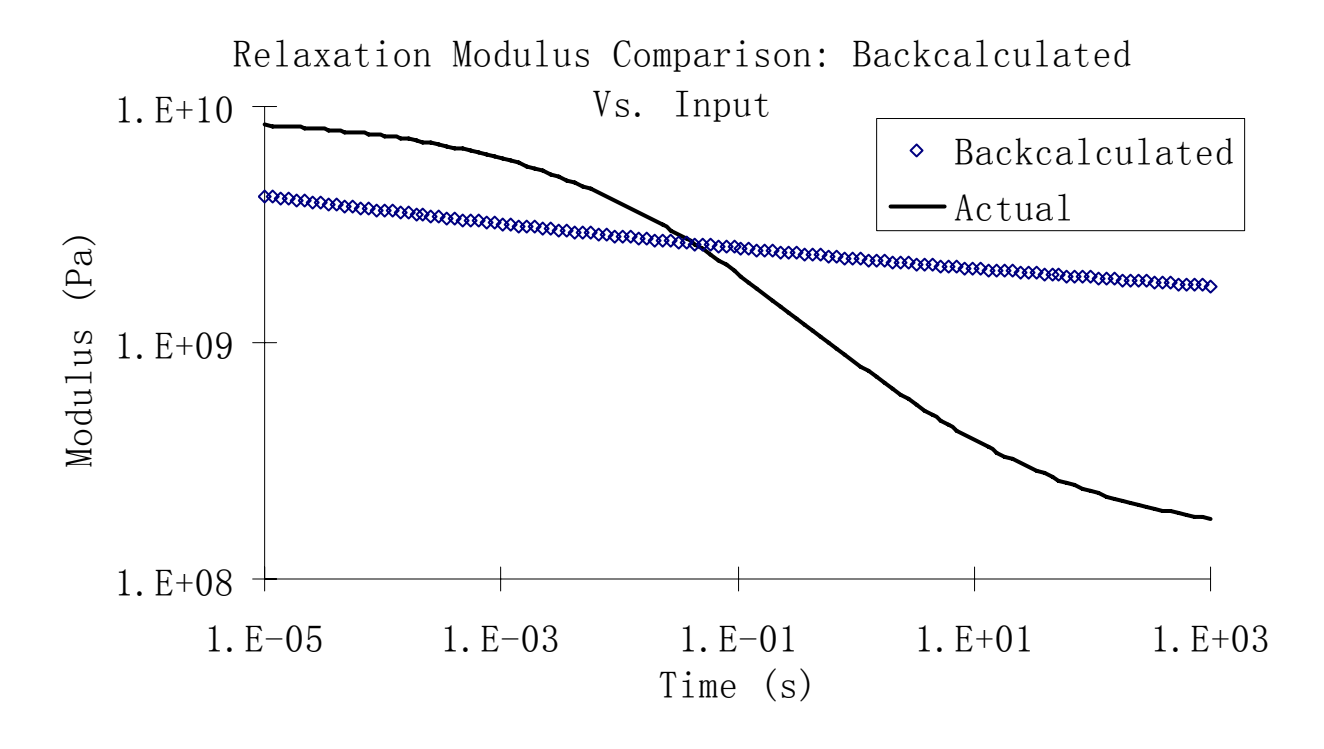


Figure 85: Input and backcalculated E(t) in Texas site

Fig. 84 and 85 illustrate that the backcalculated and actual deflection time histories and E(t) curves do not match well. The reason of this discrepancy is that the stiff layer traps the wave energy within the pavement structure, and thus it cannot be simulated by the layered VE solution.

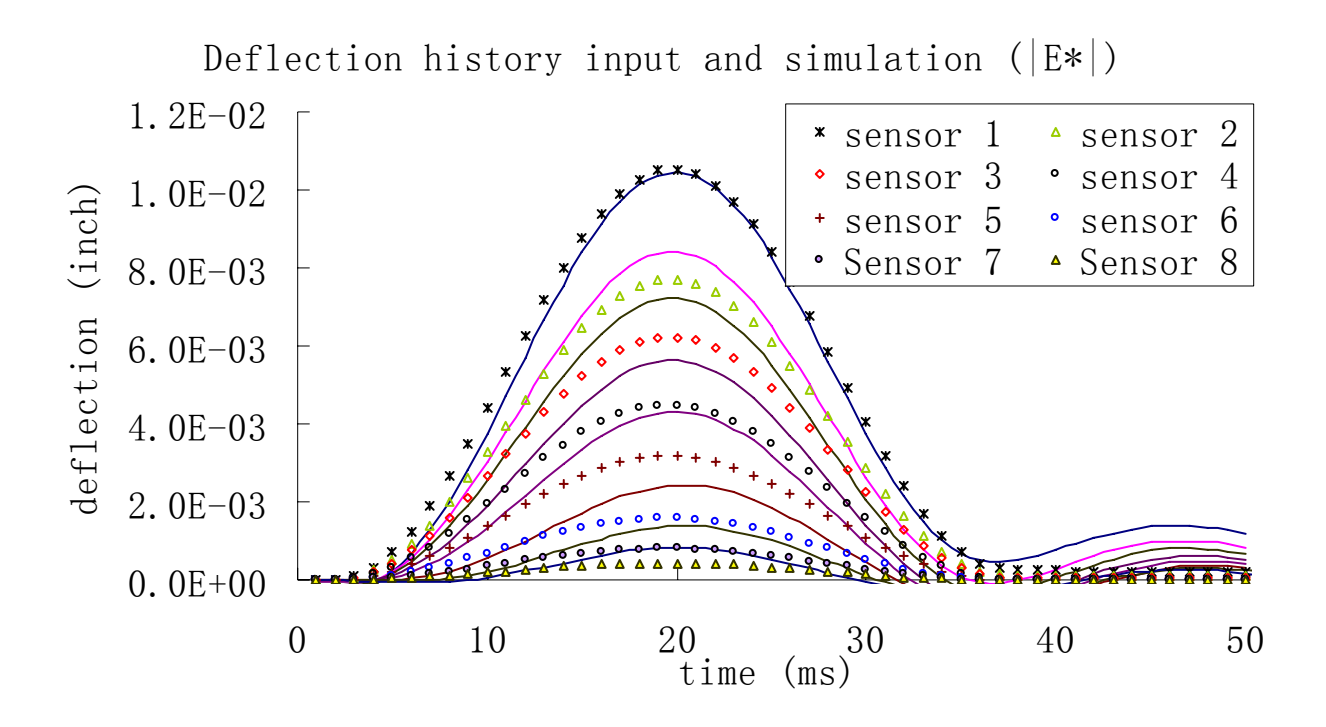


Figure 86: Input and simulated time-histories by backcalculation of  $|E^*|$  in Texas site (Solid lines represent the input deflection history, symbols represent the VE simulation)



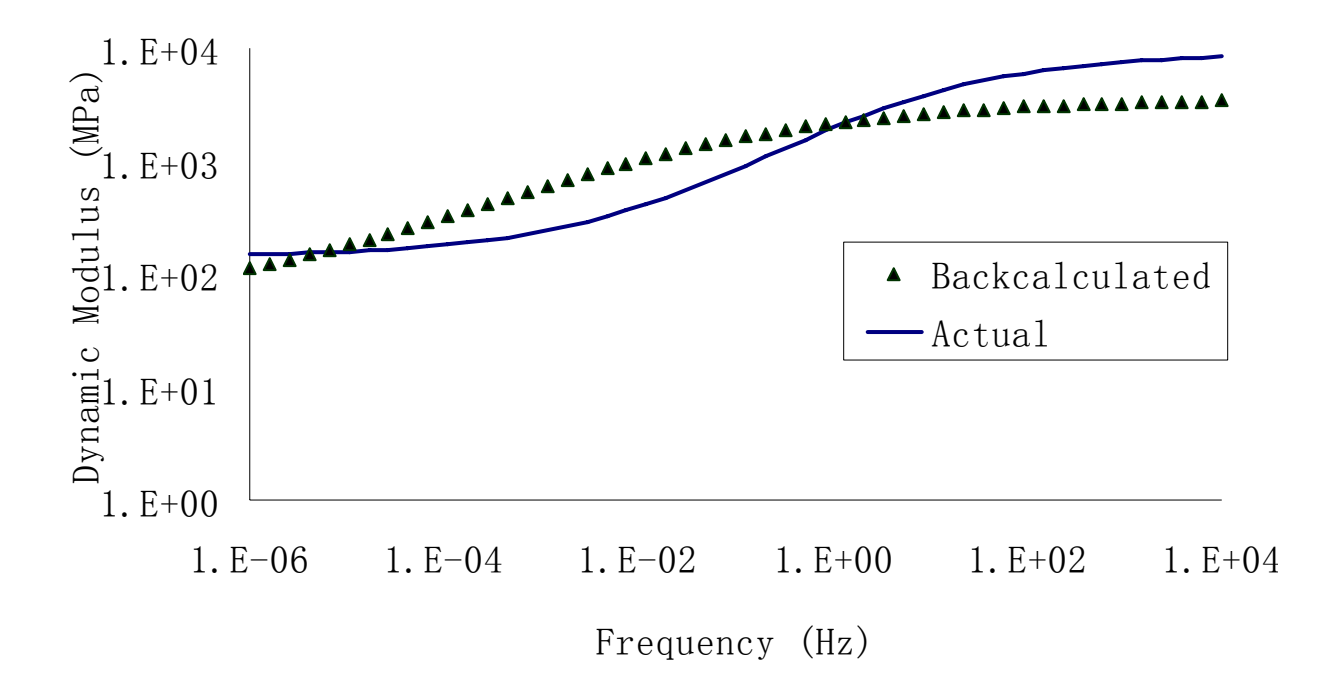


Figure 87: Input and backcalculated |E\*| in Texas site

Fig. 86 and 87 show that the backcalculated and actual deflection time histories and |E\*| curves do not match well, especially for the farther sensors. The difference between input and simulated time-history for sensor 1 is not significant in the loading region, but the differences between input and simulated time-histories for other sensors are very different. Even the base and subgrade elastic moduli are very similar, the backcalculation program is inappropriate in this example.

In summary, the VE backcalculation program does not work well, because there is shallow shift layer underneath. As discussed in Chapter 4, the VE forward solution cannot simulate the pavement response under FWD test if shallow bedrock exists. It is expected that the backcalculation program does not converge to the right value. Despites these issues, Table 39

shows the backcalculation algorithm converges to the right solution for the base and subgrade layers, with an error of about 3%.

#### **6.2.2.3** Example 7: Florence Site

A similar procedure is done for one pavement structure in Florence. The actual pavement profile and the backcalculated result of each layer are listed in Table 40. The input and VE backcalculated deflection time-histories using E(t) are shown in Fig. 88; the input and VE backcalculated deflection time-histories using  $E^*$  are shown in Fig. 90; the input and backcalculated E(t) of the AC layer are shown in Fig. 89; and the input and backcalculated  $E^*$  of the AC layer are shown in Fig. 91.

Table 40: Basic information of a Florence pavement structure and backcalculated result

Physical Layer	Elastic Modulus (MPa (ksi))	Poisson Ratio	Thickness (m (in))	MODCOMP5 Backcalculation (MPa (ksi))	E(t) Backcalculation (MPa (ksi))	E*  Backcalculation (MPa (ksi))
AC	$E^*(f)/E(t)$	0.35	0.102 (4.0)	7860.0 (1140)	Fig. 89	Fig. 91
Base	275.8 (40.0)	0.35	2.438 (96.0)	271.0 (39.3)	280.5 (40.7)	268.9 (39.0)
Subgrade	551.6 (80.0)	0.15	Infinity	385.4 (55.9)	477.2 (69.2)	657.6 (95.4)

Table 40 shows the elastic modulus of base layers are almost the same from both VE backcalculation and MODCOMP5. However, VE backcalculation gives better result for the modulus of the stabilized subgrade layer. Only one modulus value is given in MODCOMP5 for the AC layer. The VE backcalculation program can overcome this problem and gives AC modulus as a function of time or frequency.

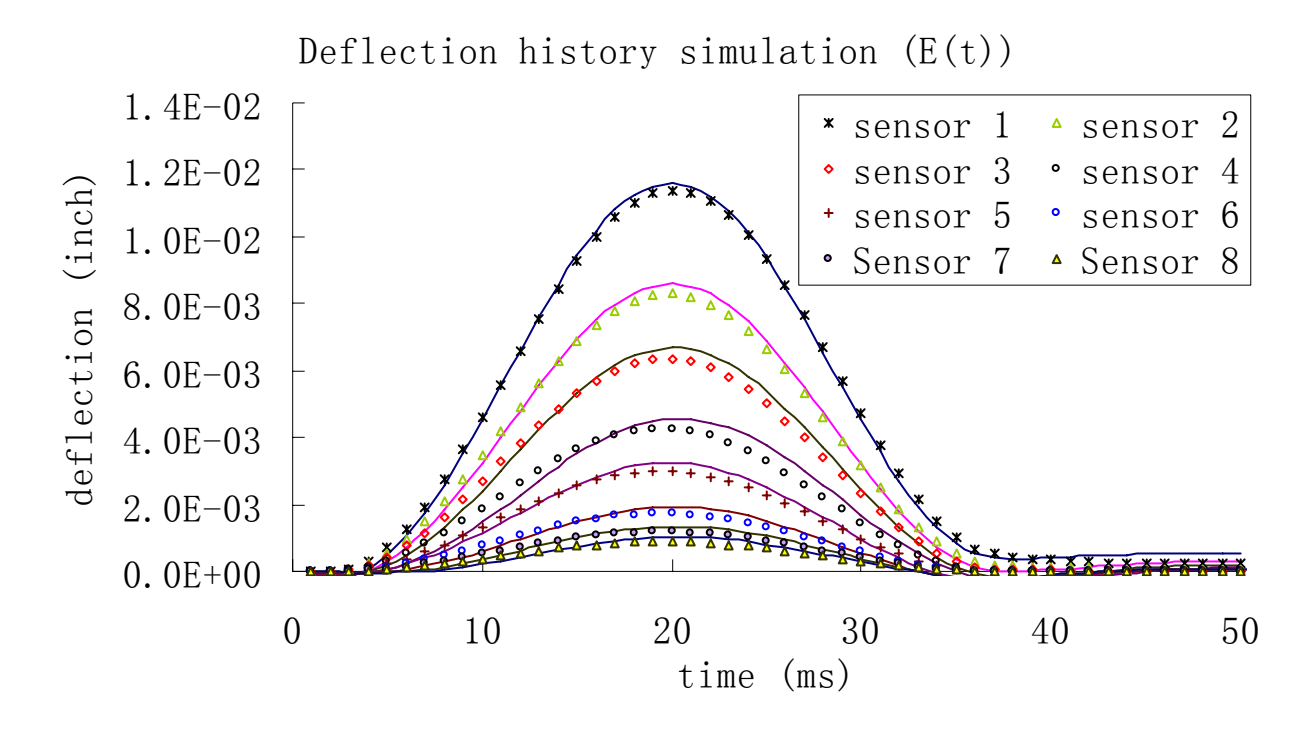


Figure 88: Input and backcalculation simulated time-histories using E(t) in Florence site (Solid lines represent the input deflection history, symbols represent the VE simulation)

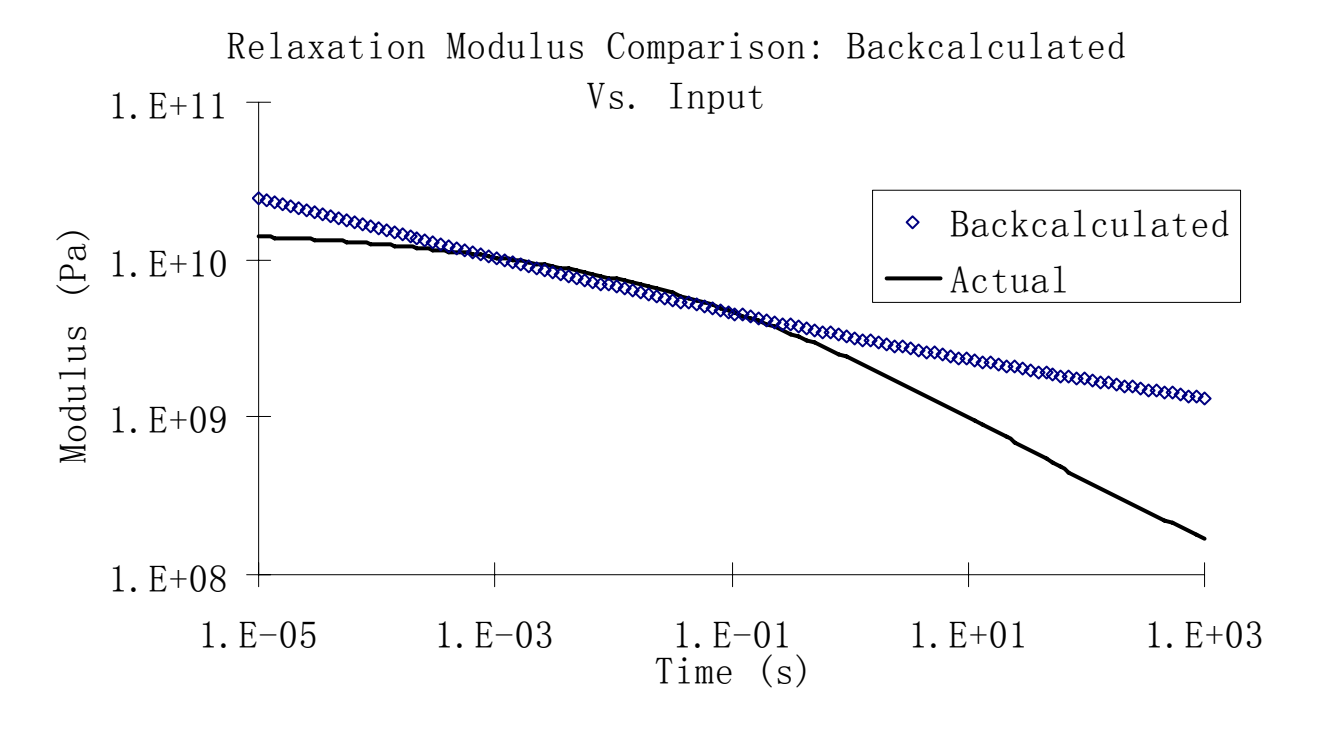


Figure 89: Input and backcalculated E(t) in Florence site

Fig. 88 and 89 illustrate good agreement between actual and backcalculated deflection time histories and E(t) curves. The backcalculated and input E(t) do not mach well for long-time part (Fig. 89). However, the backcalculated function is very close to the input function in the concerned time range 0.0001 - 0.1 s.

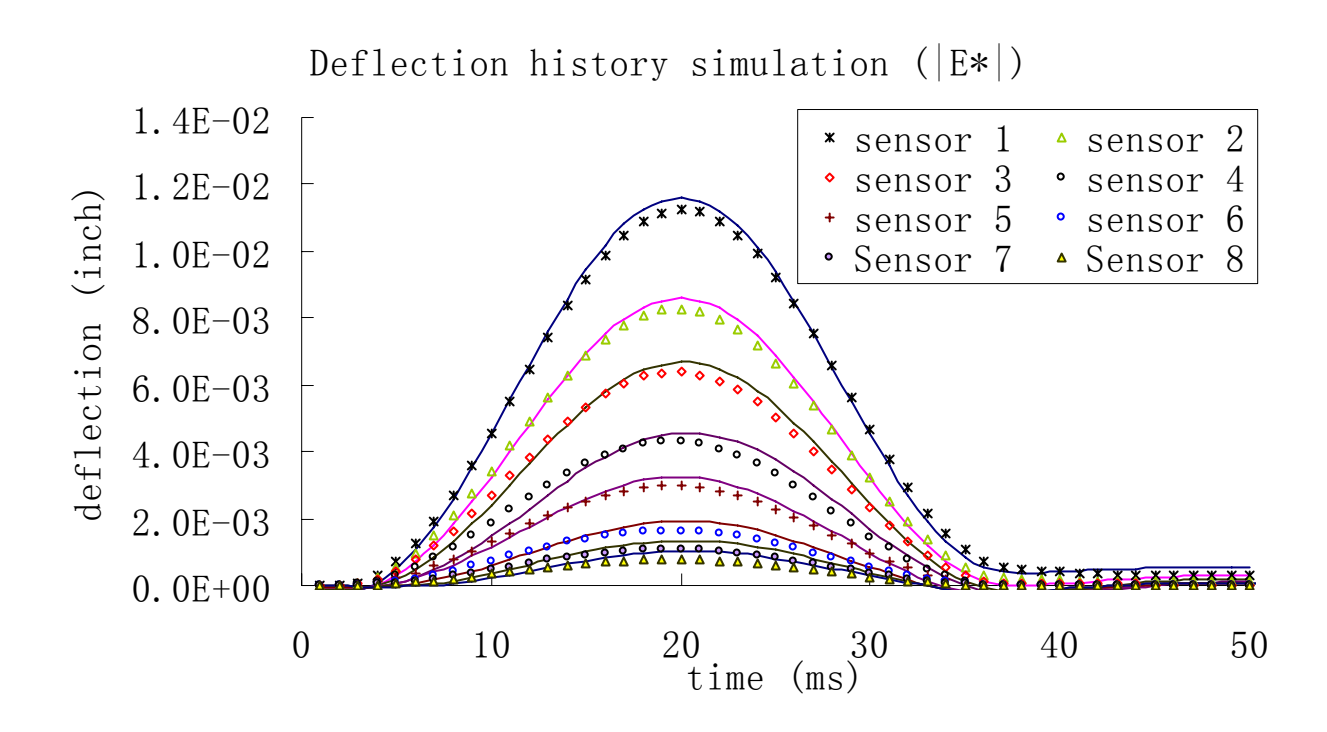


Figure 90: Input and backcalculation simulated time-histories using  $|E^*|$  in Florence site (Solid lines represent the input deflection history, symbols represent the VE simulation)

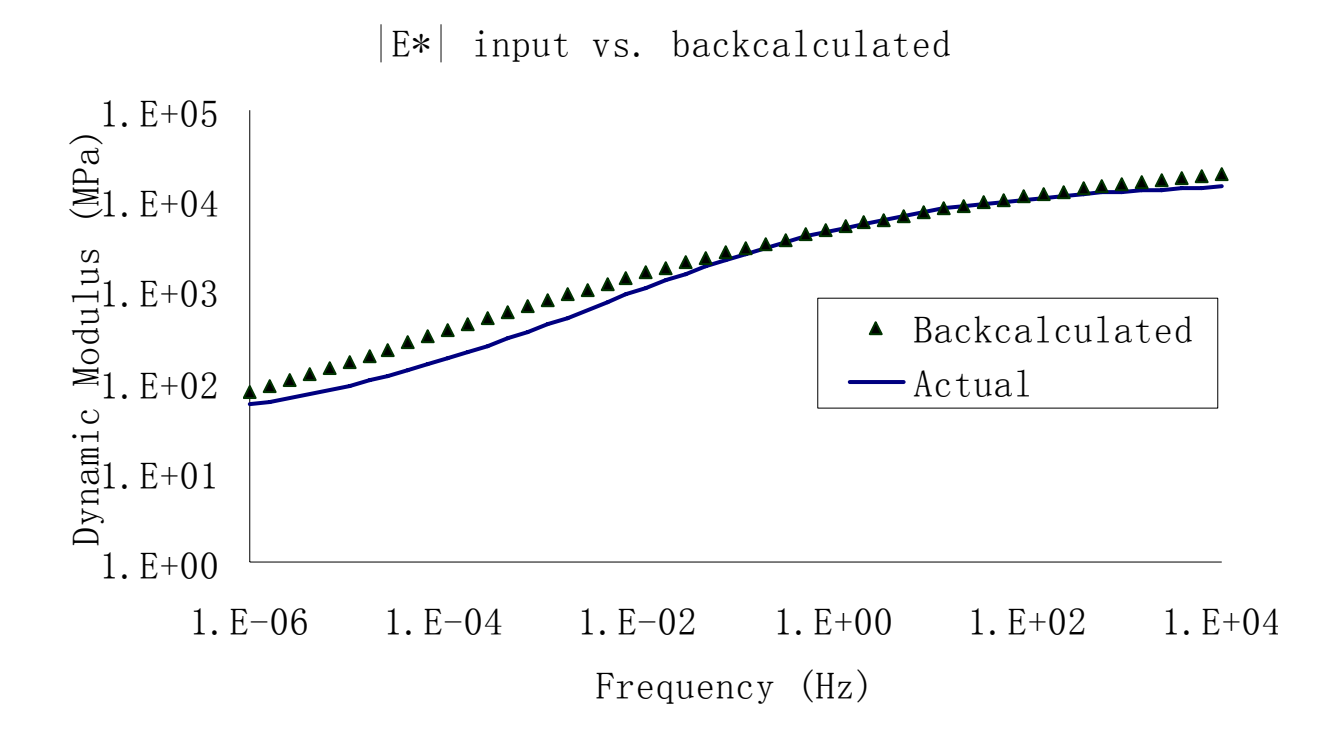


Figure 91: Input and backcalculated |E\*| in Florence site

Fig. 90 and 91 show reasonable agreement between the backcalculated and actual deflection time histories and  $|E^*|$  curves. The difference between input and simulated time-history for sensor 1 is not significant, and the backcalculated function for the AC layer is very close to the input function in concerned frequency range  $10 - 10000 \, \text{Hz}$ .

In summary, the VE backcalculation program works well for both |E\*| and E(t) backcalculation, and there is good agreement between input and backcalculated deflection time-histories. However, the elastic modulus of the subgrade layer is not as accurate, with an error around 20%, although it is much better than MODCOMP backcalculation result.

## 6.2.2.4 Example 8: Kansas Site

The actual pavement profile and the backcalculated result of each layer are listed in Table 41. The input and VE backcalculated deflection time-histories using E(t) are shown in Fig. 92; the input and VE backcalculated deflection time-histories using  $|E^*|$  are shown in Fig. 94; the input and backcalculated E(t) of the AC layer are shown in Fig. 93; and the input and backcalculated  $E^*$  of the AC layer are shown in Fig. 95.

Table 41: Basic information of a Kansas pavement structure and backcalculated result

Physical Layer	Elastic Modulus (MPa (ksi))	Poisson Ratio	Thickness (m (in))	MODCOMP5 Backcalculation (MPa (ksi))		E*  Backcalculation (MPa (ksi))
AC	$E^*(f)/E(t)$	0.30	0.102 (4.0)	5302.1 (769.0)	Fig. 93	Fig. 95
Base	413.7 (60.0)	0.35	0.356 (14.0)	447.5 (64.9)	469.1 (68.0)	513.6 (74.5)
Subgrade	482.6 (70.0)	0.45	Infinity	524.7 (76.1)	509.3 (73.9)	507.1 (73.5)

Table 41 shows the elastic modulus of base and subgrade layers are similar from both VE backcalculation and MODCOMP5, although the VE backcalculation program gives slightly better results for the subgrade layer, while MODCOMP5 gives better result for the base layer. However, only one modulus value is given in MODCOMP5 for the AC layer. The VE backcalculation program can overcome this problem and gives AC modulus as a function of time or frequency.

# Deflection history simulation (E(t))

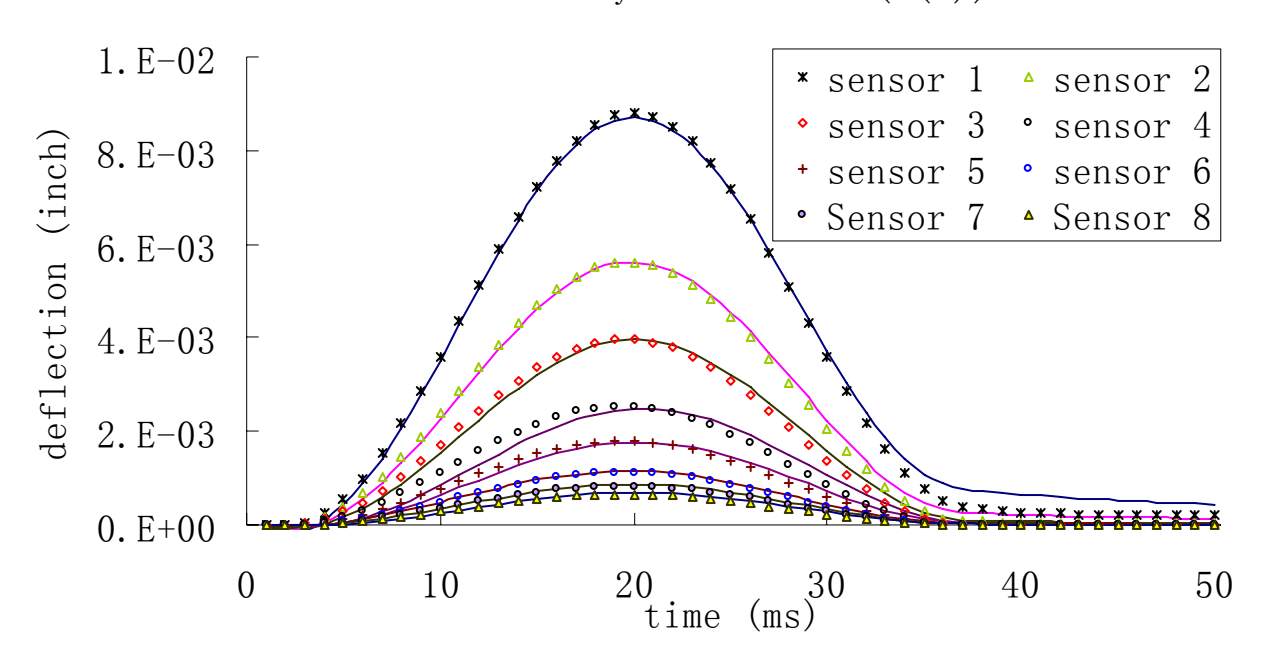


Figure 92: Input and simulated time-histories by backcalculation of E(t) in Kansas site (Solid lines represent the input deflection history, symbols represent the VE simulation)

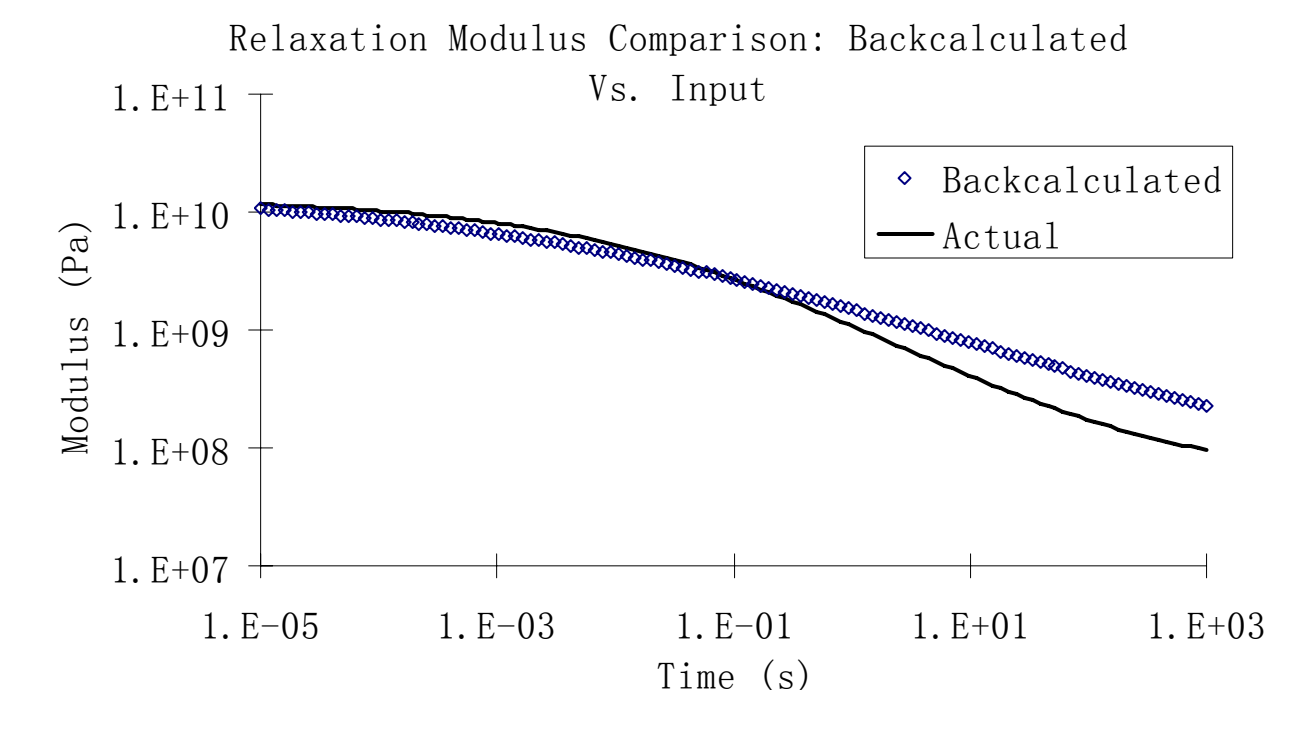


Figure 93: Input and backcalculated E(t) in Kansas site

Fig. 92 and 93 show good agreement between actual and backcalculated deflection time histories and E(t) curves. The backcalculated and input E(t) do not mach well for long-time part (Fig. 93). However, the backcalculated function is very close to actual input in the concerned time range 0.0001 - 0.1 s.

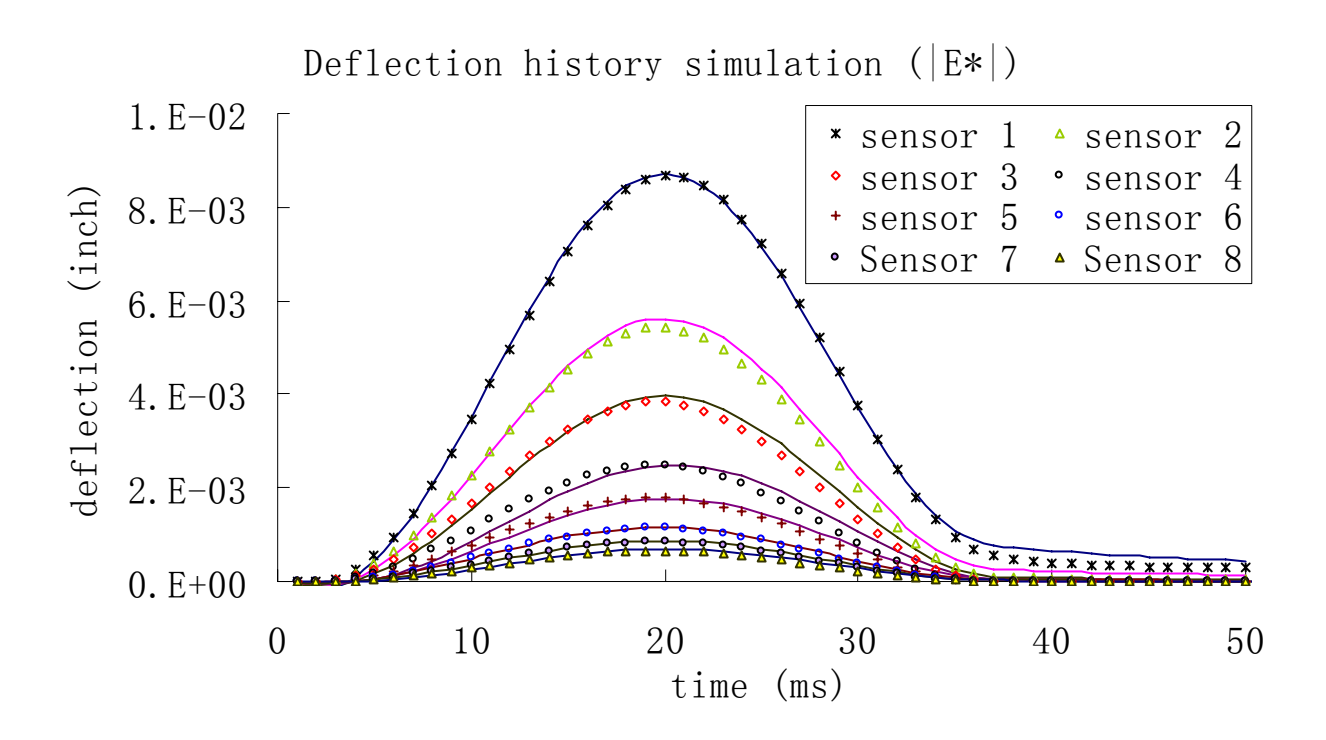


Figure 94: Input and simulated time-histories by backcalculation of  $|E^*|$  in Kansas site (Solid lines represent the input deflection history, symbols represent the VE simulation)

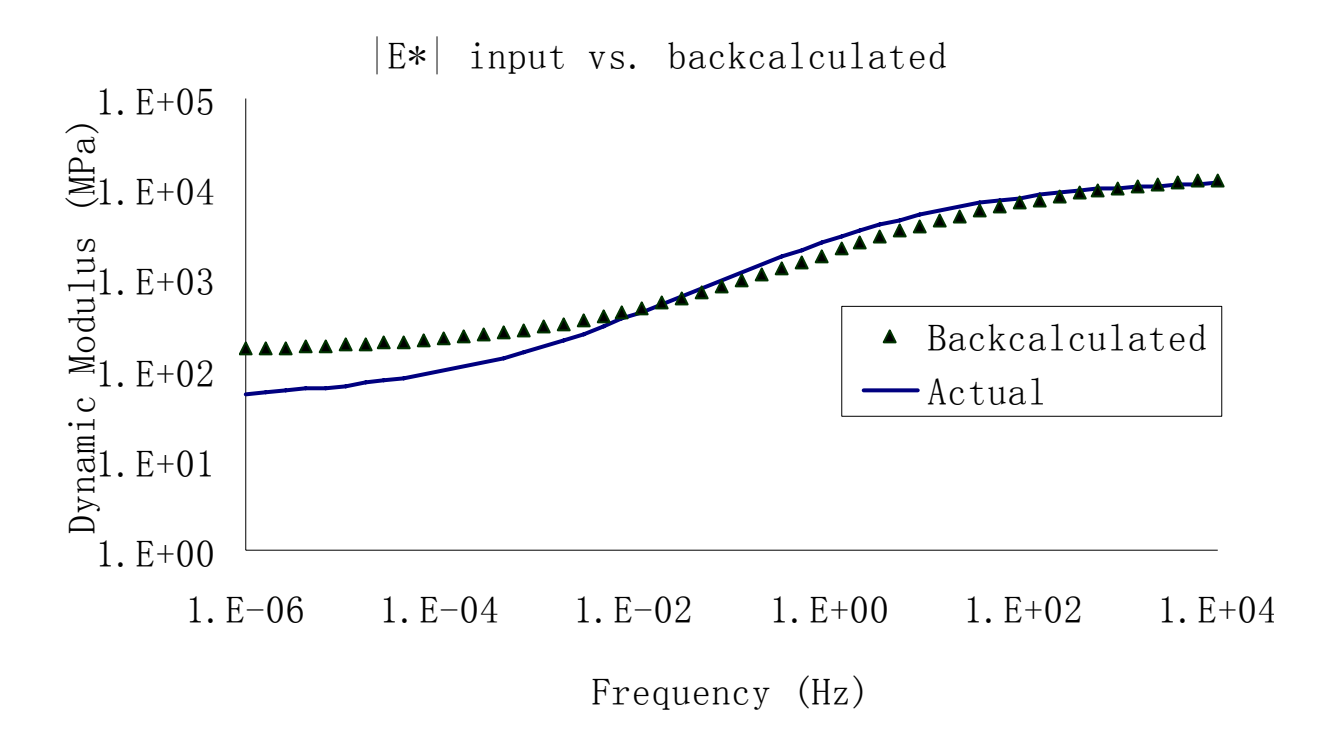


Figure 95: Input and backcalculated |E\*| in Kansas site

Fig. 94 and 95 illustrate good agreement between actual and backcalculated deflection time histories and  $|E^*|$  curves. There is almost no difference between input and simulated time-histories for sensor 1, except for the rest period, and the backcalculated  $|E^*|$  function for the AC layer is very close to the input function in the concerned frequency range 10 - 10000 Hz.

In summary, the VE backcalculation program works reasonably well for both  $|E^*|$  and E(t) backcalculation, and there is good match between input and backcalculated deflection time histories. However, the elastic modulus of the base layer using both  $|E^*|$  and E(t) backcalculation is not as accurate, with an error around 10 - 20%, although the modulus of the subgrade layer from VE backcalculation is slightly better than MODCOMP backcalculation result.

#### 6.2.2.5 Discussion

In this section, the accuracy of the backcalculation algorithm is investigated by 4 actual pavement structures with hypothetical FWD test. The backcalculation algorithm does not work well if there is shallow stiff layer underneath, as shown in the example of Texas site, although the AC property at the relevant time/frequency range is acceptable.

Since no experimental data available, the base and subgrade moduli are obtained from static/dynamic backcalculation (Ji, 2005), which may be questionable in cases. For example, the modulus of the base layer is lower than the modulus of the subgrade layer. This phenomena is unrealistic. The VE backcalculation algorithm is forced to simulate the static/dynamic backcalculation result, so the moduli for base and subgrade layers are not accurate in cases, with error as high as 20%. If the realistic pavement structure is assumed as in the previous section, the error of the elastic modulus for the base and subgrade should be much smaller.

The  $|E^*|$  and E(t) backcalculation results are very similar to each other. However, the E(t) backcalculation is much faster, as there is no need to convert from  $|E^*|$  to E(t). Therefore, E(t) backcalculation method is chosen as the VE backcalculation algorithm in future applications.

# 6.2.3 VE Backcalculation using Field FWD Test Data

Three examples of FWD test deflection histories were obtained from the FHWA's APT (Accelerated Pavement Testing) experiments at the Turner Fairbank Highway Research Center (TFHRC). Deflection histories from sensors and pavement structural information without modulus were entered into the VE backcalculation program to check the accuracy of the backcalculation results. Since tests locations are close to each other, the elastic modulus of the base and subgrade layers are expected to be very similar.

#### 6.2.3.1 FWD Test Conducted at L9S4

One record of the field FWD test was found for Lane 9 (AC mixture: SBS 64-40) in the FHWA's APT experiments. The pavement structure includes 6 in AC surface, 20 in Crushed Aggregate Base (CAB) and deep AASHTO A-4 subgrade soil (bedrock is at 25 ft from surface). The FWD test was conducted at around 10 AM on October 21, 2010, with air temperature of 14.5 °C. The dynamic modulus |E\*| was measured in the lab with the same AC mixture design, but compacted with standard gyratory compactor at 4% air void, and the temperature shift factor was also obtained from time-temperature superposition. The lab E(t) was mathmatically obtained from lab measured |E\*|, as discussed in Section 2.4. The actual modulus for each physical layer is unknown, the pavement structure and the backcalculated result of each layer are listed in Table 42. The input and VE backcalculated deflection time-histories of E(t) are shown in Fig. 96; the input and backcalculated E(t) of the AC layer are shown in Fig. 97.

Table 42: Basic information of L9S4 pavement structure and backcalculated result

Physical	Poisson's	Thickness	MODCOMP5	E(t) Backcalculation
Layer	Ratio	(m (in))	Backcalculation (MPa (ksi))	(MPa (ksi))
AC	0.35	0.152 (6.0)	4509 (654)	Fig. 97
Base	0.30	0.508 (20.0)	66.7 (9.7)	69.6 (10.1)
Subgrade	0.45	Infinity	132.4 (19.2)	135.8 (19.7)

Table 42 shows the elastic modulus of base and subgrade layers are similar from both VE backcalculation and MODCOMP5. However, only one modulus value is given in MODCOMP5 for the AC layer. The VE backcalculation program can overcome this problem and gives AC modulus as a function of time.

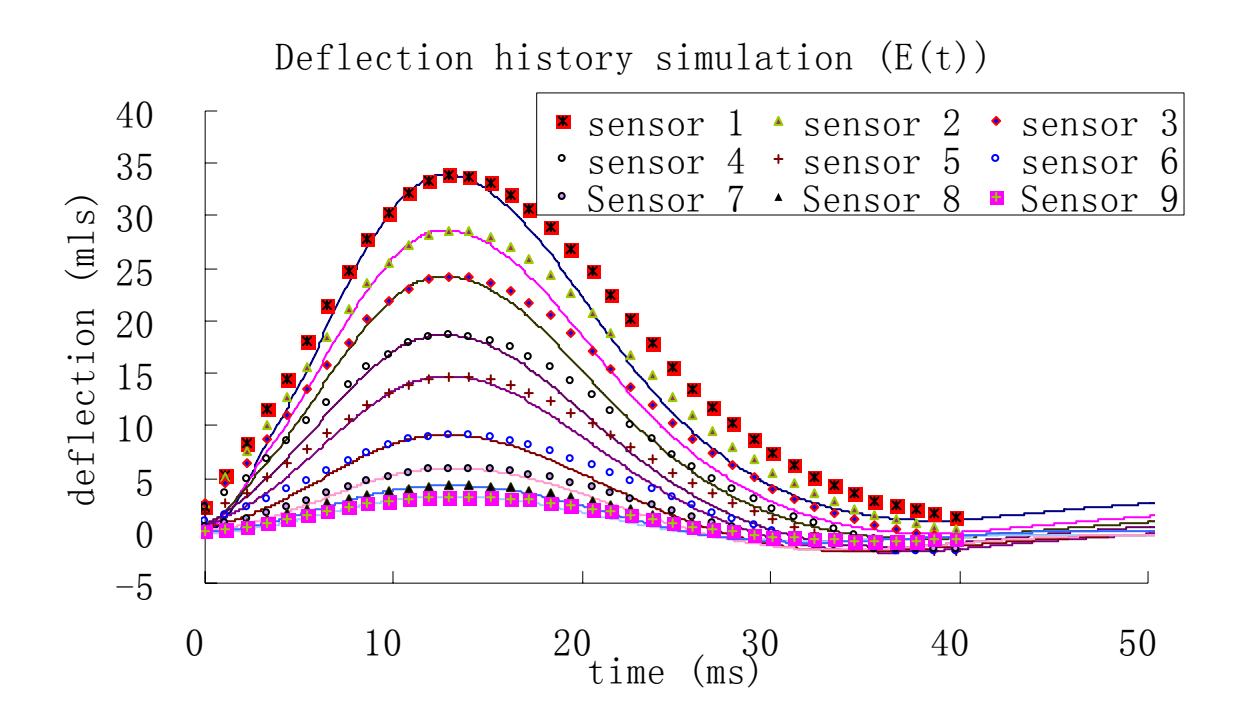


Figure 96: Input and simulated time-histories by backcalculation of E(t) in L9S4 site (Solid lines represent the input deflection history, symbols represent the VE simulation)

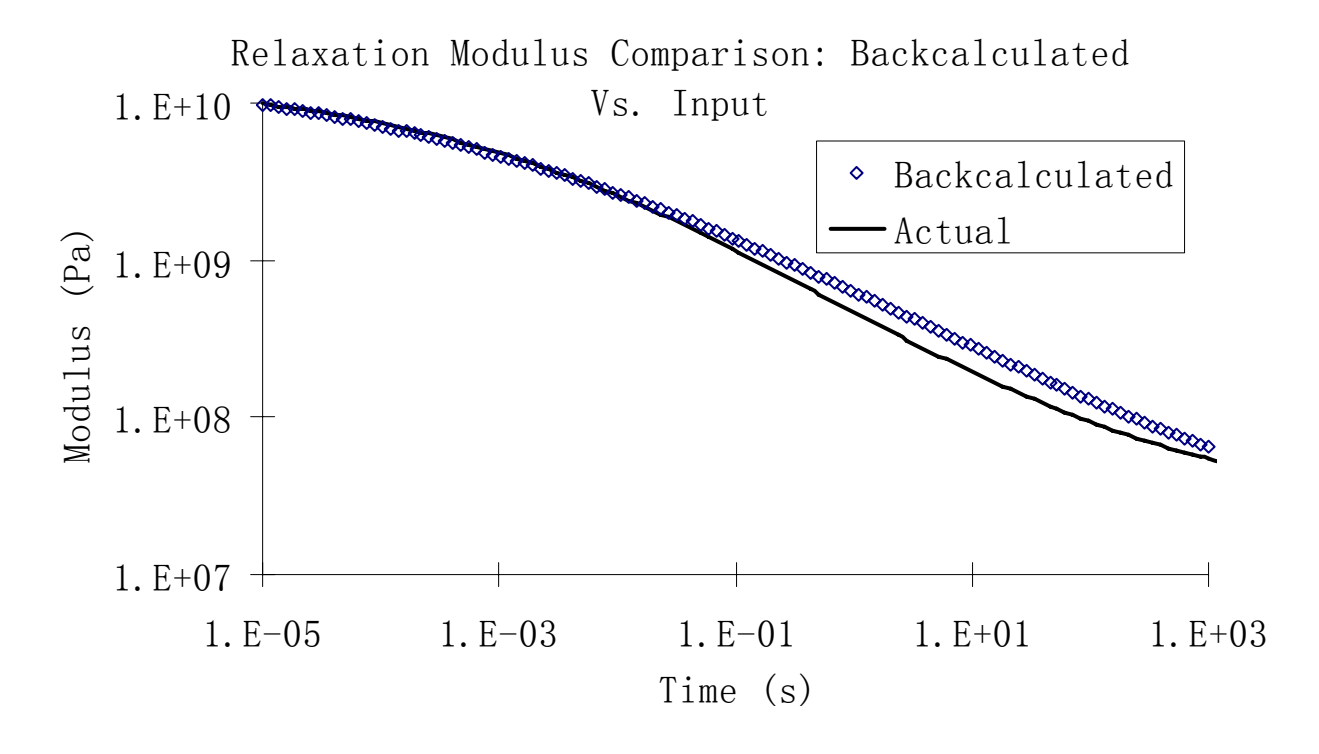


Figure 97: Input and backcalculated E(t) in L9S4 site

Fig. 96 shows that the predicted deflection time histories match very well with the actual values for all the sensors. Moreover, the backcalculated and input E(t) does mach well (Fig. 97), especially during the concerned time range 0.0001 - 0.1 s.

#### 6.2.3.2 FWD Test Conducted at L10S4

A second record of the field FWD test was found for Lane 10 (AC mixture: Air Blown) in the FHWA's APT experiments. The pavement structure is the same as for Lane 9 except for the AC materials. The FWD test was conducted at around 9 AM on October 21, 2010, with air temperature of 12.3 °C. The actual modulus for each physical layer is unknown, the pavement structure and the backcalculated results of each layer are listed in Table 43. The input and VE backcalculated deflection time-histories of E(t) are shown in Fig. 98; the input and backcalculated E(t) of the AC layer are shown in Fig. 99.

Table 43: Basic information of L10S4 pavement structure and backcalculated result

Physical	Poisson's	Thickness	MODCOMP5	E(t) Backcalculation
Layer	Ratio	(m (in))	Backcalculation (MPa (ksi))	(MPa (ksi))
AC	0.35	0.152 (6.0)	10687 (1550)	Fig. 99
Base	0.30	0.508 (20.0)	66.9 (9.7)	62.4 (9.0)
Subgrade	0.45	Infinity	178.6 (25.9)	176.6 (25.6)

Table 43 shows that the elastic moduli of the base and subgrade layers are similar between VE backcalculation and MODCOMP5. Only one modulus value is given in MODCOMP5 for the AC layer. The VE backcalculation program can overcome this problem and gives AC modulus as a function of time.

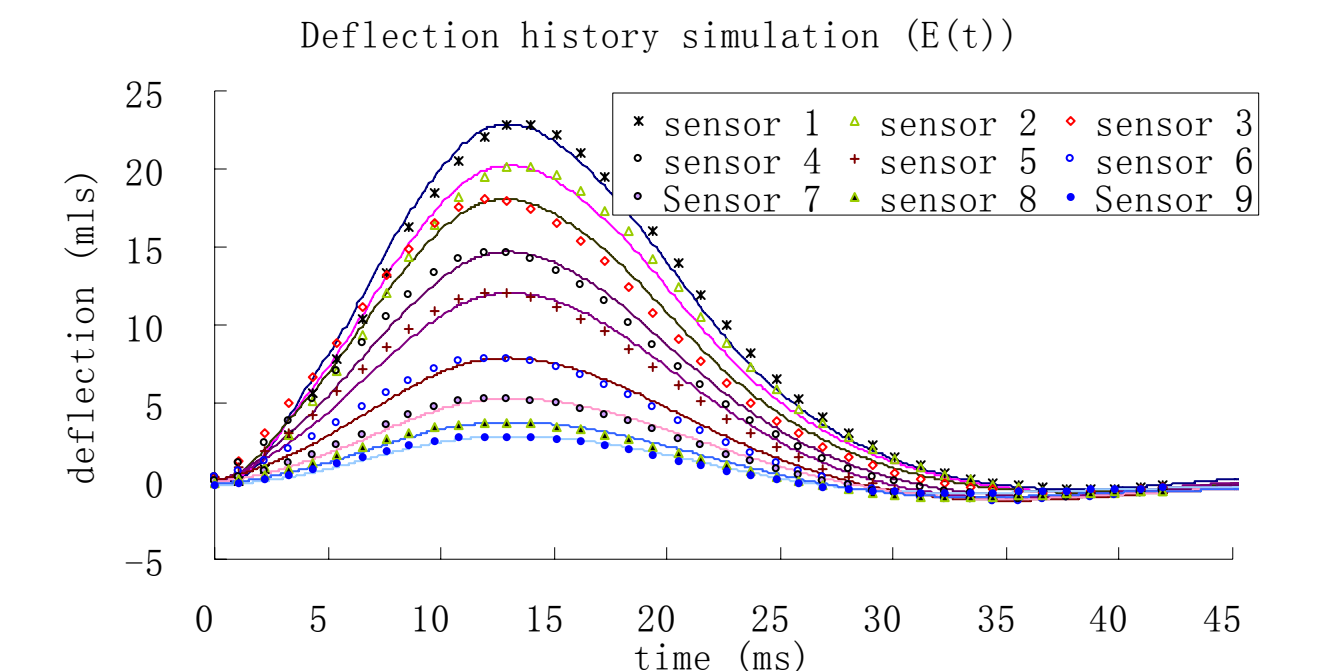


Figure 98: Input and simulated time-histories by backcalculation of E(t) in L10S4 site (Solid lines represent the input deflection history, symbols represent the VE simulation)

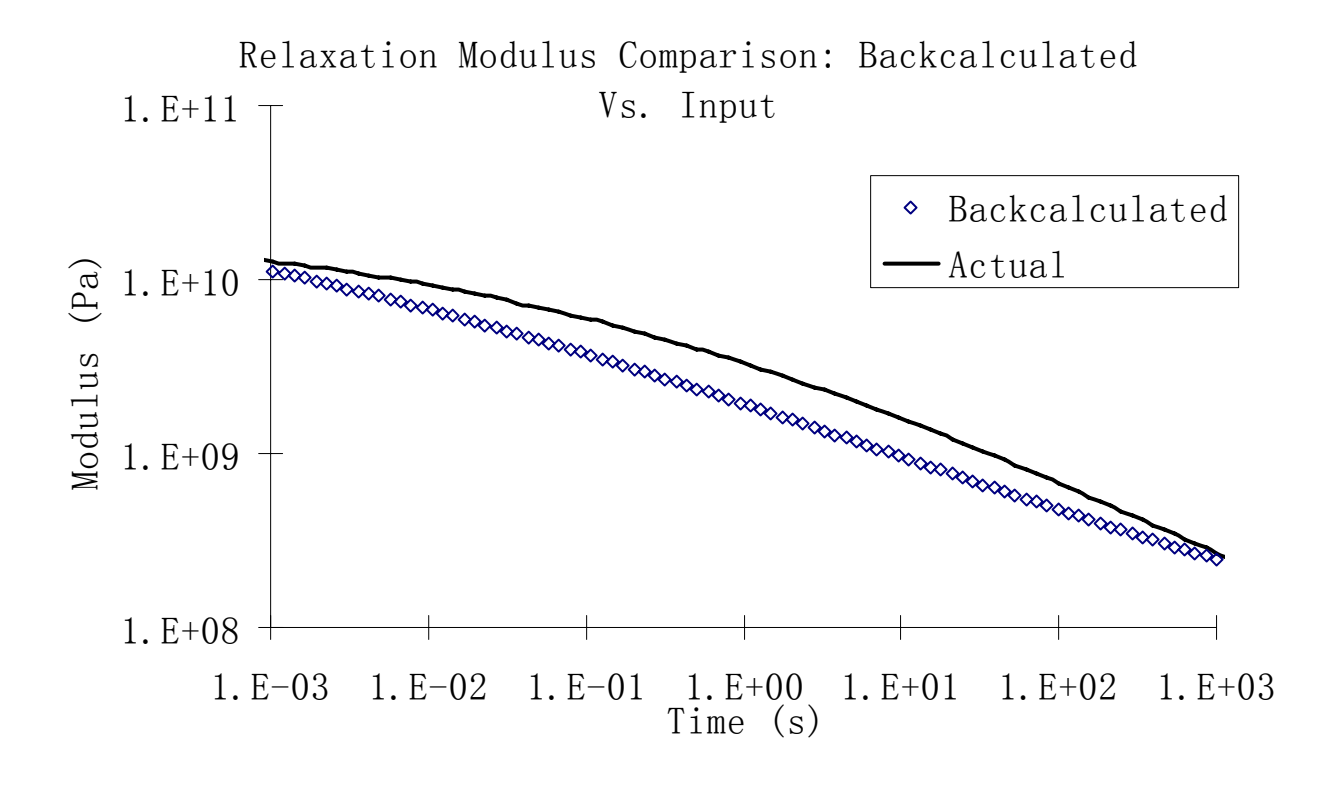


Figure 99: Input and backcalculated E(t) in L10S4 site

Fig. 98 shows an excellent match between actual and predicted deflection time histories using E(t) for every sensor. Figure 95 illustrates that the backcalculated E(t) function is very close to the lab-measured function, especially in the concerned time range 0.0001 - 0.1 s. It indicates there is a tiny shift between lab measured and backcalculated E(t), mainly because the temperature information may not be accurate.

#### 6.2.3.3 FWD Test Conducted at L11S4

A third record of the field FWD test was found for Lane 11 (AC mixture: SBS-LG) in the FHWA's APT experiments. The pavement structure is the same as that in the previous examples except for the AC mixture. The FWD test was conducted at around 2 PM on October 22, 2010, with AC surface temperature of 30.4°C; however, the record air temperature is 14.8°C. The actual modulus for each physical layer is unknown, the pavement structure and the backcalculated results of each layer are listed in Table 44. The input and VE backcalculated deflection time-histories using E(t) are shown in Fig. 100; the input and backcalculated E(t) of the AC layer are shown in Fig. 101.

Table 44: Basic information of L11S4 pavement structure and backcalculated result

Physical	Poisson's	Thickness	MODCOMP5	E(t) Backcalculation
Layer	Ratio	(m (in))	Backcalculation (MPa (ksi))	(MPa (ksi))
AC	0.35	0.152 (6.0)	2020 (293)	Fig. 101
Base	0.30	0.508 (20.0)	95.8 (13.9)	101.4 (14.7)
Subgrade	0.45	Infinity	178.6 (25.9)	142.0 (20.6)

Table 44 shows the elastic modulus of base and subgrade layer from VE backcalculation are very similar as the MODCOMP5 result. It can be noted that MODCOMP5 results are slightly more consistent since the pavement structure is the same as that from the previous examples in terms of base and subgrade materials.

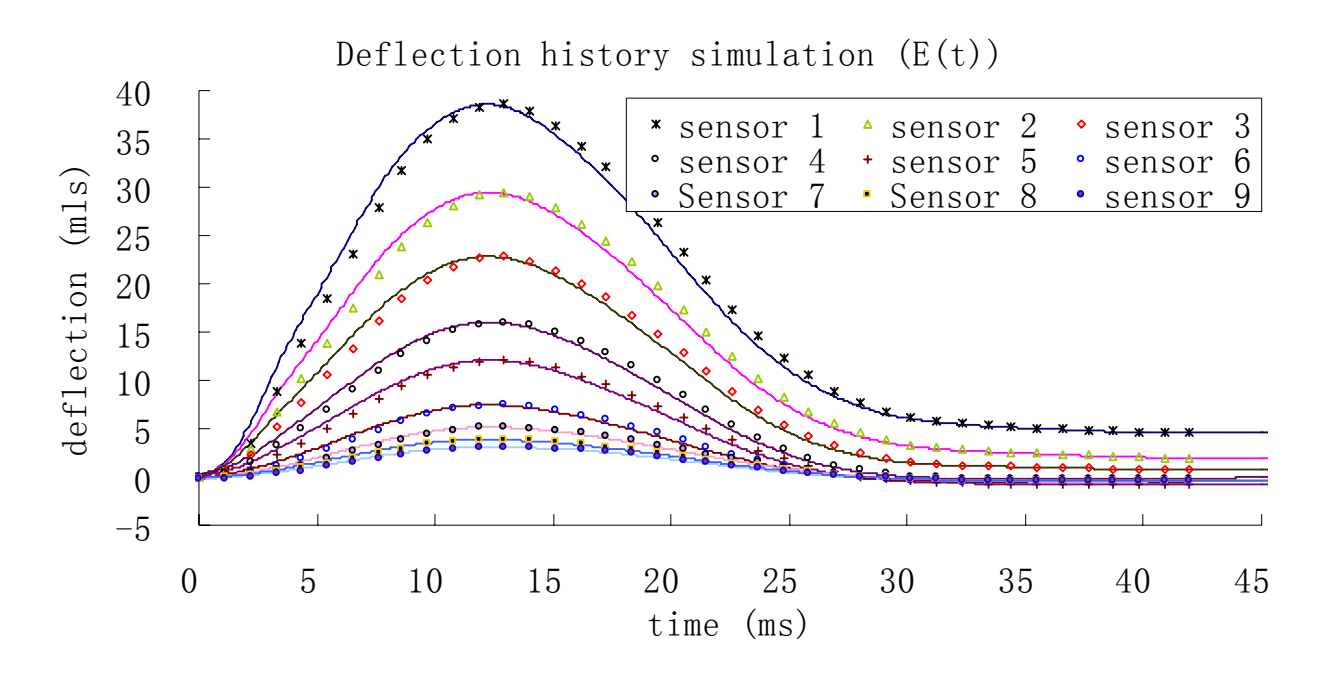


Figure 100: Input and simulated time-histories by backcalculation of E(t) in L11S4 site (Solid lines represent the input deflection history, symbols represent the VE simulation)

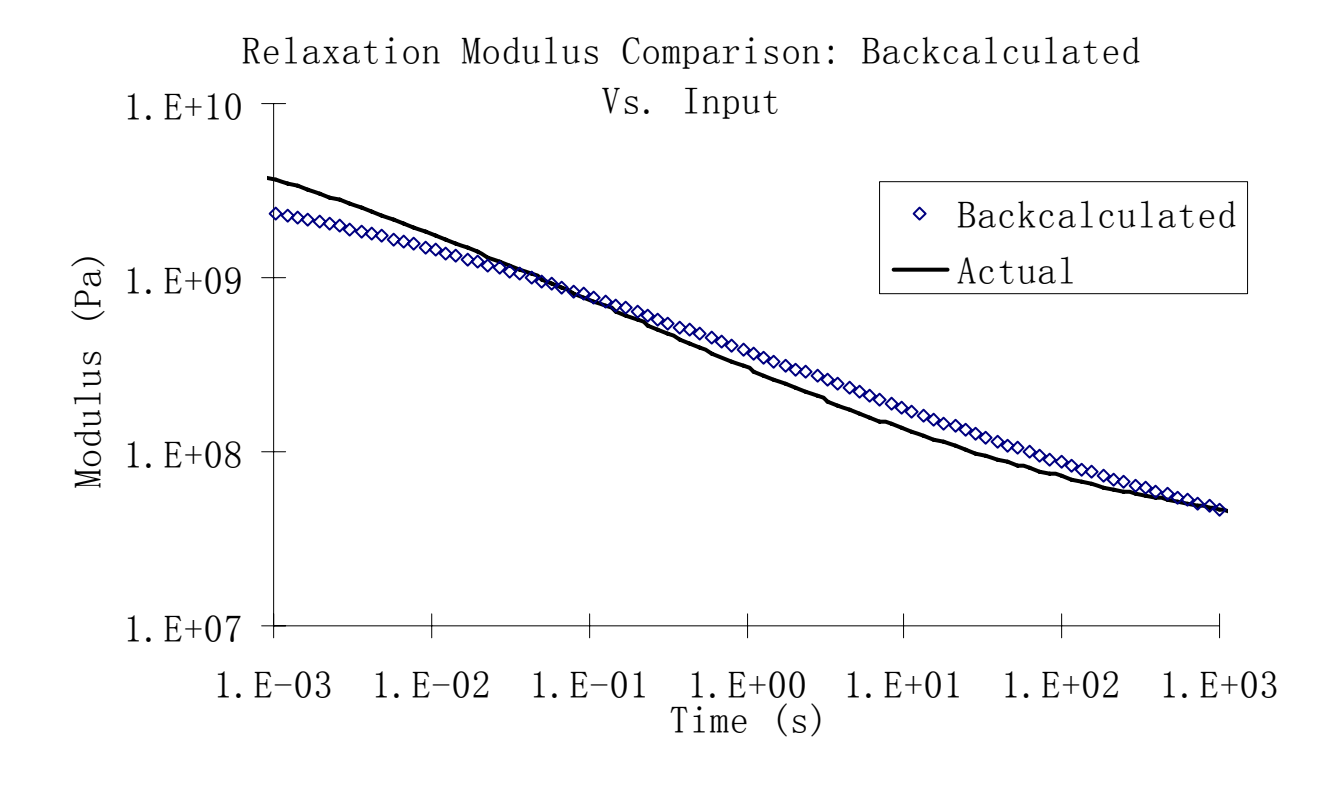


Figure 101: Input and backcalculated E(t) in L11S4 site

Fig. 100 shows that the predicted deflection time histories match very well with the actual values for all the sensors. Moreover, the backcalculated and input E(t) matches reasonably well (Fig. 101), especially during the concerned time range 0.0001 - 0.1 s.

#### 6.2.3.4 Discussion

Field FWD tests results indicate the backcalculation algorithm is appropriate in some cases, especially for the concerned reduced time range 0.0001 - 0.1 s. In other cases, the VE backcalculation algorithm does not work well, because of the data measurement issues as well as the insufficient information on the temperature profile of the AC layer. It is noted that the temperature of the AC layer can have a significant effect on the response and thus the backcalculated values. If better data acquisition and better interpretation of the FWD test data are available, the backcalculation results should be better (Kutay et al, 2011).

#### 6.3 Sensitivity Analysis for the AC Layer

The base and subgrade moduli are very sensitive in the backcalculation program, and the time efficiency is low if the base and subgrade moduli are calculated in the VE backbacalculation algorithm. Thus, given that the focus of this dissertation is the backcalculation of E(t) and  $|E^*|$ , the base and subgrade moduli are assumed to be known, and only AC unknown function is considered in the sensitivity analysis. The base modulus is typically assumed higher than the subgrade modulus, to simulate realistic pavement structures.

Four hypothetical pavement structures are given in Table 45. The effect of errors from deflection measurement and sampling time, and layer thickness are considered for the sensitivity analysis in the VE backcalculation program. The sampling time is investigated in terms of (1)

time shift of the entire deflection impulse, and (2) expansion/contraction of the deflection pulse in the post-peak zone. Illustrations of both errors in sampling time are shown below in Fig. 102 and Fig. 103. Both dynamic modulus mastercurve |E\*| and relaxation modulus E(t) for the AC layer are independently backcalculated, while assuming the elastic moduli of the base and subgrade layers are known.

Table 45: Layer information of each pavement structure for sensitivity analysis

Case	Physical	Elastic Modulus	Thickness	Poisson's
	Layer	(MPa (ksi))	(m (in))	Ratio
A	AC	Experimental Data	0.152 (6.0)	0.35
	Base Layer	206.9 (30.0)	0.610 (24.0)	0.30
	Subgrade Layer	34.5 (5.0)	Infinity	0.45
В	AC	Experimental Data	0.178 (7.0)	0.35
	Base Layer	344.8 (50.0)	0.152 (6.0)	0.40
	Subbase Layer	137.9 (20.0)	1.143 (45.0)	0.40
	Subgrade Layer	68.9 (10.0)	Infinity	0.45
С	AC	Experimental Data	0.203m (8.0)	0.35
	Base Layer	344.8 (50.0)	0.381 (15.0)	0.40
	Subgrade Layer	68.9 (10.0)	1.397 (55.0)	0.45
	Bedrock	6895.0 (1000.0)	Infinity	0.25
D	AC	Experimental Data	0.102 (4.0)	0.35
	CTB Base Layer	4998.9 (725.0)	0.152 (6.0)	0.20
	Subgrade Layer	68.9 (10.0)	Infinity	0.45

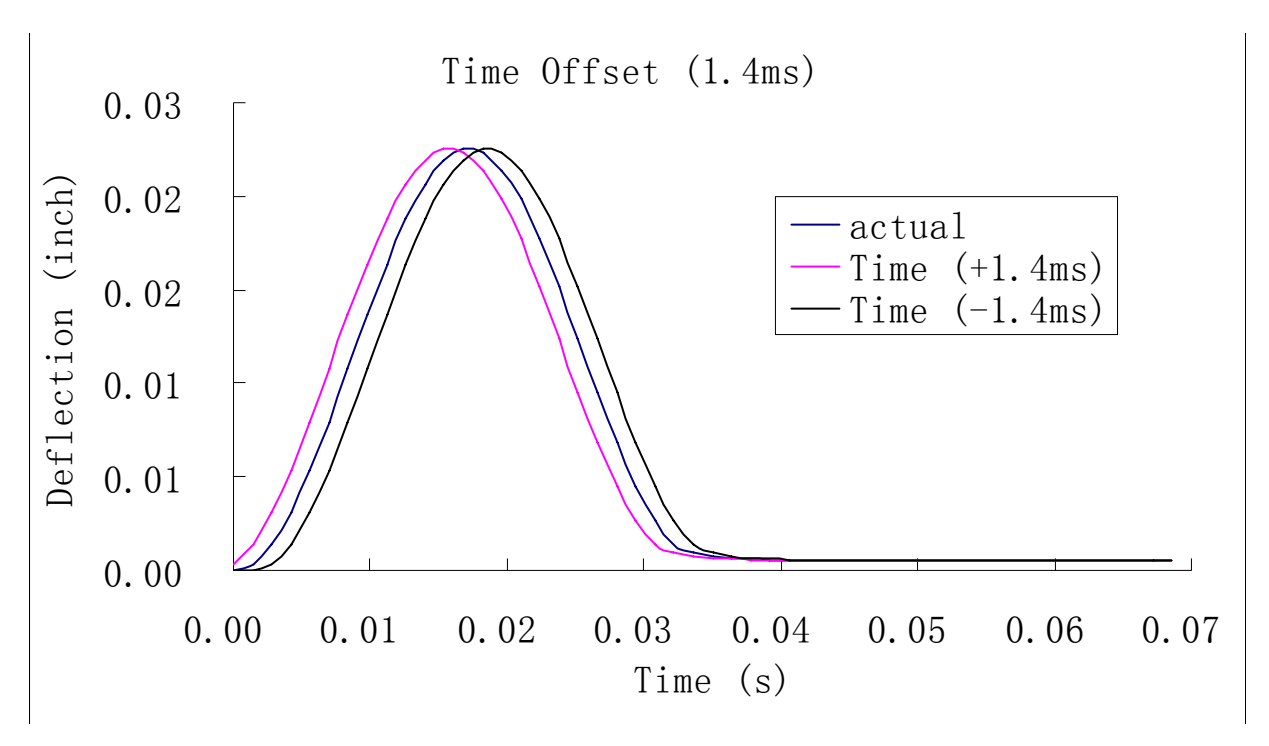


Figure 102: Error caused by time shift of entire pulse for one sensor

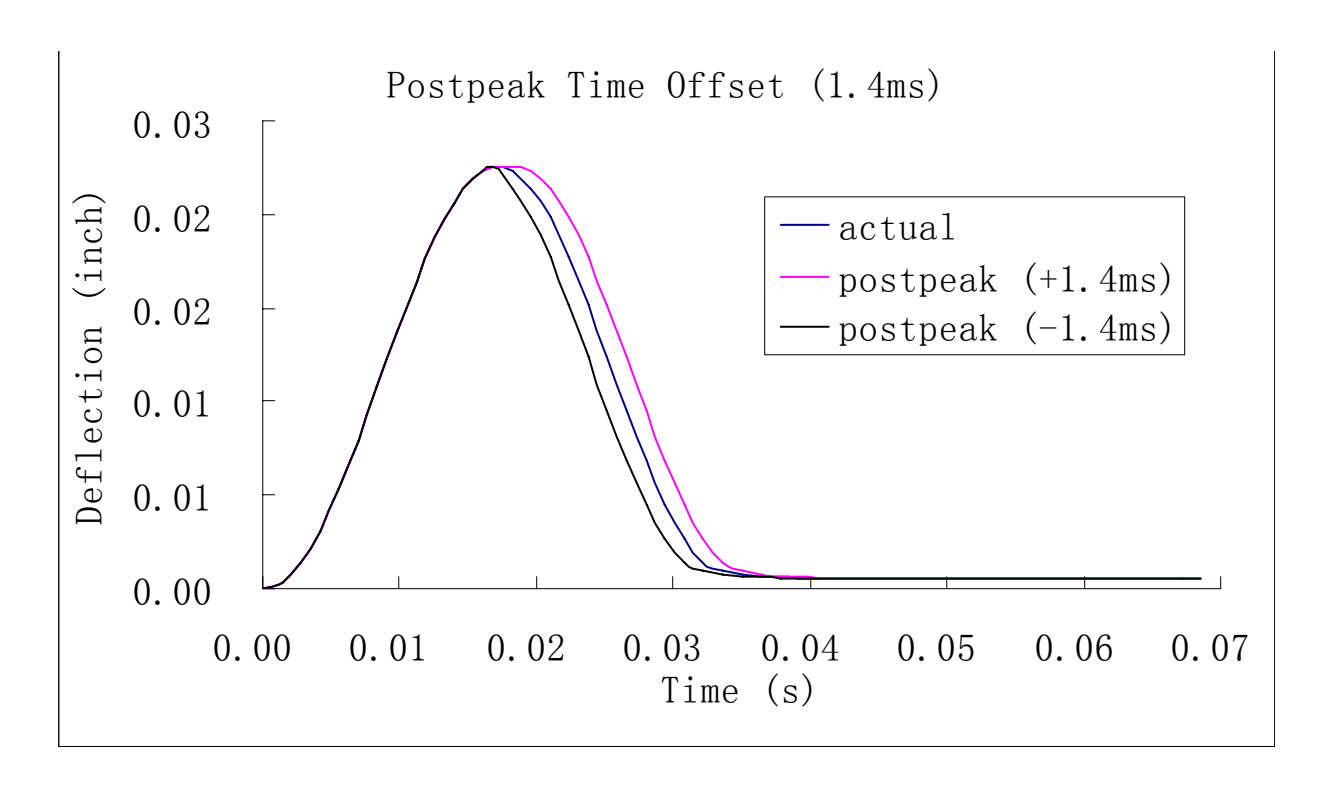


Figure 103: Error caused by expansion/contraction of deflection pulse in the post-peak zone for one sensor

#### 6.3.1 Sensitivity Analysis for Deflection Measurement of the First Sensor

Since the first sensor which is under the FWD test load affects the result of the AC modulus more, only +2% or -2% error of the deflection history for sensor 1 is considered. The backcalculation result with inaccurate input is checked with the backcalculation result with accurate input, as shown in Fig. 104 - 111.

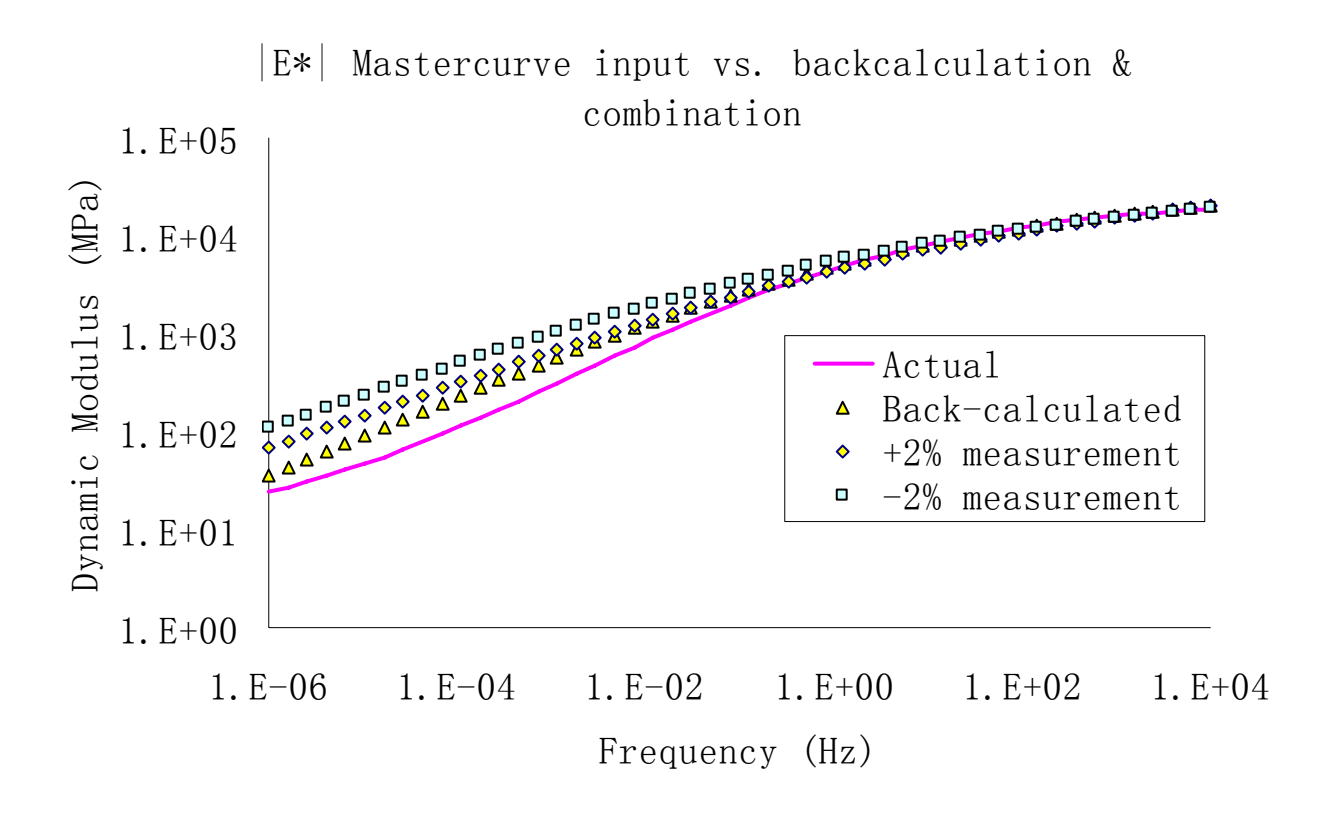


Figure 104: Sensitivity analysis of |E\*| for deflection measurement error (Case A)

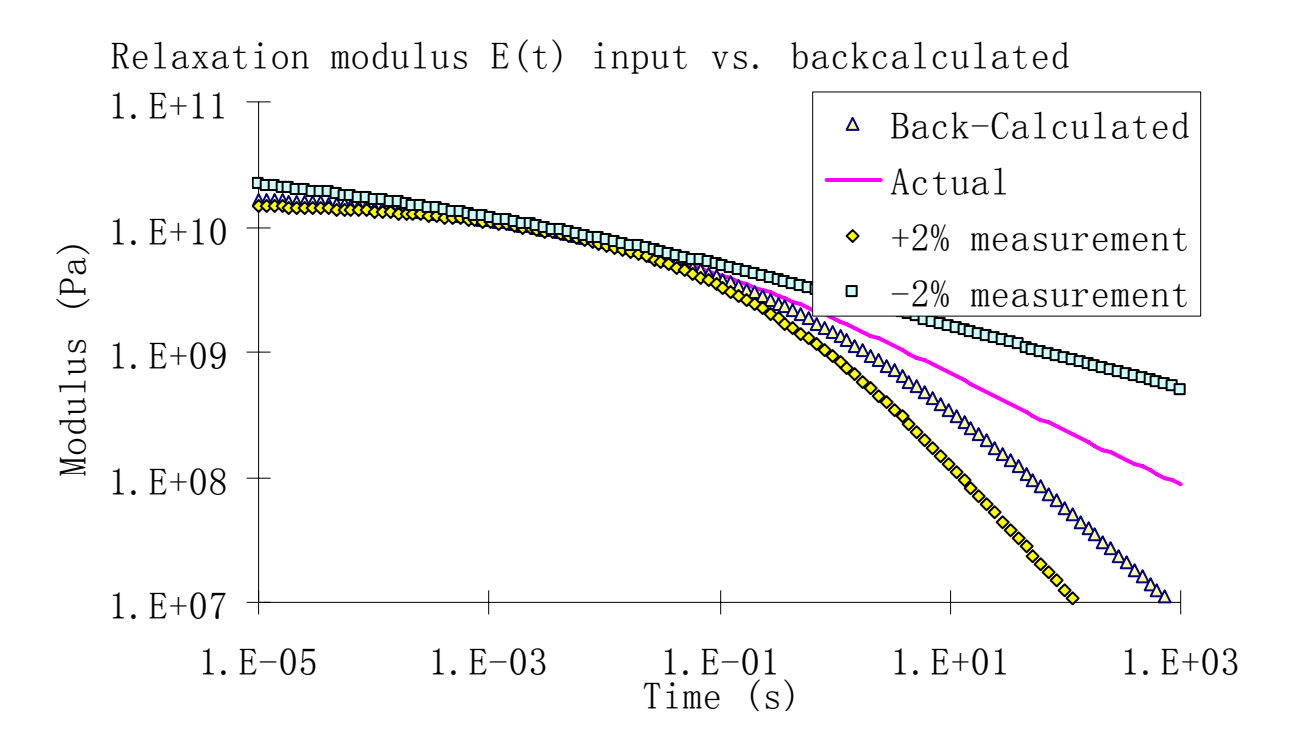


Figure 105: Sensitivity analysis of E(t) for deflection measurement error (Case A)

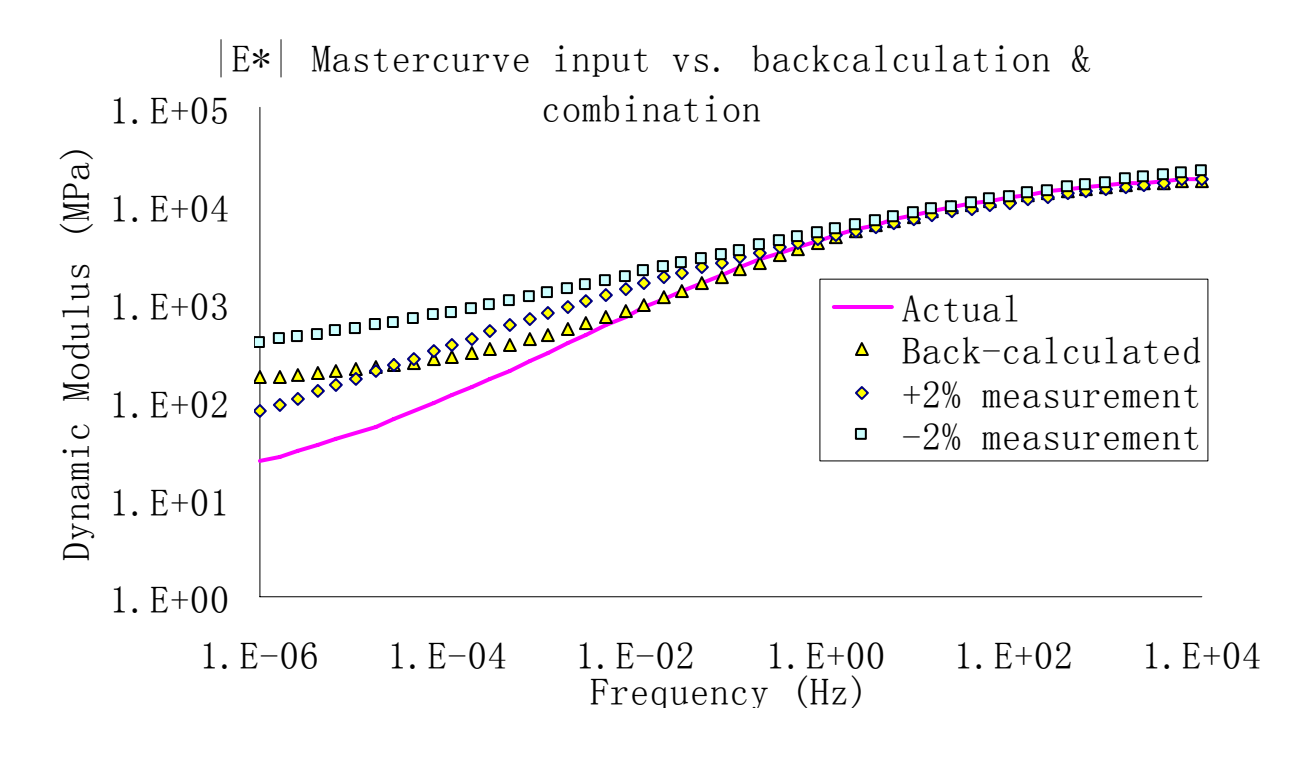


Figure 106: Sensitivity analysis of |E\*| for deflection measurement error (Case B)

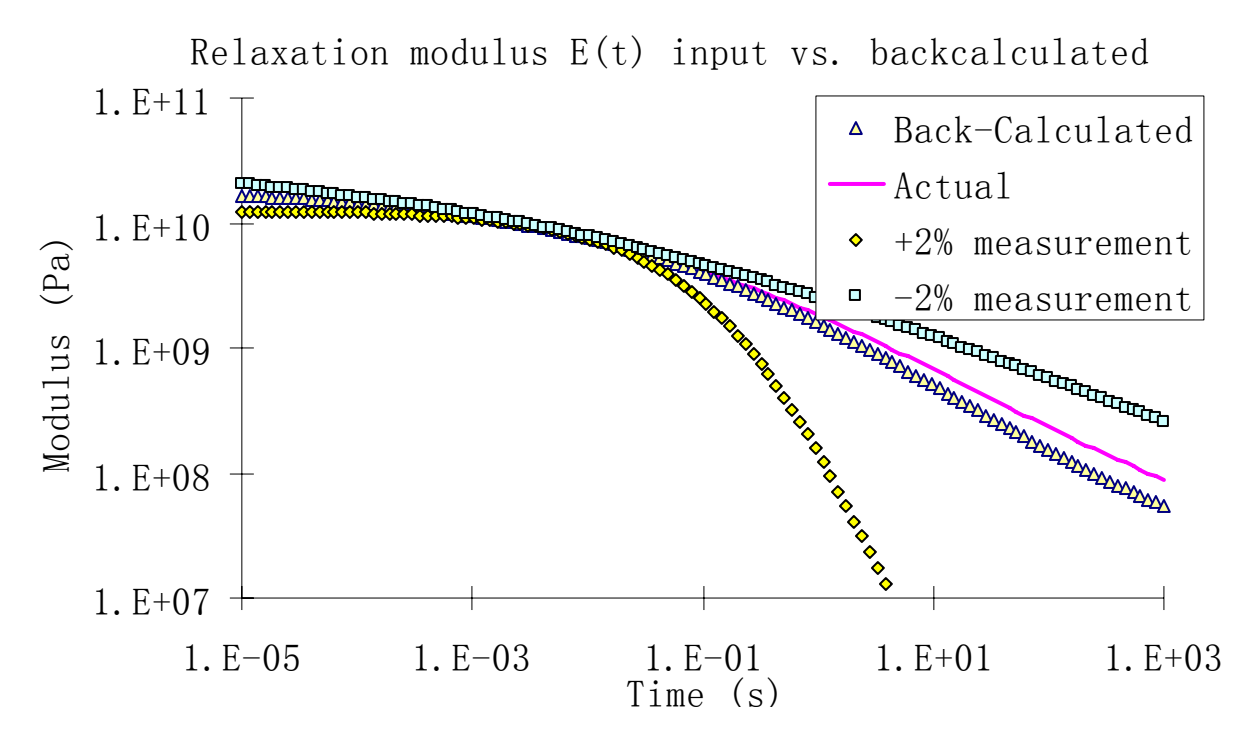


Figure 107: Sensitivity analysis of E(t) for deflection measurement error (Case B)

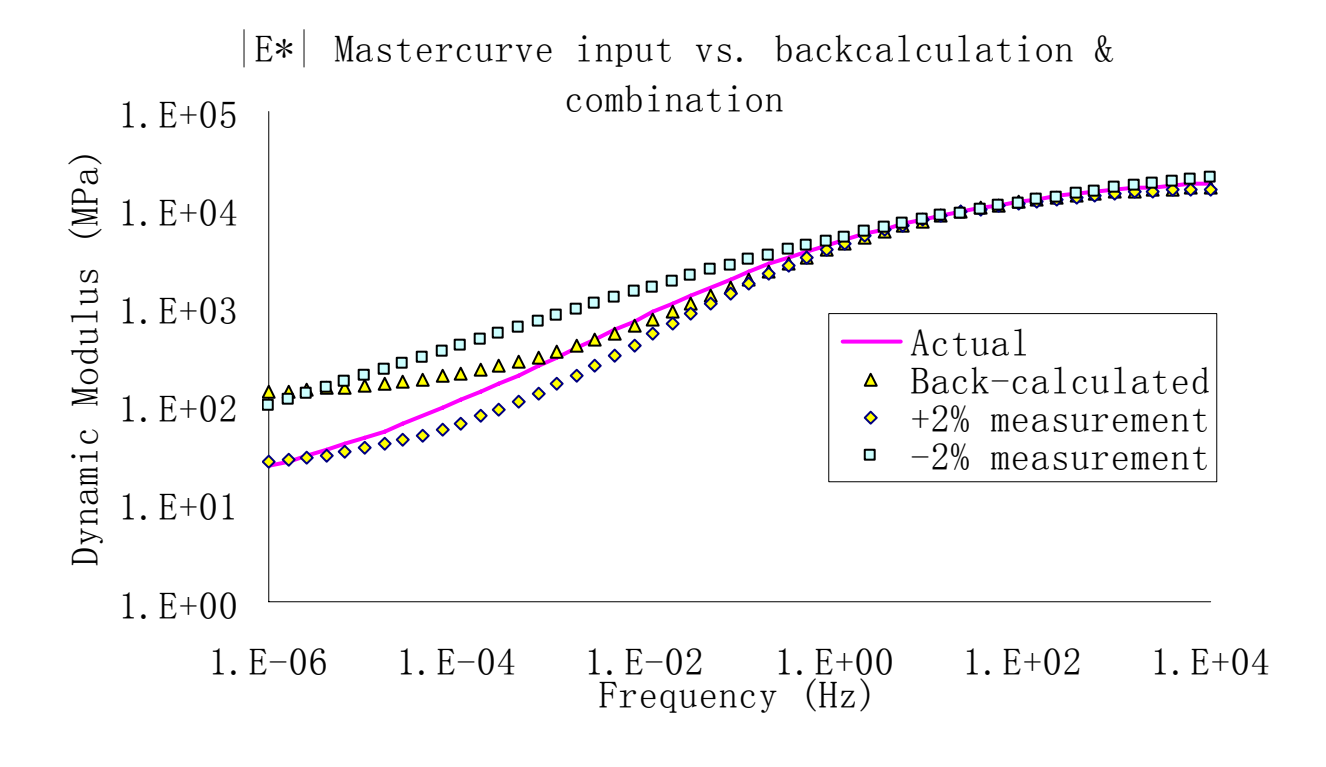


Figure 108: Sensitivity analysis of  $|E^*|$  for deflection measurement error (Case C)

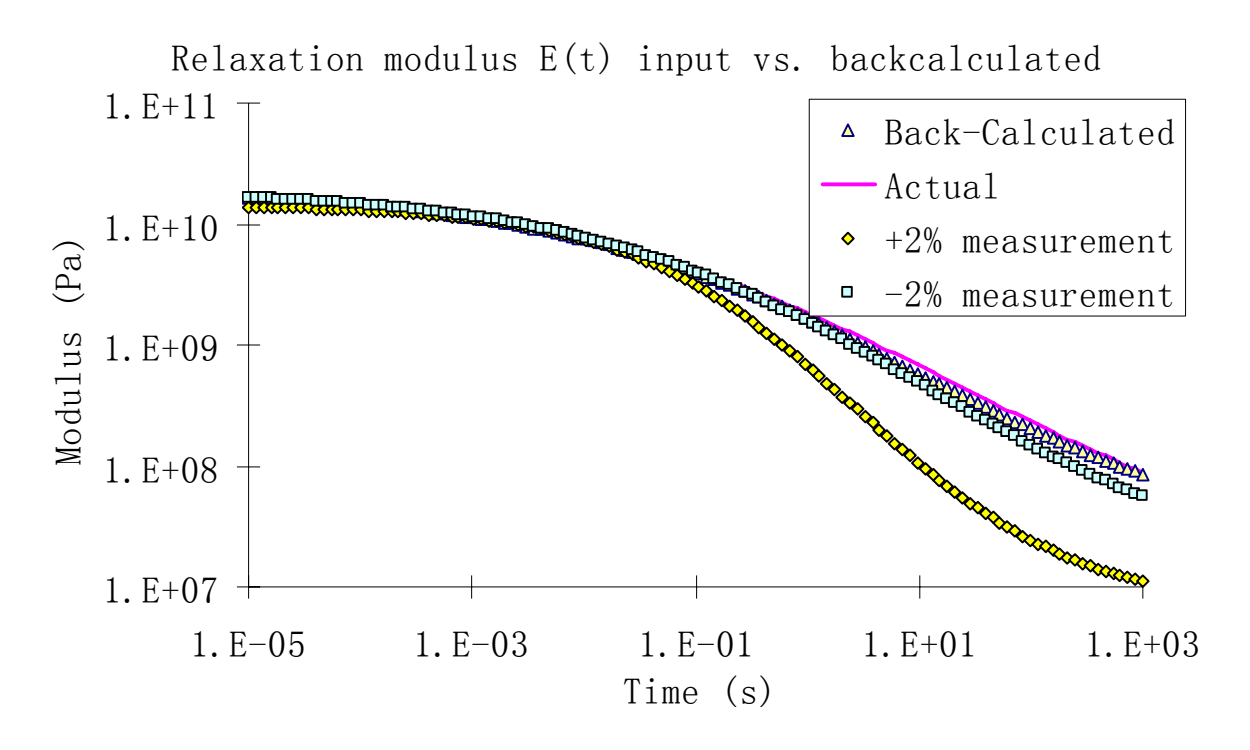


Figure 109: Sensitivity analysis of E(t) for deflection measurement error (Case C)

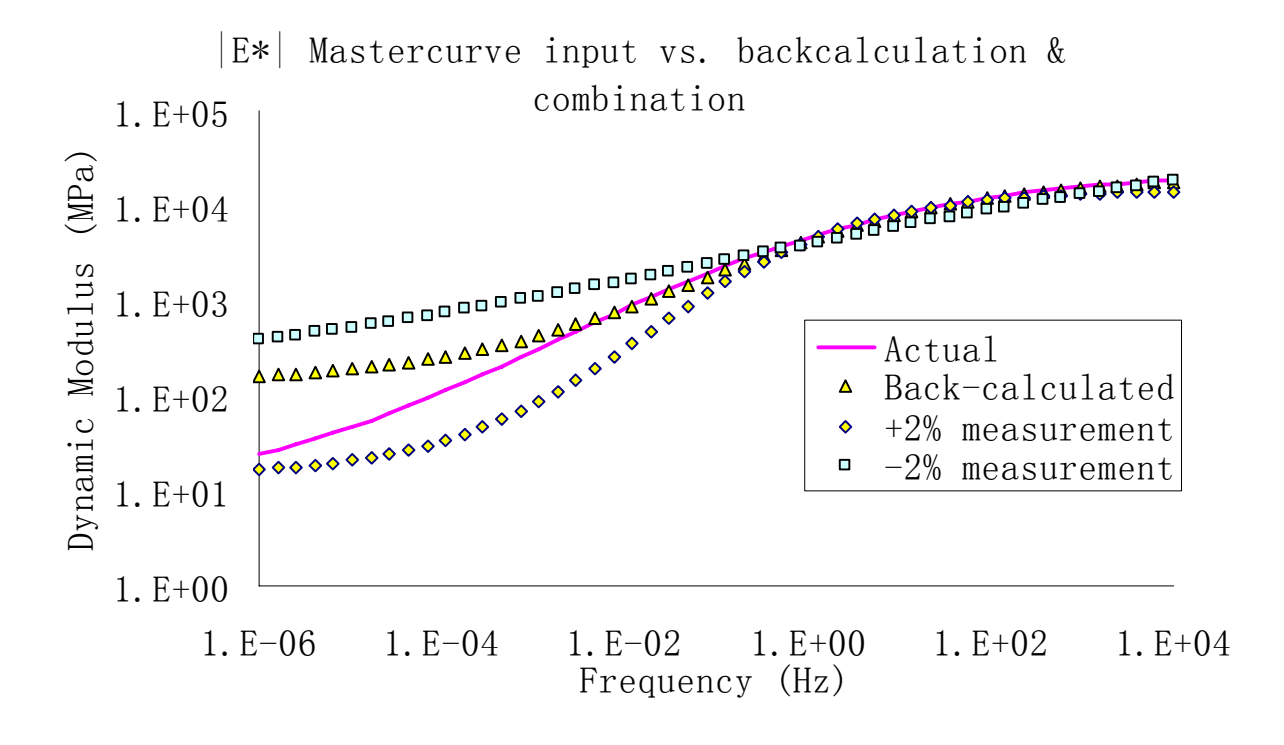


Figure 110: Sensitivity analysis of |E\*| for deflection measurement error (Case D)

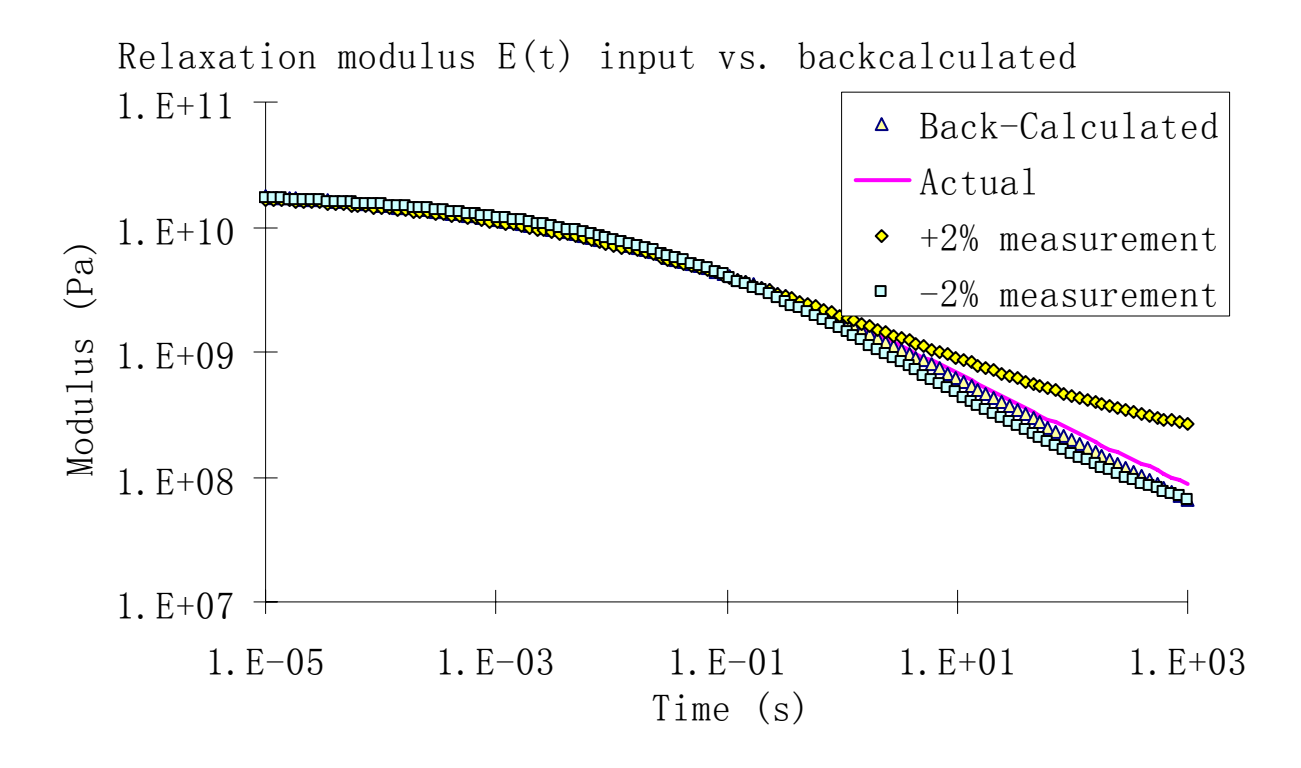


Figure 111: Sensitivity analysis of E(t) for deflection measurement error (Case D)

The above cases show the VE backcalculation program is not sensitive to the error of deflection measurement for sensor 1, especially for the range of interest, i.e., reduced frequency 10 - 10000 Hz in  $|E^*|$  or reduced time 0.0001 - 0.1 second in E(t). Thus, the measurement of the deflection in sensor 1 is not significant for the backcalculation result.

### 6.3.2 Sensitivity Analysis for Time Shift Error of the First Sensor

Still sensor 1 is considered for the sensitivity analysis, for the same reason stated above, with +1.4 ms or -1.4 ms (depending on sampling time) time shift of the deflection history. The backcalulation results with inaccurate input are checked with the backcalculation results with accurate input, as shown in Fig. 112 - 119.

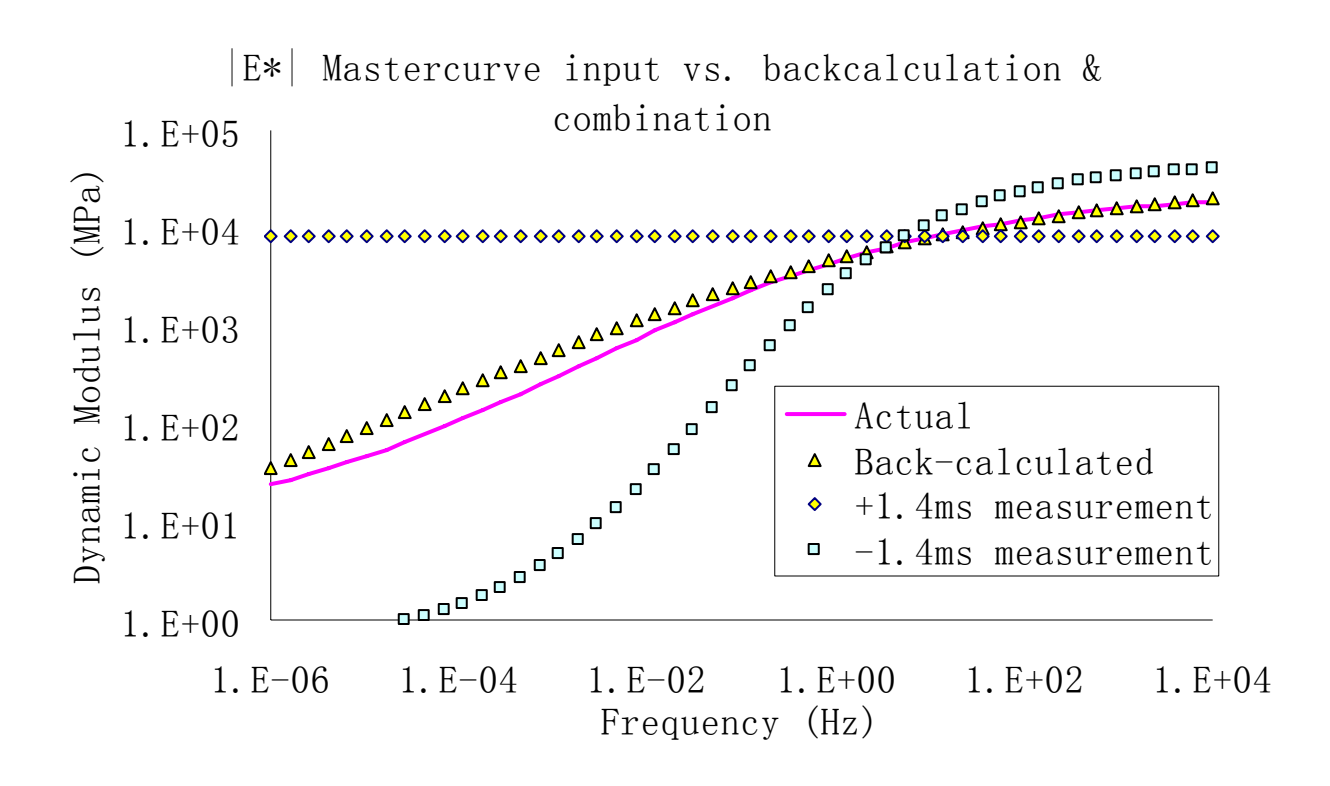


Figure 112: Sensitivity analysis of |E\*| for time shift error of sensor 1 (Case A)

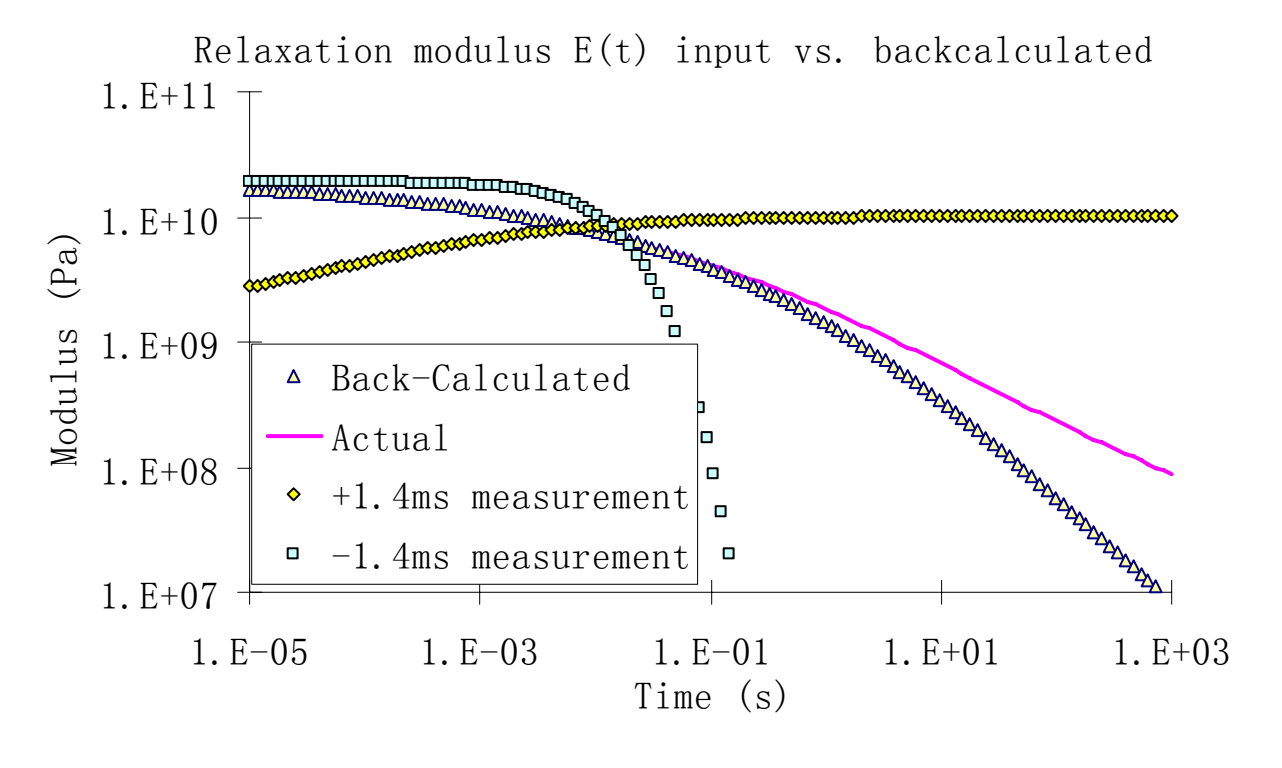


Figure 113: Sensitivity analysis of E(t) for time shift error of sensor 1 (Case A)

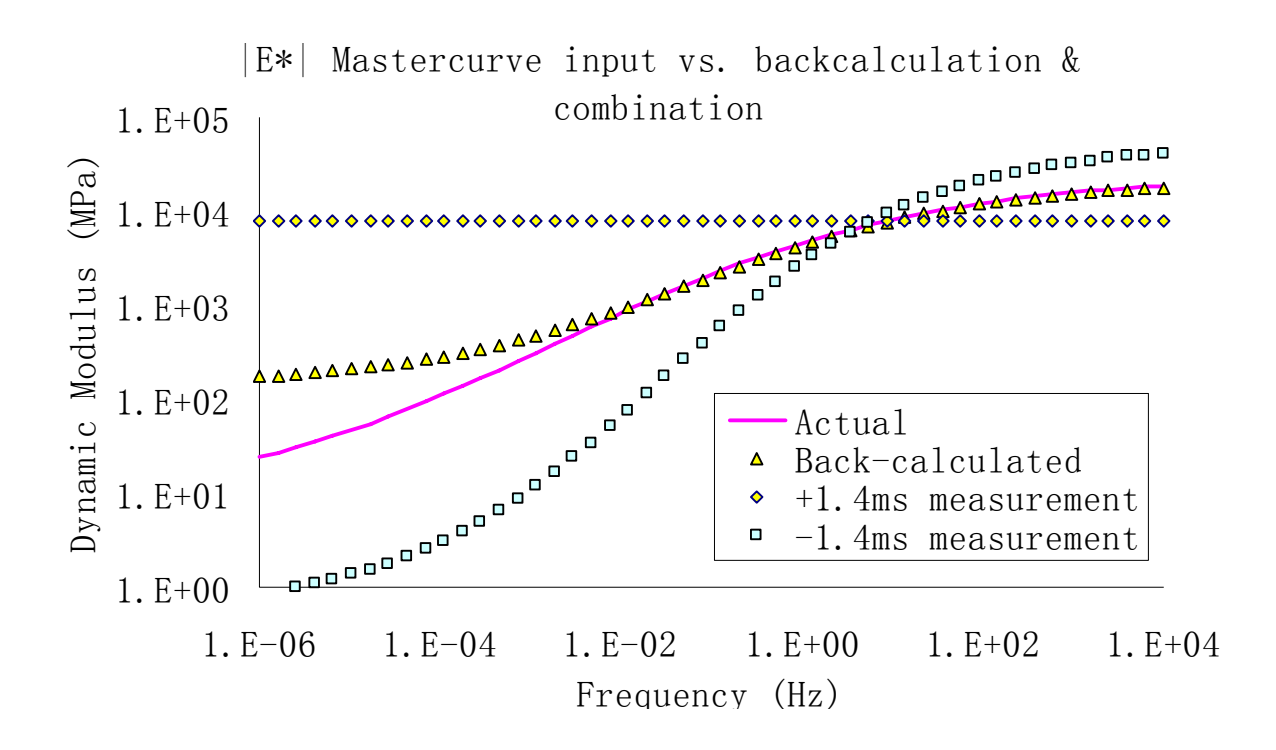


Figure 114: Sensitivity analysis of |E\*| for time shift error of sensor 1 (Case B)

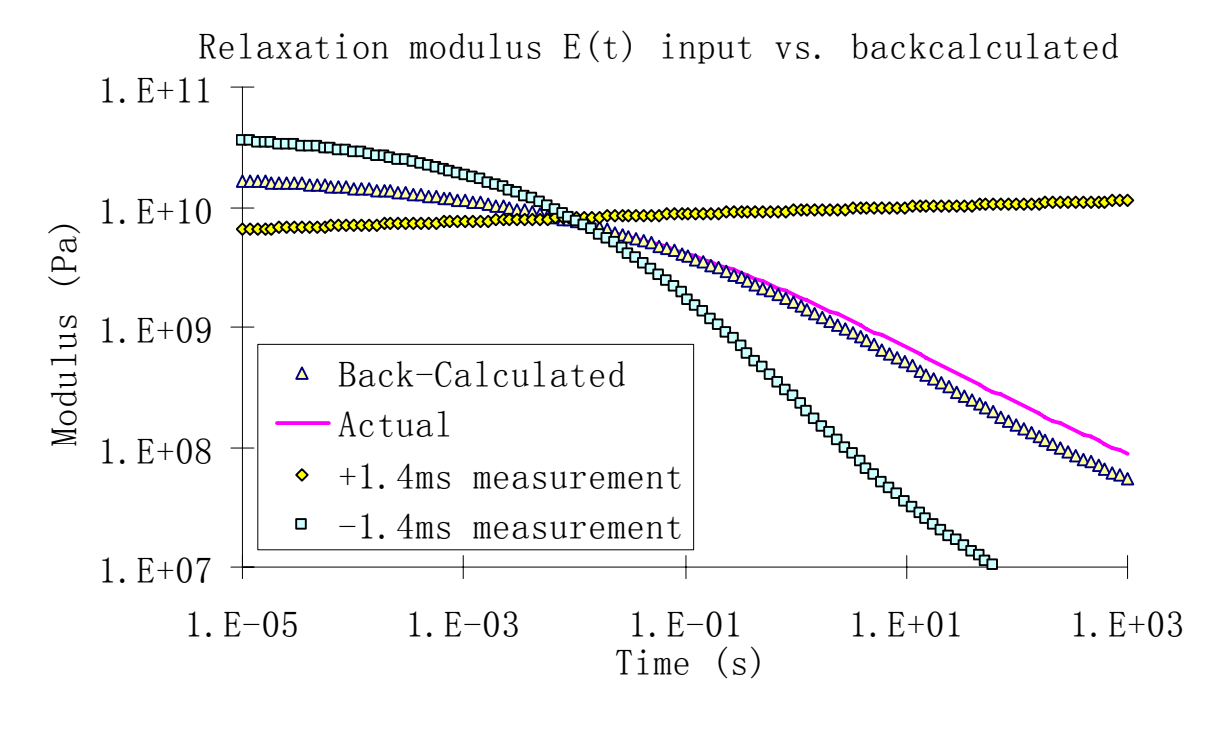


Figure 115: Sensitivity analysis of E(t) for time shift error of sensor 1 (Case B)

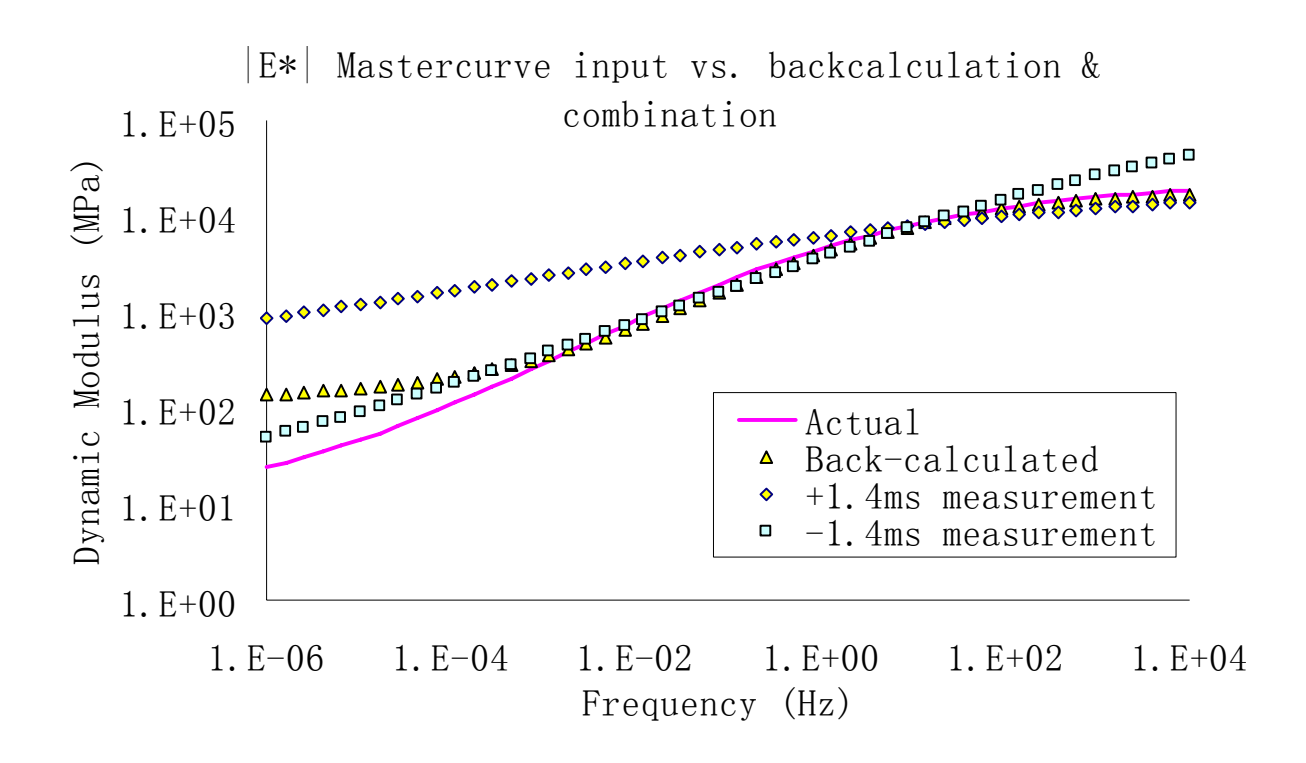


Figure 116: Sensitivity analysis of |E\*| for time shift error of sensor 1 (Case C)

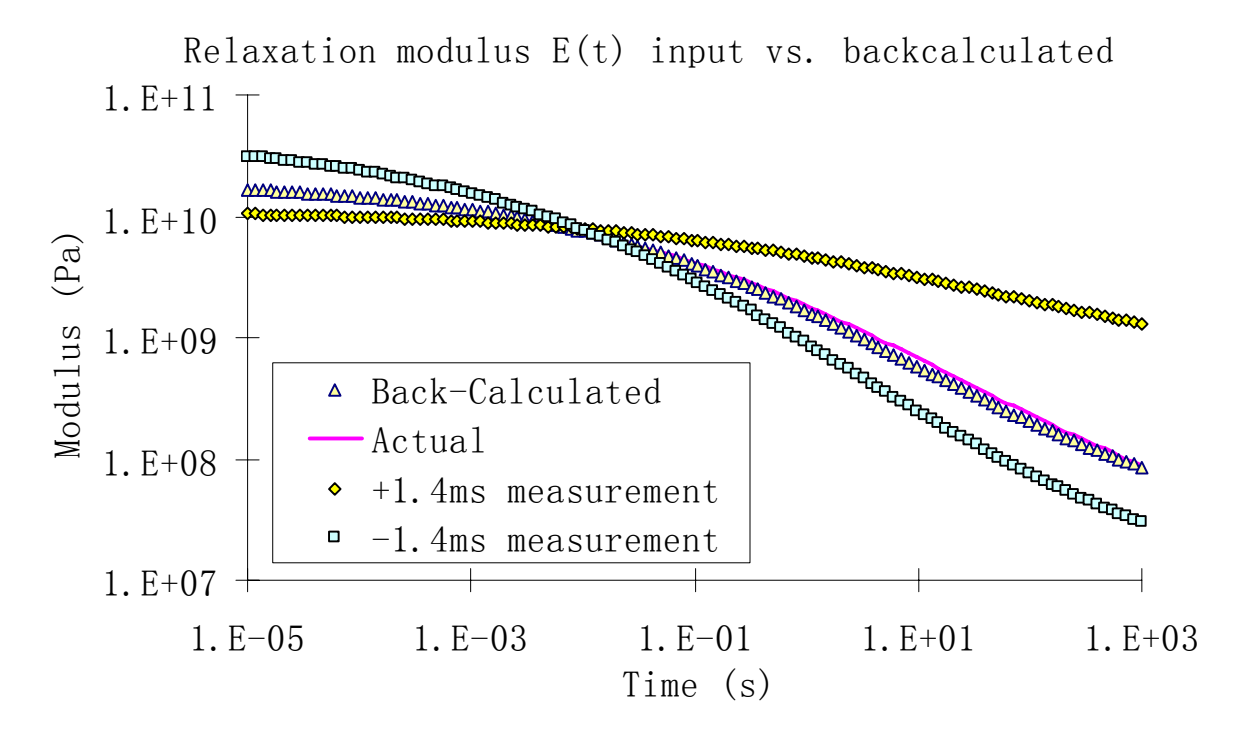


Figure 117: Sensitivity analysis of E(t) for time shift error of sensor 1 (Case C)

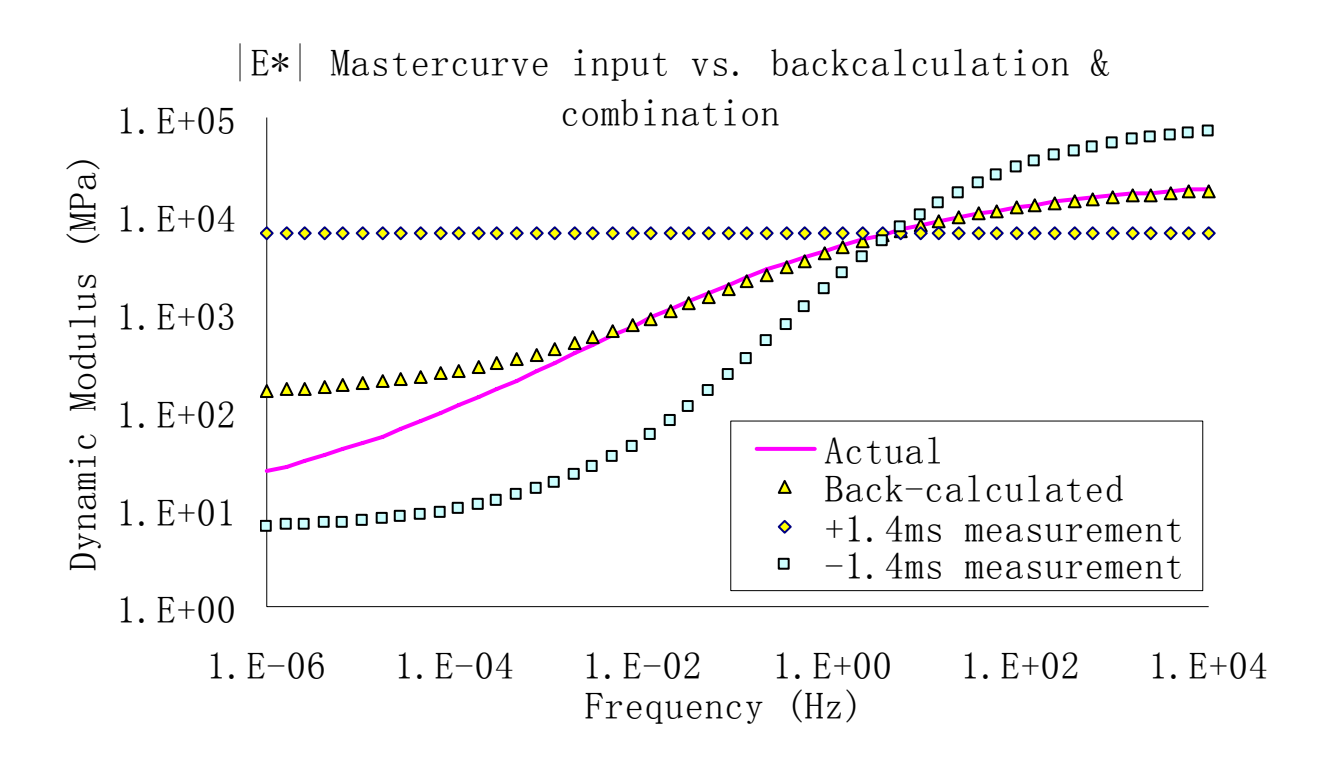


Figure 118: Sensitivity analysis of |E\*| for time shift error of sensor 1 (Case D)

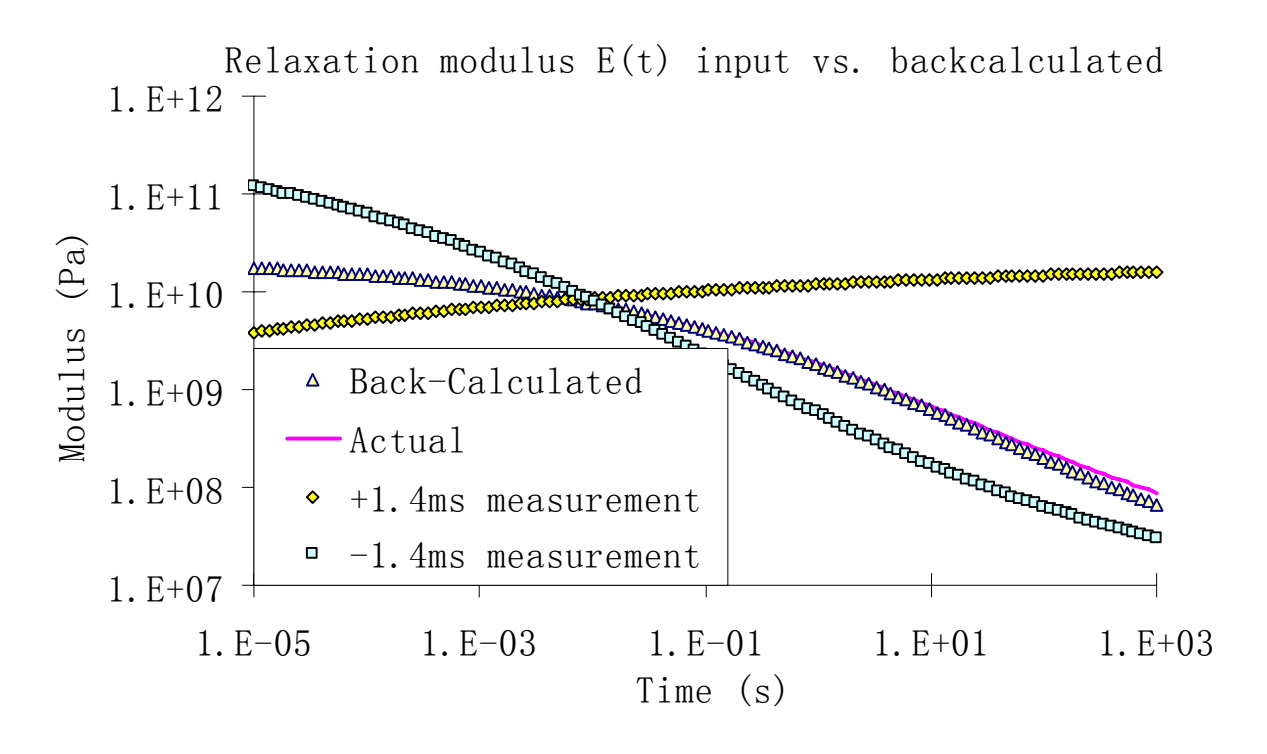


Figure 119: Sensitivity analysis of E(t) for time shift error of sensor 1 (Case D)

The above cases show the backcalculation program is significantly sensitive to the time shift error of sensor 1. Thus, there should not be any error in time recording during the field FWD test.

#### 6.3.3 Sensitivity Analysis for Post-Peak Time Offset of the First Sensor

Still sensor 1 is considered for the sensitivity analysis, for the same reason stated above, with +1.4 ms or -1.4 ms (depending on sampling time) time shift after the peak deflection occurred. The backcalculation results with inaccurate input are checked with the backcalculation results with accurate input, as shown in Fig. 120 - 127.

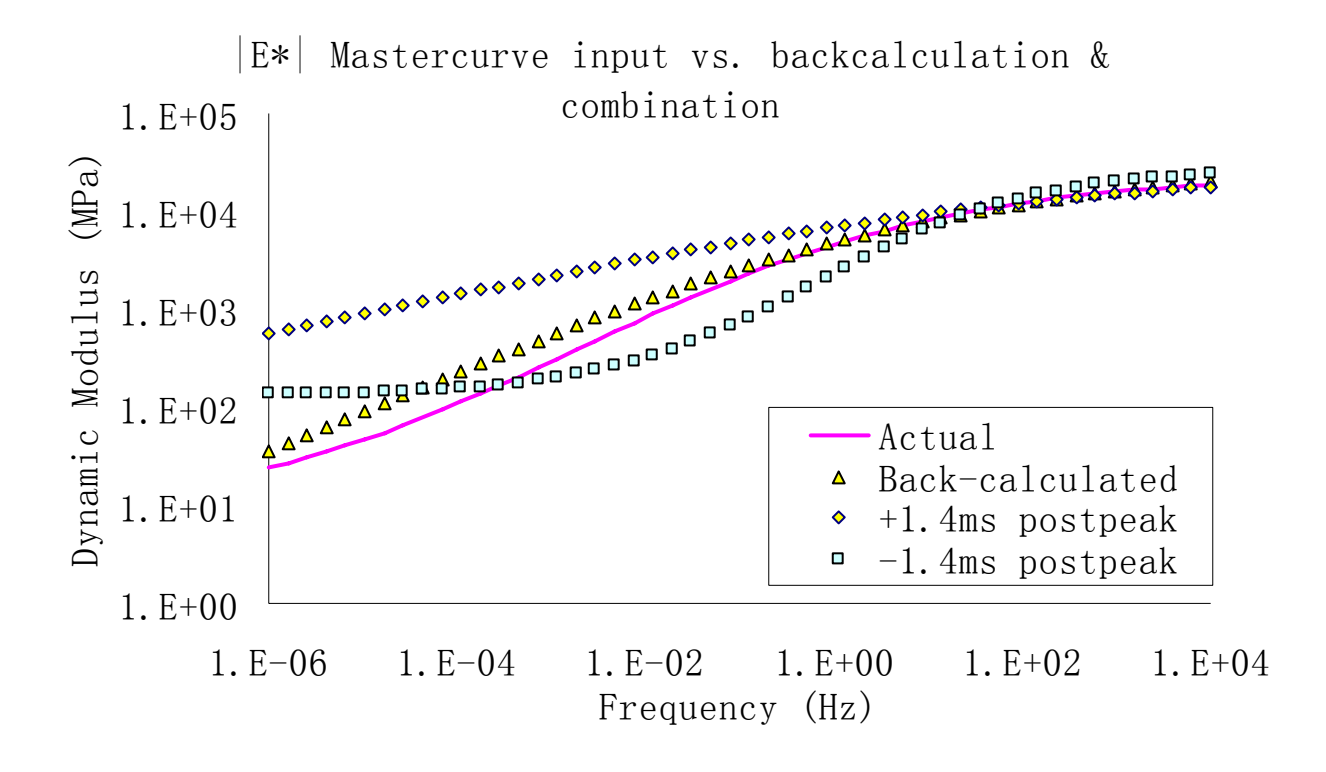


Figure 120: Sensitivity analysis of |E\*| for post-peak time offset of sensor 1 (Case A)

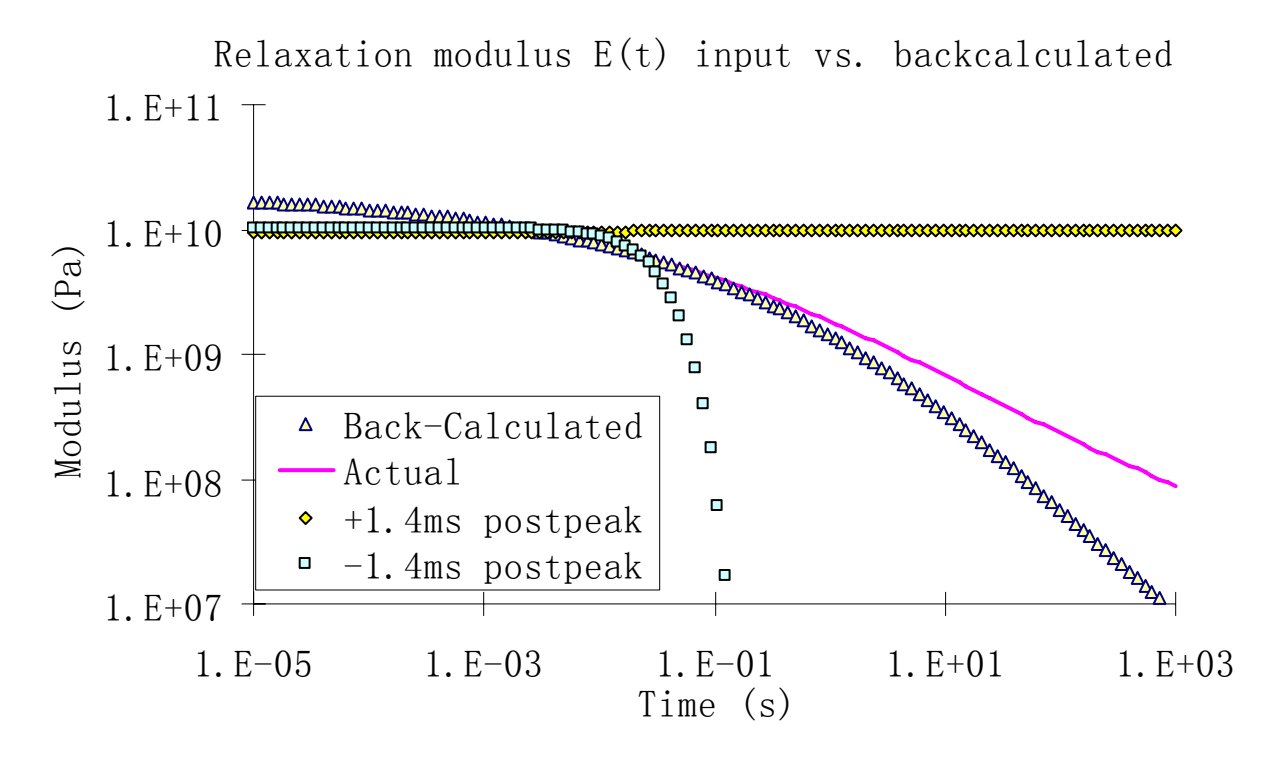


Figure 121: Sensitivity analysis of E(t) for post-peak time offset of sensor 1 (Case A)

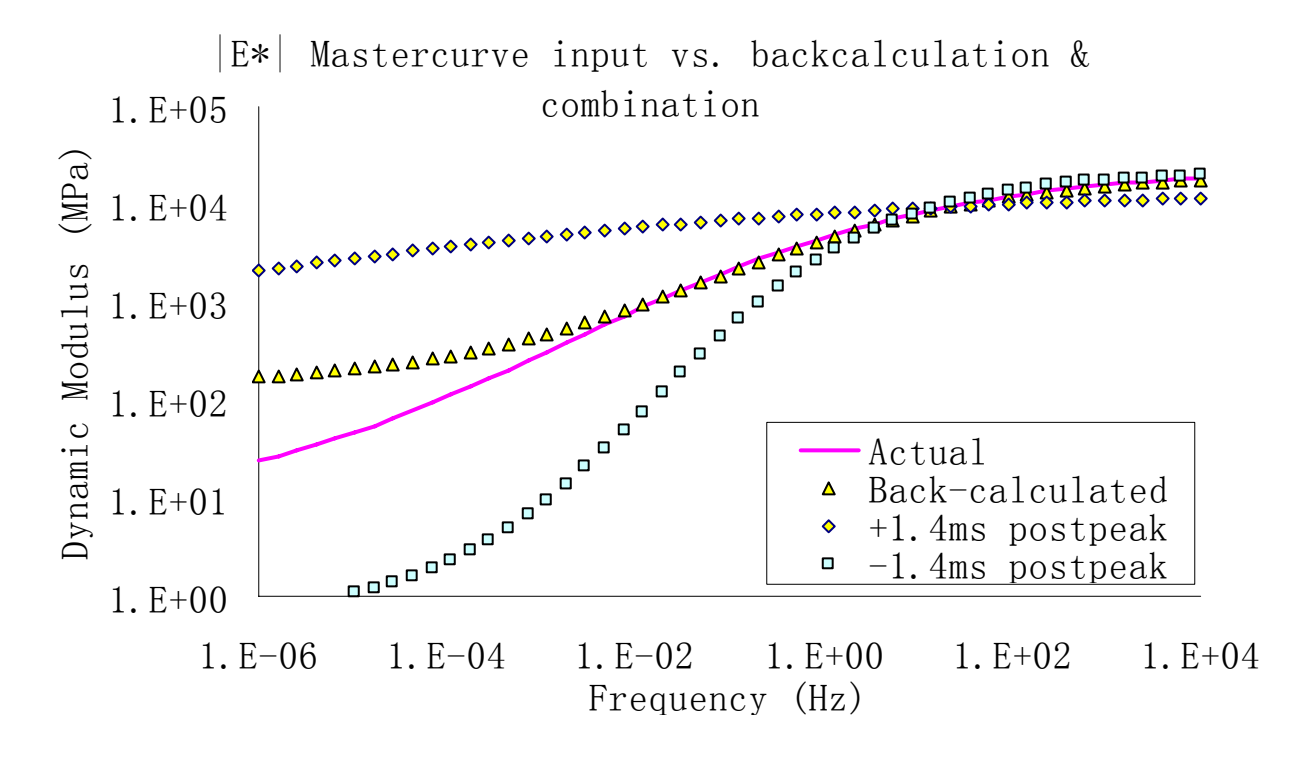


Figure 122: Sensitivity analysis of |E\*| for post-peak time offset of sensor 1 (Case B)

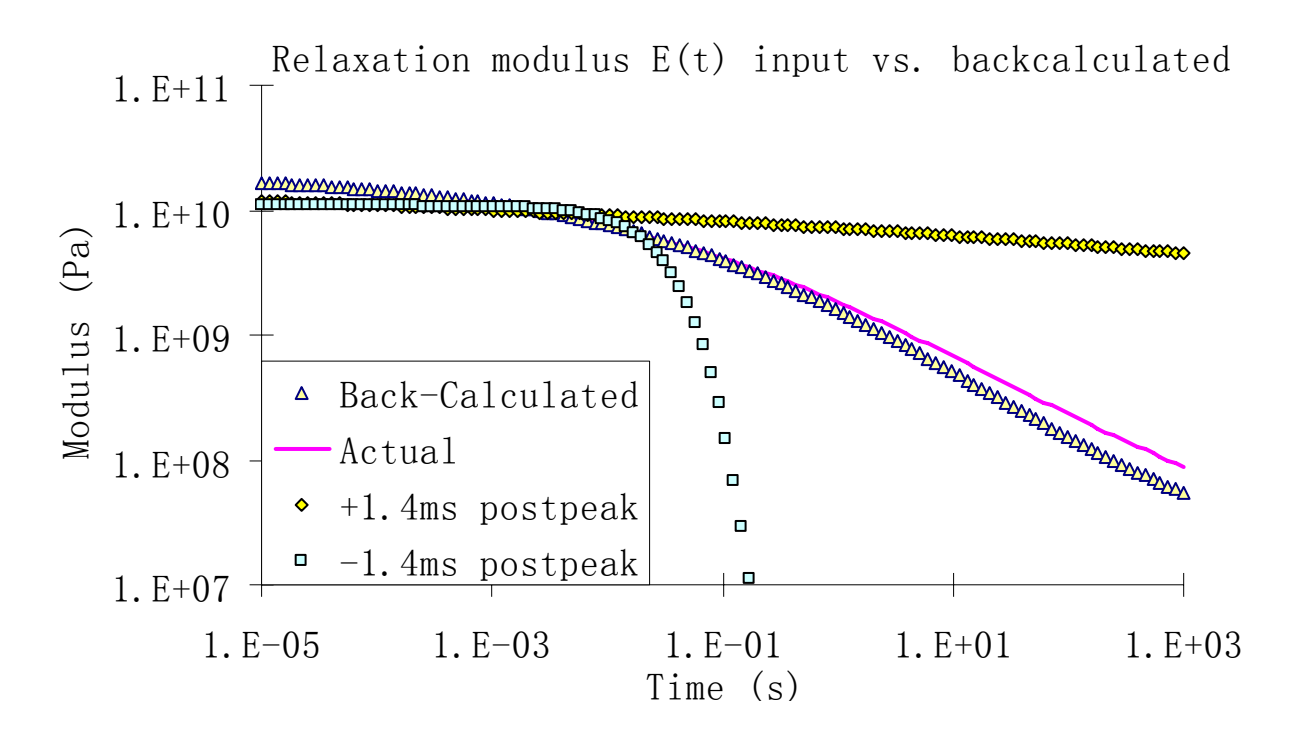


Figure 123: Sensitivity analysis of E(t) for post-peak time offset of sensor 1 (Case B)

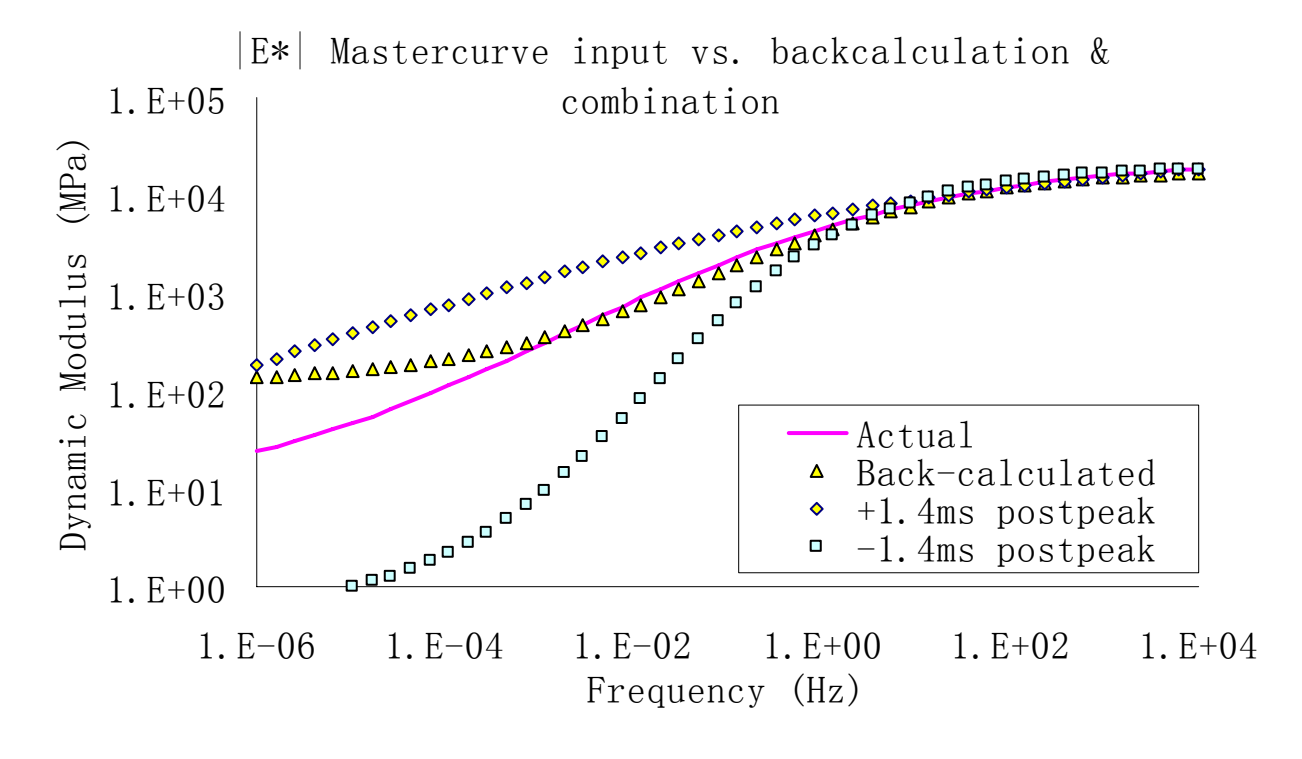


Figure 124: Sensitivity analysis of |E\*| for post-peak time offset of sensor 1 (Case C)

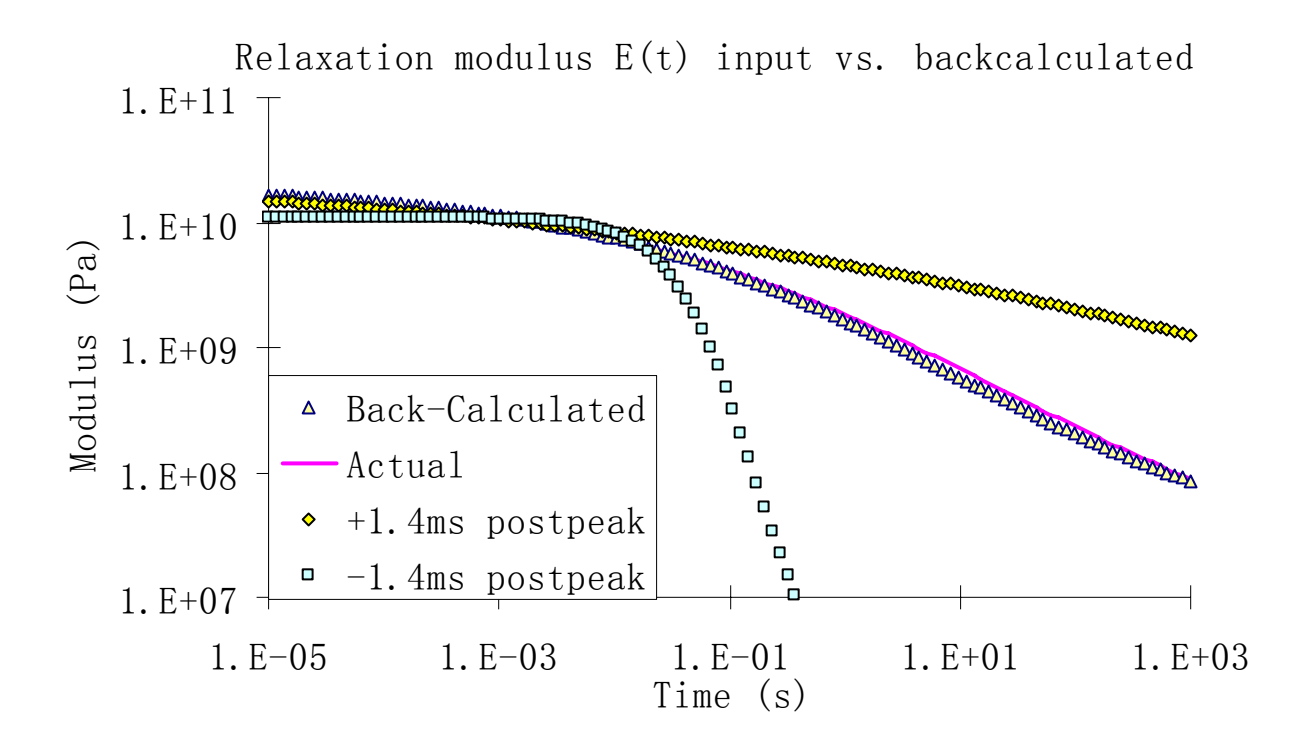


Figure 125: Sensitivity analysis of (t) for post-peak time offset of sensor 1 (Case C)

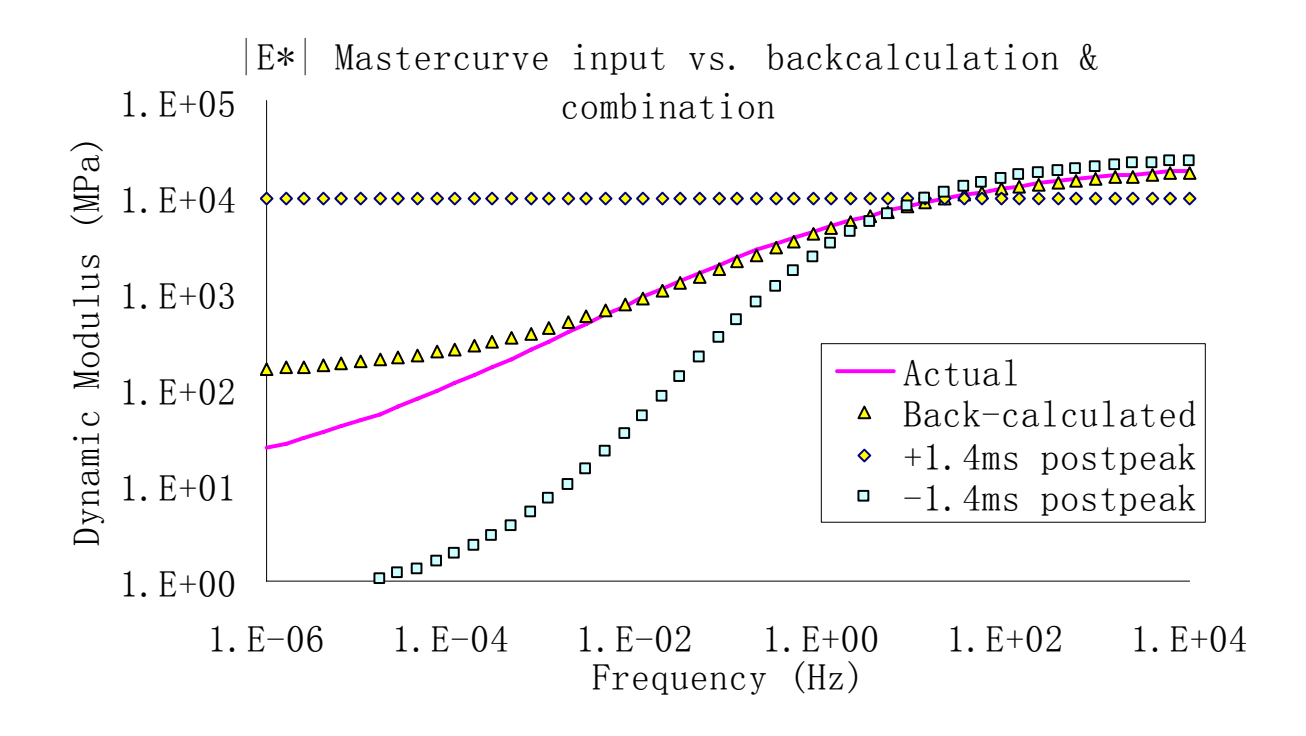


Figure 126: Sensitivity analysis of |E\*| for post-peak time offset of sensor 1 (Case D)

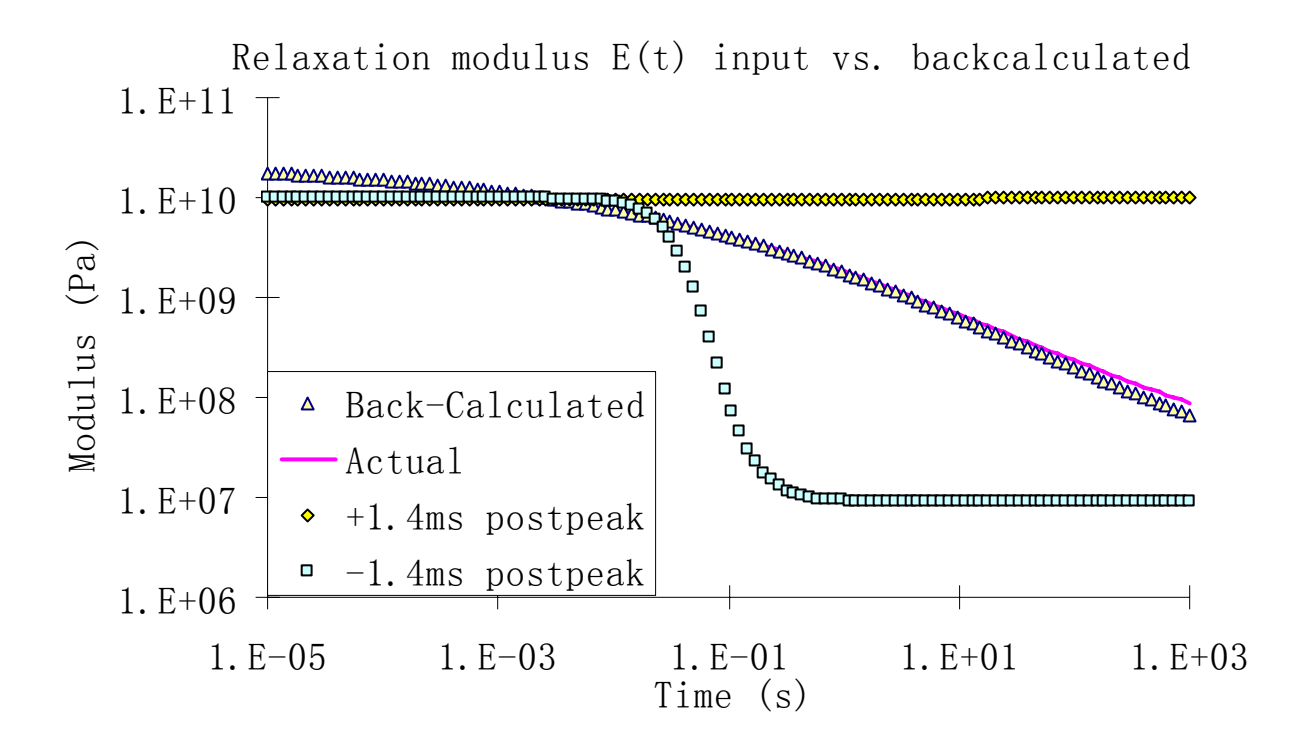


Figure 127: Sensitivity analysis of E(t) for post-peak time offset of sensor 1 (Case D)

Above cases show the backcalculation program is significantly sensitive to the post-peak time offset of sensor 1, although it works well within the interested range in some cases. Thus, there cannot be any offset in time recording after the maximum deflection occurs during the field FWD test.

#### **6.3.4 Sensitivity Analysis for Layer Thickness**

Layer thickness is known to be very sensitive in MODCOMP5, and therefore it is expected here it is as sensitive for this VE backcalculation program. In this analysis, the thickness of AC layer and base layer were varied by +0.5 in or -0.5 in individually, as well as combined. Each pavement structure may therefore have 8 cases of layer thickness for a total of 32 backcalculation runs. The backcalculation results with inaccurate input are checked with the backcalculation results with accurate input, as shown in Fig. 128 - 135.

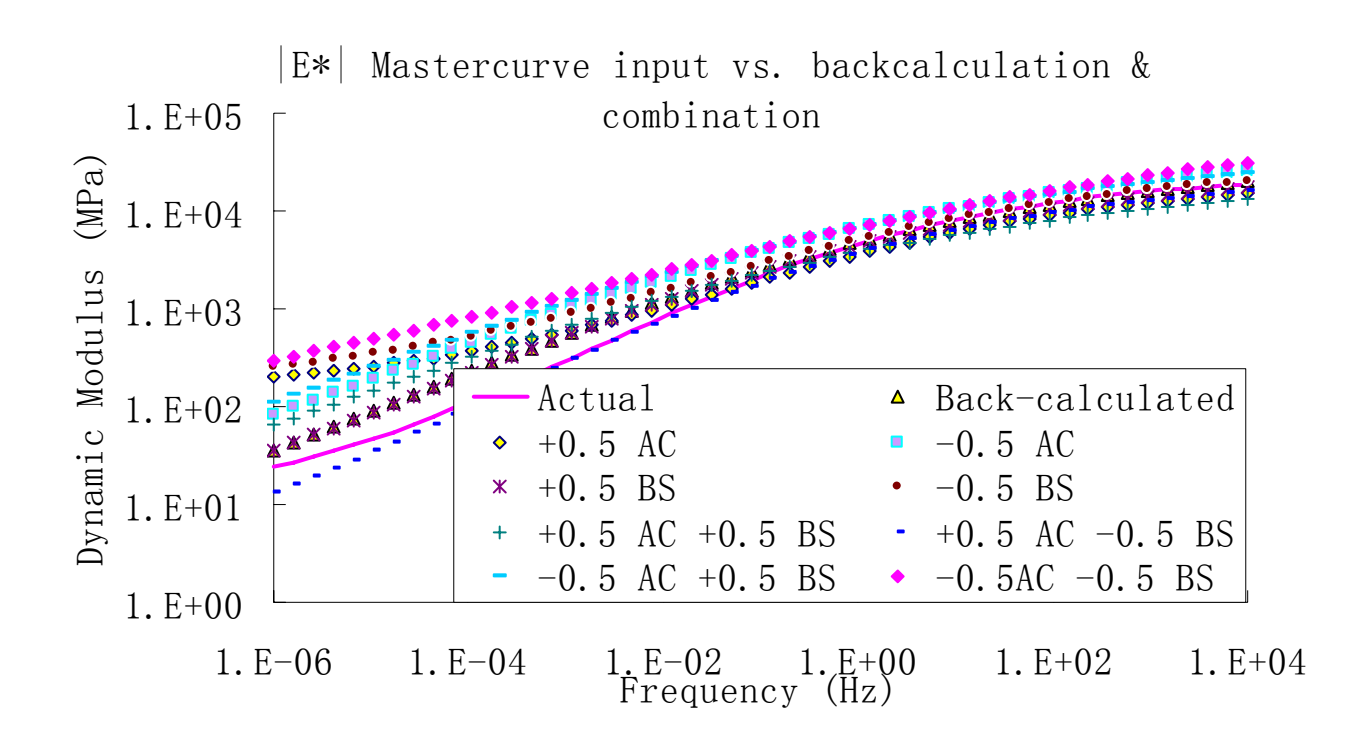


Figure 128: Sensitivity analysis of |E\*| for layer thickness (Case A)

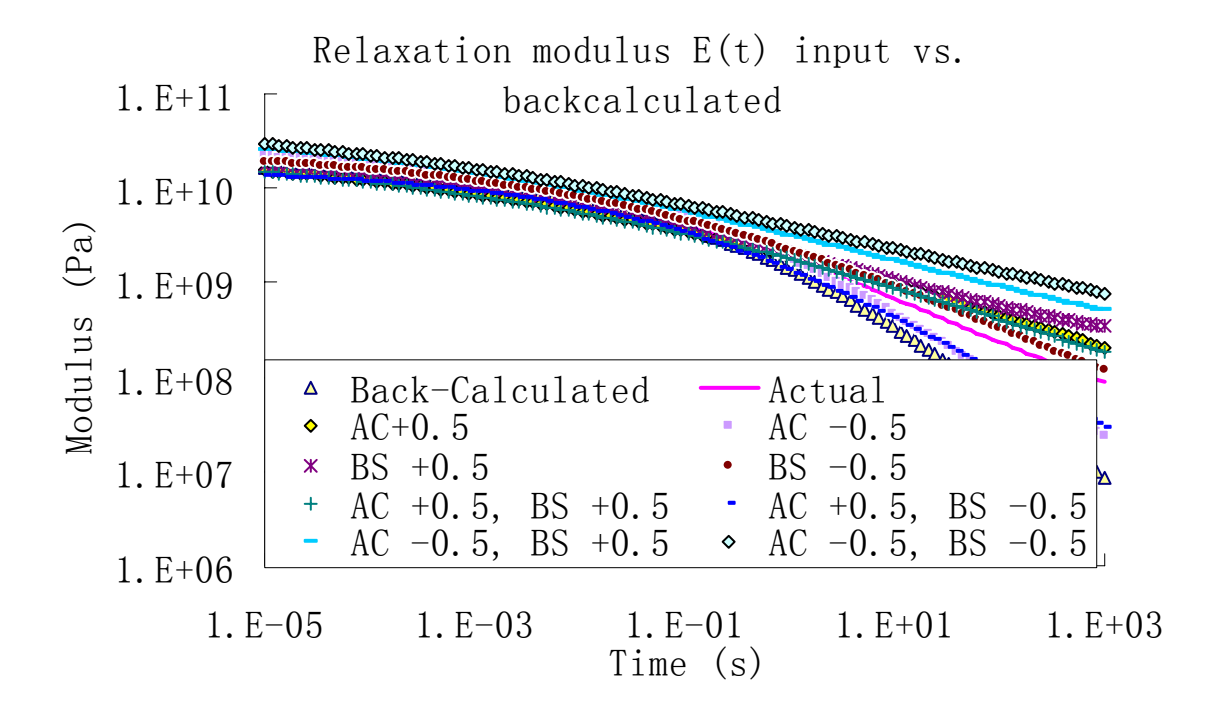


Figure 129: Sensitivity analysis of E(t) for layer thickness (Case A)

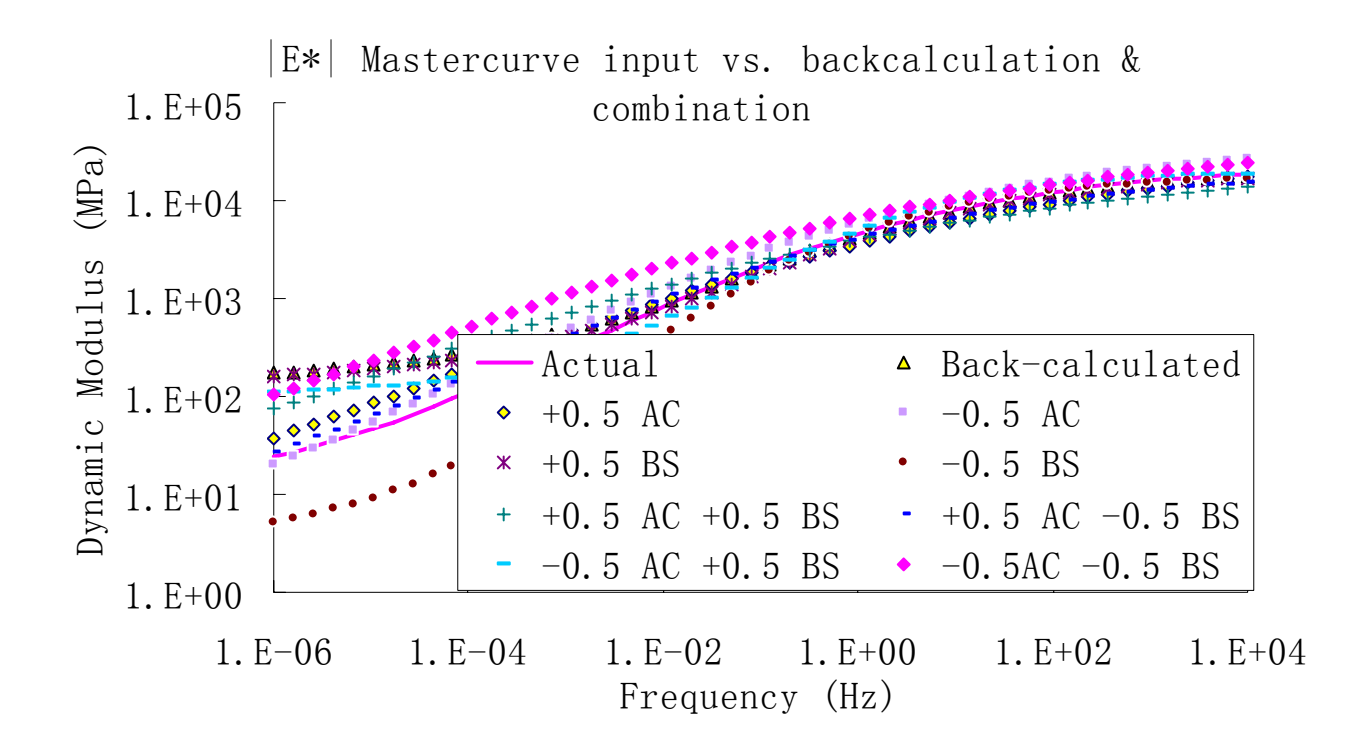


Figure 130: Sensitivity analysis of |E\*| for layer thickness (Case B)

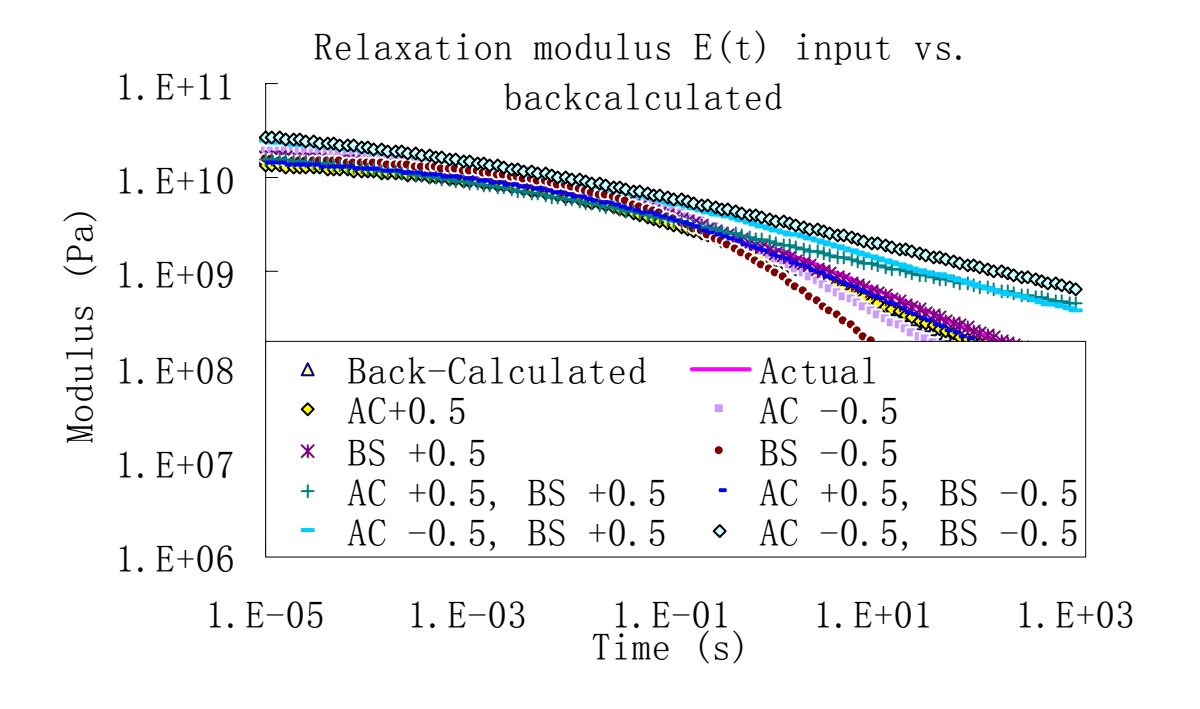


Figure 131: Sensitivity analysis of E(t) for layer thickness (Case B)

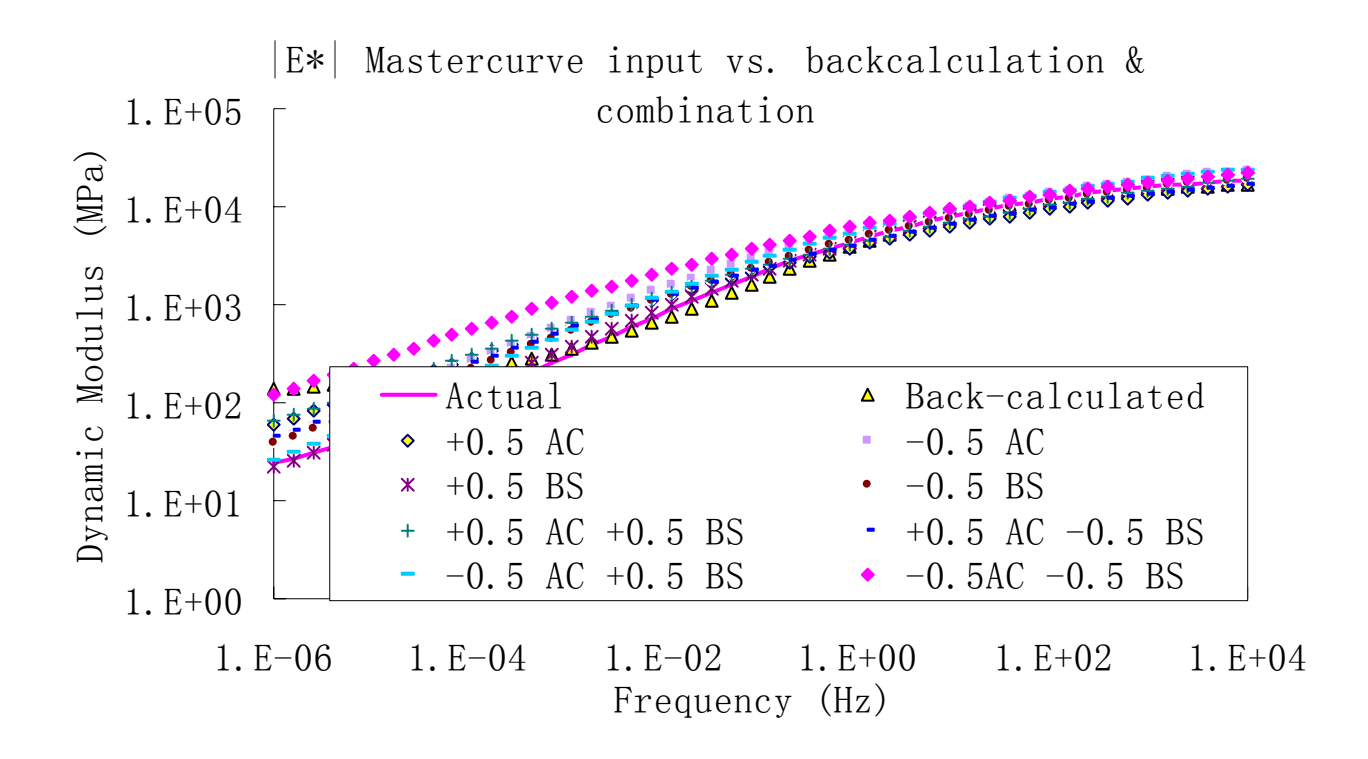


Figure 132: Sensitivity analysis of |E\*| for layer thickness (Case C)

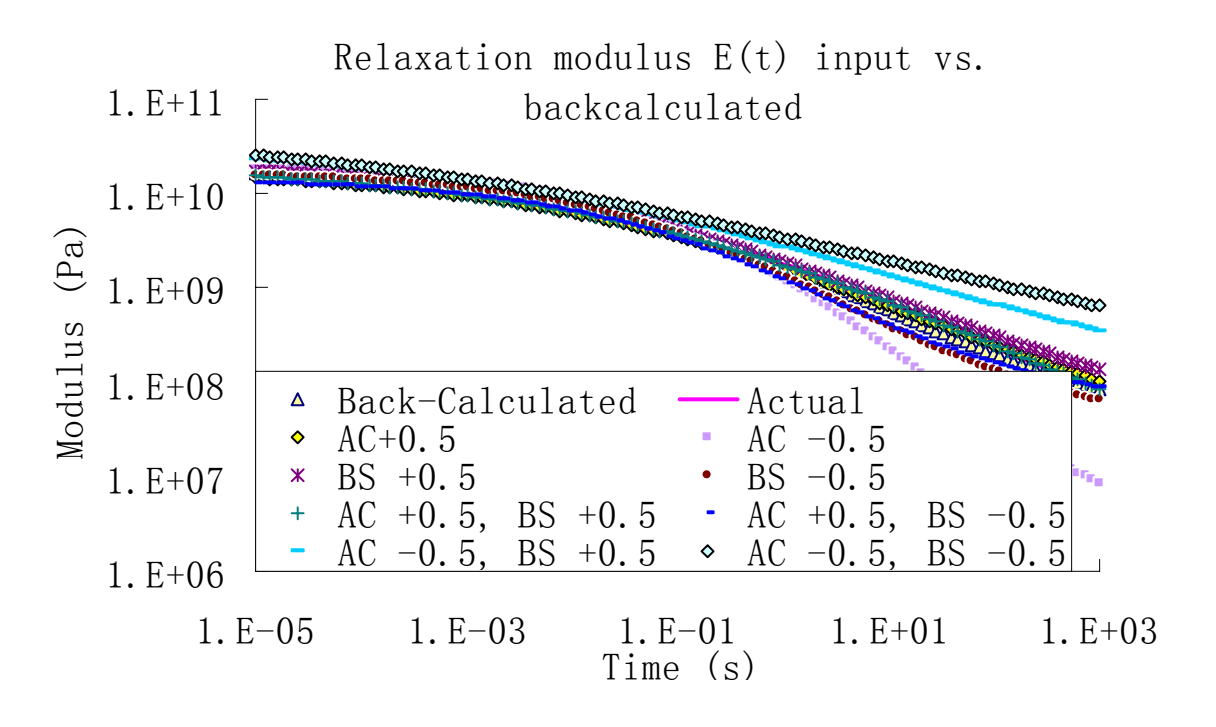


Figure 133: Sensitivity analysis of E(t) for layer thickness (Case C)

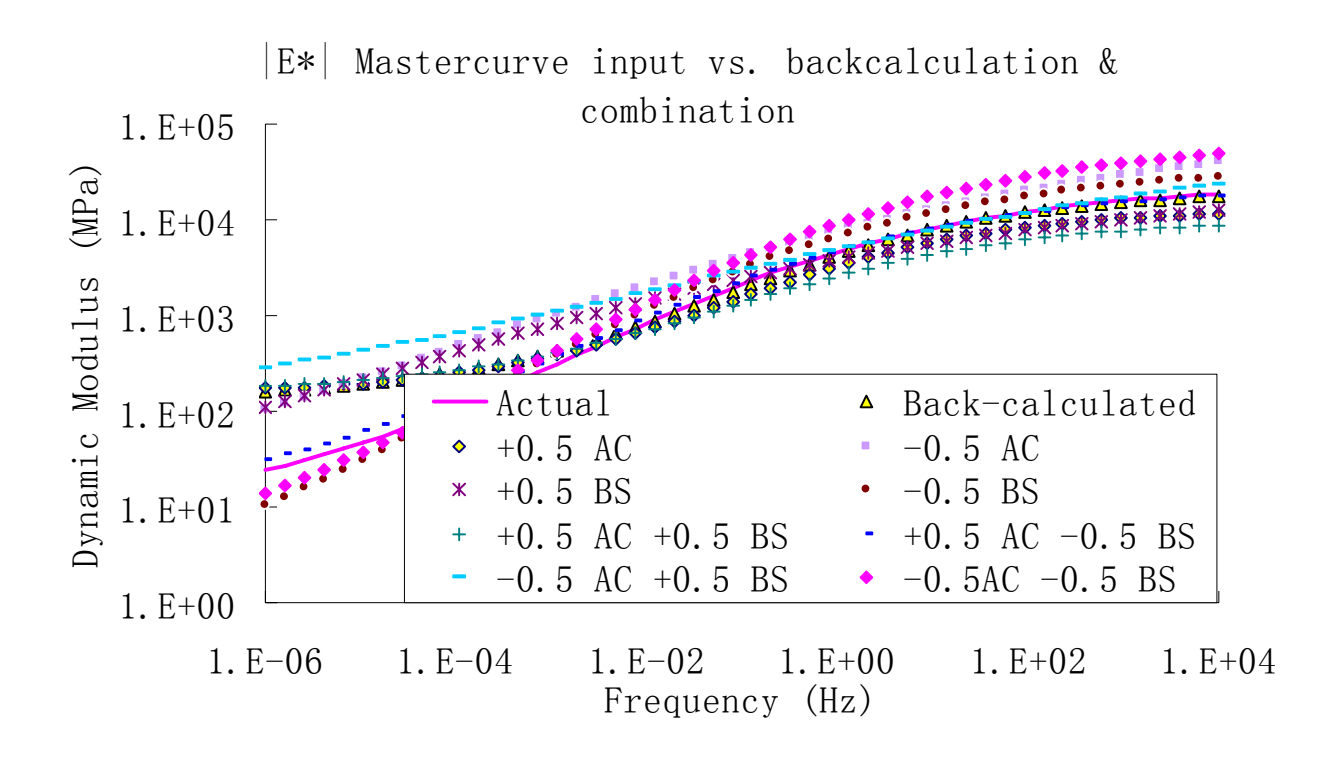


Figure 134: Sensitivity analysis of |E\*| for layer thickness (Case D)

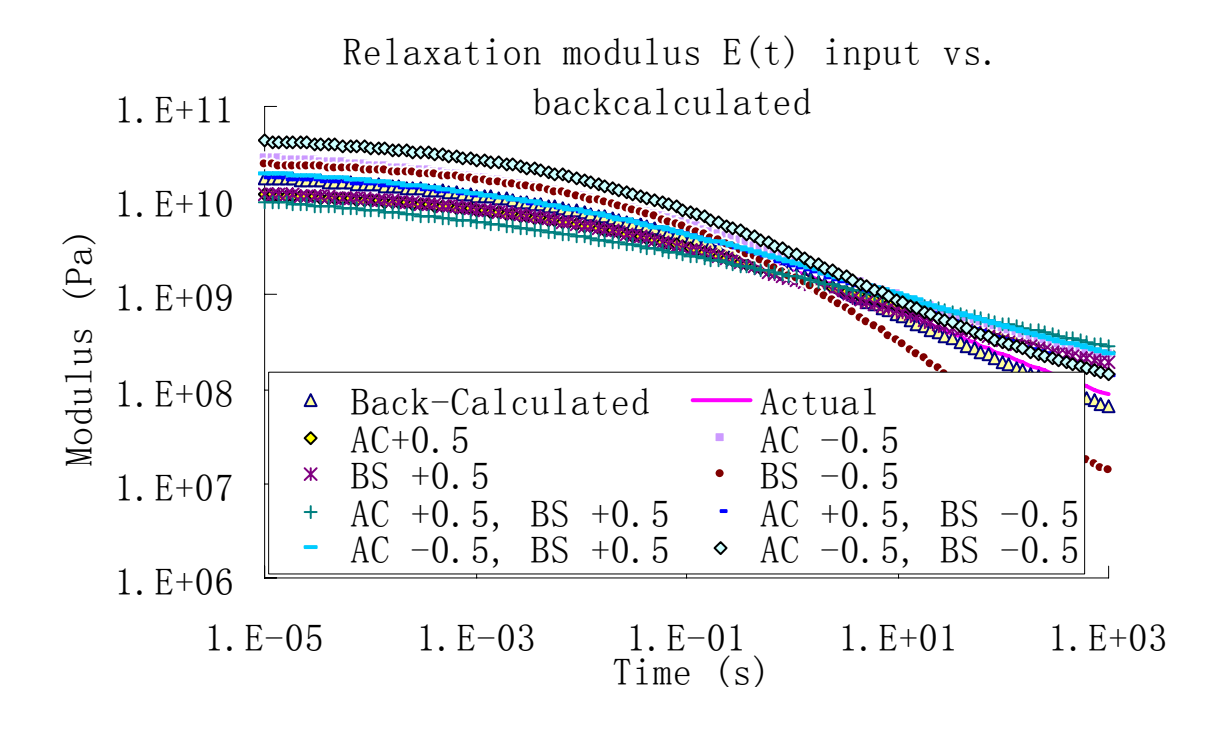


Figure 135: Sensitivity analysis of E(t) for layer thickness (Case D)

Above examples show the backcalculation program can catch the tendency very well, but the error of the dynamic modulus may vary as high as 100%. Therefore, the thickness of each physical layer should be as accurate as possible in the field FWD test.

#### 6.3.5 Discussion of Sensitivity Analyses

Above sensitivity analysis show that the time information is extremely important in the VE backcalculation; great effort is required to make sure the sensors data are sampled at the right time with the right interval. The accuracy of deflection measurement is important, but not as significant as time information. The layer thickness can significantly affect the VE backcalculation results, and it must be very accurate in the field FWD test. The best way of estimating the layer thickness is field coring or using ground penetration radar (GPR).

#### **6.4 Summary**

- Four numerical examples from VE forward solution, and four numerical examples from dynamic solution SAPSI, show the VE backcalculation algorithm works much better than the static backcalculation result from MODCOMP5. The algorithm is inappropriate if there is shallow bedrock underneath.
- The modulus of base or subgrade layer may vary from the actual result, with error around 10%. If realistic pavement structure is constructed with the base layer stiffer than the subgrade layer, like the numerical examples from VE forward solution, the error can be reduced significantly.
- Three field FWD test data were input into the backcalculation program. The program

convergence was very good; however, the results may be questionable. Because the data collection in the field test is very critical, the accuracy of the program needs further verification.

A sensitivity analysis was done for the main input variables. The analysis showed that errors in the deflection time-histories are the most significant factor affecting the backcalculated AC relaxation and complex modulus curves. Also, the layer thicknesses should be as accurate as possible.

## **Chapter 7. Conclusions and Recommendations**

#### 7.1 Summary

In this research, a new method for backcalculating viscoelastic (VE) parameters of a layered flexible pavement system, based on a layered viscoelastic solution and using FWD deflection time histories, has been developed. The method allows for theoretically backcalculating the asphalt concrete complex and relaxation modulus curves, and base and subgrade layer moduli for a three layer system. A four-parameter sigmoid function is prescribed to describe the variation of  $|E^*|$  in frequency domain and of E(t) in time domain, respectively. The total number of unknowns in the inverse problem is six. In order to effectively use the layered viscoelastic solution, the time delays for the deflection sensors are eliminated since they are due to wave propagation. On the other hand, the time delays of the farther sensors are used to estimate a seed value for the subgrade modulus based on wave propagation theory.

The VE backcalculation algorithm is an extension of the solution used in the MICHBACK program (Harichandran et al., 1994). It uses the modified Newton's method to obtain a least squares solution of an over determined set of equations. In the MICHBACK solution, these sets are real-valued and correspond to the peak deflection values. In this research, the author uses deflection time histories, or many deflection basins, since the proposed backcalculation scheme uses a layered VE solution to predict the time-dependent deflection basins. The singular value decomposition (SVD) with scaling is used to find the inverse of the gradient matrix. To avoid local minima, a random function inside the backcalculation algorithm is used to generate a

different set of values once a solution is found by the Newton's method. This is done multiple times so that a number of different potential solutions are obtained. The best candidate from these solutions is the set with the minimum error for matching the defection time histories. Finally, the best candidate set of values is input as seed values in MATLAB's internal function "fminsearch" which is then used to select the final solution.

The new program was theoretically verified using synthetic data, and was evaluated using field FWD data. For the theoretical verifications, time histories of FWD surface deflections generated from the layered viscoelastic solution and from SAPSI were used to verify the capabilities of the newly developed VE backcalculation program. Various pavement profiles of different combinations of layer thicknesses and moduli were analyzed. Some profiles included cases where there was a shallow bedrock or ground water table. In addition a sensitivity analysis was conducted to investigate the effects of measurement errors in the deflection time histories, and layer thicknesses.

To evaluate the applicability of the new VE backcalculation program to interpret field tests, measured deflection time history data from several FWD tests conducted at the FHWA Turner-Fairbanks Accelerated Loading Facility were used to backcalculate relaxation modulus curves for the AC layer. These were then compared with the laboratory derived relaxation modulus curves obtained from laboratory compacted specimens of the same AC mixtures.

#### 7.2 Conclusions

Based on the theoretical verification analysis, the following conclusions are drawn:

• The backcalculation results show very good agreement with the actual modulus values.

The error in the base and subgrade moduli is generally less than 3%. The AC layer

relaxation and complex modulus curves match the actual functions within the range of 0.0001 to 0.1 sec, and 10 to 10,000 Hz, respectively.

• When shallow bedrock exists, the backcalculated and actual deflection time histories and relaxation and complex modulus curves do not match well. The reason for this discrepancy is that the stiff layer traps the wave energy within the pavement structure, and thus it cannot be simulated by the layered VE solution.

The verification of the new VE backcalculation solution using field measured deflection time histories under FWD testing showed very good agreement between backcalculated and laboratory derived relaxation modulus curves, especially considering that laboratory and field conditions are known to be different.

Finally, a sensitivity analysis was done for the main input variables. The analysis showed that errors in the deflection time-histories are the most significant factor affecting the backcalculated AC relaxation and complex modulus curves. Also, the layer thicknesses should be as accurate as possible.

#### 7.3 Recommendations

The proposed VE forward solution is inappropriate to simulate the pavement response under FWD test if there is shallow bedrock underneath. The reason of this discrepancy is that the stiff layer traps the wave energy within the pavement structure, and thus it cannot be simulated by the layered VE solution. Therefore, for these cases, a full dynamic solution which takes into account inertial and wave propagation effects is required. Further research is necessary to improve the computational efficiency of the dynamic solution.

The proposed method (k-value) to estimate the elastic modulus of the subgrade layer does

not work well if there is shallow bedrock underneath. This is because it is based on the Raleigh wave solution which is applicable to a deep subgrade (half-space). The Love wave solution is suitable for a stiff layer condition; however, the solution does not lead to a simple relationship between wave velocities and elastic modulus of the subgrade.

In order to improve the interpretation of field measured FWD test records, it is recommended that enhancements in data collection accuracy and FWD technology are pursued. Examples of such enhancements include longer duration loading, better measurement accuracy in the unloaded time range, and more accurate temperature measurements in the AC layer. Such enhancements will improve the accuracy of the AC modulus curves in a wider range of time and/or frequency.

If the time-temperature shift function is known, FWD test can be done at different temperatures, and backcalculation is done for each temperature. By combining the results at the different temperatures, the range of |E\*| and E(t) can be extended. However, very low frequencies and/or very long times, Witczak's or similar regression equations can help in estimating the values in these ranges.

# **BIBLIOGRAPHY**

#### **BIBLIOGRAPHY**

- W. E. A. Acum, L. Fox. 'Computation of Load Stresses in a Three-Layer Elastic System', Geotechnique, Vol. 2, No. 4, pp 293 300, 1951.
- R. Al-Khoury, A. Scarps, C. Kasbergen, and J. Blaauwendraad. *'Spectral Element Technique for Efficient Parameter Identification of Layered Media. Part I: Forward Calculation'*, International Journal of Solids and Structures, Vol. 38, pp 1605 1623, 2001.
- W. S. Mogawer, A. J. Austerman, M. E. Kutay, and F. Zhou. *'Utilizing Linear Viscoelastic Continuum Damage and Fracture Mechanics Approaches to Evaluate Binder Elasticity as a Simple Performance Test for Fatigue Cracking of Polymer Modified HMA Mixtures'*. Road Materials and Pavement Design, in press, 2010.
- G. Y. Baladi. 'Integrated Material and Structural Design Method for Flexible Pavements', Vol. 1: Technical Report, FHEA, 1988.
- Gilbert Y. Baladi, Personal Communications. January, 2010.
- D. M. Burmister. 'The Theory of Stresses and Displacement in Layered Systems and Application to the Design of Airport Runways', Proceeding Highway Research Board, Vol. 23, 1943.
- A. J. Bush. 'Computer Program BISDEF', US Army Corps of Engineer Waterways Experiment Station, Vicksburg. Miss., 1985.
- A. J. Bush, D. R. Alexander. *'Pavement Evaluation Using Deflection Basin Measurements and Layered theory'*, Transportation Research Record, No. 1022, Transportation Research Board, National Research Council, Washington D. C., pp 16 29, 1985.
- K. Chatti, A. Iftikhar, and H. B. Kim. 'Comparison of Energy Based Fatigue Curves for Asphalt Mixtures Using Cyclic Indirect Tensile and Flexural Tests'. 2<sup>nd</sup> International Conference on Engineering Materials, pp. 271 282, 2001.
- E. Y. G. Chen, and E. Pan. 'Responses of a transversely isotropic layered half-space to multiple horizontal loads.' ASCE Geotechnical Special Publication: Innovations in the Characterization, Modeling and Simulation of Pavements and Materials, 2007.
- Ewan Yuanguo Chen. 'Viscoelastic Modeling of Flexible Pavement', Ph.D. dissertation, University of Akron, Akron, 2009.
- E. Y. G. Chen, E. Pan, and R. Green. 'Surface loading of a multilayered viscoelastic pavement: A semi-analytical solution.' Journal of Engineering Mechanics, ASCE, 2009.
- S. S. Chen. 'The Response of Multilayered Systems to Dynamic Surface Loads', Ph.D. dissertation, University of California, Berkeley, 1987.

- Shengkai Chen, Jianming Ling, Zhigang Luo. 'Stress-dependent Characteristics and Prediction Model of the Resilient Modulus of Subgrade Soils', China Civil Engineering Journal, vol. 40, No. 6, pp. 95 99 + 104, June 2007.
- K. M. Chua, R. L. Lytton. *'Load Rating of Light Pavement Structures'*, Transportation Research Record, No. 1043, Transportation Research Board, National Research Council, Washington D. C., pp 89 102, 1985.
- Jo Sias Daniel, Y. Richard Kim, Hyun-Jong Lee. 'Effects of Aging on Viscoelastic Properties of Asphalt-Aggregate Mixtures', Transportation Research Record, No. 1630, Transportation Research Board, National Research Council, Washington D. C., pp 21 27, 1998.
- J. F. Doyle. 'Wave Propagation in Structures: Spectral Analysis Using Fast Discrete Fourier Transforms'. Springer, New York, 1997.
- V. S. Endiran. 'Nonlinear dynamic computer modeling of flexible pavements', Ph.D. dissertation, University of Hong Kong, Hong Kong, 1999.
- W. Maurice Ewing, Wenceslas S. Jardetzky, Frank Press, 'Elastic Waves in Layered Media', McGraw-Hill Book Company, Inc. New York, Toronto, London, 1957.
- Federal Highway Administration, U.S. Department of Transportation. 'Resilient Modulus of Unbound Granular Base/Subbase Materials and Subgrade Soils', Long-Term Pavement Performance, Protocol 46, http://www.tfhrc.gov/pavement/ltpp/pdf/p46.pdf, 1996.
- V. Ganji, N. Gucunski, and S. Nazarian. 'Automated inversion procedure for spectral analysis of surface waves', J. Geotech. Engrg., ASCE, v. 124, n. 8, p. 757 770, 1998.
- R. S. Harichandran, T. Mahmood, A. Raab, and G. Y. Baladi. *'Backcalculation of Pavement Layer Moduli, Thicknesses and Bedrock Depth Using a Modified Newton Method'*, In Nondestructive Testing of Pavements and Backcalculation of Moduli (Second Volume), ASTM STP 1198, H. L. Von Quintus, A. J. Bush and G. Y. Baladi (eds.) American Society for Testing and Materials, Philadelphia, PA, pp. 68 82, 1994.
- Ronald S. Harichandran, Personal Communications. May, 2008.
- H. Y. Huang. 'Pavement Analysis and Design', Prentice Hall, Pearson Educaion, Inc., Upper Saddle River, New Jersey, 2004.
- L. H. Irwin. 'Instructional Guide for Backcalculation and the Use of MODCOMP', CLRP Publication No. 94-10, Cornell University, Local Roads Program, Ithaca, NY, March, 1994.
- Yigong Ji. 'Frequency and Time Domain Backcalculation of Flexible Pavement Layer Parameters'. Ph.D. dissertation, Michigan State University, East Lansing, 2005.
- E. Kausel and J. M. Roesset. 'Stiffness Matrices for Layered Soils'. Bulletin of the Seismological Society of America, Vol. 71 No. 6, pp.1743 ~ 1761, December, 1981.

- E. Kausel, R. Peek. 'Dynamic Loads in the Interior of a Layered Stratum: An Explicit Solution', Bulletin of the Seismological Society of America, Vol. 72, No. 5, pp 1459 1482, 1982.
- Y. Richard Kim, Youngguk Seo, Mark King, and Mostafa Momen. 'Dynamic Modulus Testing of Asphalt Concrete in Indirect Tensile Mode'. Transportation Research Record, n 1891, pp. 163 173, 2004.
- Y. Richard Kim. 'Modeling of Asphalt Concrete', McGraw-Hill, August, 2008.
- Y. Richard Kim, N. Guddati Murthy, B. Shane Underwood, et al. 'Development of a Multiaxial VEPCD-FEP++'. Final report, May, 2008.
- M. E. Kutay, N. Gibson and J. Youtchef. *On-going unpublished research involving analysis of FHWA ALF data*, 2008 2009.
- M. E. Kutay, K. Chatti, L. Lei. 'Backcalculation of Dynamic Modulus (|E\*|) Mastercurve from FWD Surface Deflections'. Transportation Research Board, Proceeding, Washington D.C., 2011.
- E. Levenberg, 'Validation of NCAT Structural Test Track Experiment using INDOT APT Facility', Final Report. North Central Superpave Center, Joint Transportation Research Program Project No. C-36-31R SPR-2813, Purdue University, 2008.
- T. Mahmood. 'Backcalculation of Pavement Layer Properties from Deflection Data', Ph.D. dissertation, Michigan State University, East Lansing, 1993.
- NCHRP. '2002 Design Guide: Design of New and Rehabilitated Pavement Structures', Draft Final Report, NCHRP Study 1-37A, National Cooperative Highway Research Program, Washington D.C., July, 2004.
- A. T. Papagiannakis and E.A. Masad. 'Pavement Design and Materials', John Wiley & Sons, Inc., Hoboken, New Jersey, 2008.
- S.W. Park and R.A. Schapery, 'Methods of Interconversion between Linear Viscoelastic Material Functions. Part I a Numerical Method Based on Prony Series.', International Journal of Solids and Structures, Vol. 36, pp. 1653 1675, 1999.
- W. H. Press, B. P. Flannery, S. A. Teukolsky, W. T. Vetterling. 'Numerical Recipes', Cambridge University Press, Cambridge, 1989.
- Lufti Raad, Jose L. Figueroa. 'Load Response of Transportation Support System', Journal of Transportation Engineering, American Society of Civil Engineers, Vol. 106, No. 1, pp 111 128, 1980.
- F. E. Richart, Jr., R. D. Woods, J. R. Hall, Jr. *'Vibrations of Soils and Foundations'*, Prentice-Hall, Inc., Englewood Cliffs, New Jersey. 1970.

- S. A. Rizzi, J. F. Doyle. 'A spectral element approach to wave motion in layered solids'. Journal of Vibration, Acoustics, Stress, and Reliability in Design. Vol. 114, No. 2, pp 133 140, April, 1992.
- J. M. Roesset, Kenneth H. Stokoe II, Chia-Ray Seng. 'Determination of Depth to Bedrock from Falling Weight Deflectometer Test Data', Transportation Research Record, No. 1504, Transportation Research Board, National Research Council, Washington D. C., pp 68 78, 1995.
- R.A. Schapery. 'Method of Viscoelastic Stress Analysis using Elastic Solutions'. Journal of the Franklin Institute, Vol. 279, No. 4, pp 268 ~ 289, 1965.
- R.A. Schapery. 'Viscoelastic Behavior and Analysis of Composite Materials'. Mechanics of Composite Materials. New York, Academic Press, Inc., pp 85 168, 1974.
- R. A. Schapery. 'Correspondence Principles and a Generalized J Integral for Large Deformation and Fracture Analysis of Viscoelastic Media'. International Journal of Fracture, No. 25, pp 195 223, 1984.
- Richard N. Stubstad, Shiraz D. Tayabji, Erland O. Lukanen. 'LTPP Data Analysis: Variations in Pavement Design Inputs', NCHRP Web Document 48 (Project 20-50[5]), http://onlinepubs.trb.org/onlinepubs/nchrp/nchrp\_w48.pdf, 2002.
- Richard Stubstad, Jiang Y. Jane, Erland Lukanen. 'Forwardcalculation of Pavement Moduli with Load-Deflection Data', Transportation Research Record, No. 2005, pp 104 111, 2007.
- J. Uzan. 'Dynamic Linear Backcalculation of Pavement Material Parameters', Journal of Transportation Engineering, American Society of Civil Engineers, Vol. 120, No. 1, pp 109 126, 1994.
- H. Warren, W. L. Dieckmann. 'Numerical Computation of Stresses and Strains in a Multiple-layer Asphalt Pavement System', Internal report, Chevron Research Corporation, Richmond, AC, 1963.
- Ning Xiang, Personal Communications. November, 2009.
- M. S. Yeh. 'Nonlinear Finite Element Analysis and Design of Flexible Pavements'. Ph.D. Dissertation. Michigan State University, East Lansing, 1989.
- E. J. Yoder, M. W. Witczak, 'Principles of Pavement Design', Wiley, New York, 1975.